INVESTIGATION ON MICRO-CUTTING MECHANICS WITH APPLICATION TO MICRO-MILLING

A thesis submitted in partial fulfillment of the requirements of Brunel University London for the degree of Doctor of Philosophy

By

Feifei Jiao

College of Engineering, Design and Physical Sciences

Brunel University London

October 2015

Abstract

Nowadays technology development places increasing demands on miniature and micro components and products, and micro-milling is one of the most flexible machining processes in manufacturing 3D structures and complex structured surfaces. A thorough and scientific understanding on fundamentals of the micro-milling process is essential for applying it in an industrial scale. Therefore, in-depth scientific understanding of the micro-cutting mechanics is critical, particularly on size effect, minimum chip thickness, chip formation, tool wear and cutting temperature, etc. so as to fulfil the gap between fundamentals and industrial scale applications. Therefore, three key fundamental research topics are determined for this research, and a comprehensive study on those topics is conducted by means of modeling, simulation, experiments. The topics include chip formation process in micro-milling, novel cutting force modeling in multiscale and study on the tool wear and process monitoring.

The investigation into chip formation process in micro-milling consists of three stages; the micro-cutting process is firstly simulated by means of FEA with a primary focus on finding the minimum chip thickness for different tool/material pair and explaining the size effect; the simulation results are then validated by conducting micro-cutting experiment on the ultra-precision lathe. Experiments are carried out on aluminium 6082-T6 with both natural diamond and tungsten carbide tool. By knowing the minimum chip thickness for different tool/material pair, the chip formation process is investigated by performing comparative study by using the diamond and tungsten carbide micro-milling tools. As the minimum chip thickness for diamond micro-milling tool is smaller than that for tungsten carbide tool compared to nominal chip thickness, MCT is ignored in diamond micro-milling. Thus the comparative study is conducted by utilizing both tools with perfectly sharpened cutting edge and tools with the rounded cutting edge in micro-milling. The chips are inspected and associated with cutting force variations in the micro-milling process. The findings are further consolidated by comparing with research results by other researchers.

The cutting force modeling is developed in three different aspects, e.g. cutting force on the unit length or area and cutting force on the unit volume in order to better understand the micro-cutting mechanics in aspects of size effect, tool wear mechanism and the cutting energy consumption. The mathematical modeling firstly starts with a novel instantaneous chip thickness algorithm, in which the instantaneous chip thickness is computed by taking account of the change of tool geometry brought about by the tool runout; then the collected cutting forces are utilized to calibrate the model coefficients. For accurate measurement on cutting forces, the Kalman Filter technique is employed to compensate the distortion of the measured cutting force. Model calibration is implemented using least-square method. The proposed cutting force model is then applied in micro-milling to represent the conditions of tool wear and the cutting energy consumption. Further study on the surface generation simulation is based on force model and its comparison with the machined surface is also performed.

Cutting experiments using the new tungsten carbide tool are carried out and the tool wear is monitored offline at different machining stages. The dominant tool wear types are characterised. Tool wear is investigated by mainly analysing cutting force at different tool wear status. Frequency analysis by Fourier Transform and Wavelet Transform are carried out on the force signals, and features closely related to the tool wear status are identified and extracted. The potential of applying these features to monitoring the tool wear process is then discussed. Experimental studies to machine the structured surface and nano-metric level surface roughness are presented, the machining efficiency, dimensional accuracy and tool-path strategies are optimised so as to achieve the desired outcomes. Moreover, investigation on cutting temperature in micro-cutting is also studied to some extent by means of simulation; the influence of cutting edge radius on cutting temperature is particularly investigated. Investigation on above aspects provides systematic exploration into the micro-milling process and can contribute substantially to future micro-milling applications.

Acknowledgement

First and foremost, I would like to express my wholehearted gratitude to my supervisor, Professor Kai Cheng, for his precious advices, instructions, guidance and encouragement throughout the research process. I wouldn't finish the PhD study without his help and support.

Special thanks are due to the China Scholarship Council for the financial support on living expenses throughout the four years. I would also like to extend my thanks to Korean Institute of Machinery and Materials for financially sponsoring me the tuition fees.

Personal appreciation is given to my colleagues Dr Atanas Ivanov, Dr Worapong Sawangsri, Dr Hui Ding and Dr Chao Wang for their invaluable discussion and support throughout the research, also to Mr Paul Yates for his helpful assistance in all the experiments. I am also grateful to Mr Amir Mir from University of Strathclyde, Professor Anthimos Georgiadis and Mr Antoni Barceló from Leuphana University, Germany.

I would also like to acknowledge my postgraduate tutor Professor Xiaoqiang Peng for his support and encouragement even in such a distance.

This thesis is also dedicated to my beloved family for their constant belief, endless support and unconditional love, which is the source of power and motivation for all I have achieved so far in my life.

Table of Contents

Abbreviations

ANOVA	Analysis of variance
ALE	Arbitrary Lagrangian–Eulerian
CER	Cutting edge radius
CVD	Chemical vapour deposition
CWT	Continuous wavelet transform
DAQ	Data acquisition
dbN	Daubechies wavelets
DOC	Depth of cut
DWT	Discrete wavelet transform
FEM/A	Finite element method/analysis
FRF	Frequency response function
FT	Fourier transform
FTS	Fast tool servo
ICT	Instantaneous chip thickness
KF	Kalman filter
LSM	Least square methods
MCT	Minimum chip thickness
MD	Molecular dynamics

MEMS	Micro electro-mechanical systems
MRR	Material removal rate
MS	Multiscale simulation
PCD	Polycrystalline diamond
PMMA	Poly methyl methacrylate
PSD	Power spectral density
RMS	Root mean square
SCD	Single crystal diamond.
SEM	Scanning Electron Microscope
SNR	Signal to noise ratio
SPDT	Single point diamond turning
STFT	Short-Time Fourier Transform
TCM	Tool condition monitoring
WC	Tungsten carbide
WT	Wavelet transform

Nomenclature

A	Initial yield strength	(MPa)
$\dot{\varepsilon}$	Equivalent plastic strain-rate	(s^{-1})
$\dot{\varepsilon}_0$	Reference strain-rate	(s^{-1})
T_0	Room temperature	(℃)
T_m	Melting temperature of the material	(℃)
P	Density	(kg/m3)
E	Elastic modulus	(GPa)
Cp	Specific heat	(J/kg/ ℃)
λ	Thermal conductivity	(W/m/C)
α_d	Expansion coefficient	(µm.m/°C)
G_f	Fracture energy	(J/m2)
τ_p	Ulimate shear stress	(MPa)
h	Heat transfer coefficient	($Wm^{-2}K^{-1}$)
r	Tool run-out	(µm)
α	Tool run-out angle	(°)
w	Spindle angular speed	(rad/s)
f	Feedrate	(mm/min)
R	Nominal radius of each tool tip	(µm)

γ_c	Tool rake angle	(°)
θ	Position angle of kth tooth	(°)
$h(t,k)$	Computed instantaneous chip thickness	(μm)
$h_a(t,k)$	Actual instantaneous chip thickness	(μm)
K_{rp}	Radial ploughing coefficient	(N/mm^2)
K_{tp}	Tangential ploughing coefficient	(N/mm^2)
A_p	Ploughed area between the tool and workpiece	(μm^2)
K_{re}	Radial edge coefficient	(N/mm^2)
K_{te}	Tangential edge coefficient	(N/mm^2)
dz	Axial height of each differential flute element	(μm)
r_e	Cutting edge radius	(μm)
h_{min}	Minimum chip thickness	(μm)
F_r, F_t	Force in radial and tangential direction	(N)
F_x, F_y	Force in x and y direction	(N)
l	Contact length between tool and material	(μm)
s	Cutting area in micro-milling	(μm^2)
$H(s)$	Transfer function of measuring system	
T	Transformation matrix	
L	Kalman filter gain	
$T(s)$	Kalman filter transfer function	

k	Tooth number
N	Number of tool teeth
μ	Friction coefficient
d_1	Initial failure strain
d_2	Exponential factor
d_3	Triaxiality factor
d_4	Strain rate factor
d_5	Temperature factor
ν	Poisson's ratio
B	Model parameters
N	Strain-hardening exponent
m	Thermal softening exponent
C	Strain-rate sensitivity

List of Figures

List of Tables

1 Introduction

1.1 Brief history of micro-milling and its challenges

1.1.1 Research background

The past two decades have witnessed global increase in demand for high-accuracy miniaturized components and micro-parts, especially in sectors like electronics, medical, biotechnology, telecommunications, and energy fields, whose wide applications have the potential to significantly improve quality of life and personal wellbeing(Masuzawa 2000; Alting et al. 2003; Liu et al. 2005b; Chae et al. 2006). The micro-manufacturing technology is significantly boosted due to this ever-increasing demand. Micro-manufacturing refers to the fabrication of high-accuracy three-dimensional products on a variety of materials and possessing features whose sizes range from tens of micrometres to a few millimetres. It is a key enabling technology for the widespread exploration of micro-technology developments which bridges the gap between the nano- and macro-worlds (Ehmann et al. 2005), in fact of the difficulty in achieving micro feature size and accuracy with macroscale machining.

Micro-mechanical machining including micro-turning, micro-milling, micro-drilling and micro-grinding is widely applied in micro-manufacturing as they have higher material removal rate and great ability to machine 2D and 3D micro parts on a variety of engineering material. Among the aforementioned techniques, micro milling has the most flexibility and therefore obtains most popularity in various applications.

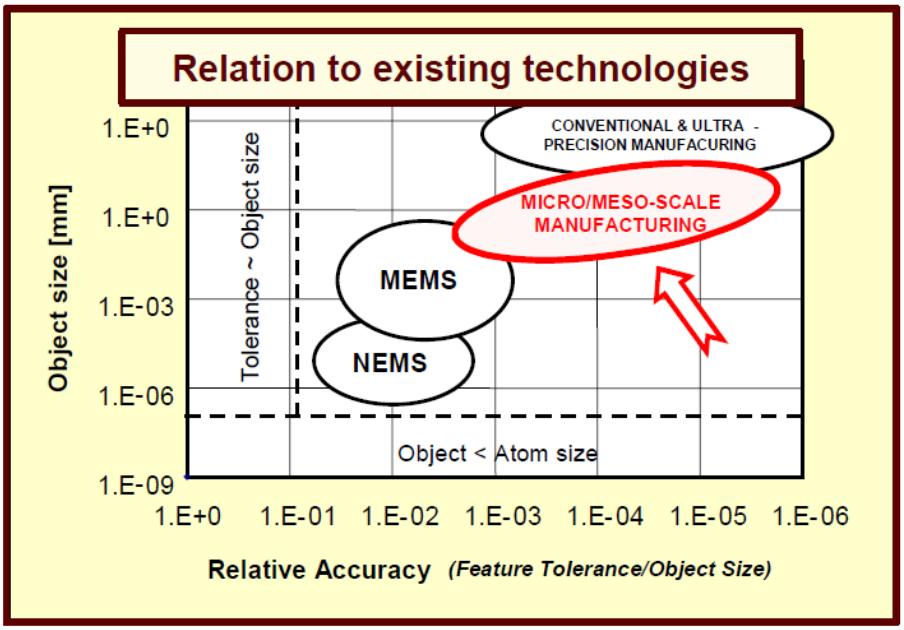

Figure 1.1 Micro-manufacturing size/precision domain (Ehmann et al. 2005)Research on micro-milling process has been extensive since then as a result of the strongly industry-driven demand. It is the scaled-down version of conventional macro-milling process with the miniaturization of machine tools, cutting tools, and process variable. There are similarities between macro- and micro-milling with both of them referring to employing geometrically defined cutting edge to remove material away from workpiece and create the desired shapes, thus it is kinematically similar to conventional cutting, however, there are a number of issues that prevail in micro-cutting which influence the mechanism of cutting and invalidate most of the knowledge and physics laws in macro-scale (Cheng and Huo 2013).

1.1.2 Macro- and micro-milling

The macro-milling process has been investigated massively and well understood in its cutting mechanics, process dynamics, tool wear mechanism and machining performance (Altintas 2000). Apart from similar issues in micro-milling process, more features differentiate itself from macro-milling.

From aspect of hardware, the size and geometry of micro-milling tool determine the limit of size and dimensional accuracy of micro features. For micro-milling tool, its diameter usually falls in the range of tens of micrometres to 1mm. Consequently, it requires the machined tool to have sufficient spindle speed and high accuracy in order to achieve the needed cutting speed and machining accuracy on micro parts.

Since the machines usually work in high spindle speeds, the related dynamic performance of the machine such as damping, dynamic stiffness, motion accuracy, and thermal distortion, therefore, needs to be superior.

Process variables including feedrate and depth of cut tend to be more conservative due to the fragility of micro-milling tool. Masuzawa et al. (1997) defines the micro-macro border around 200μm which changes accordingly to advances in machining technology. Currently uncut chip thickness less than tens of microns is widely accepted by micro-machining community. With regards to dimension and accuracy of micro features or parts, their size usually falls below 1mm in at least two dimensions, and it should achieve accuracy better than a few microns or relative accuracy of 10^{-3}~10^{-5}.

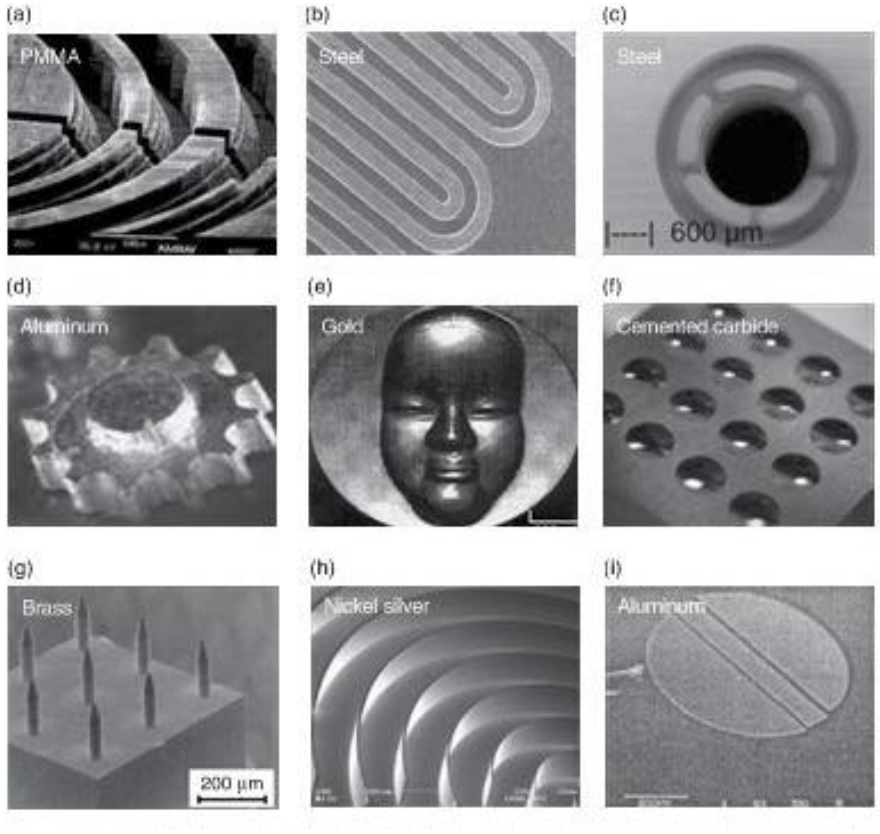

Figure 1.2 Examples of high precision component made by micro-cutting (Cheng and Huo 2013)

Material microstructure effect is another aspect which differs greatly from conventional milling. In conventional cutting, materials are considered to be homogeneous and isotropic; in micro milling, typical grain size varies between a few micrometres to approximately 100μm, which is the same order of cutting parameters and tool diameter. This factor has significant impact on cutting mechanism, researchers have found that changing the microstructure of material such as grain

size, crystallographic orientation, can affect the cutting force, chip formation, surface roughness and burr formation (Yuan et al. 1994; Simoneau et al. 2006a; Simoneau et al. 2006b).

Last and the foremost, the underlying cutting mechanics is quite different from what is known in conventional milling. In micro-milling, the cutting edge radius for tungsten carbide tool is normally around several microns. Under this condition, it is comparable in order with the uncut chip thickness and material grain size, a variety of issues are arisen including cutting edge radius effect, negative rake angle, minimum chip thickness effect, material microstructure effect and elastic recovery effect, most of which are usually ignored in conventional milling. To thoroughly understand the micro-milling process and give instruction in machining, the fundamental micro-cutting mechanics must be fully investigated and well understood. Moreover, in macro-machining, the product is mostly characterised by dimension, tolerance and surface roughness; while in micro-milling, additional requirements on functional properties (physical, chemical and biological etc.) are attached to the products(Alting et al. 2003). Especially in recent years, structured surfaces with particular designed functions are gaining wide applications (Evans and Bryan 1999, Bruzzone et al. 2008); Structured surfaces may refer to surfaces with a deterministic pattern of usually high aspect ratio geometric features designed to give a specific function (Evans and Bryan 1999; Bruzzone et al. 2008) as shown in Figure 1.3. Functional properties are of the key importance in characterising the product, traditional characterising parameters are not sufficient to define the product any more.

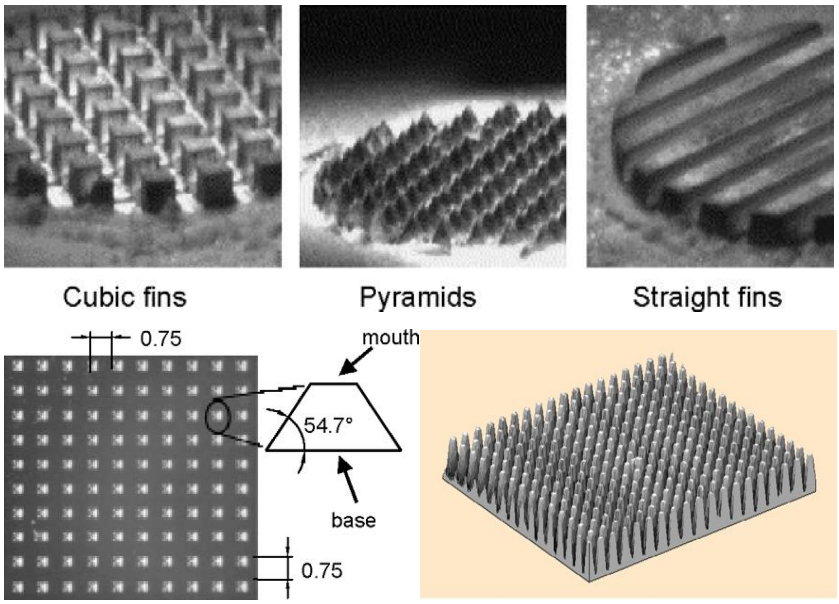

Figure 1.3 Structured surfaces in micro domain (Bruzzone et al. 2008)

1.1.3 Scientific and technical challenges

Micro-cutting mechanism

In micro-milling, the effects of scaling on the process mechanism – including chip formation, cutting forces, vibration, process stability, and the surface quality – are some of the important issues that are not fully understood (Ehmann et al. 2005). A fundamental and comprehensive understanding on the cutting mechanics in micro-milling is of great importance, as the issues raised by scaling-down may demonstrate in various forms for different tool/material pair. As distinguished from other forms of cutting, micro-milling is an intermittent process with uncut chip thickness varies periodically. Research interests should particularly focus on the size effect, minimum chip thickness effect and its manifestation in micro-milling process. Thus the chip formation process is critical in interpreting the cutting mechanics in micro-milling.

Cutting force modeling

The cutting force is the mostly used process signal to analyse the micro-milling machining, it's directly related to cutting mechanism such as chip formation, surface generation, process dynamics; it also contains concealed information on process cutting temperature, tool wear status etc. However, cutting force in micro-milling is different from conventional milling in terms of both amplitude and characteristic due to the scaling effect. Conventional force models are mostly based on work by Oxley, Armarego, Shaw and Trent, which are not sufficient enough to explain the process behaviour in micro-milling; force models in micro-milling proposed by many researchers (Bao and Tansel 2000; Vogler et al. 2003b; Zaman et al. 2006; Afazov et al. 2010) by means of analytical, numerical or empirical approaches are focused on prediction of force magnitude. While the force amplitude in micro-milling is usually less than 1N, thus the magnitude is of less significance. A cutting force which can better explain the cutting mechanics such as size effect, chip formation, cutting temperature change and tool wear etc. is critically important. In this thesis, an innovative approach to model the cutting forces is implemented to better interpret these phenomenon in the micro-domain. It can be further extended to monitor the tool wear progress which is another challenge to be addressed.

Tool wear

The structures to be machined are small in size, but high in demands of dimensional accuracy. The cutting parameters result in only small amplitude of cutting force. However, experiments and machining results show that tool wear in micro-milling is significant and can seriously deteriorate the machining accuracy and surface quality. The tool wear is also a major factor in burr formation which adversely impact micro-part's function. For small batch production of single piece, the machining quality can be controlled by replacing the worn tool, however, for structured surface machining, with an array of structure in quantity of hundreds, tool wear monitoring is of great importance in maintaining machining accuracy and consistency. Valid and effective methods to monitor the online tool wear status are much needed. Many research attempted to solve this issue by analysing process signal such as cutting force and acoustic emission based on different algorithms (Altintas 1992; Ghosh et al. 2007; Zhou et al. 2011), while there needs a reliable way to accomplish the task.

Process optimization

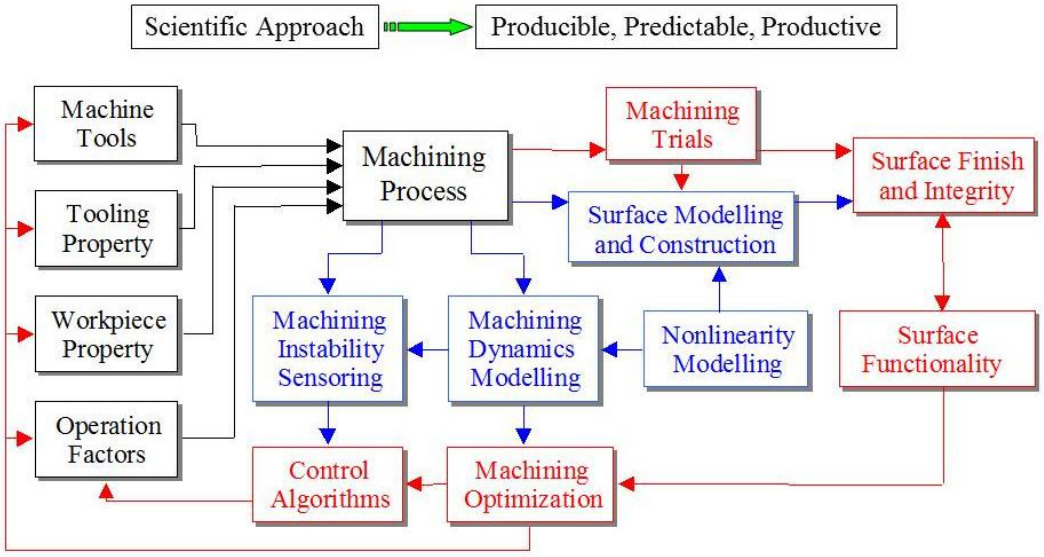

Figure 1.4 'Brunel' approach towards ultraprecision and micro manufacturing

The micro-manufacturing is a holistic process involving many factors that can affect machining quality as shown in Figure 1.4. The main influencing factors come from four aspects including machines, tool, material and cutting parameters. Various combinations of these four can result in different machining qualities. For industrial applications, it not only requires accuracy and consistency, but also efficiency and

cost-effectiveness. Thus, an optimised process will be of great importance to improve machining quality and efficiency.

1.2 Aim and objectives of the research

The aim of this research is to obtain thorough understanding on the fundamental micro-cutting mechanics and thus achieve scientific understanding in micro-milling process, and study its realistic application in micro-machining. The distinct objectives of the research are:

1) To develop simulation and experiment based approach to investigate the micro-cutting mechanics with application to micro-milling process particularly.
2) To comprehend the chip formation process in micro-milling, especially the manifestation of scaling-down effect, size effect in micro-milling.
3) To construct new cutting force modeling using specific cutting force in different dimensions to gain better understanding in micro-milling process in terms of size effect, tool wear origins and surface generation process.
4) To study the temperature in micro-cutting, mainly the difference introduced the by the unneglectable cutting edge radius.
5) To investigate the tool wear progress and related parameter to represent tool wear at different stages.

1.3 Scope of the dissertation

The dissertation consists of eight chapters which are shown in Figure 1.5 and further explained below.

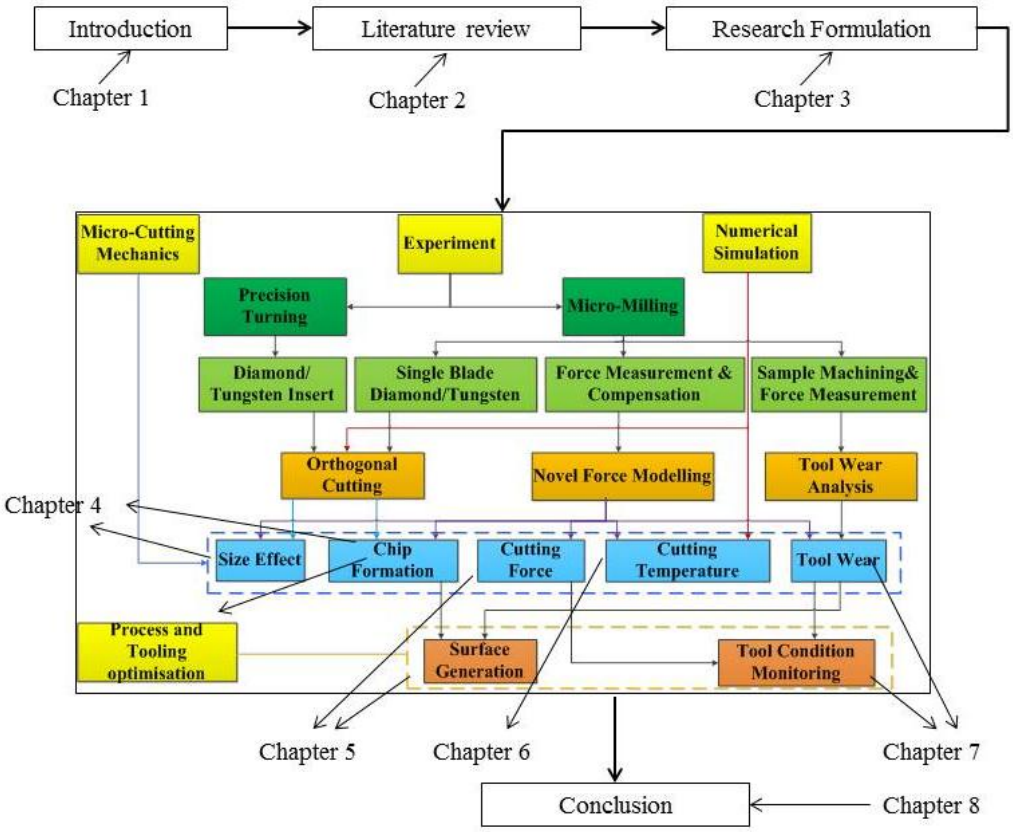

Figure 1.5 Thesis structure

Chapter 1 introduces the research background and reviews the difference between macro- and micro- milling process, the scientific and technical challenges are also presented. Research aim plus objectives and structure of the thesis are introduced.

Chapter 2 reviews the state-of-art and relevant fundamental issue in current micro-cutting community. Literatures on surface generation and process optimization are also conducted.

Chapter 3 explains the formulation of the research methods to micro-milling; particularly the experimental facilities and setup are elaborated in detail.

Chapter 4 investigates the micro-cutting mechanics with particular application to micro-milling; simulation of the micro-cutting process is conducted in software Abaqus/Explicit to study the size effect and to determine the minimum chip thickness. The simulation results are validated by carrying out experiment on the precision turning lathe with diamond and tungsten carbide tools. Chip formation process in micro-milling is emphasised by comparative study using diamond and

tungsten carbide tools, the manifestation of micro-cutting mechanics is analysed in micro-milling process.

Chapter 5 proposes the new cutting force modeling in multiscale. In this chapter, a novel chip thickness algorithm in micro milling is proposed and applied in the force model. Experiments are carried out to validate the cutting force model, its related issues such tool runout and accurate force measurement are tackled. The Kalman Filter technique is employed to compensate the distortions in measured cutting force. The proposed cutting force model is applied to analyse the micro-cutting mechanics, further the surface generation process based on the force model is analysed and compared with the experimental results.

Chapter 6 studies the cutting temperature in micro-cutting by means of finite element analysis; it's mainly focused on the change brought about by the cutting edge radius.

Chapter 7 investigates the tool wear process based on experiments; the experiments are carried out throughout the tool serving life, tool wear at different stages are measured and inspected using different devices. The cutting forces are utilized to monitor the tool wear; analysis based on Fourier Transform and Wavelet Transform are presented and potential parameters which relates to the tool wear process are identified and discussed in application of tool wear monitoring. Finally, two case studies on micro-milling of structured surfaces and nano-metric level surface finish are presented.

Chapter 8 draws conclusions derived from this research work, and recommends the future work for investigation.

2 Literature Review

2.1 Introduction

The rapid technology development in industries makes the miniature components in increasing demands in the past decade. This trend in return boosts significantly the application of micro-cutting process, such as micro-turning, micro-milling, micro-drilling etc. to keep up pace; among the available techniques, the micro-milling process attracts most intense interest as its inherent flexibility in manufacturing 3D component on a variety of materials. However, there are a number of scientific and technical challenges to be solved if micro-cutting technology and equipment are to be deployed in reliable, economic, efficient and large-scale fashion by industries. In this chapter, the extensive background and summarization of previous research on micro-cutting are reviewed.

Micro-cutting is quite different from convention cutting process in many aspects. These differences stem from the miniaturization of feature size, cutting tools and processes (Chae et al. 2006). The thorough fundamental comprehension on micro-cutting mechanics will help understand the intrinsic nature of micro-cutting process. It will be investigated from aspects of size effect, the chip formation process, modeling of cutting forces, the temperature generation and distribution and tool wear mechanism in micro cutting.

The miniaturized component, although downscaled in size, usually has complex shapes and geometries, and demands superior machining accuracy and surface qualities to fulfil desired functions. Surface generation in micro-cutting is very important in determining the usability of manufactured products (Dornfelda et al. 2007);

Nowadays large batch product requires the machining process not only to be stable and repeatable, but efficient and cost-effective. Researchers have also carried out massive investigation into the optimisation of micro-cutting process in areas of cutting process and tool design.

Literatures are reviewed in the above areas; subsequently the knowledge gaps are identified in particular topics where this study concentrates on.

2.2 Micro cutting mechanics

The characteristic phenomenon found in micro-cutting process reveals itself quite different from conventional macro-cutting process, which has been proven by numerous studies (Chae et al. 2006; Miao et al. 2007; Liu et al. 2005b). This part will look at the fundamental issue that underpins the micro-cutting mechanics and differentiate from macro-cutting.

2.2.1 Size effect

The size effect in micro-cutting, commonly known as the increases of specific cutting forces with decreases in cutting depth, is firstly reported in 1952 (Backer et al. 1952). These effects are also discovered by Masuko (1956) in turning operations and Finnie (1963) in grinding processes. Many researchers (Aramcharoen and Mativenga 2009; Shaw 2003; Vollertsen et al. 2009; Nakayama and Tamura 1968; Lucca et al. 1991) have investigated the causes. They mainly attribute the reason for it to several aspects: (1) The size effect results from the variation of material strength with specimen volume due to work-hardening, strain gradients (Subbiah, 2006) and less probability of encountering stress-reducing defects(Shaw,1962), which is in accordance with dislocation theory. (2) The ratio of the uncut chip thickness to the cutting edge radius changes the effective rake angle, which is the direct reason of size effect discovered in research. In machining, the latter speculation gained wide attention and research has been extensively on various materials.

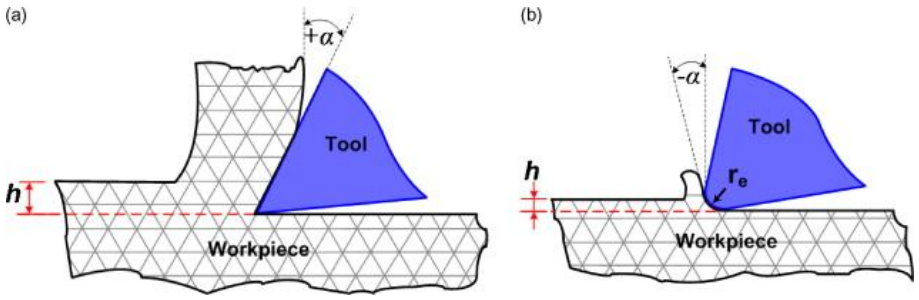

Figure 2.1 Schematic diagram of round cutting edge in micro cutting (a) conventional cutting (b) micro cutting (Aramcharoen and Mativenga 2009)

Armarego (1962) performed a series of experiments with cutting tools of varied geometry on aluminium workpiece and concluded that the rapidly increasing specific

energy is due to the high rubbing force on the clearance face of the tool. It also deduced that the shearing 'plane' concept is untenable at very small depth of cut.

Nakayama et al. (1968) carried out experiments on orthogonal cutting of brass, and proposed that the increase in specific cutting energy with decreased depth cut is caused by the decrease in shear angle, then he again performed many cutting tests at very small cutting depth and also found that the sharpness and roundness of cutting edge is an important factor which cannot be ignored.

The researchers in Japan (Furukawa and Moronuki 1988; Moriwaki 1989) also studied the phenomenon of size effect on various materials with diamond tools; they found that the specific cutting energy increases exponentially as the cutting depth reduces. Figure 2.2 clearly shows the tendency as depth of cut approaching zero. It also found that part of the increased specific cutting energy is due to the elastic recovery of material on the flank face of cutting tool which results in more friction.

The significance of ploughing and rubbing on the flank face of cutting tool is again stressed by Lucca et al.(Lucca et al. 1991). They performed diamond turning on OFHC copper and found shearing process can't account for the energy increase when cutting chip thickness approaching the edge radius. Their follow-up research (Lucca et al. 1993) investigated the influence of tool geometry on cutting forces by varying the tool's rake angle and cutting edge radius. The results show both of the two variables play significant roles in cutting. Experiments on the new tool and worn tool reveal the thrust force turns bigger than cutting force, which validates the real rake angle's significance. The larger the edge radius, the bigger the thrust than the cutting force. The resultant cutting force will be close to the thrust direction.

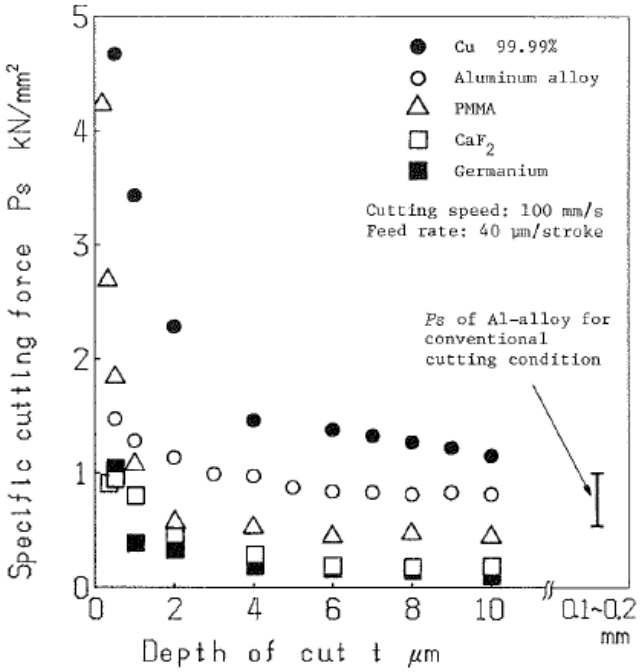

Figure 2.2 Specific cutting force in micro-cutting (Furukawa and Moronuki 1988)

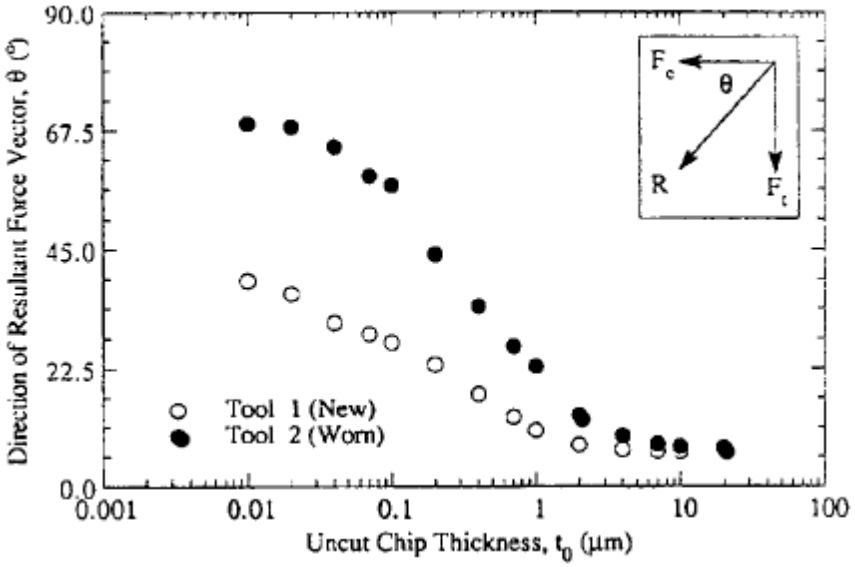

Figure 2.3 Cutting direction versus cutting depth (Furukawa and Moronuki 1988)

More recently, Bissacco et al (2006a) studied the size effect on surface generation in micro-milling process and observed the effect of increasing ratio between uncut chip thickness and edge radius. They found that the size effect is strongly revealed by the plastically deformed material accumulated in the ridge of machined surface, this is largely related to the cutting tool geometry; the second thing they discovered is that the smearing of material left behind by the tool which forms small wave-like profiles in the feed direction.

Later, research (Bissacco et al. 2008; Lai et al. 2008a; Aramcharoen and Mativenga 2009) on modeling the size effect in micro milling are also conducted. They mainly attribute the size effect in micro-milling to cutting tool geometry and material strain-hardening effect. Experiments are carried out and cutting force in machining are collected and used to interpret size effect.

The work conducted by Aramcharoen (2009) studied the size effect in micro-milling of hardened steel, in which they investigated on the ratio of chip thickness to cutting edge radius, the conclusions they drew include many aspect related to size effect. In their work, they claimed the size effect is significant when the ratio is less than unity. And the ratio is closely related to the formation of burr, the burr size will reduce along with the increase of this ratio. Another conclusion claims that surface finish and burr size can be significantly affected by cutting edge geometry. Good surface finish is more prone to achieve if under rounded cutting edges or chamfered geometries.

Some other research in recent years (Mian et al. 2011) found that the size effect is also influenced by the cutting parameter in micro-milling. They performed micro-milling tests on nickel alloy with 500um micro milling tools based on the L9 Taguchi orthogonal array. The dominant factors for size effect are determined by analysis of variance based on the acoustic emission signals. It found that improving cutting speed can reduce the specific cutting energy and improve surface finish.

Sooraj and Mathew (2011) confirmed the existence of size effect by micro-milling brass material when specific cutting forces are measured between 10 and 20 GPa for f=1–5 μm/tooth and about 70 GPa for f=0.5 μm/tooth.

Oliveiraa (2015) performed cutting trials on both macro-milling and micro-milling scale and compared the cutting results in terms of cutting forces, surface roughness, chip morphology etc. they noticed that size effect takes place in both macro and micro milling process, the significance of size effect in micro milling is due to large ratio of the uncut chip thickness to the cutting edge radius. They also found that cutting section area influences the size effect, but different geometries of cutting section result in material deformation under varied strain levels and diverse magnitudes of specific cutting forces, even if equal cutting parameters are used.

2.2.2 Chip formation

The chip formation in micro-cutting are closely related to the size effect. It is one of the most distinct characteristic in micro milling different from traditional milling process. Due to the existence of unneglectable cutting edge radius, when cutting at very small depth of cut, it results in very big negative rake angle, and no chips are produced. Only if the uncut chip thickness approaches certain threshold, chips start to form. It is widely known as minimum chip thickness effect(Vogler et al. 2002; Vogler et al. 2003a; Liu et al. 2004; Weule et al. 2001a; Kim et al. 2004a; Kang et al. 2007). This effect distinguishes itself from macro-milling very clearly. Figure 2.4 shows schematically the minimum chip thickness effect.

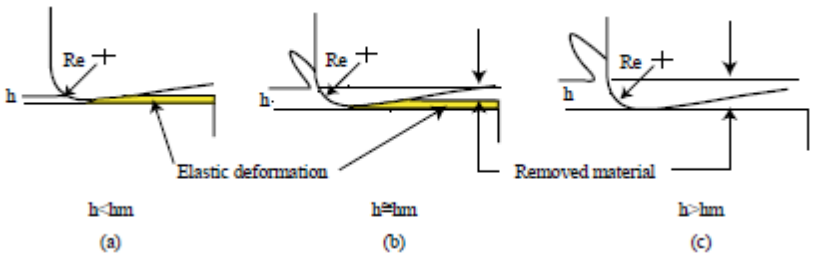

Figure 2.4 Schematic diagram of minimum chip thickness (Re, radius of cutting tool; h, undeformed chip thickness; hm, minimum chip thickness).(Chae et al. 2006)

It can be seen that when cutting takes place at very small depth of cut, material undergoes pure elastic deformation and then recovers to the original height. If the cutting depth continues to increase, the material deforms partly plastically and only if the minimum chip thickness is exceeded, the chips can be removed. Much research is conducted to determine the minimum chip thickness either by finite element simulation or experimental analysis.

Yuan (1996) is among the first to study the minimum chip thickness. They performed cutting trial on aluminium alloy to study the effect of sharpness of diamond cutting tool on chip formation; they derived the relationship between cutting edge radius and minimum chip thickness by using diamond tools of different of cutting edge radius, which are 0.3μm and 0.6μm respectively. It was found that the attainable minimum chip thickness is around 0.25~0.33 of the cutting edge radius. For fine polished diamond tools, the cutting edge can be even smaller, and the minimum cutting chip thickness can be further reduced. But the relation between minimum chip thickness and cutting edge radius doesn't change too much.

Kim (2004b) proposed a static model of chip formation to predict the minimum chip thickness based on the level of periodicity of cutting force at varied feedrate. It finds there exists a local maximum in thrust force when feedrate is at the order of minimum chip thickness. It also suggested that the periodicity of cutting force is dependent on the minimum chip thickness, tool position angle and feedrate per revolution. The following equation shows the relationship.

$$p(h_m, f_t, \theta) = \text{roundup}\left(\frac{h_m}{f_t \cdot \sin(\theta)}\right) \tag{2-1}$$

where h_m is the minimum chip thickness, f_t is the feedrate per revolution and θ is the position of tool tip.

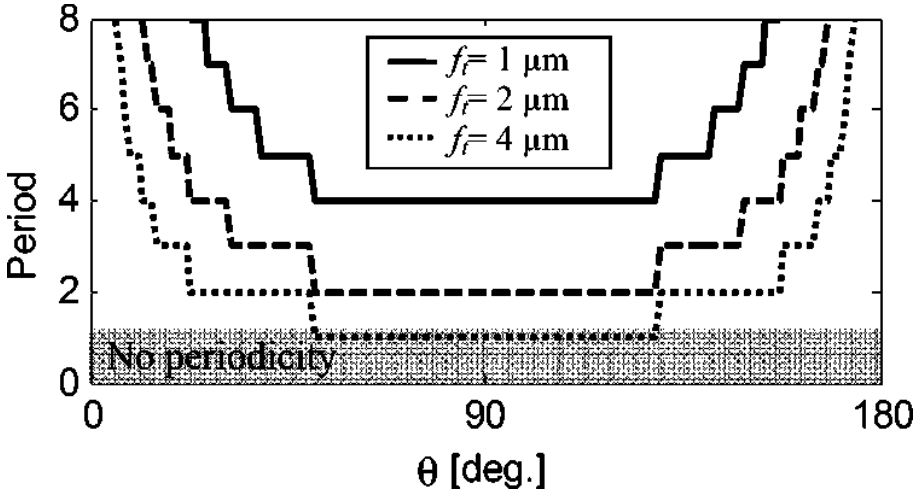

Figure 2.5 Cutting force periodicity versus position angle when minimum chip thickness is 3µm(Kim, 2004)

Figure 2.5 shows the conception of using the periodicity to approximately estimate the minimum chip thickness. They performed tests on cutting brass and found the ratio for minimum chip thickness is around 30% of the edge radius.

Other experimental work (Kang et al. 2011; Ramos et al. 2012) carried out cutting trial on AISI 1045 steel to determine the ratio of MCT to cutting edge radius in micro-milling process. Cutting force in thrust and cutting directions are decomposed and utilized to find the minimum chip thickness, which is around 0.3 of the cutting edge radius. Ramos (2012) also found that the surface roughness are closely related to the minimum chip thickness, in addition, strong independency of the minimum chip thickness value on cutting velocity and cutting edge radius is found, which will enlarge alongside the increase in the two variable.

Beside experimental effort, analytical derivation of minimum chip thickness is also investigated. Son (2005) proposed an algorithm to determine the minimum chip thickness based on the friction coefficient. In this study, he claimed that the cutting edge radius and the friction coefficient are the principal factors that determine minimum chip thickness. It assumes material in front of the cutting is divided into two types: perfectly plastic which forms the chip and perfectly elastic which recovers after machining. The cutting forces at the round edge are modelled. The relation of minimum chip thickness to friction coefficient is determined as following equation:

$$t_{\mathrm{m}} = r\left(1 - \cos\left(\frac{\pi}{4} - \frac{\beta}{2}\right)\right) \tag{2-2}$$

where β is β_e or β_p . β_e is the friction angle between tool and workpiece material. β_p is the friction angle between the tool and chips. β_e and β_p are equal in magnitude but opposite in direction. Base on this equation, the ratio between minimum chip thickness and cutting edge radius for many materials are predicted and compared with experimental results which show good agreement. They found the ratio for aluminium, copper, brass materials, the ratio lies among 0.2~0.4.

Liu (2005a) also developed an analytical model to find the minimum chip thickness values, in this model, apart from the cutting speed and tool cutting edge radius normally accounted by many research, it also takes account of other effects on the minimum chip thickness including thermal softening and strain hardening. Experiments on 1040 steel and Al6082-T6 over a range of cutting speeds and tool edge radius are performed to validate the model. The model can be expressed as follows:

$$\lambda_n = \frac{h_r}{r_n} = \frac{tc_{\min}}{r_e} = 0.5 - \frac{\tau_a}{\sigma} \tag{2-3}$$

where h_r is the minimum chip thickness in micromachining, r_n is cutting edge radius, σ is the effective flow stress of strain-hardened material, and T_a is the shear strength at chip/tool interface, which has following expression:

$$\tau_a = \frac{0.427}{3} L_m \rho \ln\left(\frac{T_m}{T_2}\right) \tag{2-4}$$

It's a function of material density ρ, latent heat of melting L_m, material's melting temperature T_m and cutting temperature T_2.

Their results found that the minimum chip thickness for carbon steel changes both with cutting velocity and cutting edge radius, while that for aluminium alloys doesn't change too much over wide range of cutting velocity

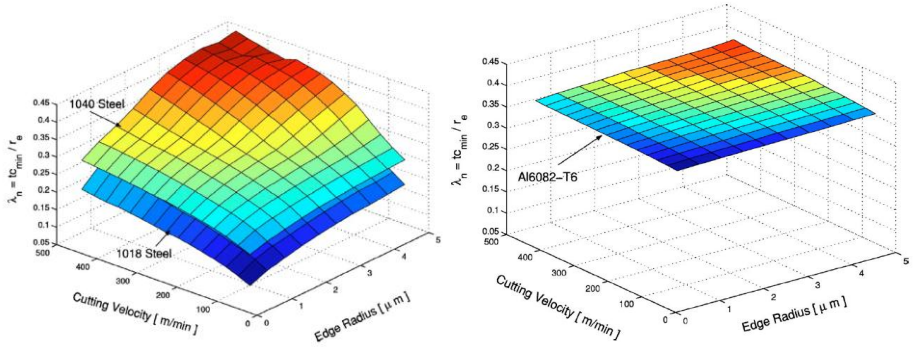

Figure 2.6 Minimum chip thickness for carbon steels (left) and aluminum alloys (right)(Liu et al. 2005a)

Malekian et al. (2012) also investigated analytically the relation of minimum chip thickness to material properties and tool geometry. The concept of stagnation point is introduced to simulate the chip formation shown in Figure 2.7. The stagnation point is solved by using the minimum cutting energy theory or infinite shear strain approach, then the minimum chip thickness is calculated as follows:

$$h_m = r_e(1 - \cos\theta_m) \tag{2-5}$$

where θ_m is the position angle of the stagnation point.

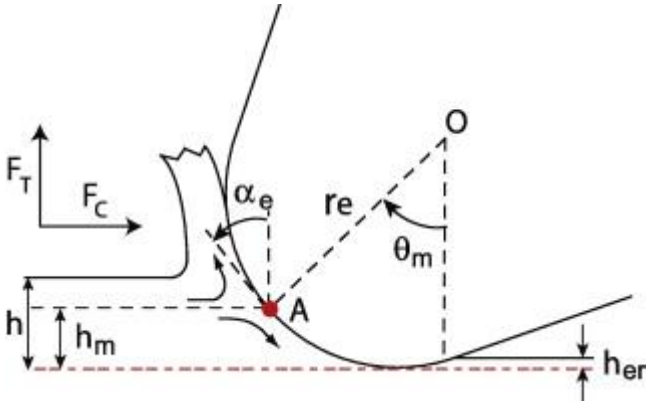

Figure 2.7 Stagnation point in chip formation (Malekian et al. 2012)

Experiments are carried out on aluminium 6061 and find the ratio of minimum chip thickness to cutting edge radius is around 23%.

Numerical simulation on chip formation also becomes very popular in recent years. Vogler (2004) used finite element methods to determine the minimum chip thickness for ferrite and pearlite steel, they found that the minimum chip thickness for pearlite and ferrite is 0.2 and 0.3 times of the edge radius, respectively.

Woon et al (2008a) conducted finite element simulation of micro-machining using the arbitrary Lagrangian–Eulerian (ALE) method; they reported that the chips are formed through the extrusion of material at depth of cut less than the cutting edge radius. The intense deviatory and hydrostatic stresses are highly localized around the deformation area which is the root of changes in chip formation. The simulation is carried out on basis of material AISI 4340 steel and finds the minimum chip thickness is around 0.26 of the cutting edge radius.

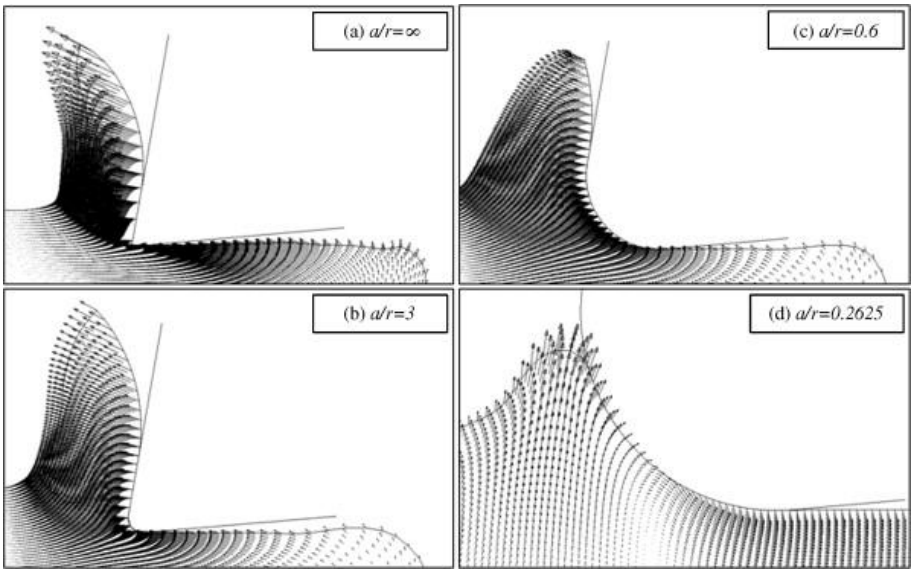

Figure 2.8 Finite element simulation on chip formation (Woon et al. 2008b)

To summarize, the chip formation process is quite different from that in conventional milling process due to the cutting edge radius. It's clearly separated into two regimes: ploughing-dominant regime and shearing dominant regime. The machining takes in different form at different depth of cut. Especially for micro-milling process, the two regimes take place in every single revolution, due to the periodicity of chip thickness. The understanding on chip formation will greatly help interpret its cutting mechanics.

2.2.3 Cutting force

Cutting force has always been an important issue to analyse the cutting mechanics in micro-milling process. It can reflect most micro-milling phenomenon collectively such as size effect, chip formation and the effects of cutting temperature on material and cutting process. It's also an imperative process variable which indicates tool wear status. At the production level, the cutting force can help to optimise the machining conditions and tool geometry. Thus many researchers conducted

extensive study on cutting force modeling and its application in interpreting cutting process (Arrazola et al. 2013).

There are mainly four principal modeling techniques based on different principles: analytical modeling, numerical modeling, empirical modeling and hybrid modeling which combines the strength of previous three approaches.

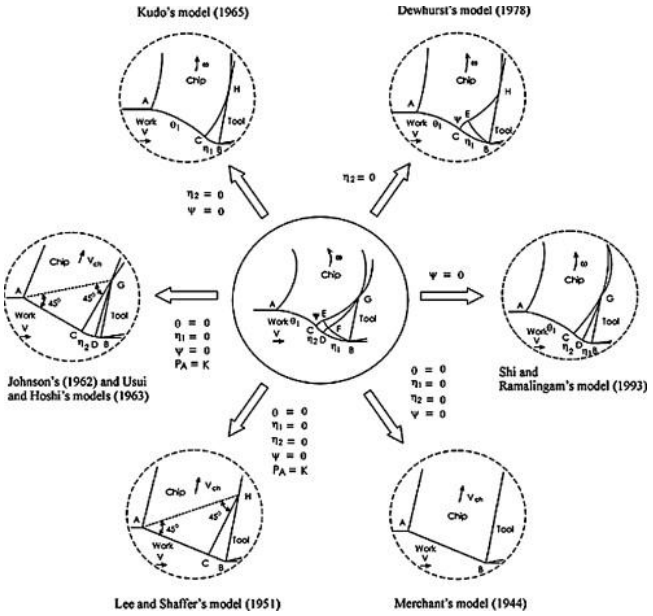

Figure 2.9 Universal slip-line model and its transformation to six previous models (Fang et al. 2001)

Analytical modeling is mostly based on slip-line field theory firstly proposed by Merchant (1944) and developed by many other researchers as shown in Figure 2.9. Fang et al. (2001) constructed a universal slip-line model that incorporates all six previously presented slip-line models. The advantage of this approach is that its capabilities to predict the physics-related variable such cutting force, chip geometry and its contact length on tool. Stress, strain rates and temperatures can also be calculated by this mean; however, the model is usually built on many assumptions which simplify the cutting conditions and are limited to 2D analysis.

Numerical modeling gains wide popularity due to the significant improvement of computation algorithm and computer power. It is based on the continuum mechanics and simulates the cutting process in real machining. It also has the advantage of ability to output in-process variable like analytical model and ease to use. However it requires accurate material constitutive model and friction model as the input. In addition, sufficient computation power must be satisfied and usually long time computation is normal. Extensive efforts are also concentrated on this method (Movahhedy et al. 2000; Arrazola and Özel 2010; Ozel et al. 2011).

Empirical model implies carrying out numerous experiments and by using the curve fitting technique on the data. They can provide practical, fast and direct estimation on industry-related parameters. It's applicable to many process and variables. Thus it's very useful in modeling the cutting process. However, the model is only valid for the range of experiments, changes on other parameters can also result change in model coefficients. In addition, extensive experiments have to be implemented, thus it's very time-consuming and costly. Table 2-1 shows some of the cutting force models in micro-milling process.

Table 2-1 Summary of the cutting force models for micro-milling in recent years

Methodology	Author	Principle	Innovation
Analytical	Vogler et al. (2005)	Slip-line field	--Obtain minimum chip thickness by FE simulation; --Chip formation in two: cutting and non-cutting; --Success in explaining size effect
Analytical	Karpat and Özel (2008)	Slip-line field	--Insert with six different round and chamfered edge; --Explain the dead-meat cap
Analytical	Ren and Altintas (2000)	Minimum energy approach	--Chamfered tool; --Estimate friction energy in deformation
Analytical	Bao, Tansel (2000)	Material properties geo-mechanics	--Introduce instantaneous chip thickness in micro milling
Analytical	G. Bissacco (2008)	Adaption of unified mechanics by Armarego	--Instantaneous chip thickness including tool runout; --Analytically calculate minimum chip thickness
Empirical	Malekian et al. (2009a)	LSM	--Shearing and ploughing regime are separately modelled; --Ploughing modelled by the

			contact area
Empirical	Vogler et al. (2003b)	LSM	--Cutting force based on cutting area
Empirical	Kang et al. (2007)	LSM	--Contact at the flank face is considered
Empirical	Park, Malekian (2009)	LSM	--Incorporate the dynamics of the tool, ploughing and elastic recovery
Empirical	Pérez et al. (2007)	LSM	--Cutting forces in micro-milling based on specific cutting pressure
Numerical	Lai et al. (2008b)	Abaqus	--Revision on Johnson-cook model; --Minimum chip thickness by simulation
Numerical	Afazov et al. (2010)	Abaqus	--Material constant obtained by simulation

From the cutting force models, it's widely accepted that the cutting force in micro-milling process should be model in two regimes, shearing-dominant and ploughing-dominant regime. Vogler (2005) firstly modelled the cutting force in separate regime. The difference among these models lies in the calculation of force under different cutting regime. Experimental results show that they have good capability in predicting the cutting force magnitude. However, these models are formulated through approach towards at the absolute value of cutting forces and the associated quantitative analysis, which is basically the same model with that employed in conventional milling. This inevitably has discrepancy in interpreting the phenomenon encountered micro-milling process generically. Cutting force models with new capability accounting for the process difference in micro-milling are needed.

2.2.4 Cutting temperature

Cutting temperature is of critical importance as it has direct influence on material properties, cutting force magnitude, friction and tool wear, surface generation and integrity and machining accuracy. The heat generated in micro-cutting is relatively small, but it cannot be neglected. Among the aforementioned cutting force models, temperature in the cutting area is a very important input factor. The cutting temperature and heat partition still remains a challenge for micro-milling process (Arrazola et al. 2013). Many researchers are concerned with the temperature field and its influence on cutting process.

Moriwaki (1990) studied the effect of cutting heat on the machined accuracy on copper component and found that even with small amount of heat generated, it can cause great expansion in the tool and result in poor machining accuracy. it can't be negligible as the thermal deformation can cause machining errors.

Kim (1999) proposed a finite element model to predict the temperature and stress distribution in micro-cutting process. They conducted the simulation on material of OFHC copper at varied depth of cut and found that even at small depth of cut, the temperature rise in the local area can reach high temperature. It also suggested that the flow stress of material will be over-estimated if temperature is ignored, which can lead to twice higher in estimating cutting force. However, this model didn't take the cutting edge radius into account.

Lazoglu (2002) presented a model based on finite element method in predicting the temperature on cutting tool and chip in continuous machining and time-varying milling process. The heat transfer at the tool-chip interface is simulated and temperature distribution is solved. The steady state model is then extended to the interrupted milling process where chip thickness varies with time, the transient temperature on the tool and chip is calculated. Experiments carried out on AI2040 steel provide good agreement. They suggested that cutting temperature is a severe constraint on tool life. Thus better understanding in cutting temperature and heat partition can help optimize the cutting tool geometry and cutting process.

Yang et al.(2010) investigated the effect of cutting edge radius on cutting temperature by using finite element method. The simulated tool has cutting edge radius of 0μm, 3.2μm, 5μm and 7μm respectively in simulation setup. Results show the cutting temperature rise in micro-milling is very small and localized around the

contact area. It also suggests under same cutting conditions, the increase of cutting edge radius will results in increase in cutting forces, but slight decrease in the temperature on mill cutter as shown in Figure 2.1. The shown maximum temperatures on the tool are 57.5, 51.5, 45.5 and 40.4, respectively.

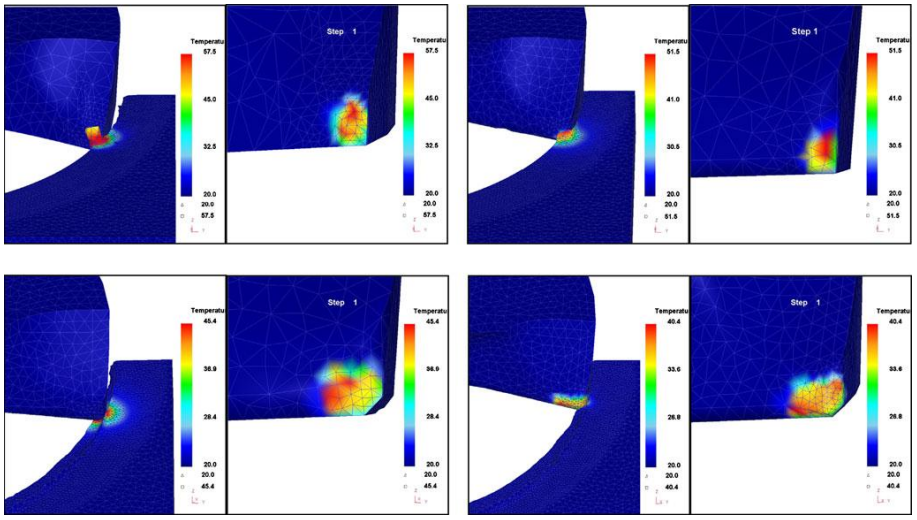

Figure 2.10 Cutting temperature on the cutting area with different cutting edge radius (Yang, 2010)

Experimental research on cutting temperature is another area of interest and extensively investigated. Ueda (2001) used two-colour pyrometer with a chalcogenide optical fibre to measure the temperature of tool flank face in high speed milling, the study investigated the influence of cutting speed and feedrate on the cutting temperature at flank face. Experiment results show that the temperature on the flank face is almost constant. In contrast, the temperatures at the tool edge and at the tool–workpiece boundary are a little higher.

Saoubi (2004) used charge-coupled device (CCD) sensor based near infrared light imaging technique to study the effect of varied tool edge radius and shape on tool temperature.

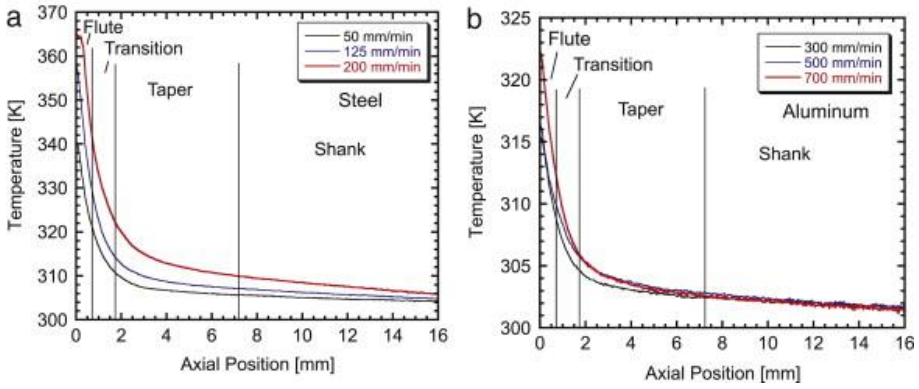

Figure 2.11 Cutting temperature distribution in axial direction (Wissmiller and Pfefferkorn. 2009)

Wissmiller (2009) carried out temperature measurement on the micro end mill in machining using the infrared camera. The experiments are conducted on aluminium 6061 and steel 1018 using 300μm tungsten carbide micro end milling tool. The results found that the largest thermal gradient occurs at cutting flute where biggest thermal resistance locates. It also found that the temperature distribution can be established in the first 10s, then the temperature across tool increases gradually to the steady state. However, the cutting temperature they measured doesn't include the temperature at the tool tip.

Yang (2010) also carried temperature measurement on micro-milling process using infrared cameras. The temperature at the tool tip is measured and results indicate the larger tool in diameter, under same cutting conditions, results in lower temperature rise. However, the explanation for this particular phenomenon is given by the author, which still needs to be investigated.

To sum up, cutting temperature and heat partition have been extensively investigated; however, most of them are concentrated in conventional macro-cutting process, investigation into micro-milling process is still limited. The temperature and heat distribution under the existence of cutting edge radius and its effect on machining process are still required.

2.2.5 Tool wear

The tool used in micro-milling is very small in diameter and works in high spindle speed usually above 10,000rpm. It is frequently subject to cyclic size effect, rising temperature, changing chip thickness, repeated tensile and compressive stress. These conditions make it more likely to experience large vibration and wear. Tool wear, as shown in Figure 2.12, in return makes the micro-cutting process even more complicated and unpredictable. In, addition, excessive tool wear will be detrimental to its longevity and also could result in bad surface quality and part accuracy. Therefore, the monitoring of micro-milling tool is critical and practical to optimise cutting parameter and ensure machining quality.

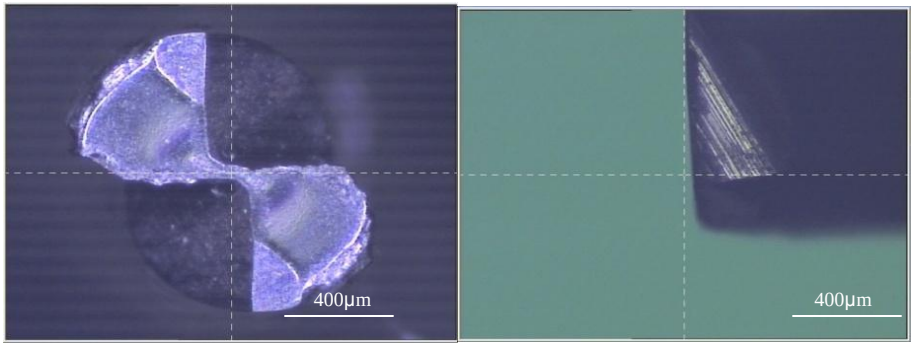

Figure 2.12 Seriously worn micro-milling tool

Extensive research is carried out on this issue, early research involves adopting various variables and sensors to detect tool wear process. Matsushima et al. (1982) have used motor current and power as parameters for tool wear monitoring; Altintas(1992) and Kim (1999) presented the use of motor current for detect tool wear and failure, it found that that tool failure in milling can be determined within one spindle revolution by adaptively filtering the average current at tooth passing periods. Youn(1994) presented a method to detect massive tool failure and small fracture of tool constituent by using both acoustic emission signal and cutting forces.

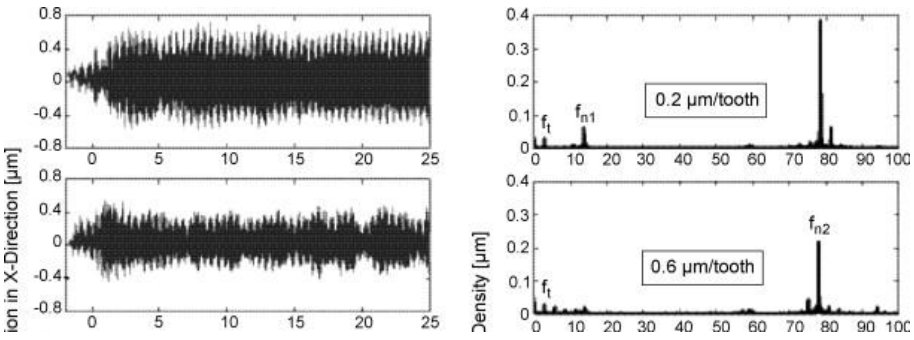

Figure 2.13 Spindle vibration from machining of pearlite (Jun et al. 2006)

Tansel and co-workers (2000) studied the tool wear effect on micro-milling process. Their study revealed that unlike progressive tool wear in conventional cutting, tool wear can quickly lead to tool breakage due to the induced increasing cutting force exceeding the tool strength. The cutting force is applied as the monitoring signal and it found that the force in feed direction is found to be a reliable indicator of tool condition. The average of cutting force in feed direction and its wavelet transform coefficients are utilized to examine the online tool wear status. Later(1998), they also applied acoustic emission signal to detect tool breakage and to estimate tool wear status, the AE signals were classified by using the Adaptive Resonance Theory (ART2) and Abductory Induction Mechanism (AIM) to represent different stages of tool wear. Apart from single type of signal used in tool wear monitoring, sensor

fusion of several signals are also employed such as the work by Ghosh et al (2007), they fused cutting force, tool vibration and spindle current via a neuro-network to estimate the tool wear in face milling operation.

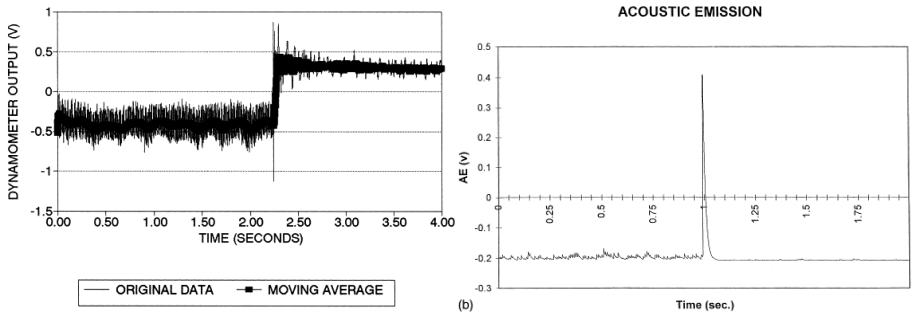

Figure 2.14 Cutting force and acoustic emission when tool is broken (Tansel et al. 1998)

Among these various signals, cutting forces and AE signals can regarded as the most effective methods for tool wear monitoring in machining, since they both yield higher signal-to-noise ratio and contains collectively most information in terms of machining process, system dynamic and tool-wear related variations.

Recently, research is more focused on intelligent analysis on process signals. Malekian (2009b) developed a tool wear monitoring system based on fusion of several signals. The signals are fused through the neuro-fuzzy approach and predict the condition of cutting tool. Zhou (2011) proposed a dominant feature identification algorithm to reduce the dimension and number of AE sensors. Bisu et al. (2011) presented an envelope spectral analysis to monitor the milling process, which gives contribution for qualitative and quantitative characterization of milling capacity. Hsieh (2012) built a neural network model based on the collected spindle vibration signals to monitor the tool wear process. The frequency domain features which indicate tool wear are selected based on the class mean scatter criteria after Fourier transform. Zhu (2015) developed an online approach for tool monitoring by correlating tool conditions with the force waveform variations and estimating the tool condition based on their corresponding singularity degree density functions.

In spite of the extensive research carried out on this issue, however, tool wear monitoring that can accurately represent the tool wear status with high resolution is still not yet accomplished. More research and new algorithm need to be developed.

2.3 Surface generation

The quality of produced component in micro-machining is directly related to its performance in real working environment. Apart from machining accuracy, surface quality including surface integrity, surface roughness and surface damage can influence its usage significantly. Other demands like surface functionality put more stringent requirements on the machined workpiece's surface texture and structures. The existence of cutting edge radius makes the surface generation in micro-milling quite different from conventional milling process, as the feedrate is almost the same order of edge radius.

2.3.1 Surface generation in micro-milling

Weule et al. (2001b) studied the micro-milling process using tungsten carbide tool on workpiece of SAE 1045 steel and found that cutting edge radius plays an important role in generating the surface. The tool has cutting edge radius around 5µm; measured surface topography demonstrates saw-tooth-like profile, which the author attributes to material ploughing due to cutting edge radius. Experiments show that surface roughness deteriorates in ploughing-dominant machining.

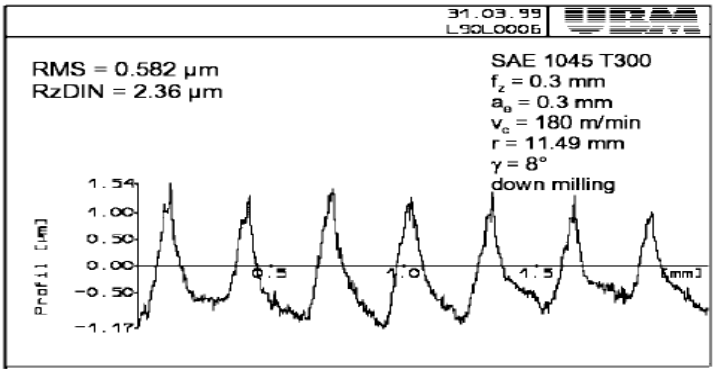

Figure 2.15 Measure saw-tooth-like surface topography (Weule et al. 2001b)

The same phenomenon is also found by Vogler et al (2004), the surface roughness is strongly affected by cutting edge radius. For feedrate less than cutting edge radius, surface roughness changes inversely with the feedrate as shown in Figure 2.16. The author concludes that good surface roughness is achieved when the proper trade-off between feed marks and minimum chip thickness achieves. Bissacco (2006b) studies the surface generation with ball-end micro-milling tool and also found that the size

effect due to cutting edge radius is inevitable in surface generation. This is verified by the smearing of material behind the tool which forms small waves in feed direction.

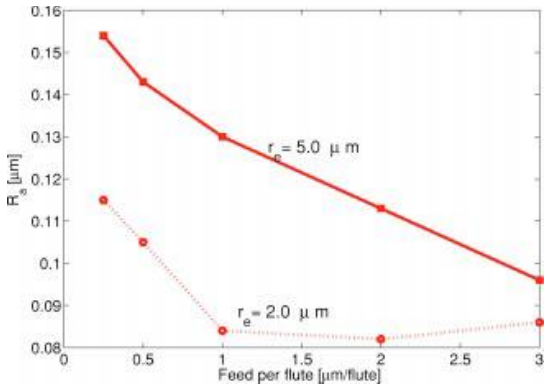

Figure 2.16 Effect of cutting edge radius on surface roughness (Vogler et al. 2004)

Apart from the effect of tool edge radius on surface generation, material micro-structure effect is also investigated by much research. In micro-milling, material grains normally ranges from several microns to hundreds of microns, which is quite significant compared to the cutting tool diameter and cutting parameters.

Vogler et al (2004) also studied the surface generation in multiphase materials and compared it with surface generation in each single phase material. Results find that roughness value in multiphase material is bigger than that in single phase materials. Spectra of the machined surface shows large surface roughness can be found at wavelength corresponding to phase boundaries. At those boundaries, small burrs are formed. Based on these findings, the author concludes that surface roughness is the combination of feed mark effect, minimum chip thickness effect and effect of burr formation at boundaries.

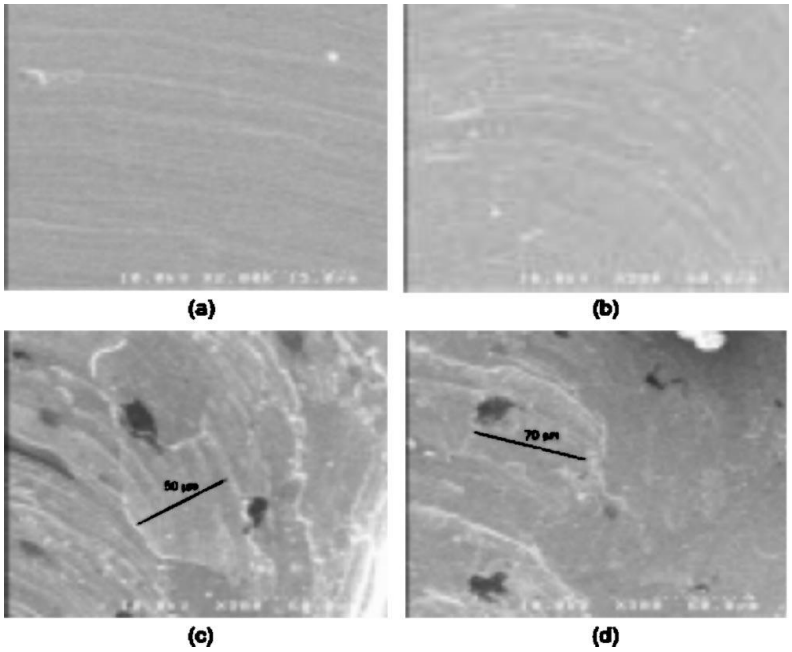

Figure 2.17 SEM image of slot floor machined in micro-milling (a) pearlite (b) ferrite (c) ferritic DI (d) pearlitic DI (Vogler et al. 2004)

Wang (2007) conducted micro-milling experiments on aluminum 6061 and investigated the influence of different metal phase grain on surface generation. The physical properties of different grains including the friction coefficient and elastic modulus and its anisotropy are especially considered. Experiment results demonstrate different phase grain shows differently on the machined surface. Soft phase tends to deform plastically and be removed by cutting tool, while brittle phase grain shows resistance to plastic deformation and is dragged by the tool which leaves cavities behind.

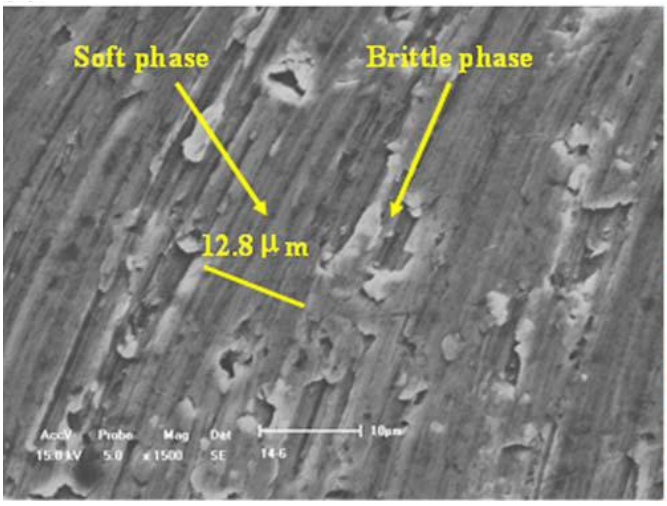

Figure 2.18 Machined surface by micro-milling on aluminum 6061(Wang. 2007)

The effect of crystal orientation on surface generation is also investigated by many researchers. To (1997) conducted micro-cutting of single crystal aluminium with the crystallographic axis normal to <100>, <110> and <111>. They found that best surface finish is obtained with the {100} plane as the cutting plane, whereas the {110} cutting plane results in the worst surface roughness.

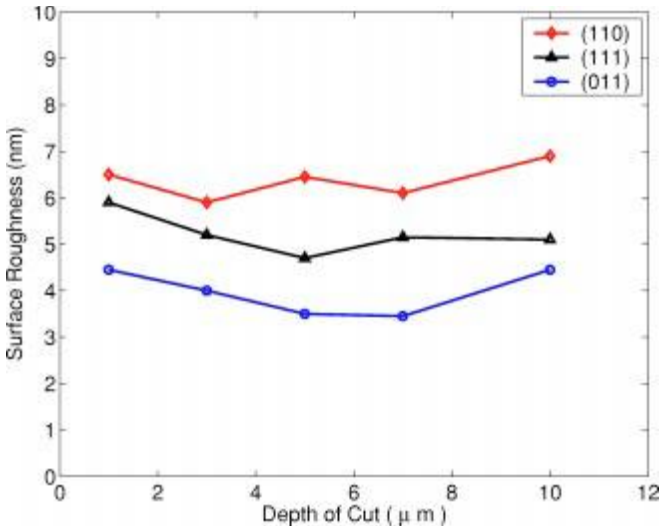

Figure 2.19 Effect of crystal orientation on surface roughness (Wang. 2007)

Efforts on modeling the surface generation process are another area worth investigation. Many researchers (Vogler et al. 2004; Li 2007) have simulated the surface generation by taking the minimum chip thickness effect into account. The tool edge is modelled as round arc; the profile is obtained by comparing the cutting depth and minimum chip thickness. The final surface profile has tooth like shapes, however, this model can be only approximate at large feedrate. Considering the dynamic displacement of tool and workpiece in micro-milling, Ding (2010) calculates the real tool trajectory and simulated the machined surface apart from taking minimum chip thickness into account. Simulation results show acceptable agreement with experimental outcome.

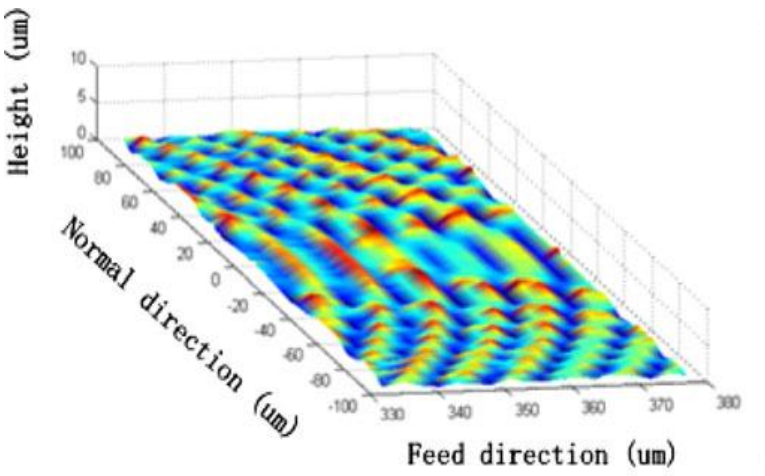

(a) Simulation

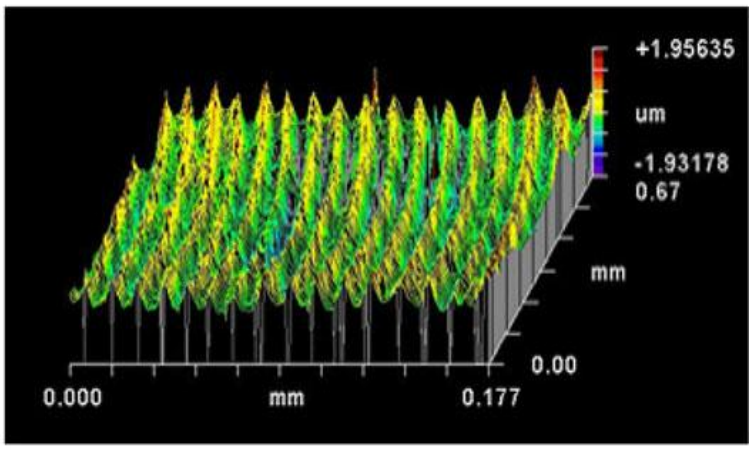

(b) Experiment

Figure 2.20 Simulated surface generation and experiment result (Ding 2010)

2.3.2 Burr formation in micro-milling

Most machining processes removing material from workpiece can't produce sharp or smooth edges; instead, ragged and protruding burrs are often seen on parts. However, in micro-cutting process, as the characteristic dimensions of micro-parts are usually small, burr's presence can seriously deteriorate machining accuracy and jeopardize its function in usage. If deburred, it may cause damage to component structure. Therefore it's important and necessary to investigate burr formation thus prevent or minimise its formation in micro-milling.

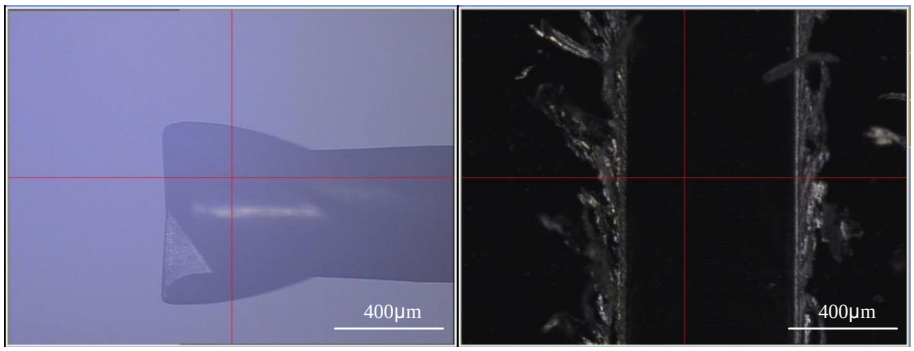

Figure 2.21 Micro-milling tool and burrs formed in slot milling

Much research has been focused on macro-burr formation. Ko (1991) studied the burr formation for ductile materials which does not include fracture during orthogonal machining and proposed a quantitative model. Chern (1996) found that a negative deformation plane is formed when steady-state chip formation stops as the tool approaches the end of the cut. The bending and shearing of this plane contributes to the burr formation. Besides the modeling, experiments focusing on the effects of cutting parameter on burr formation are also carried out by many researchers. Gillespie (1976) studied the burr formation mechanism and found that three basic mechanisms are involved. They are lateral deformation, chip rollover, and material tearing. He also pointed out that changes in feed, speed, or tool geometry alone will not prevent burr formation. However, it can be significantly minimized by choosing appropriate machining parameters.

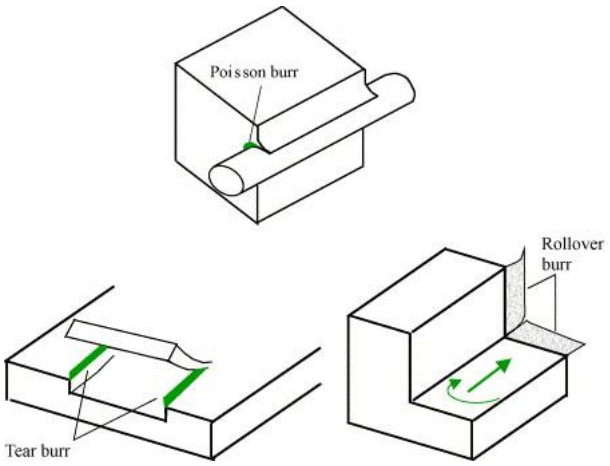

Figure 2.22 Schematic of Poisson, tear and rollover burr formation.(Gillespie and Blotter 1976)

The burr formation in micro-milling process is also investigated. It should be noted that in micro-milling, the ratio of feed per revolution to cutting edge radius is very large compared to that in conventional milling process. This factor alters the chip

formation mechanism in micro-milling and possibly changes the burr mechanism as well, which needs specific study.

Hashimura (1999) studied the burr formation in milling 304L stainless steel, and found that burr remains near exit position of the tool disengaging the workpiece. The burrs in milling process are classified according to their locations, shapes and formation mechanisms based on fractography.

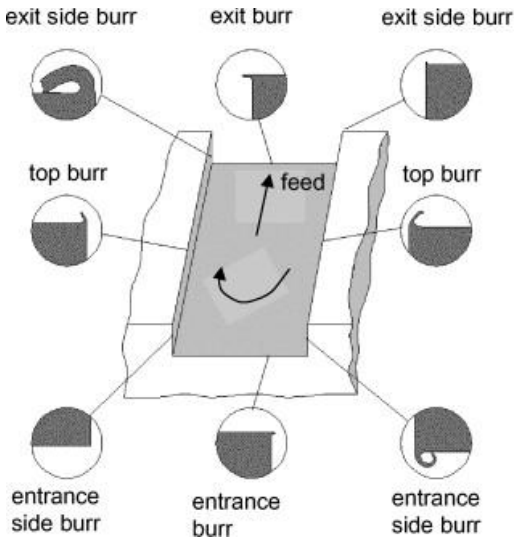

Figure 2.23 Types of burrs in milling(Hashimura et al. 1999)

Lee (2005) investigated the top burr formation in micro-milling of holes using tungsten carbide tools. In their study, the size and height of burr is formulated as a function of feedrate, cutting speed and cutting edge radius. Results find that burr height is linearly proportional to feedrate per tooth and it's also closely related to tool wear. In addition, the burr size is comparatively larger than that in conventional milling due to the large ratio of feedrate per tooth to cutting edge radius.

Luo et al. (2008) investigated the mechanism of burr formation on the feed direction; experiments conducting both orthogonal milling with varied exit angles and oblique milling with varied oblique cutting angles are carried out. They found that the size of exit burr increases with the exit angle, besides, the size of exit side burr on up milling side increases with the oblique cutting angle.

Lekkala (2011) performed micro-end milling experiment on material of aluminium 2124 and stainless steel SS-304 to study the influence of principal cutting parameter i.e. speed, feed rate, depth of cut, tool diameter and number of flutes on the formation of various burrs as shown in Figure 2.23. It is discovered that the cutting depth and tool diameter have most significant influence on burr height and thickness, whereas the cutting speed and feed rate every revolution only have very

small impact on the burr thickness and height. They also found that increasing the number of flutes has the effect of decreasing burr height in up and down milling. In up milling, the burrs are torn and the fractured portion of the slot increases with increase in the number of flutes.

The above review shows the burr formation has been extensively studied, work done until now has reported on mechanism of burr formation, and methodology on prediction of burr height and size on different materials. Experimental study to prevent and minimise burr formation and its size are also largely carried out. However, the research on burr formation in micro-milling is still far from comprehensive and thorough. The fundaments of burr formation and its mechanism are still not well understood, more research is still necessary on this special issue.

2.3.3 Micro-featured surfaces

The micro-milling process has strong flexibility in manufacturing 3D structured surfaces. The miniaturized components and structured surface have wide application in different industries such electronics, energy, transportation, automotive and mechanical parts. Much research and effort are focused on machining microstructures by micro milling.

Friedrich (1996) conducted experiments on rapid and direct fabrication of micro-molds and masks using micro-milling process. The micro milling tools are manufactured by the focused-ion beam machining process with diameter ranging from 22 to100µm. Experiments are carried out on material PMMA. Trench-like features with nearly vertical sidewalls are machined with good smoothness. It's also able to machine sharp external corners and stepped features. Trenches as deep as 62µm with 8µm thickness are successfully machined by using a tool of 22µm in diameter.

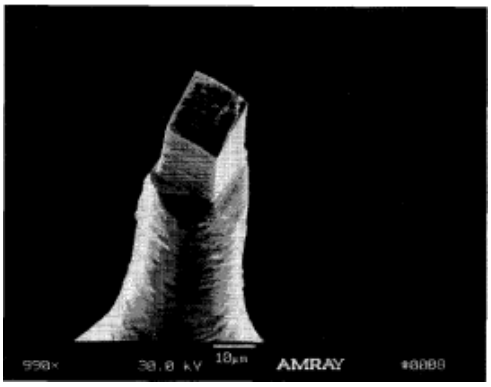

Figure 2.24 Two-fluted micro-milling tool made with FIB(Friedrich, 1996)

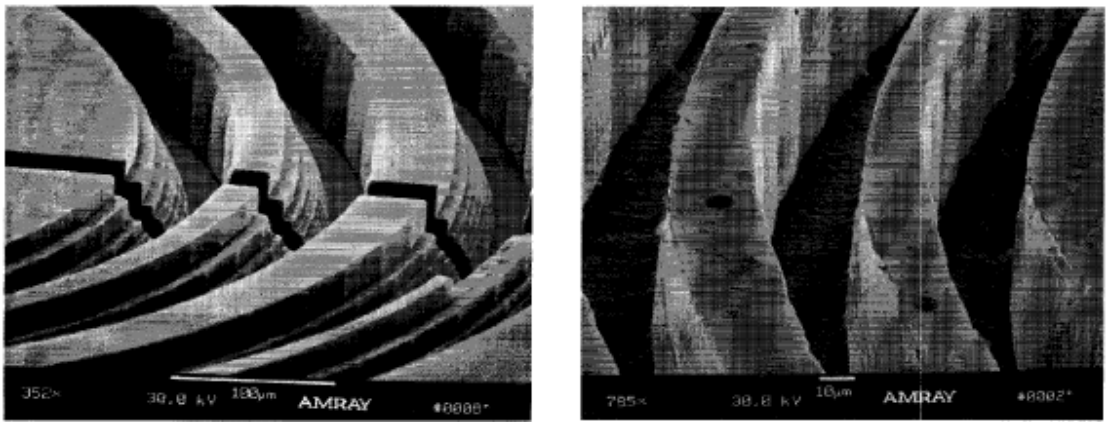

Figure 2.25 Micro-milled trenches with step and straight wall (left) micro-milled wall with thickness of 8µm(Friedrich, 1996)

Weck (1996) also conducted experiments on machining microgrooves and V-grooves using micro diamond milling process on nickel-coated workpiece.

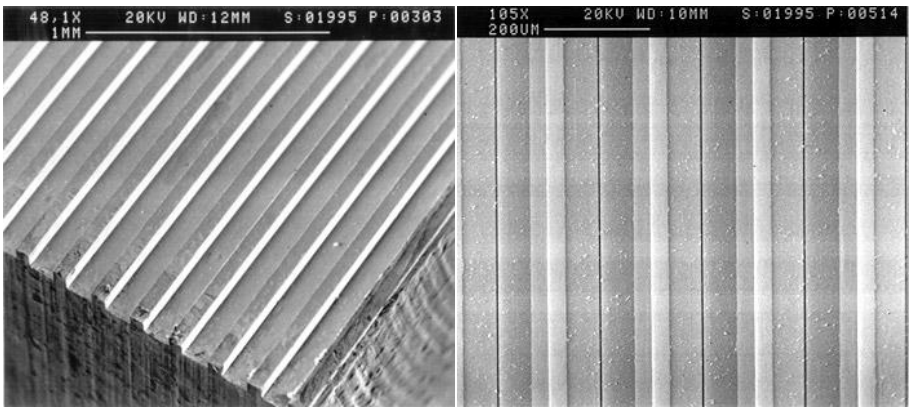

Figure 2.26 Diamond milling of microstructures, (a) microgrooves for fiber lignement and (b) V-grooves machined into nickel-coated surface.(Weck, 1996)

Friedrich (1998) conducted further investigation on micro-milling structures on PMMA components. The process is used to fabricate masks for deep x-ray lithography with lateral absorber features down to 10 micrometers. Machining results show the average accuracy of mask absorber features was 0.65 micrometers, with an

average standard deviation of 0.55. The process introduced some absorber burrs, and the absorber wall is slightly tapered, which introduces an additional process bias. However, the process still proves to be quicker and less costly than conventional methods.

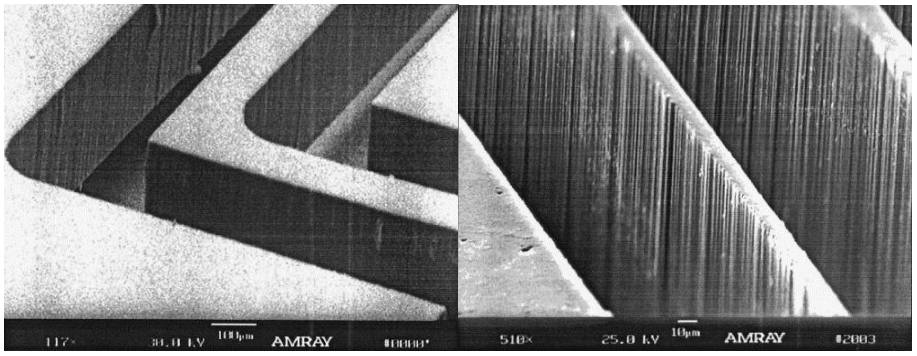

Figure 2.27 Joule–Thomson microcooler (left) machined trenches 10µm in width (right)(Friedrich, 1998)

Schaller (1999) investigate the micro-milling process to machine micro-structures used for molds for injection molding and hot embossing. They successfully machined microstructures on brass and stainless steel workpieces with hard metal micro end mills. The minimum groove width machined is less than 50 mm on brass and about 100 mm on stainless steel. They observed remarkable burr formation on micro-structure edges. They also studied the subsequent step to remove the occurring burrs by using electrochemical polishing or diamond cutting techniques.

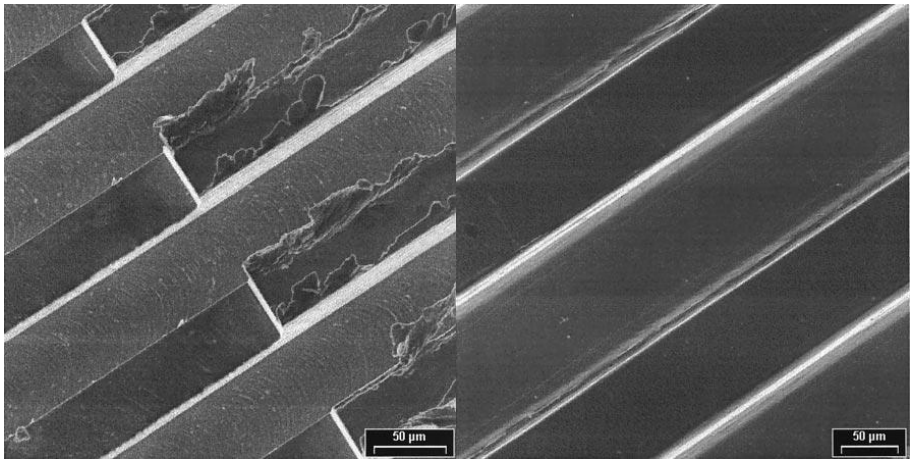

Figure 2.28 Microgrooves on brass material with burr partly removed (left) and stainless steel after deburring (right)(Schaller, 1999)

Adams (2000, 2001) presented a series of micro-end mills with application to manufacturing microstructures, the fabricated tools can have small diameter down to 25µm and specified tool geometry. The tools are deployed in micro-grooving tests

and result shows that the cross-section of the machined groove is an excellent replication of the micro-tool geometry. This tool proves not only in good machining results but extends the geometry that micro-milling process can machine and improves the machining efficiency.

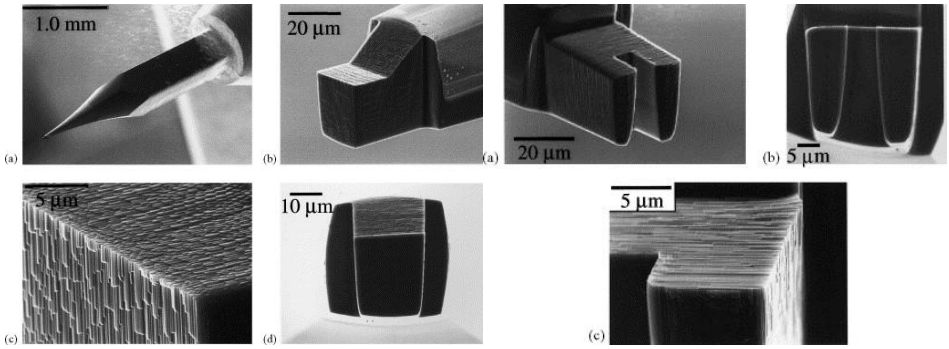

Figure 2.29 Micro tools made for specific geometry (Adams, 2000)

More recently, Gietzelt (2008) investigated the feasibility of micro-milling process in manufacturing micro-structure with high aspect ratio. In his study, a micro milling tool with aspect ratio of 10 is utilized. Micro-structures with aspect ratio of 10 are presented in brass and ceramics material.

Li (2010) also conducted research on micro-milling thin rib with high aspect ratio. They studied the cutting force in manufacturing thin ribs in order to keep it low as the tin ribs have low stiffness. In addition, they used FEM analysis to simulate different milling strategies (up-/down-milling) and tool paths and studied their effect on quality of thin features. Experiment results show cutting force is much lower in up-milling, adopting up-milling will also result in ribs of better quality. Final result demonstrates that thin ribs of 15µm in width with an aspect ratio of more than 50 are successfully machined.

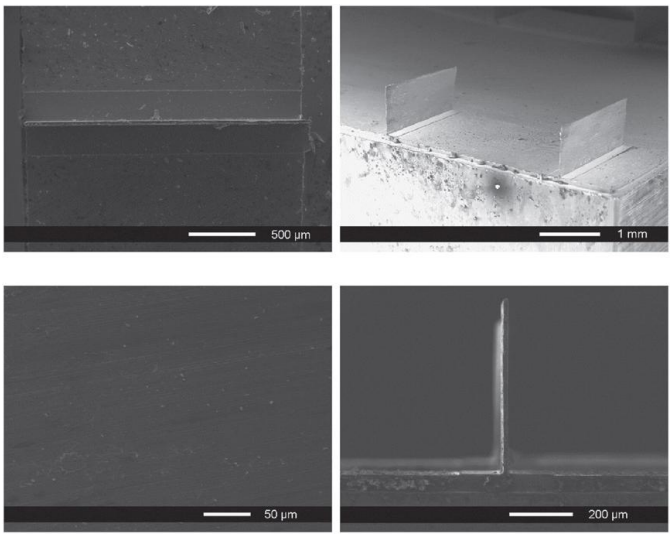

Figure 2.30 Thin rib with aspect ratio of 54(15µm in width and 800µm in height)(Li, 2010)

Besides the normally used tungsten carbide micro-milling tools, diamond micro-milling tools are also now being frequently used in manufacturing micro-structures. Holme (2008) applied diamond micro-milling for manufacturing of masters for wafer-based replication applications. It has the capability to manufacture large radius of curvatures. Various forms are machined including spherical, aspherical and free form surfaces.

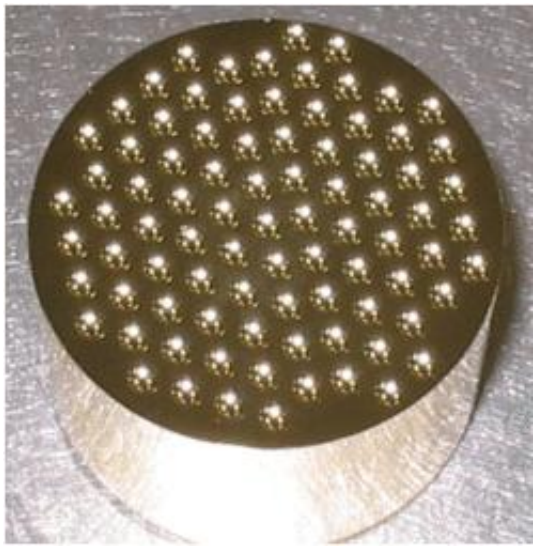

Figure 2.31 Lens array with 94 identical spherical lenses(Holme, 2008)

McCall (2010) also performed diamond micro-milling to manufacture lens arrays on PMMA components. It turns out this process is able to produce micro-milled lens of high optical quality in terms of form error and surface roughness obtained with other technique such as plastic injection molding. The machined lenses have very good surface roughness around 12nm.

Figure 2.32 Array of concave lenses (left) and a 4×5 array of convex lenses (right)(McCall,2010)

2.4 Micro-milling process optimisation

Due to the fragility of micro-milling tools, micro-milling process tends to adopt conservative cutting parameters including feedrates and depth of cut; on the other side, it needs higher spindle speed to increase the cutting speed and feedrate for higher volumetric material removal to improve the machining efficiency, meanwhile, tool deflect and chatter should be minimised in order to extend its serving life. In addition, machining quality including dimensional accuracy, surface roughness and functional performance should also be warranted.

2.4.1 Optimisation on cutting parameters

The adopted cutting parameters have direct influence on the machining quality and tool wear progress. Ghani (2004) conducted investigation on optimization of cutting parameters such as cutting speed, feed rate and depth of cut to obtain low cutting force and good surface finish. In their study, the Taguchi method is adopted. A standard L27 orthogonal array is used. Experiments are carried out on hardened steel AISI H13. Signal-to-noise (S/N) ratio and Pareto analysis of variance (ANOVA) are employed to analyse the milling parameters. Results show that high cutting speed, low feed rate and low depth of cut can lead to low cutting force and good surface finish.

Cardoso et al. (2010) carried out experiments on aluminium alloy to study process optimization. Several samples are machined with varied feedrate and milling strategies. Spindle speed, machining step-over and depth of cut are the three variables kept constant. Feedrate are varied from 2 to 8µm with increment of 2µm; three machining strategies are applied, namely constant overlap spiral, parallel spiral,

and parallel zigzag. Experiment results show that the strategy and feed rate values are fundamental to achieve good surface roughness results, the strategy with which the best results were achieved was strategy "constant overlap spiral."

Natarajan (2011) applied response surface methodology to optimize multiple parameters including maximal material removal rate and minimum surface roughness. Second order quadratic model using central composite design is employed to achieve the optimization considering the cutting speed, depth of cut and feedrate. Experiment results show that surface finish is improved when the feed rate is low and influence of cutting speed on surface roughness is low.

Thepsonthi (2012) performed process optimization on hard-to-machine material titanium alloy with major aim to reduce burrs and improve surface roughness; statistically based methods were used to obtain the optimal cutting parameters for desired surface quality. They also used particle swarm optimization method to select the cutting parameters for multi-criteria process. Experiments find that depth of cut is the major factor that causes top burrs and feedrate is the mainly responsible for the surface roughness. In contrast with conventional milling, a higher feed rate provides better surface quality and channel quality.

Apart from optimizing cutting parameters to obtain better surface finish and less burr formation, other techniques are introduced. Chern (2006) introduced two-dimensional vibration into micro-milling. They developed a two-dimensional vibrating table on which the workpiece sits. The workpiece is vibrated during machining in two directions with the amplitude of 10μm and frequency of 600Hz.

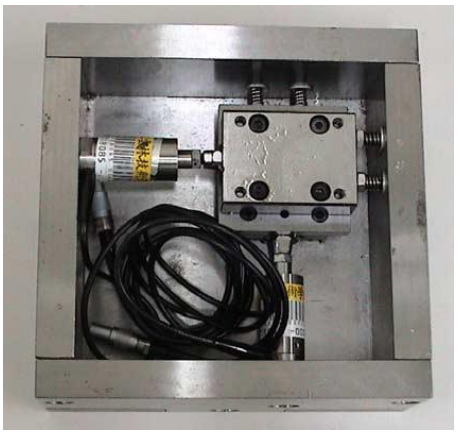

Figure 2.33 Image of the vibration table (Chern, 2006)

In their experiment, tungsten carbide tool of 1mm in diameter is used. Cutting tests are carried out on aluminium 6061 by machining slots. The machining accuracy,

surface roughness and topography of the machined slots are analysed. Results show that the vibration introduced can improve surface roughness, reduce slot oversize and displacement of slot centre. It also finds that the tool life can be extended when high amplitude and proper frequency are imposed. They also find that vibration in the feed direction can significantly improve the slot width accuracy.

2.4.2 Optimisation on tooling geometry

In order to prolong the tool service life and improve the machining efficiency, much research is also focused on re-designing the tool, it usually includes investigation from two aspects, refining the tool geometry design to improve its strength and fit specific cutting circumstances and applying proper coatings on tool to improve its resistance to wear. In this study, the literature on tool geometry design will be reviewed.

Uhlmann (2005) conducted optimization on the normally used two-fluted helical micro-end mill based on the load and strain analysis by means of FEA simulation. It is found that the commercially available micro end mills are not appropriate for the type of load they are subject to. They compared the conventional milling tool and the designed tool with new geometry and showed that new designed tool can effectively improve the tool usability. Experiments are also carried out to cut PMX190CrVMo20 with the hardness of 52HRC and 62HRC to verify the tool design. Results show that the risk of tool breakage is reduced and the tool life is extended by almost 30% compared to commercially available tools. Based on their results, the author suggested that limits of micro cutting with cemented carbide end mills can be further improved via optimal design of new tool geometry.

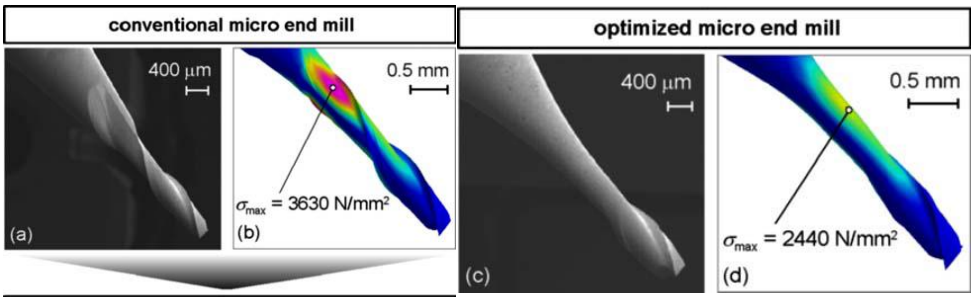

Figure 2.34 Conventional design and FEA analysis (top) optimized design and FEA analysis (bottom)(Uhlmann, 2005)

Jin et al. (2007) developed two types of cBN ball-nosed end mills; the first one has a very simple no-flute unchamfered cutting edge with negative rake angle of approximately −45◦; the other one has the same cutting edge shape but its rake angle is approximately −20◦. Experiments are carried out to cut die steel SKD11 (60HRC) and hardened stainless steel STAVAX (Wood Horm) (52HRC). Comparison between proposed tools and conventional tools is conducted and it shows that the newly designed tool has higher machining accuracy and longer tool life. Surface roughness obtained by the two designed tools is 1.8 and 1.0 μm, respectively, which is superior to that achieved by conventional tools

Fleischer et al. (2008) proposed a new design of micro-milling tool, in their study, a single edge micro-milling tool is developed, which has the advantage of clear adjustment of the process parameters, feed per edge and lateral infeed. They conducted stability analysis of the tool to optimize its geometry by means of FEA simulation. A wire electro-discharge grinding (WEDG) process was used to manufacture the tool, and it's applied in experiment to verify its capability.

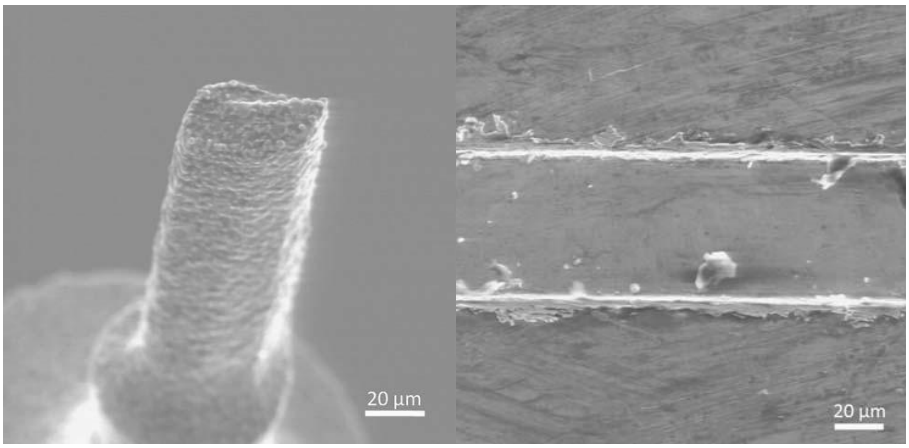

Figure 2.35 Designed micro-milling tool Φ50μm (left) machined slot (right)(Fleischer, 2008)

Apart from tungsten carbide tools, other material which has superior properties is also utilized to make micro-end mills in recent years. Cheng (2010) developed micro straight edge end mills made of PCD diamond in order to machine hard and brittle materials. Static and dynamic FEM analyses are conducted on the tool with different rake angles to identify their stiffness and natural frequencies. PCD micro-end mills with three different rake angles are fabricated. Simulation and experiment results show that micro-end mill with smaller rake angles have better stiffness and lower tool wear rate. Moreover, the newly designed tool can achieve good side and bottom

roughness; it also has higher machining accuracy in machining thin wall with aspect ratio of 20.

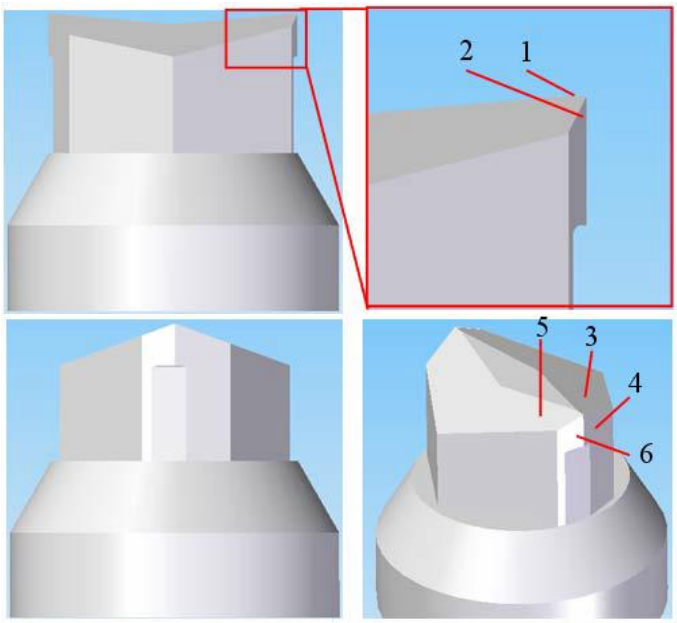

Figure 2.36 Different views of straight edge endmill with 20 °rake angle (Cheng, 2010)

2.5 Summary

In this chapter, the related literature on micro-milling is systematically reviewed. Firstly, micro-cutting mechanics are classified and reviewed, which help to understand the fundament and nature of the cutting process different from conventional milling process; secondly, the surface generation process is another important issue worth investigating, which directly affects the machining quality and function performance of machined micro-parts. Finally, related work on micro-milling process optimization is reviewed in aspect of optimization on cutting parameters and tooling geometry which provides detailed look into the practical means to improve machining quality and efficiency, meanwhile, to optimize tool design and extend its life in service.

On the basis of above literature review, the issues of research interest and practical significance are selected in three main topics:

1. The chip formation process needs to be investigated thoroughly which is the strongly collective combinations of size effect, cutting edge radius effect and minimum chip thickness effect etc. The different aspects need to be addressed separately in order to understand the micro-milling process. Thus, new methods

and design of experiments are critical. The chip formation process is investigated by separately investigating the perfectly sharpened tool and round-edge tool. The identification of minimum chip thickness for different tool/material pairs is another gap which lacks investigation.

2. Since the cutting force in micro-milling is very small around 0.1~1N, However it is still very important in terms of interpreting micro-cutting mechanics and assisting in machining optimization. Given the small cutting force, the absolute value alone cannot thoroughly interpret the micro-milling process. Thus novel cutting force modeling approach is to be proposed to account the unique phenomenon related to the scaling-down of milling process. Cutting force model in multiscale is constructed in this research.
3. The industrial scale application of micro-milling process requires close monitoring on tool wear to maintain machining accuracy and process stability. The tool wear mechanism and its form in micro-milling needs to be characterised and investigated in order to give deterministic representation on tool wear status during machining.

Base on the identified research issues existing in current micro-milling community, the research methodology and experiment setup in chapter 3 are designed to fill the gaps. Findings and contributions will be presented and discussed in chapter 4, 5, 6 and 7.

3 Research Approach and Experimental Setup

3.1 Research methodology

The literature review in previous chapter reveals that micro-milling is quite different from conventional milling. The existing knowledge and research findings on conventional milling can't be converted to interpret micro-milling directly. Generally the reasons which cause these differences are in 3 aspects: the cutting edge radius cannot be ignored, material microstructure effect plays an important role, and conservative cutting parameters are usually adopted. The forms it takes to appear, from previous chapter, can be classified into 5 issues including cutting forces, chip formation mechanism, distinct size effect, low cutting temperature and tool wear (Figure 3.1); However, these issues are strongly linked and mutually coupled: the chip formation is strongly influenced by tool geometry which will be worn during machining; under conditions of tool wear, size effect will be more obvious; higher cutting forces, as a result, are needed to overcome resistance of work material and remove chips. Consequently, the amount of heat generated due to plastic deformation and friction are increasing which in turn affects cutting forces, material properties and tool wear rate. All these issues are contributory factors to the part machining quality, i.e. dimension, form and surface roughness, etc. High volume industrial production demands good consistency in product quality. Thus tooling performance is imperative for this to happen, another aspect is to optimize the cutting process in order to improve the machining quality and extend tool life. The aim of this study is to obtain scientific understanding of micro-cutting mechanics and other related issues in micro-milling, identify the key problems in need of solution, and propose practical methods to help optimize the cutting process and tooling geometry in order to make the industrial-scale application of micro-milling in manufacturing miniaturized parts happen.

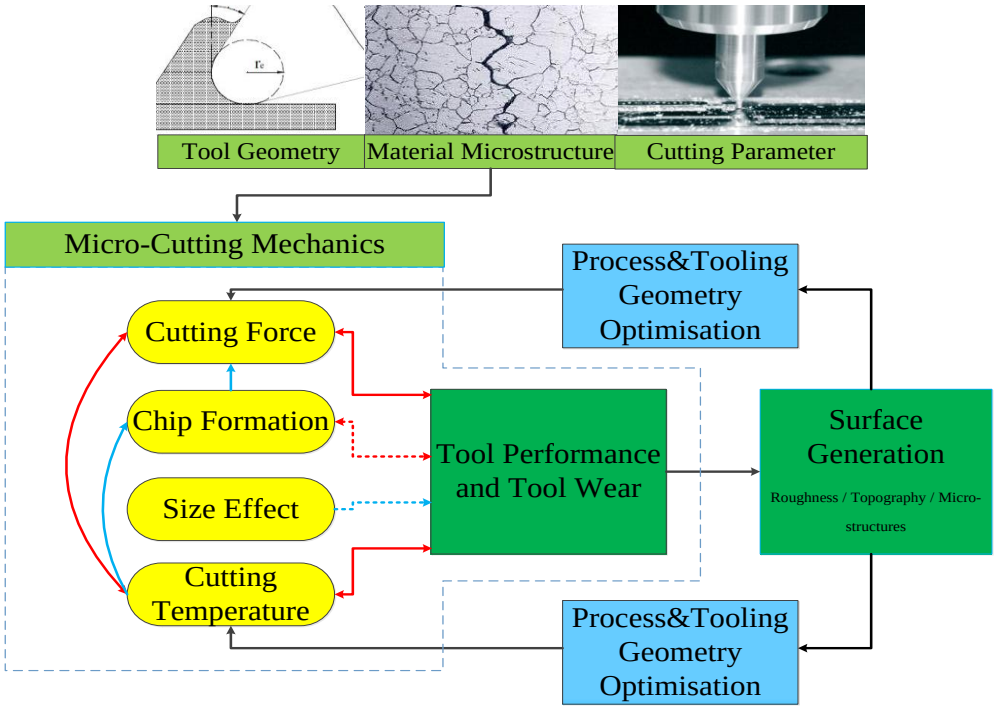

Figure 3.1 Scientific and technological challenges in industry-scale micro-milling

To fulfill the aim and objectives of the study, experimental investigations are carried out to study the micro-cutting mechanics; meanwhile numerical modeling and simulation is also conducted to complement and assist in understanding problems such as chip formation, size effect and cutting temperature. Results from experiments and simulation are compared and analyzed. Figure 3.2 illustrates the schematic of the investigation approach to micro cutting mechanics and related issues.

Experiments are carried out on both turning and micro-milling machines to study orthogonal cutting. In this way the disturbance from complex tool geometry can be eliminated so as to concentrate on investigation of the interaction between tool and material, but still having practical meaning. It eases experiment and simulation set-ups. Chip formation mechanism and its relations with tool material, cutting edge radius and cutting speed are particularly studied on precision turning machine; Based on the knowledge gained in turning process, chip formation in micro-milling process is further investigated by applying diamond and tungsten carbide tools to study the size effect and cutting force behavior. Chips removed by different tools are compared.

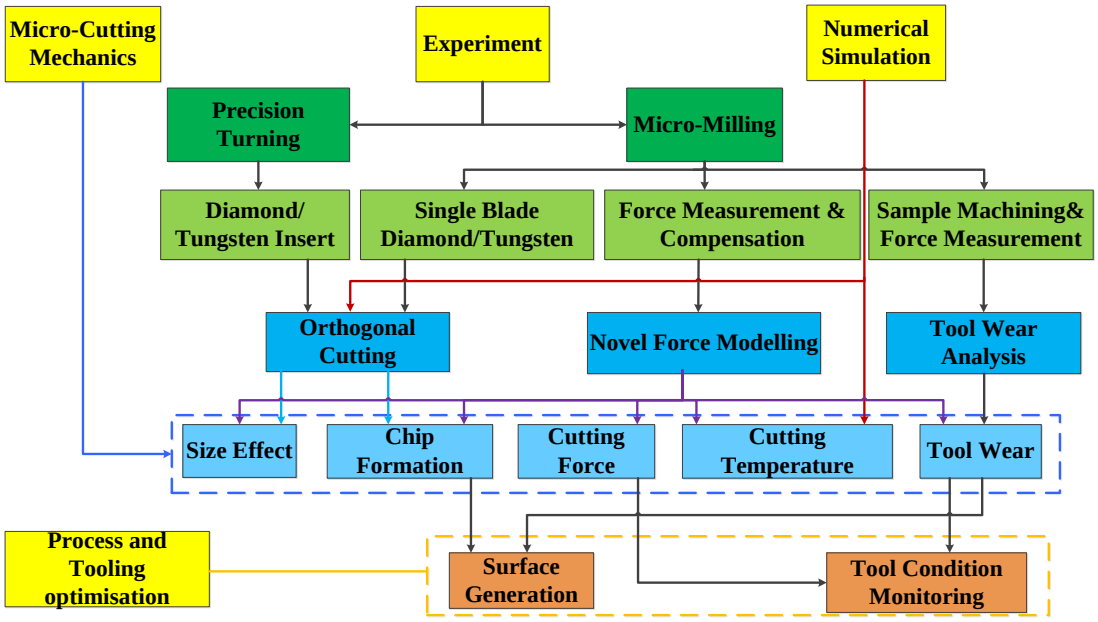

Figure 3.2 Schematic of the investigation approach to micro-cutting mechanics and other issues

A new force modeling approach is introduced to gain understanding of the micro-cutting mechanics in micro-milling through theoretical analysis and experimental validation. The outcome of this model attempts to attain scientific understanding on issues such as size effect, chip formation, burrs formation, tool wear and cutting temperature etc.

Thirdly, tool wear is selected as a research topic in this study due to its great importance in ensuring machining quality and consistency in large volume production. The experiments are carried out on micro-milling machine by deliberately wearing the tool against hard-to-machine materials. The tool wear is inspected under microscope, its type and magnitudes are classified and measured, respectively. Various techniques are utilized to analyze tool wear process.

Finally, heat partition and cutting temperature is another issue worth investigation. To study the difference on this issue between micro-milling and conventional milling, numerical simulation is performed with focus on the heat partition among tool, workpiece and chip. Besides, the simulation also helps interpret chip formation in micro-milling.

3.2 Experimental facilities

In this chapter, the measurement equipment and machines used in this study will be introduced.

3.2.1 Machine tools and cutting tools

3.2.1.1 Precision turning machine

Cutting trials studying micro-cutting mechanics were performed on a diamond turning machine Nanotech 250 UPL. This commercially available machine is equipped with two brushless DC linear motor-driven axes, on fully constrained oil hydrostatic box way slides. The usage of ultra-fine linear scale makes the machine able to achieve 1nm linear motion accuracy, which is more than sufficient for our experiments. An air bearing spindle with a center mounted thrust plate is installed on X-axis, It is driven by a frameless, brushless DC motor, with a maximum speed of 10,000rpm. Radial and axial runouts are both controlled less than 12.5 nanometers. Thermal stability and spindle center repeatability are maintained by a closed loop chiller which control temperature variation to $\pm 0.5^{o}C$. A Delta Tau controller is adopted for this machine.

Figure 3.3 Ultra-precision turning machine and cutting trial

3.2.1.2 Micro-milling machine

Experiments of micro-milling process are conducted on a 5-axis precision Kern HSPC 2825 micro-milling machine. It is consisted of 3 linear and 2 rotary axes driven by Maxon motors; Heidenhain TNC426 control system is installed and ensures the positioning accuracy to $\pm 1\,\mu m$, which is adequate in this study. A Step_Tec ceramic bearing supported spindle is equipped on this machine, its

maximum speed is 35000rpm. Thermal stability is provided with a controlled cooling system which can adjust the temperature within $\pm 0.5^{o}C$. Milling tool is clamped to spindle via collets; the static radial runout of the spindle-collet-tool system is controlled within $5 \mu m$ by fine adjustment.

The machine is also equipped with a Blum-Laser Tool Setting System which measures the radius of the spinning milling tool. It uses visible red light laser and has good measuring accuracy and repeatability up to $0.1 \mu m$, as shown in Figure 3.4

Figure 3.4 Precision micro-milling machine, cutting trial and laser measuring system (zoom-in view)

3.2.1.3 Cutting tools

Various cutting tools are utilized in experiments. Diamond and tungsten carbide tools are primarily used for conducting cutting trials on ultra-precision turning machine to study micro-cutting process. Single blade diamond and tungsten carbide milling tools are used to investigate the micro-cutting mechanics in micro-milling process. Besides above tools, normal micro-milling tools with helix angle flute are also utilized in micro-milling trials to develop process modeling, tool wear are also studied for these tools.

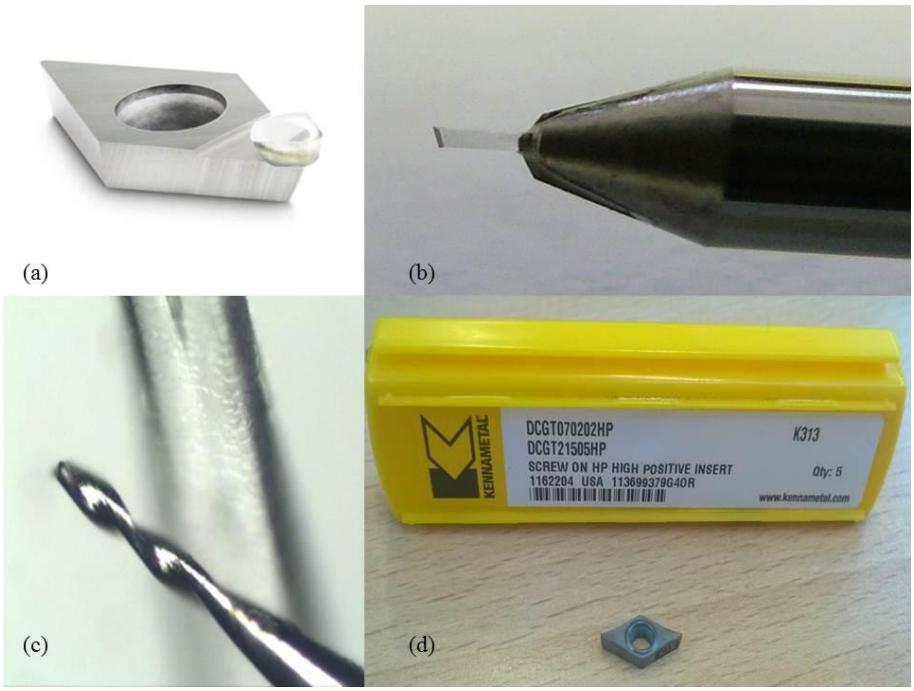

Figure 3.5 Cutting tools used in the study (a) diamond insert (b) diamond micro-milling tool(c) tungsten carbide micro-milling tool (d) tungsten carbide insert

3.2.2 Measurement devices

3.2.2.1 Zygo NewView white light interferometer

Machined surface topography and microstructure dimensions of workpiece are mainly measured by using a Zygo NewView 5000 white-light interferometer. It is equipped with an objective (20×), which is motorized by piezoelectric actuator. This guarantees to achieve 0.1nm resolution in the vertical direction. The lateral measurement resolution is $0.64\mu m$. It has an objective lens and field-of-view lens (0.4× to 2×). The MetroPro software is used to analyze the collected data and images.

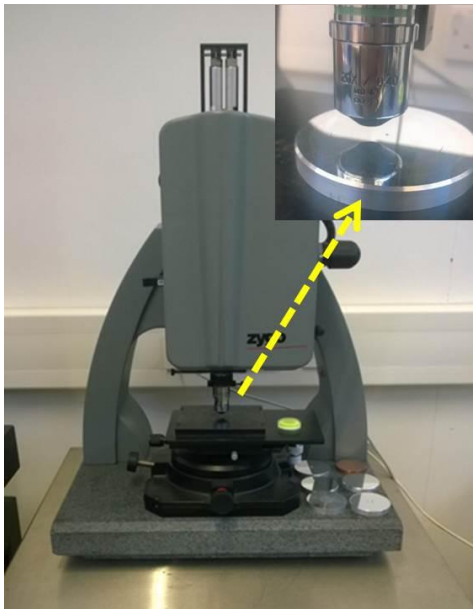

Figure 3.6 Zygo NewView 5000

3.2.2.2 TESA V-200 microscope

This microscope is a complement to white light interferometer and is primarily used to measure larger structure and feature dimensions of workpieces and parts. The different measuring principle from white-light interferometer makes it easier to handle and operate. It has an integrated Telecentric objective lens of 42× with indexable manual zoom option to 4×. Besides, an additional lens of 2× is optional, so the magnification can range from 40× to 340 ×. It uses opto-electronic measuring system with resolution of 0.05um, the positioning accuracy of the 3 linear axes are all within 2um. The microscope is connected to affiliated software TESAVISTA 2.0.

Figure 3.7 TESA V-200 microscope

3.2.2.3 JCM-6000 benchtop scanning electron microscope (SEM)

This SEM further extends the lab's capability with nano-scale resolution. It provides well focused 2D morphological observation. A small grid gun integrating filament is used under the highest accelerating voltage of 15keV. Two working modes are supported: secondary electron (SE) imaging and backscattered electron (BSE) imaging, which provides magnification up 30000× and 60000× respectively. In addition, the SEM is equipped with an energy dispersive X-ray spectrometer (EDS) for elemental analysis. The SEM is primarily used for tool edge radius measurement, tool wear inspection, chip observation and elemental analysis.

Figure 3.8 JCM-6000 NeoScope benchtop SEM (measuring cutting edge radius)

3.2.3 Data acquisition system

3.2.3.1 Kistler dynamometer 9256C2

It is widely considered that in-process signal can assist in interpreting the micro-cutting process in detail and in depth. Many signals such cutting forces, acoustic emission, tool vibrations have been analyzed by previous research. Of all signal types, cutting forces are mostly investigated. In this study, a mini-dynamometer is employed to measure the cutting forces in order to comprehend micro-cutting process.

The dynamometer can measure three orthogonal components of cutting forces by piezoelectric elements. Its very low threshold allows measuring extremely small forces (<0.002N). The measuring range is from -250N to 250N for each axis, and the

linearity on full scale output falls within ±0.4%. The crosstalk between among axes is smaller than ±2%.

Working as the sensing unit, the dynamometer is connected to the multi-channel charge amplifier 5080A, which possesses a liquid crystal display to show all channels' settings. Measuring error on full range is kept within ±0.3% in temperature range from 0 to 50°C, while the drift is kept below $\pm 0.05 pC/s$. The charge amplifier is connected to voltage output modules 5067 whose output voltages are $\pm 10V$. It has very wide working bandwith up to $200 kHz$, but with time delay around $2 \mu s$.

Afterward the system is sequentially connected to NI9234, which is a four-channel AC/DC signal acquisition module; the four channels are able to simultaneously digitize signals at rates up to $51.2 kHz$ per channel with built-in anti-aliasing filters. The output voltage range on each channel is $\pm 5V$. The DAQ module is connected to a computer; data are collected by using self-developed software using LabView. The entire sensing system is shown in Figure 3.10.

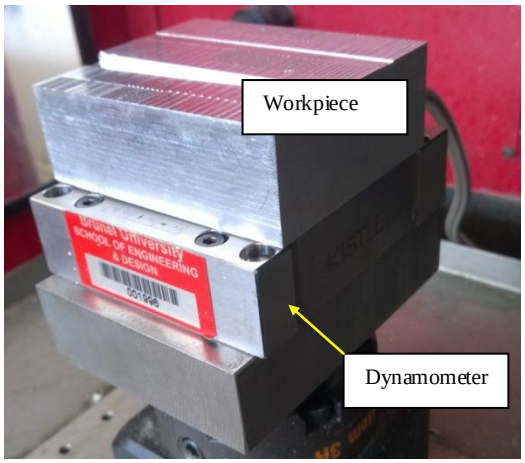

Figure 3.9 Dynamometer 9256C2 with a workpiece sitting on the top

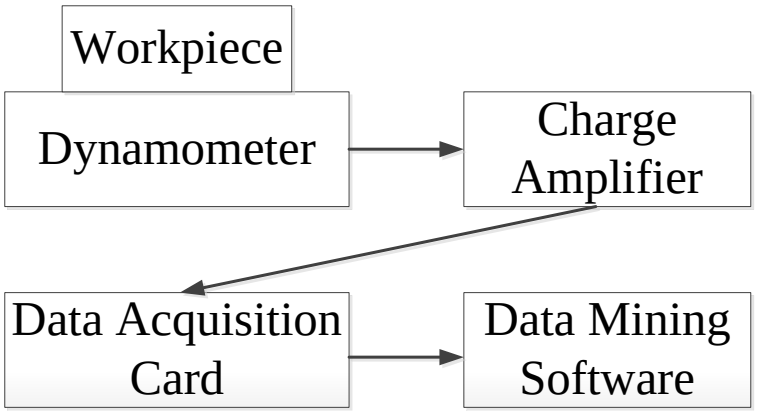

Figure 3.10 Data acquisition system

3.2.3.2 Impact hammer

Cutting process is highly nonlinear, thus it is a necessity to identify the dynamic response of the tooling and workpiece system, the transfer function from workpiece to dynamometer is another point of concern. An impact hammer 9722A500 is used in this study to perform the test. It incorporates a quartz measuring cell and outputs voltage signal in a range of $\pm 5V$. Multiple impact tips are selectable allowing for different force levels and different impact duration which control the frequency range of excitation. In general, harder tip usually deforms less and therefore has shorter duration. The harder tips can generate wider effective frequency range. A plot of the spectrum response of different tips made from various materials is shown in Figure 3.11. To facilitate maximum excitation frequency range, hard steel tip (circled in red) is always used in this study.

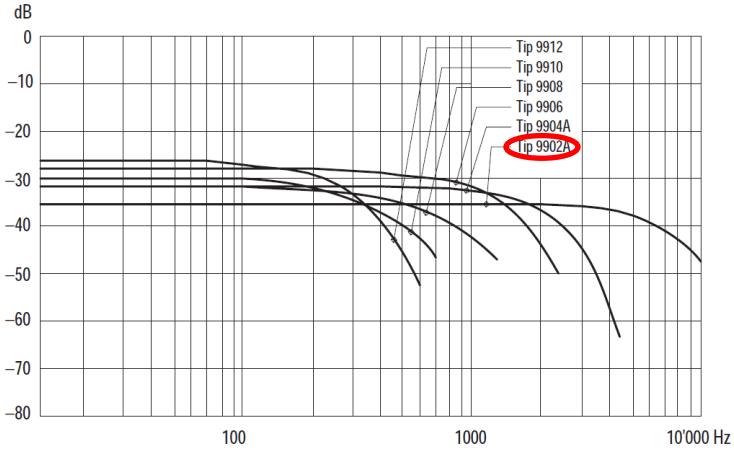

Figure 3.11 Spectrum response of tips made from different materials

As the hammer itself can't generate power and store signal, it has to be connected to other external devices such as piezotron coupler and power supply. Signals are also collected by NI 9234 module. Wire connections are shown in Figure 3.12.

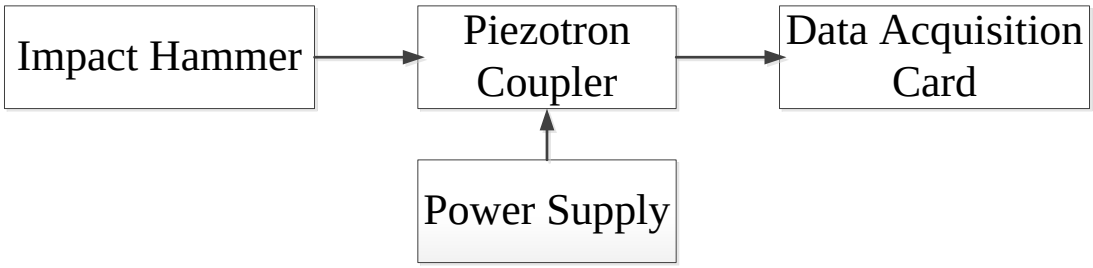

Figure 3.12 Impact test system

3.2.3.3 Capacitance sensor

A capacitance sensor MicroSense 5810 is adopted to measure the tool runout and its vibration. It is a non-contact displacement sensor with nanometer resolution, the measurement range is $\pm 100 \mu m$ and working bandwidth is $20 kHz$. Another function of it is to serve as a tachometer in this study. The sensor's output is also connected to NI DAQ 9234 module and data are collected by computer.

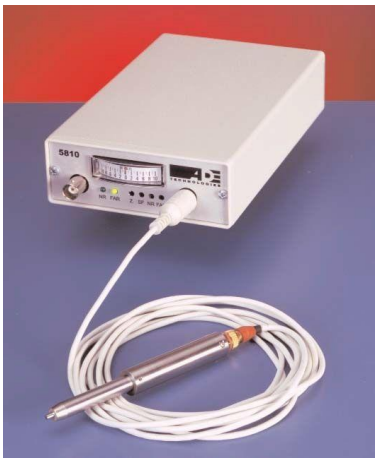

Figure 3.13 Capacitive sensor MicroSense 5810

3.3 Cutting trials and analysis

3.3.1 Orthogonal cutting

There are many factors affecting micro-cutting process. One of them is the cutting edge radius. It can be reason for size effect and minimum chip thickness (MCT). Other factors to be considered include cutting direction, material micro-level anisotropies and heterogeneity. To study the chip formation mechanism at micro-level, orthogonal cuttings were carried out both on the turning machine and micro-milling machine. Meanwhile, finite element based analysis is also conducted to complement experimental investigation.

3.3.1.1 Finite element analysis

Finite element based analysis is primarily used to study the relations between cutting edge radius and chip formation. It is widely believed that the MCT is closely associated with cutting edge radius. To investigate this, simulations are conducted

while using series of cutting edge radius and cutting speeds. Besides, its relation with tool material is also studied. Details will be elaborated in next chapter.

3.3.1.2 Cutting trials on the precision turning machine

Cutting trials are firstly performed on precision turning lathe. Two tools are used, one is diamond cutting tool with 0^o rake angle (Figure 3.5(a)), and the other is tungsten carbide tool with 0^o rake angle (Figure 3.5(d)). Cutting edge radius of both tools is measured using the SEM presented in 3.2.2.3. Most natural diamond cutting tools has very small cutting edge radius at the range of 30nm~400nm according to the manufacturer. Compared with that of tungsten carbide tools, which are normally around $3\mu m$ or larger, it is very small. Thus its edge radius in micro-cutting can be overlooked. Workpiece is firstly machined with diamond tool to create a datum surface, and then tungsten carbide tools are used to conduct the cutting trials. With the aid of this ultra-precision turning, the tungsten carbide tool is able to execute accurate movement down to nanometer level. The depth of cut in experiments increases from very small value at which no chips are formed to the value when distinct chips are removed. The relations between cutting edge radius and minimum chip thickness can be used to approximately predict the minimum chip thickness in micro-milling process. Cutting forces are recorded and analyzed as the primary process variable. The tungsten carbide tool sits on top of the Kistler dynamometer which in Figure 3.14. Other analysis including surface generation, comparison with simulation results is also conducted. Details can be found in next chapter.

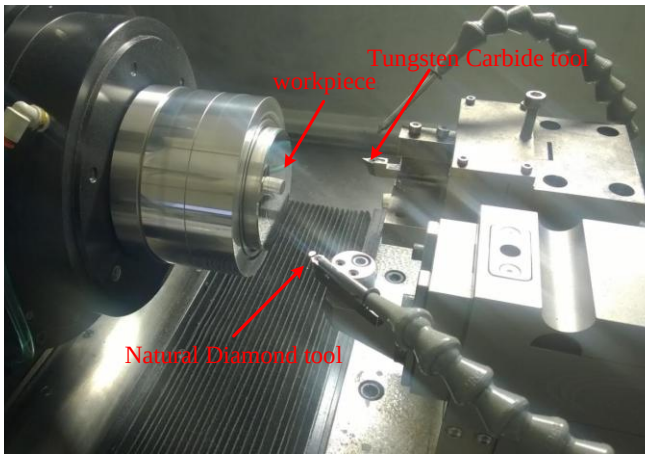

Figure 3.14 Orthogonal cutting trial on turning machine

3.3.1.3 Cutting trials on the micro-milling machine

To investigate the role of cutting edge radius in micro-milling and avoid the complexity brought about by oblique cutting, two tools are employed. The first one is a single blade diamond milling tool with radius of 0.2mm, the second one is a single blade tungsten carbide tool with the same radius. Since the cutting edge radius of natural diamond tool is extremely small, in micro-milling process, the diamond tool can be treated as perfectly sharp tool. Thus cutting process under conditions of sharp and round cutting edge can be investigated separately. Cutting edge radius of tungsten carbide tools is measured using SEM. Series of cutting trials are conducted with both tools. The cutting forces are collected as the main signals to be analyzed (Figure 3.15(a)). Surface roughness and burr size are also measured and analyzed while using these two tools.

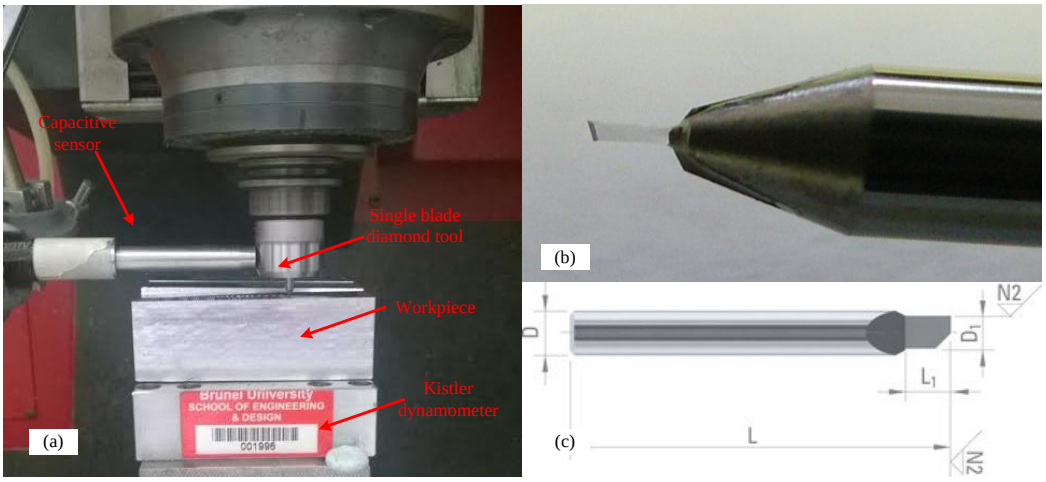

Figure 3.15 (a) Experiments of single blade tool on micro-milling machine (b) natural diamond single blade tool (c) tungsten carbide single blade tool

3.3.2 Novel cutting force modeling

Micro cutting force modeling is developed based on the cutting trials. In this section a normal micro-milling tool with helix angle is adopted, cutting forces in three directions are recorded with Kistler dynamometer as shown in Figure 3.16. The capacitive sensor is used to synchronize the signal of cutting forces and the tool spinning motions. There are two marks on the tool holder with interval angle of 180^{o}, which are aligned with the two tool tips of micro-milling tool. As the tool tip enters workpiece, the capacitive sensor captures the mark indicating the entering point of cutting process. The measured cutting forces are compensated by a Kalman filter as

the transform of the cutting forces at the tool tip to the dynamometer is not linear. The compensation on measured cutting forces is conducted on every cutting trial. The novel cutting force model is proposed in aspects of length, area and volume, respectively. It is built theoretically based on currently available force model, and validated by experimental results. The different aspects of force model will be applied to interpret the chip formation, burr formation, tool wear and cutting temperature. Experiment details, results and discussion will be presented in following chapter.

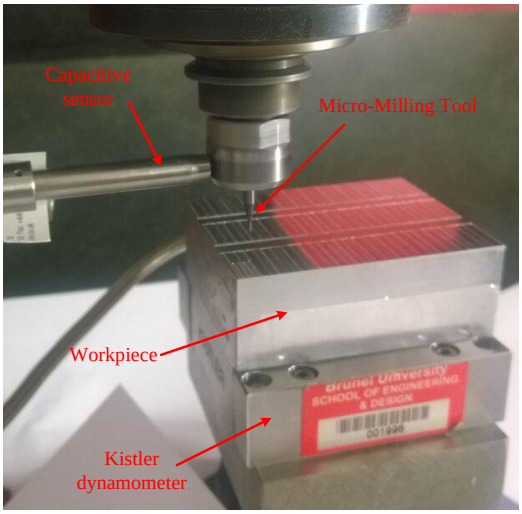

Figure 3.16 Experimental validation for novel cutting force modeling

3.3.3 Tool wear monitoring

Tool wear will not only deteriorate the quality of workpiece including accuracy, surface integrity and roughness, but result in large machining resistance which might cause premature failure and disrupt the machining process. Thus it's very critical to monitor the tool wear and avoid excessive wear to ensure machining reliability. This is very important in industrial-scale production.

Figure 3.17 shows the experimental setup for analyzing tool wear process; the tool is worn intentionally against hard-to-machine material to accelerate its wear rate. The tool cuts a slot on the reference workpiece which sits on top of the Kistler dynamometer, the cutting forces are recorded. The same procedures repeat several times. The types of tool wear are summarized and classified. The cutting forces at different stage of tool wear are recorded and compared to identify the key parameter which can best represent the tool wear status in machining. Analysis based on

wavelet transform is conducted. Besides, the influence of tool wear on surface roughness and burrs size are also investigated.

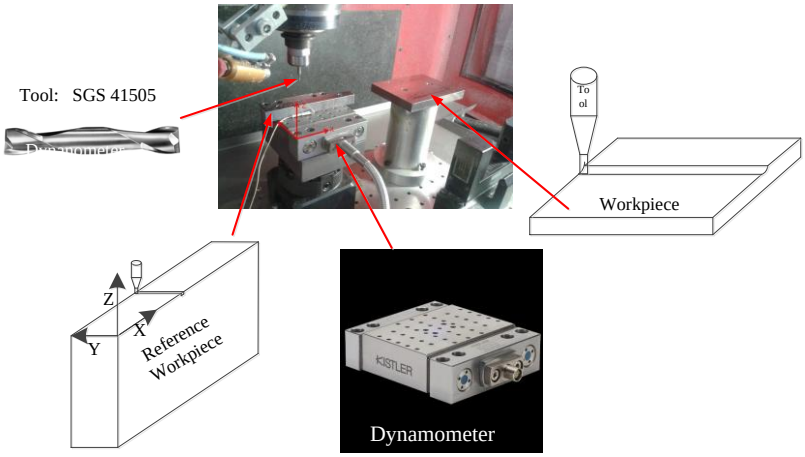

Figure 3.17 Experiment setup for tool wear analysis

4 Chip Formation in Micro-Milling Process

4.1 Introduction

The chip formation in micro milling process is different from that in conventional milling process. The most prominent is the well-known size effect, which is commonly known as the increases of specific cutting force with decreases in cutting depth. As a result of unneglectable cutting edge radius, when cutting at very small depth of cut, it results in large negative rake angle, and no chips are produced. Only if the uncut chip thickness approaches certain threshold, chips start to form. This is commonly known as minimum chip thickness effect(Vogler et al. 2002; Vogler et al. 2003a; Liu et al. 2004; Weule et al. 2001a; Kim et al. 2004a; Kang et al. 2007). This effect distinguishes itself from macro-milling very clearly. When cutting takes place at very small depth of cut, material undergoes pure elastic deformation and then recovers to the original height. If the cutting depth continues to increase, the material deforms partly plastically and only it exceeds the minimum chip thickness, the chips can be removed. The identification of it is a critical issue in micro-milling and has been investigated by many researchers (Yuan. 1996; Kim. 2004b; Kang et al. 2011; Ramos et al. 2012) either experimentally or theoretically. It is widely accepted that the chip formation in micro-cutting is separated into two regimes: ploughing-dominant regime and shearing dominant regime.

This chapter attempts to investigate the chip formation process in micro-milling process by means of simulation and experimental trials. The chip formation is firstly simulated using FEA approach to study the size effect and identify the minimum chip thickness value for different tool/material pairs. This can give us better understanding on related micro-cutting mechanics, and the simulation results are validated by experiments on the ultra-precision turning machine. Further, the scenario of comparative study is conducted by utilizing both a tool with perfectly sharpened cutting edge and a tool with the rounded cutting edge in micro-milling. The chips are inspected and associated with cutting force variation in periodical material removal process. The findings are further consolidated by comparing with research results by other researchers.

4.2 Finite element analysis of chip formation in micro-cutting

4.2.1 Model setup

4.2.1.1 Material constitutive model

Material flow stress in metal cutting defines the point of commencement of continuous material flow. It is often dependent on strain, strain rate and temperature. These properties must be fully captured by material constitutive model in a wide range of strain, strain rate and temperature, especially under complicated circumstances in metal cutting. An accurate model is highly necessary and prerequisite for FE simulation. To construct the constitutive behavior of Aluminum 6082-T6, Extensive research has been conducted, and many models are developed. The most frequently used is called Johnson-Cook model (Johnson and Cook 1983) as given in Eq.4-1

$$\bar{\sigma} = [A + B(\bar{\varepsilon})^n]\left[1 + C \ln\left(\frac{\dot{\bar{\varepsilon}}}{\dot{\bar{\varepsilon}}_0}\right)\right][1 - \left(\frac{T - T_0}{T_m - T0}\right)^m] \quad (4\text{-}1)$$

A : initial yield strength of the material at room temperature;

$\dot{\bar{\varepsilon}}$: equivalent plastic strain-rate;

$\dot{\bar{\varepsilon}}_0$: reference strain-rate;

T_0 : room temperature;

T_m: melting temperature of the material;

B, *C*, *n* and *m* are model parameters. *n*, *m* and *C* are the strain-hardening exponent, thermal softening exponent and strain-rate sensitivity, respectively.

These parameters are usually obtained through testing of sampled materials such as Taylor's impact test or Hopkinson's compression and shear devices. Although these techniques are not quite adequate to simulate metal cutting conditions (Jaspers and Dautzenberg 2002b). Jaspers and Dautzenberg (2002a) used Split Hopkinson Pressure Bar (SHPB) to conduct material test in conditions similar to metal cutting and obtained the material data. Özel and Zeren (2005) revised Jaspers-Dautzenberg's results by analyzing conditions in cutting area. The revised material constants are shown in Table 4-1 and are used in the simulation, whereas the physical properties of

the aluminum workpiece and cutting tool used in the simulation are listed in Table 4-2.

Table 4-1 Material constant for Johnson-Cook plasticity model

Material	T_m(℃)	A (MPa)	B (MPa)	C	n	m
6082-T6	582	442.95	324.62	1e-6	1.0261	1.3116

Table 4-2 Workpiece and tool properties

Physical parameter	Aluminium 6082	Diamond	Tungsten carbide
Density, ρ (kg/m3)	2700	3510	15700
Elastic modulus, E (GPa)	71	1200	696
Poisson's ratio, ν	0.33	0.2	0.22
Specific heat, Cp (J/kg/ ℃)	896	507.9	210
Thermal conductivity, λ (W/m/C)	170	2000	110
Expansion, αd (μm.m/°C)	24	1.18	5.2
Tmelt (℃)	583	3642	2870
Troom (℃)	20	20	20

4.2.1.2 Damage initiation and evolution

Chips are formed when work material is under high compressive or shear stress and experience large strain rate to start to damage, fracture and finally fails. Figure 4.1 shows the typical stress-strain behavior undergoing failure process. The ductile materials will firstly deform elastically under stress (a-b) and then plastically with combined strain hardening and thermal softening effect (b-c). Point c in the figure defined the onset of material damage. Beyond this point, material undergoes damage evolution, stress required to further strain the material is reduced due to the existence of material damage, the damage accumulates until it reach failure at point e. the dashed line represents the stress-strain curve in absence of damage, the real stress-strain curve is represented by solid line c-d-e. So the material failure process can be divided into two sections: the first section undergoes softening of material yield stress until initial damage occurs (point c in figure); and the second section concerns the degradation of elasticity until final failure occurs (point e in figure).

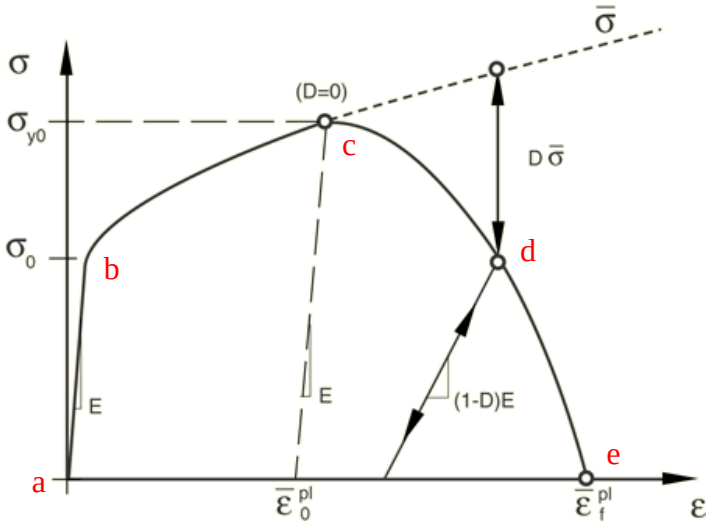

Figure 4.1 Stress-strain curve with progressive damage degradation

To simulate the damage initiation, The Johnson–Cook shear failure model is adopted, which has following expression:

$$\bar{\varepsilon}_D^{pl} = [d_1 + d_2 \exp(d_3\eta)]\left[1 + d_4 \ln\left(\frac{\dot{\bar{\varepsilon}}^{pl}}{\dot{\varepsilon_0}}\right)\right]\left[1 + d_5\left(\frac{T-T_r}{T_m-T_r}\right)\right] \quad (4\text{-}2)$$

where $d_1 \sim d_5$ are the model parameters, η is the stress triaxiality, $\dot{\bar{\varepsilon}}^{pl}$ is the equivalent plastic strain rate and $\dot{\varepsilon_0}$ is the reference strain rate, T is the material temperature, T_r and T_m are the room temperature and material melting temperature. The Johnson-Cook damage model shows that the equivalent plastic strain at the onset of damage is a function of temperature, stress triaxiality and strain rate. The parameters used for aluminum 6082-T6 are shown in Table 4-3, it should be noted that, as indicated in the table, the material used in simulation has very strong dependence of stress triaxiality and temperature change, but very little dependence on strain-rate.

Table 4-3 Material parameters for Johnson-Cook damage model

Material	d_1	d_2	d_3	d_4	d_5
6082-T6	0.0164	2.245	-2.798	0.007	3.658

The Johnson-Cook model defines the damage initiation criterion at the point c, however the law for damage evolution is still absent. To better follow the strain-softening behavior of material after damage initiation, Hillerborg's (1976) created a stress-displacement relation after damage initiation and proposed the fracture energy which is assumed to open a unit area of crack, G_f, as a material parameter.

$$G_f = \int_{\bar{\varepsilon}_0^{pl}}^{\bar{\varepsilon}_f^{pl}} L\sigma_y \, d\bar{\varepsilon}^{pl} = \int_0^{\bar{u}_f^{pl}} \sigma_y d\bar{u}^{pl} \tag{4-3}$$

The fracture energy G_f introduces the concept of equivalent plastic displacement, $\bar{u}^{pl}$, as the fracture work conjugate of the yield stress after the initialization of damage. Before damage initiation, $\bar{u}^{pl}$ is 0, once damage is initialized, $\bar{u}^{pl} = \int_0^{\dot{\bar{\varepsilon}}^{pl}} L d\dot{\bar{\varepsilon}}^{pl}$ where L is the characteristic length of element in simulation. Thus the damage evolution can be formulated in terms of either equivalent plastic displacement $\bar{u}^{pl}$ or fracture energy G_f. In FE simulation, the two terms can both be specified directly.

Since there isn't available data about equivalent plastic displacement for aluminum 6082, fracture energy is specified in the simulation. It can be described as:

$$\left(G_f\right)_{I,II} = \left(\frac{1-v^2}{E}\right)\left(K_C^2\right)_{I,II} \tag{4-4}$$

where v is Poisson's ratio, and E is the Young's modulus, $(K_c)_{I,II}$ are material's fracture toughness in opening mode and sliding mode respectively. For aluminum 6082, K_c is 29 MPa-m½.

The overall damage indicator as shown in Figure 4.1, D, evolves in an exponential form,

$$D = 1 - exp\left(-\int_0^{\bar{u}^{pl}} \frac{\bar{\delta}_y \dot{\bar{u}}^{pl}}{G_f}\right) \tag{4-5}$$

This ensures that energy dissipated in progressive failure of material is equal to G_f. When damage initiates, D is 0, it gradually increases as damage accumulates until failure, D becomes 1, which means material is fully degraded.

4.2.1.3 Tool-workpiece contact and friction

The interactions between the tool and workpiece is of critical importance, as the contact conditions and friction between them directly affect cutting forces, heat generation and tool wear rate etc. thus accurate modeling is critical. In Abaqus, it solves contact problems using either a kinematic contact algorithm or a penalty contact algorithm (Outeiro et al. 2015). The penalty method is essentially based on insertion of a stiff spring between the two contacting bodies. A penalty factor is used here and can be interpreted as the stiffness of the spring. Contact pressure in normal direction is computed as:

$$T_n = \begin{cases} -p_n g + p_0 & if\ g < p_0/p_n \\ 0 & if\ g \geq p_0/p_n \end{cases} \quad (4\text{-}6)$$

g is the gap between two contacting bodies. p_n is the penalty factor which is updated in accordance with material deformation. p_0 is the pressure when g is zero.

Friction in cutting is another imperative aspect, conventional machining adopts Coulomb-type models where frictional forces are proportional to the normal pressure with friction coefficient. However, this is only suitable to describe the tool flank face, not on the rake face. Zorev (2001) proposed a stick-slip friction law based on normal and shear stress distribution on the rake face.

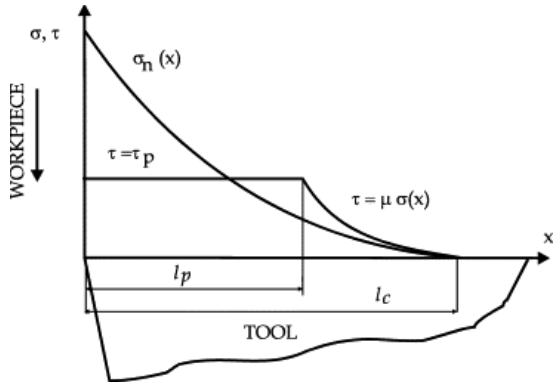

Figure 4.2 Normal stress and frictional stress on tool rake face (Zorev,2001)

The similar friction model is applied in the simulation.

$$\tau_f = \begin{cases} \tau_p & \text{if } \mu\delta_n \geq \tau_p \\ \mu\delta_n & \text{if } \mu\delta_n < \tau_p \end{cases} \quad (4\text{-}7)$$

where δ_n is the normal contact pressure, μ is the dynamic friction coefficient, τ_p is limit shear stress, where a relation $\tau_p = \delta_y/\sqrt{3}$ holds, δ_y is material initial yield stress. In this case, regardless of the normal contact pressure, sliding will occur if the limit shear stress reaches this value.

The mean friction coefficient between tool and workpiece materials is usually calculated from experiment cutting force. In this simulation the friction coefficient for diamond/aluminum pair and tungsten-carbide/aluminium pair are 0.15 and 0.25 respectively.

4.2.1.4 Heat generation and transfer

It is widely acknowledged that in metal cutting there are three shear zones; Figure 4.3 depicts the schematic of micro-cutting by extending the same assumption from conventional cutting. Similarly there are 3 deformation zones which are hardly

distinguishable due to the round cutting edge. The dissipated energy due to plastic deformation in the three shear zones almost all turn into heat which serves as the first heat source in micro-cutting. Part of the heat will be conducted to chip and taken away with it; the other part will be conducted to other parts of the workpiece. In addition, the frictional work at the tool/chip and tool/workpiece interface is another appreciable heat source. It is distributed across the interface according to Charron's relation (Issa et al. 2011).

$$r = \frac{1}{1+\sqrt{\frac{\rho_u C_{p,u} k_u}{\rho_d C_{p,d} k_d}}} \tag{4-8}$$

where $C_{p,u}$ and $C_{p,d}$ are heat capacity of upper and down surfaces, k_d and k_u are conductivities of the downside and upside surface respectively; ρ_u and ρ_d are the material density of the upside and downside surface respectively.

The heat flux at the tool/chip or tool/workpiece interface can be formulated as following:

$$\begin{cases} -\mathbf{n}_d * (-k_d \nabla T_d) = -h(T_u - T_d) + rQ_{fric} \\ -\mathbf{n}_u * (-k_u \nabla T_u) = -h(T_d - T_u) + (1-r)Q_{fric} \end{cases} \tag{4-9}$$

h is the heat transfer coefficient at the interface, which is $46 \times 10^6\ Wm^{-2}K^{-1}$ for diamond/aluminum pair and $1.3 \times 10^6\ Wm^{-2}K^{-1}$ for tungsten-carbide/aluminium pair.

Due to varied thermal properties such conductivity, specific heat and CTE, The amount of heat transferred to different parts are not the same thus it results in varying temperature distribution, which is another issue worth in-depth investigation. Meanwhile, in real machining, ambient temperature usually stays constant, thus temperature rise in different part of the cutting system will lose heat to the environment due to convection and radiation.

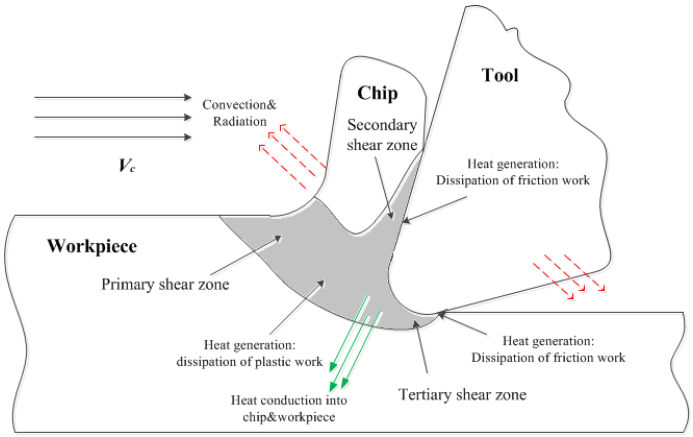

Figure 4.3 Schematic of the orthogonal micro-cutting

4.2.1.5 Finite element geometrical model

The simulation is carried out by using Abaqus/Explicit^{TM} software. A schematic FEA is shown in Figure 4.4; the tool rake angle and clearance angle are defined according to experimental conditions, which are 0^o and 6^o respectively. Cutting tool edge radius is set at various values. Given high strength tool properties, the tool is configured as rigid body to simplify the computation process while heat transfer is still active. Quadrilateral continuum elements CPE4RT are used to model the workpiece for the fully coupled displacement-temperature computation. The interaction at the interface between the tool and workpiece are simulated by a surface contact pair. In simulation, the tool is fixed, while the workpiece moves towards it with the cutting velocity. The indicated edges in figure are modelled as open boundary which means material in these directions is infinite. The remaining surfaces are defined as external surfaces through which heat are lost to environment by radiation. Simulations are carried out under different tool material, various cutting speed and cutting edge radius.

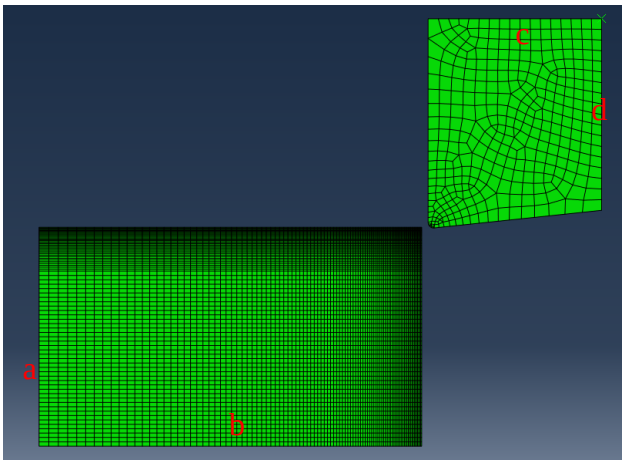

Figure 4.4 Geometrical model of the orthogonal micro-cutting

4.2.2 Simulation results and discussion

Two sets of simulations are carried out to study the chip formation considering tool geometry, tool/material pair and cutting parameters. Particular interests are focused on explaining phenomenon in micro cutting such size effect, minimum chip thickness, etc. Factors that dominate MCT are investigated, meanwhile, material behaviour under different cutting regime is also studied. In addition, study on the position of stagnation point where chips split with material are also conducted. Parameters used in simulation are listed in Table 4-4.

Table 4-4 Cutting parameters used in simulation

Tool	Natural diamond	Tungsten carbide
Workpiece	Aluminium 6082-T6	
Cutting edge radius	10μm 20μm 30μm	
Depth of cut	1μm 2μm 3μm 4μm 5μm 6μm 8μm 10μm 12μm	
Cutting speed	180m/min 360m/min 540m/min	

4.2.2.1 Size effect in chip formation

Simulations are firstly carried out on tungsten carbide with cutting edge radius of 20μm machining workpiece at various depth of cut. Cutting speed is set at 360m/min, simulation time is 25μs. Simulation results show the MCT is around 3.5μm at which chips are formed. Cutting forces in cutting and thrust direction are shown in Figure 4.5. it clearly indicates that when cutting depth is less than MCT, forces in cutting direction (Fc indicated in figure) are smaller than that in thrust direction (Ft indicated in figure). When it exceeds MCT, forces in cutting direction become greater than that in thrust direction. As cutting depth increases, cutting forces increase more quickly

than thrust force at larger slope, as the chips start to accumulate on the rake face before it splits with the tool.

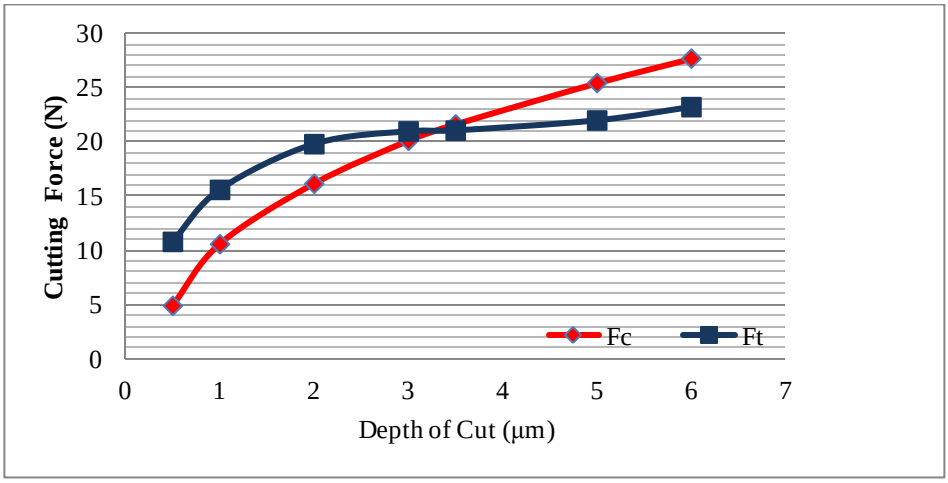

Figure 4.5 Plot of cutting force versus depth of cut

In Figure 4.6, it can be seen that the large ratio between the tool edge radius and actual cutting depth is the main factor that affects size effect. Given the large edge radius, it results in very big negative rake angle at the tool/material interface when cutting at small depth of cut. As shown in the Figure 4.6(a), tool ploughs over workpiece, material in contact with the rounded edge undergoes very large compressive stress and deformation, instead of shearing, as at this point chips can't be formed. Most of the energy consumed is dissipated in generation of material deformation and to overcome the friction at the interface. Figure 4.6(b) shows the material instantaneous velocity under deformation. Due to the strong interaction between tool and material, material beneath the tool deforms downward, but material in front of the contact area has resultant velocity in up-forward direction, which produces a small pile-up of material. If the depth of cut exceeds MCT, the material pile-up accumulates and will finally be removed as chips; however, if the depth of cut is less than MCT, the material pile-up will stay constant and remain, in result, chips can't be formed.

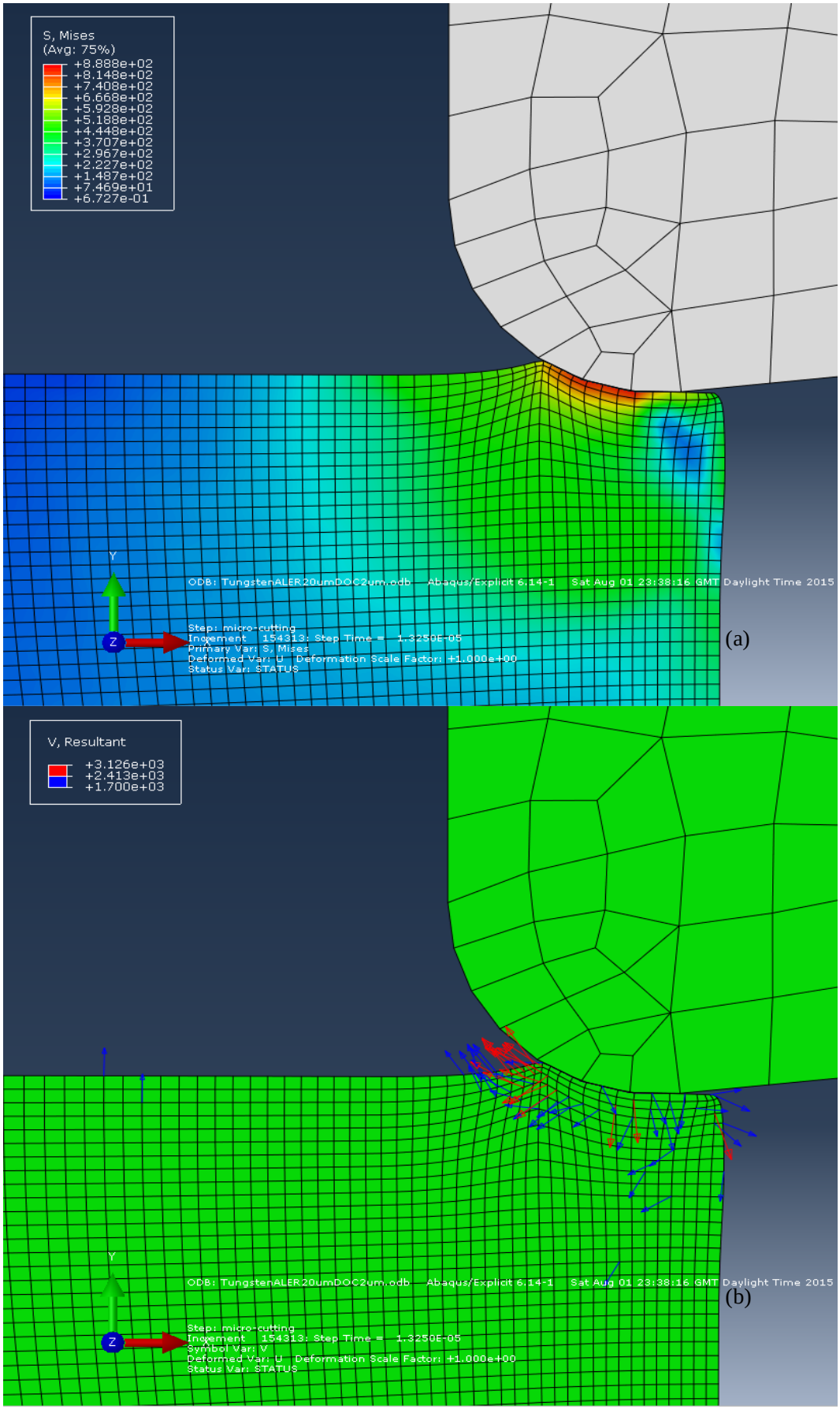

Figure 4.6 Simulation outcomes (a) Stress distribution (b) velocity distribution

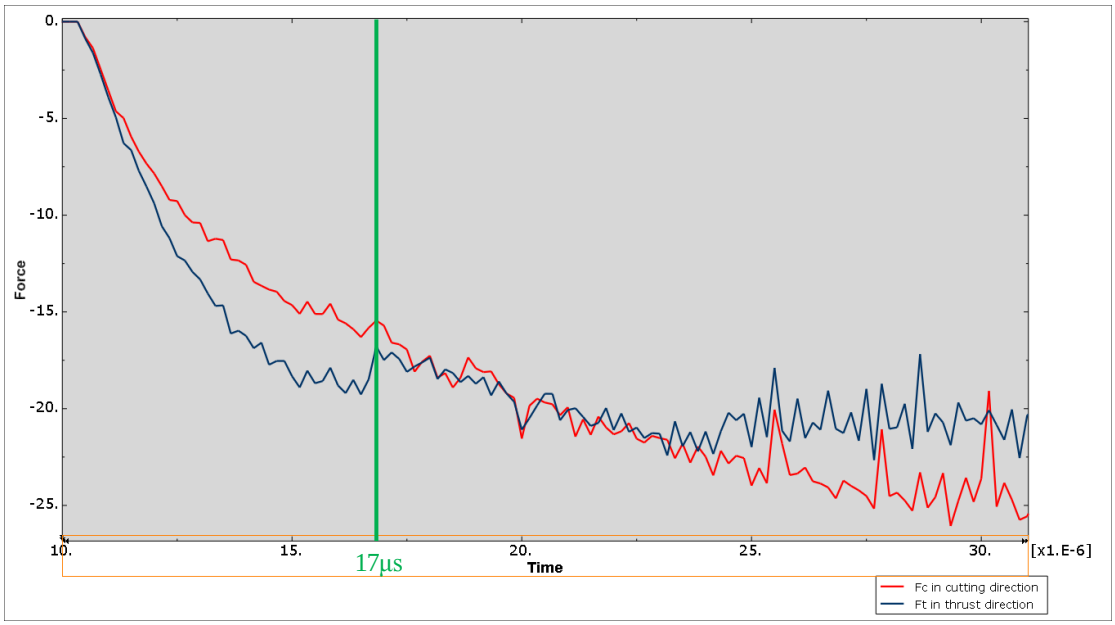

Figure 4.7 Forces in cutting and thrust direction during chip formation (simulation)

The cutting forces in the cutting and thrust directions during chip formation process are shown in Figure 4.7. The depth of cut is 3.5μm, which is very close to MCT. The thrust forces (dark blue) increase quickly once the tool engages with the material, while cutting forces (red) gradually increase at slower pace; at this moment, material deforms and pile-up appears, but chips aren't formed. When the pile-up in front accumulates to certain level (t=17μs in figure), chips start to form; Noticing that there is a sudden drop in thrust forces which can be explained that the upward flow of material along the cutting edge has counteract part of the forces incurred by the downward flow of material. From this point and onward, thrust forces increase at very low speed before it reaches constant around 20N, cutting forces continue to grow and finally exceed the thrust forces and chips are removed. When stable cutting conditions are achieved, and chips are removed consistently, forces in both directions stay constant.

Figure 4.8 shows the forces at two varied depth of cut. It can be seen that at depth of cut less than MCT, as no chips are formed, forces in both direction increases to a stable value and levels out; however, at depth of cut greater than MCT, a sudden drop in thrust force can also be identified at 16μs in Figure 4.8(b).

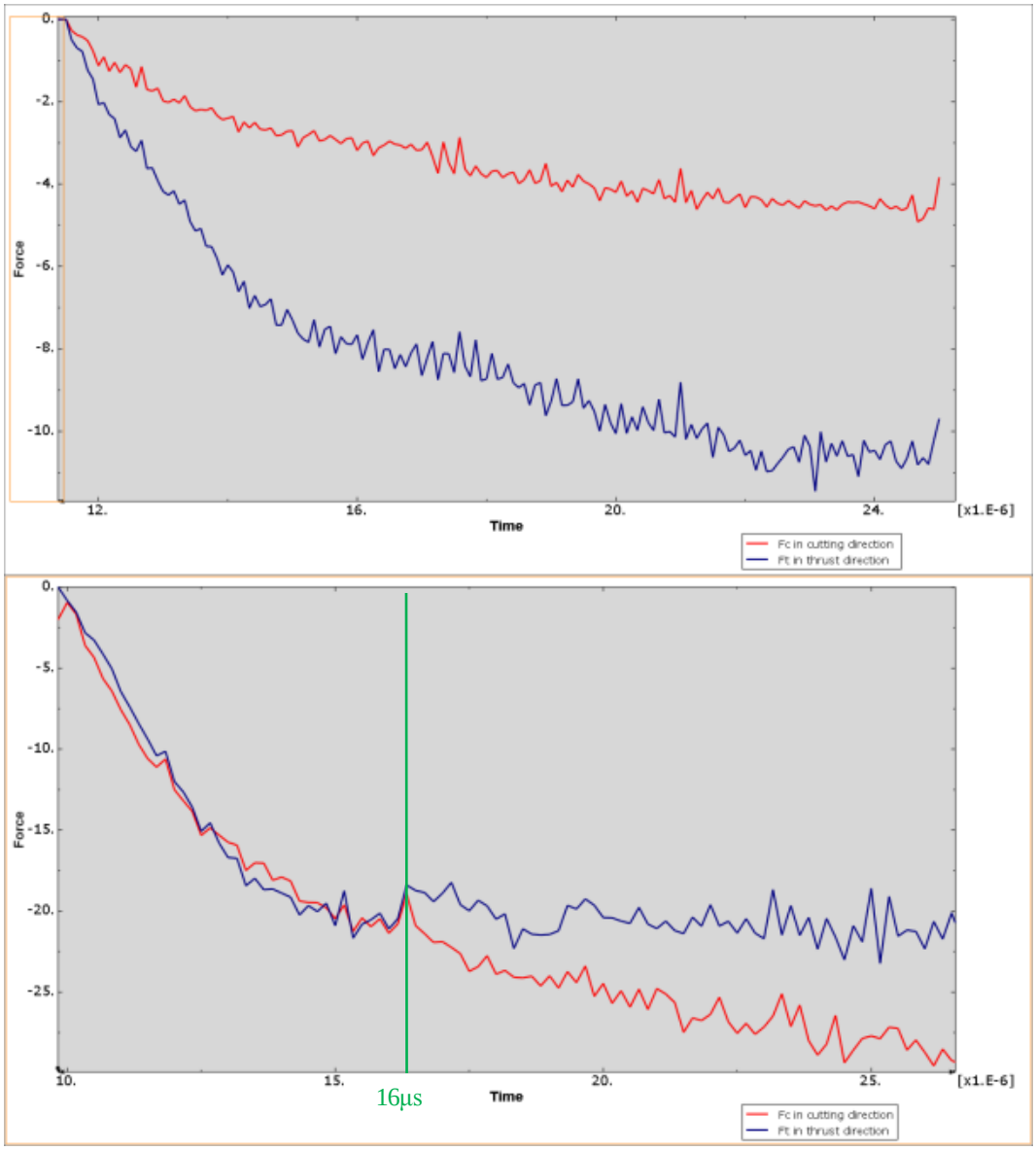

Figure 4.8 Forces in cutting and thrust direction (a) DOC, 0.5µm (b) DOC, 6µm

Also shown in Figure 4.8 is the fact that the smaller the depth of cut compared to the edge radius, the more obvious the size effect. Size effect will disappear once chips are formed. The bigger the cutting depth, the quicker cutting forces exceed thrust forces.

4.2.2.2 Minimum chip thickness in chip formation

Simulations are also carried out to study the role of edge radius variation in determining minimum chip thickness, as this is quite practical considering the inconsistency in tool manufacturing which may produce varied edge radius. Besides, to better study the chip formation process, the stagnation point where the chip splits

with material are investigated. Simulations are conducted based on two tool/workpiece pairs, diamond/aluminium and tungsten-carbide/aluminium, to study the influence of tool material on chip formation. Cutting edge radius is set to be 10µm, 20µm and 30µm respectively for both diamond and tungsten carbide tools. Cutting speed in simulation is 480m/min.

Figure 4.9(a) presents the minimum chip thickness for diamond and tungsten carbide tools at different cutting edge radius. In the figure, a linear relationship between the cutting edge radius and minimum chip thickness can be identified for both tools. The ratio of minimum chip thickness to cutting edge radius is around 25% for diamond micro-milling tool, while it is around 16% for tungsten carbide tool. The tools used in simulation are treated as rigid body due to their extreme hardness and high mechanical strength, the main difference among the two tool/workpiece pairs lies in friction and heat transfer coefficient at the interface, so the minimum chip thickness depends both on tool and workpiece materials.

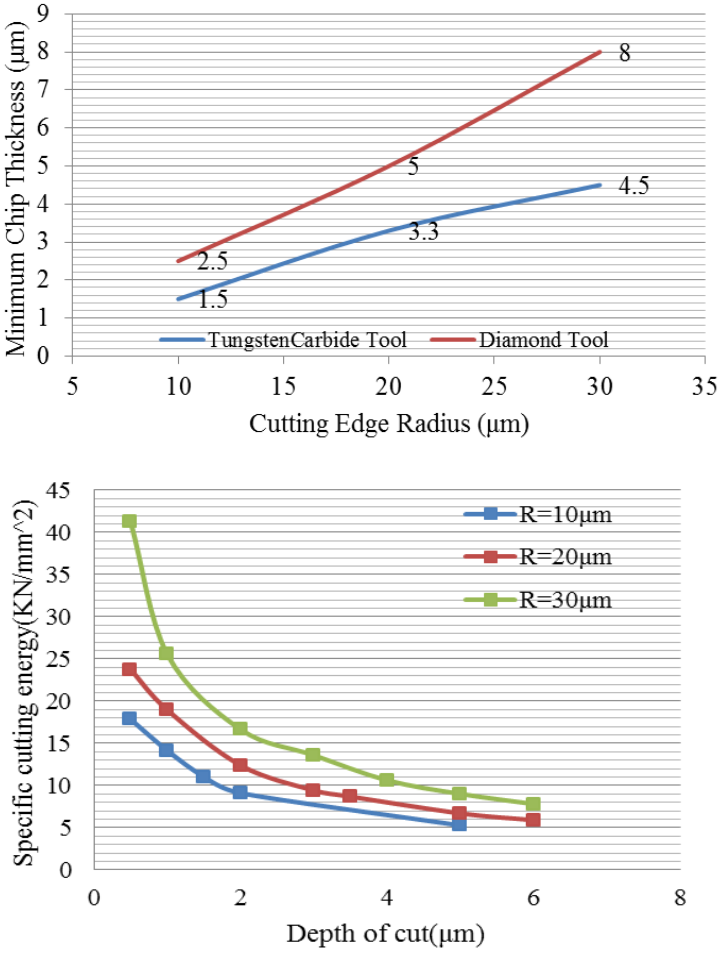

Figure 4.9 (a) Minimum chip thickness vs depth of cut

(b) Specific cutting energy vs varied depth of cut

The specific cutting energy, defined as cutting force consumed on unit cutting area, gives good understanding on the size effect as shown in Figure 4.9(b). It plots the specific cutting energy of the tungsten carbide tool with varied cutting edge radius against the depth of cut. It can be concluded from the plot that the bigger the ratio of cutting edge radius to depth of cut, the more pronounced the size effect. When depth of cut is very small, the highly negative rake angel leads to severe ploughing which contributes substantially to the energy consumption. Once the depth of cut turns greater than the minimum chip thickness, the specific cutting energy becomes much less. Therefore, if the energy is of great concern, sharp tool and cutting depth larger than the minimum chip thickness should be employed.

The influence of cutting speed on minimum chip thickness is also studied. Simulations are carried out at speeds of 180m/min, 360m/min and 540m/min respectively with respect to diamond and tungsten carbide tools. As the cutting speed changes, it can be predicted that the strain rate the material undergoes changes significantly, the heat generated due to inelastic deformation and friction can grow exponentially. Material properties and behaviour under these conditions vary drastically.

Minimum chip thickness at varied cutting speed for the diamond and tungsten carbide tool are shown in Figure 4.10(a), which indicates negligible variation in MCT. The reason may lies in the material properties. Figure 4.10(b) gives the specific cutting energy of the tungsten carbide tool cutting material along the tool displacement until chips are produced. The simulations are carried out at same depth of cut at varied cutting speed. It is worth noticing the fact that the lower cutting speed results in bigger specific cutting energy when chip removal occurs. The higher cutting speed will undoubtedly lead to larger strain and strain rate, which strengthens material strain hardening. This makes the material harder to cut, however, as the cutting speed increases, the heat generated due to plastic deformation and friction will significantly raise the cutting temperature which strengthens the thermal softening effect. Parameters in Table 4-1 show that Aluminium 6082-T6 is more sensitive to cutting temperature changes compared to the strain or strain rate variations. This may result in the outcome as shown in Figure 4.10(b).

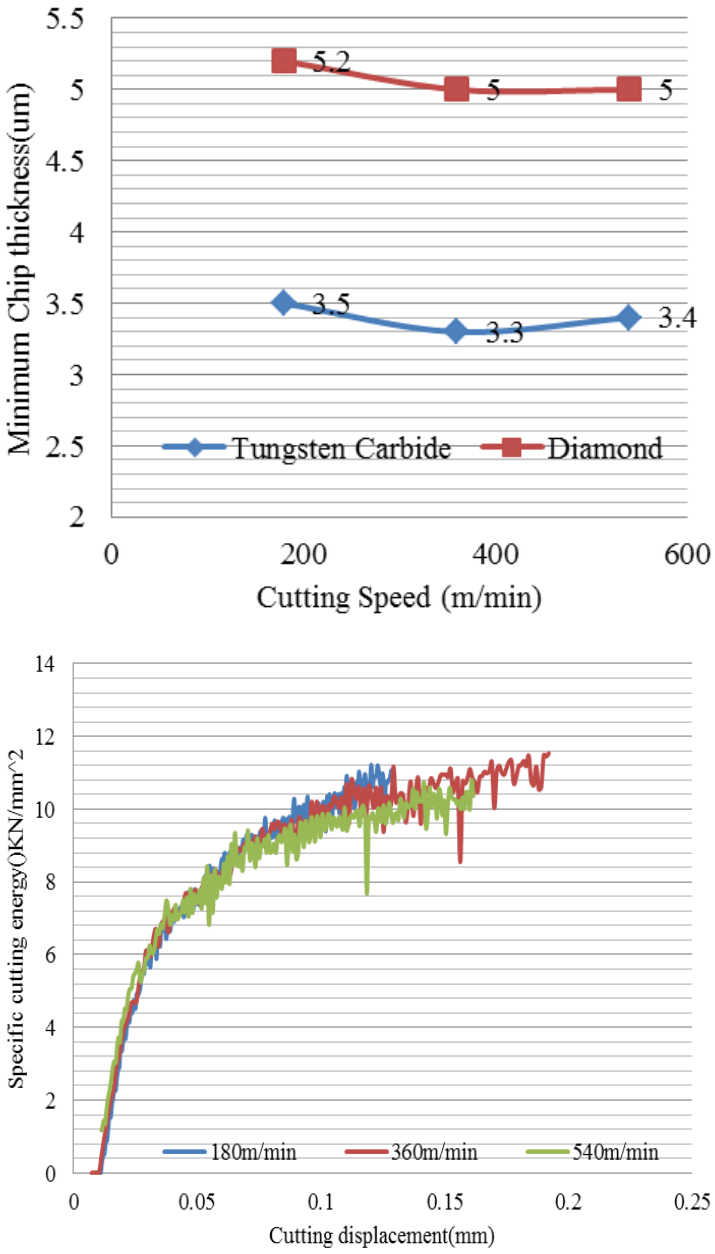

Figure 4.10 The effect of cutting speed on (a) MCT (b) Specific cutting energy

4.2.2.3 Stagnation point in chip formation

Another issue of concern is the stagnation point or region in chip formation, as this particular point determines the real depth of cut. From this point, the upper part of material moves upward and splits with workpiece, which produces the chips, whereas the lower part flows beneath the cutting edge and generates the machined surface. The stagnation point can be decided by observing displacement distribution of element in simulation.

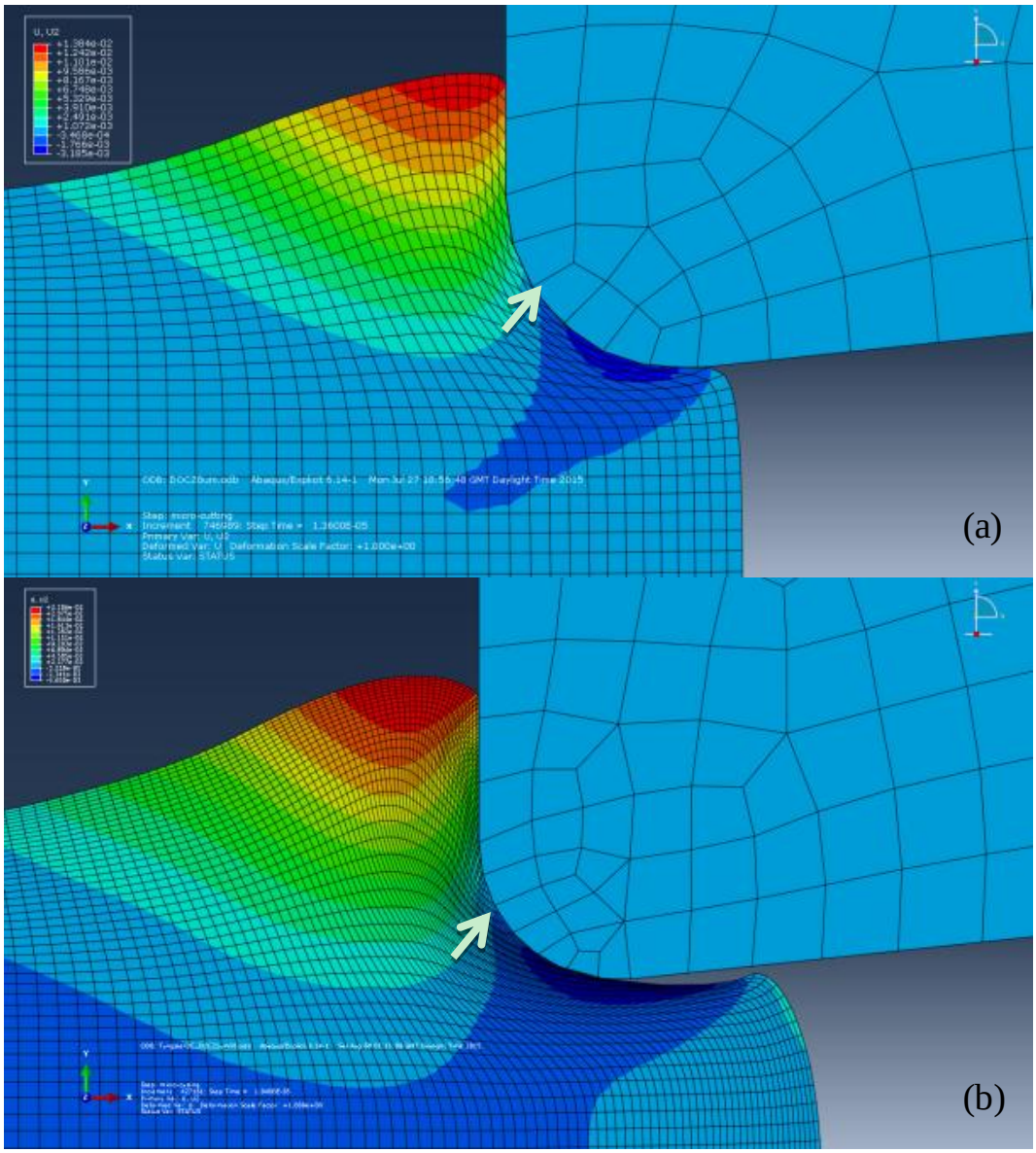

Figure 4.11 Displacement distribution for (a) diamond/aluminum (b) tungsten carbide/aluminum

Figure 4.11 shows the displacement distribution in the y direction when stable chips are removed. The stagnation points are indicated in the figure, they both are located on the edge radius with angle of 58 ° and 55 ° to the vertical Y axis respectively for diamond and tungsten carbide tools.

The stagnation point aforementioned is its stable position when chips are formed, however, if machining takes place at smaller depth of cut, its position may be varied.

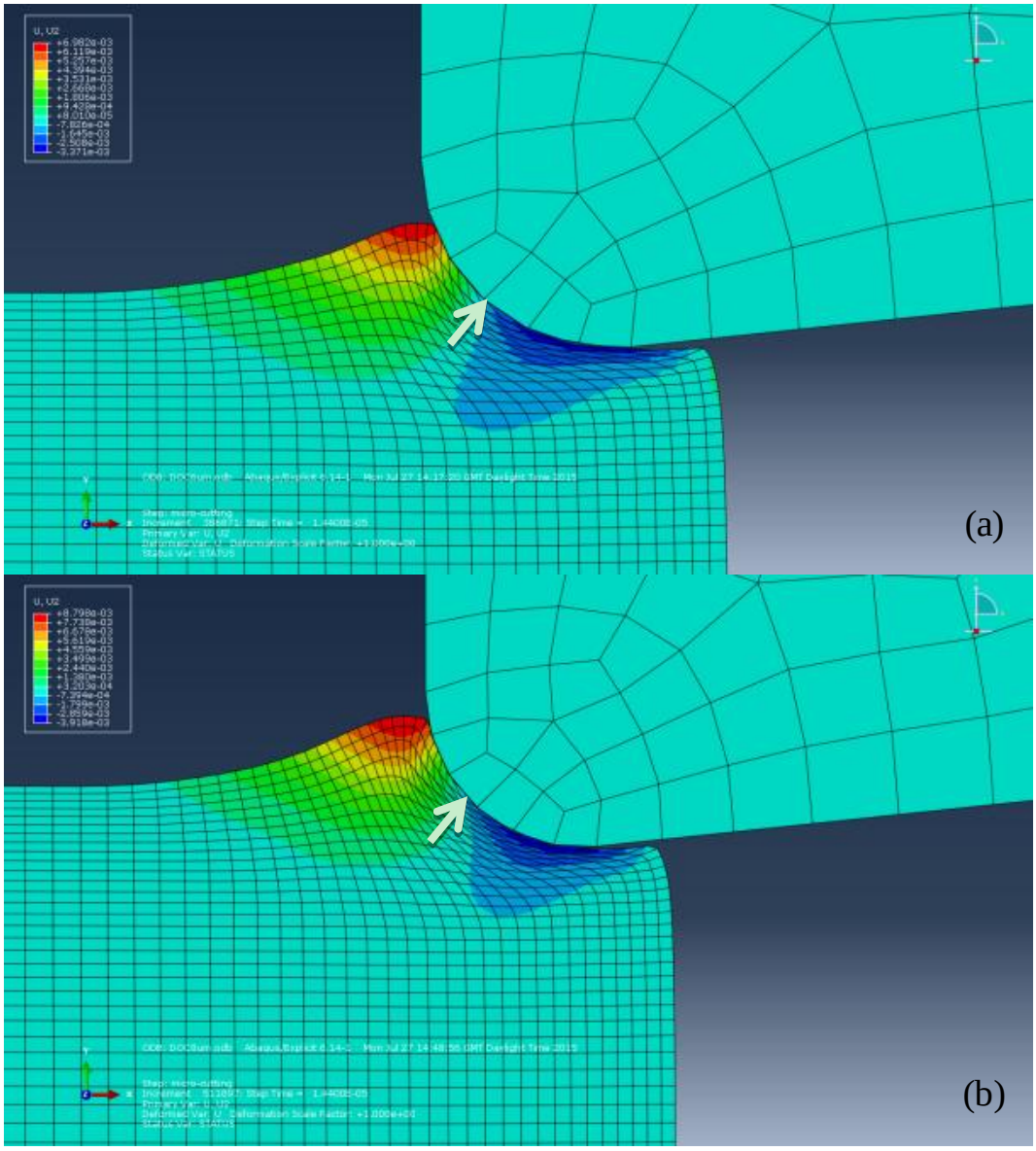

Figure 4.12 Displacement distribution for diamond tool (a) DOC 6µm (b) DOC 8µm

Figure 4.12 shows the positions of stagnation point at depth of cut of 6µm and 8µm, respectively. They are located on the cutting edge radius with angles of 45 °and 53 °respectively to the Y axis. In the case of smaller depth of cut, the first point on material that contacts the tool will be strongly attached to it due to high compressive stress, and can't flow; thus this point will become the stagnation point from which material splits in two directions, as the material in front accumulates and produces chips, the stagnation point will shift to its stable position. There exists a threshold where the first point that comes into contact with tool flows upward, simulation outcomes give this value for diamond and tungsten carbide tools around 55% and 65% of the cutting edge radius. Machining taking place at cutting depth less than minimum chip thickness are not accounted since no chips are produced.

4.3 Experiment on ultra-precision turning machine

Experiments to validate the simulation results, especially the minimum chip thickness, are carried out firstly on precision turning machine, as this is more approachable to configure the setup similar to that used in simulation. Besides, measurement will be easy to facilitate and can take place directly on parameters of interest with accurate results under the help of lab facilities. The verified results will be applied to help interpret the chip formation process in micro-milling.

4.3.1 Experimental procedures

4.3.1.1 Tools used in experiments

Experiments on precision turning machine to validate simulation outcomes are carried out on both diamond and tungsten carbide tools which are shown in Figure 3.5(a) and (d). Tool geometries are shown in Figure 4.13, the diamond tool has a nose radius of 1.836mm, and the tungsten carbide tool has a radius of 0.4mm. Considering the small cutting parameters used, it is reasonable to treat the tool edges as straight cutting edges. Both of the tools have zero rake angles.

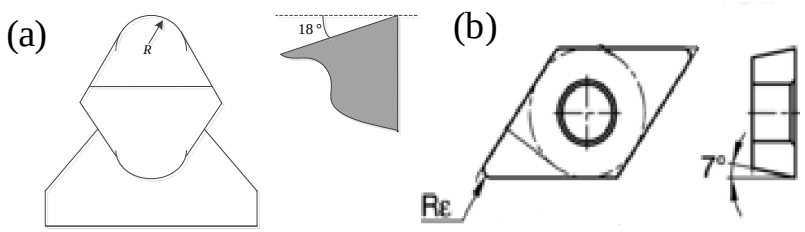

Figure 4.13 Tool geometry (a) diamond tool (b) tungsten carbide tool

Before cutting trials take place, cutting edge radius of both tools are measured, due to measurement capability of laboratory facilities, the cutting edge radius of the diamond tool cannot be measured , it is known between 100~300nm according to the tool manufacturer. Edge radius of the tungsten carbide tool is measured using the benchtop SEM in the lab (Figure 4.14) before each experiment. The tools from the same batch have very similar cutting edge radius.

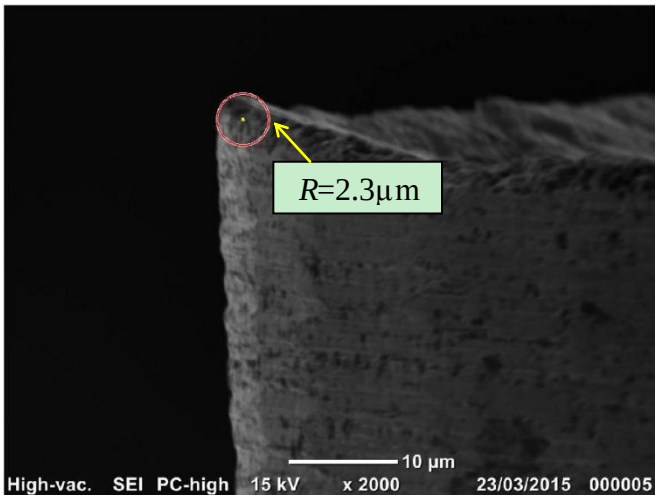

Figure 4.14 Cutting edge radius of a tungsten carbide tool

4.3.1.2 Experimental procedures

Cutting trials are conducted on a cylinder aluminium 6082-T6 workpiece with diameter of 70mm, it is pre-machined with a controlled radius diamond tool before real experiment. Firstly, the minimum chip thickness with different tools and its correlation with cutting edge radius are investigated and compared with the simulation results. Secondly, experiments with varied cutting speed are performed to determine its influence on minimum chip thickness; results are also compared with simulation outcomes. The adopted cutting parameters are shown in following table.

Table 4-5 Cutting parameters used in cutting trial

Tool	Diamond	Tungsten Carbide
Material	Aluminum 6082-T6	
Cutting speed	0~660m/min	
Depth of cut (µm)	0.03, 0.05, 0.08, 0.1, 0.13, 0.16, 0.26, 0.36	0.3, 0.4, 0.5, 0.6, 0.7, 0.8, 0.9, 1, 1.1, 1.3, 1.4, 1.7

To determine the minimum chip thickness of different tools, the tool approaches material and cuts at varied depth of cut as shown in above table. The machined grooves are measured under white light interferometer to determine commencement of chip formation. Then the cutting trials are conducted at different locations on the radius to study the effect of cutting speed, grooves are also examined by the interferometer. By identifying the minimum chip thickness of different tool at varied cutting speed, surfaces are machined at varied depth of cut from less than the minimum chip thickness to above the minimum chip thickness, and forces are recorded.

It is assumed that the workpiece is perfectly machined to get the datum surface, and the relatively large radius of the tool compared to the depth of cut adopted makes the tool edge a straight line; in addition, the tool wear during the slot cutting is negligible.

4.3.2 Experimental results and discussion

4.3.2.1 Determination of the minimum chip thickness

Machined slots at varied depth of cut are measured using the interferometer as shown in Figure 4.15. The profile of each slot with smooth bottom is extracted at 5 different locations and its depth is defined as the difference between the mean line of datum surface and valley point. The real depth is computed as the average of 5 measurements. The figure shows the measured surfaces at 50nm and 360nm of programmed cutting depth, while the measured depth of each slot is actually 30nm and 357nm. The actual depth will be used to determine the minimum chip thickness.

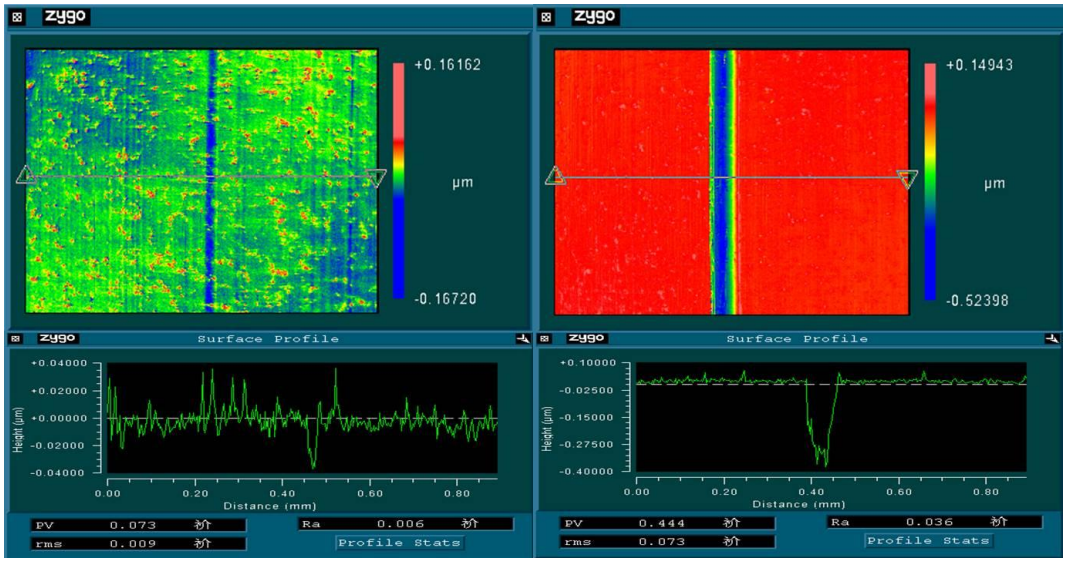

Figure 4.15 Measured surface at programmed cutting depth (a) 50nm (b) 360nm

The results from slot cutting are shown in Table 4-6 for diamond and tungsten carbide tools. By comparing the programmed depth of slot with the measured real depth, we can deduce the minimum chip thickness for each tool/material pair. As for the diamond tool, it shows that the programmed depth of cut at 30nm can't produce any mark, while the programmed depth of cut at 50nm only results in a slot of 30nm deep; only if cutting depth increases to 80nm, slots with same depth are generated. Considering the elastic and plastic behaviour of material, it can be concluded that material undergoes pure elastic deformation at 30nm cutting depth and partly plastic

deformation at 50nm cutting depth. So the minimum chip thickness for the pair of diamond/aluminium is around 70nm. While the actual cutting edge radius is around 100~300nm, so the estimated ratio between minimum chip thickness and cutting edge radius is around 18%~35%, which is in good agreement with the ratio of 25% from simulation results. The small difference between the programmed and measured depth at which chips are produced may be due to the voids and imperfections in the material.

Similar results are obtained for the tungsten-carbide/aluminium pair, the chips start to be removed at cutting depth of 0.4μm, elastic and plastic deformation take place when cutting depth is less than it and no chips are formed. Given the cutting edge radius of 2.3μm, the ratio of minimum chip thickness to cutting edge radius is around 17% which is very close to 15% predicted by simulation.

Table 4-6 Experiment results of diamond cutting slot on workpiece

Diamdon tool	Cutting edge radius	Programmed Depth (nm)	30	50	80	100	130	160	260	360
	100~300nm	Measured Depth (nm)	0	30	76	98	157	162	261	357
Tungsten Carbide tool	Cutting edge radius	Programmed Depth (μm)	0.2	0.3	0.4	0.7	0.9	1.1	1.3	1.7	2.5
	2.3μm	Measured Depth (μm)	0	0.2	0.41	0.67	0.9	1.08	1.32	1.72	2.53

4.3.2.2 Minimum chip thickness vs cutting speed

Simulation results recommended that the influence of cutting velocity on minimum chip thickness for same tool/material pair is negligible, to validate this, four new tungsten carbide tools are employed to perform the cutting trials at four different cutting speeds. Cutting speed is ranged from 180m/min, 360m/min, 540m/min to 740m/min. The depth of machined slots is measured using the interferometer.

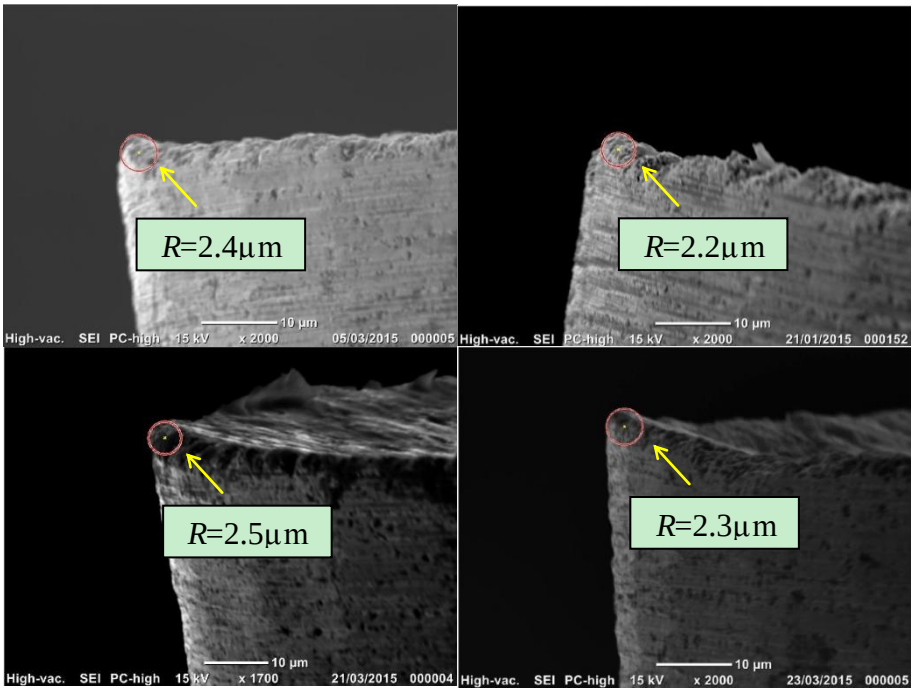

Figure 4.16 Tools used in experiment and cutting edge radius

Measurement results of the four tungsten carbide tools reveals that chip formation occurs at cutting depth around 0.3~0.4µm, which shows negligible influence of the cutting speed on minimum chip thickness. Figure 4.17 shows the measured slot at depth of cut of 0.4µm and 0.3µm under varied cutting speeds. The differences can be clearly seen between the topography of machined slots, the slots machined at depth of cut 0.4µm distinctly shows material removal, while the slots machined at depth of cut of 0.3µm only displays tool marks and scratches. The minimum chip thickness at varied cutting speeds is almost the same, thus it can be concluded that the influence of cutting speed on minimum chip thickness is negligible, which is in alignment with simulation outcomes.

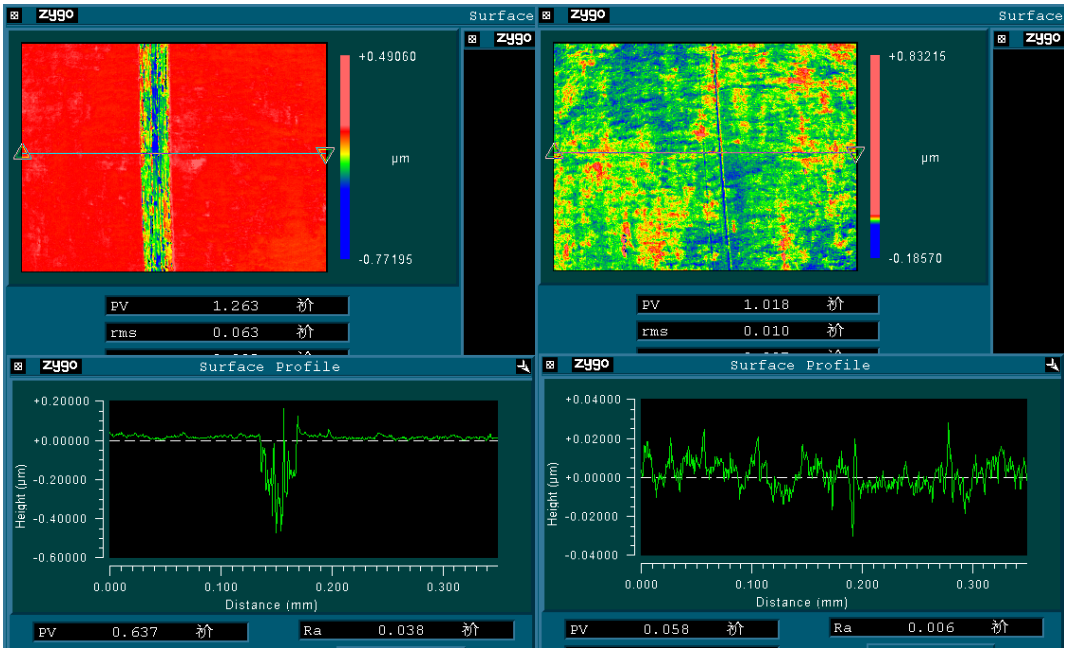

(a) Cutting speed at 180m/min at depth of cut: left: 0.4µm, right: 0.3µm

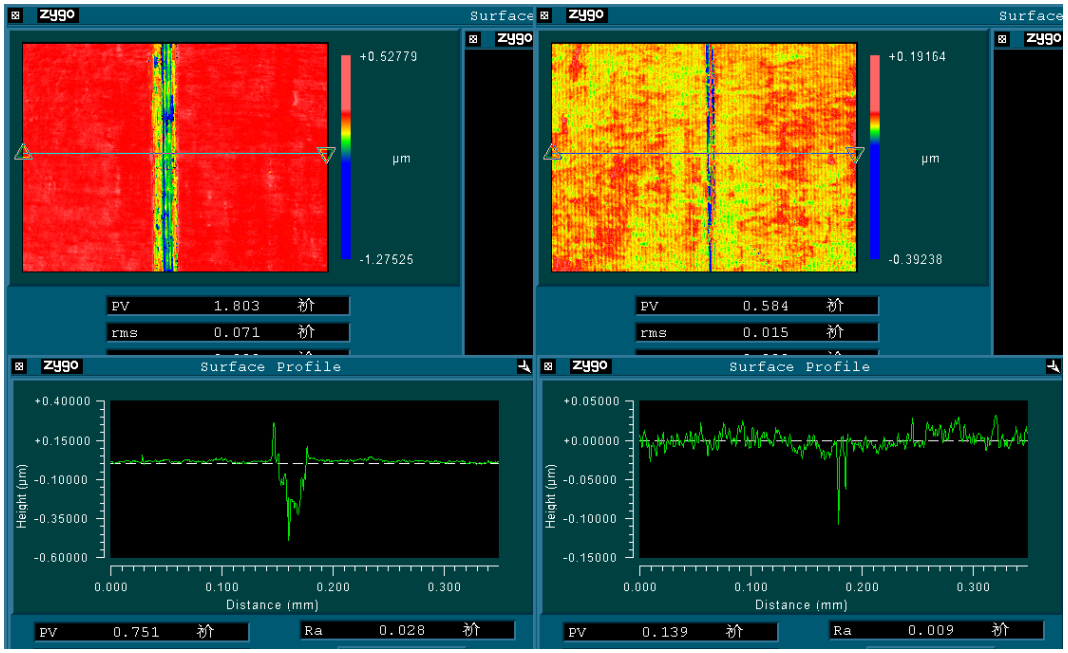

(b) Cutting speed at 360m/min at depth of cut: left: 0.4µm, right: 0.3µm

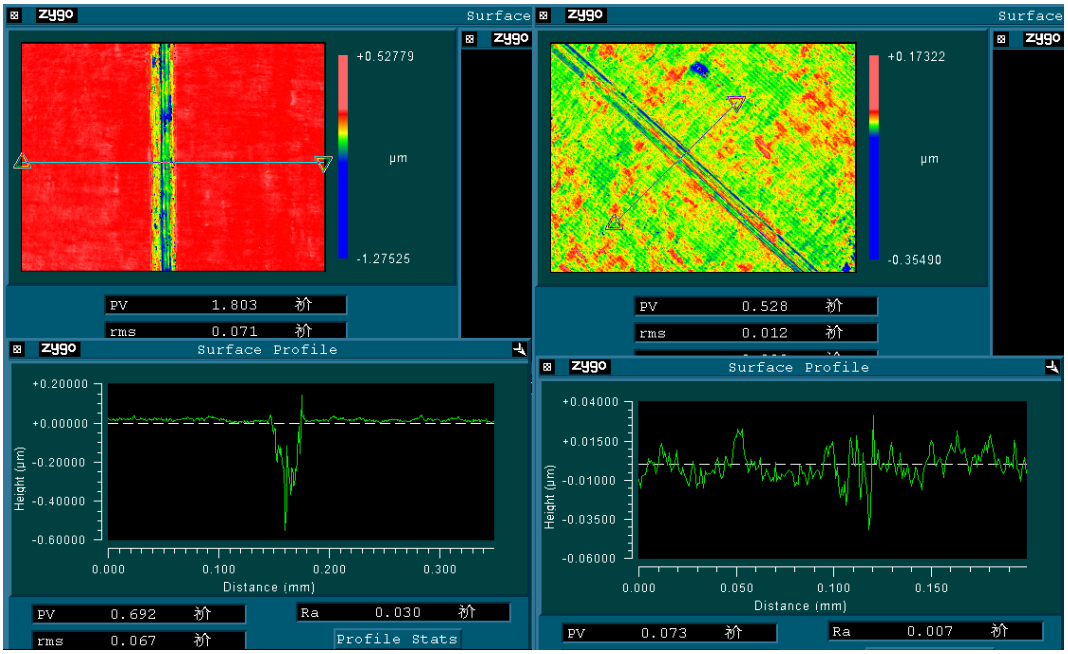

(c) Cutting speed at 540m/min at depth of cut: left: 0.4µm, right: 0.3µm

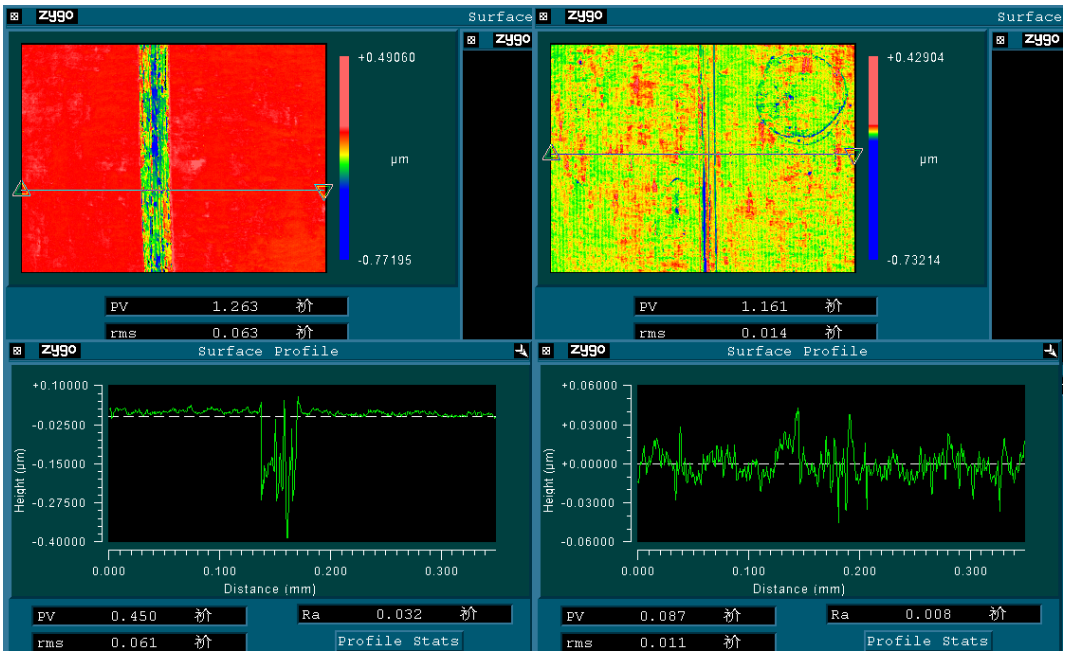

(d) Cutting speed at 740m/min at depth of cut: left: 0.4µm, right: 0.3µm

Figure 4.17 Machined slots at varied cutting speed

4.4 Chip formation in micro-milling

4.4.1 Experimental procedures

4.4.1.1 Tools used in experiments

The main difference between macro cutting and micro cutting lies in the distinct cutting edge radius compared to the adopted cutting parameters. To simulate this in micro-milling, two specially made tools are utilized, one is single flute tool made of natural diamond; the other is single flute tool made of tungsten carbide. Both of them have the same diameter of 0.4mm. The natural diamond milling tool has a very sharp cutting edge radius which is normally around 100 nm, whereas the tungsten carbide milling tool, due to the manufacturing process and material properties, cutting edge radius is often around 1~3µm. In micro-milling, cutting parameters are usually around micrometers, which is more than tens of times bigger than the cutting edge radius of diamond tool. Given this fact, it is reasonable to assume that the natural diamond has sharp cutting edge. The two tools are shown in Figure 4.18, the cutting edge radius of tungsten carbide tool is measured using the benchtop SEM with value shown in Figure 4.19.

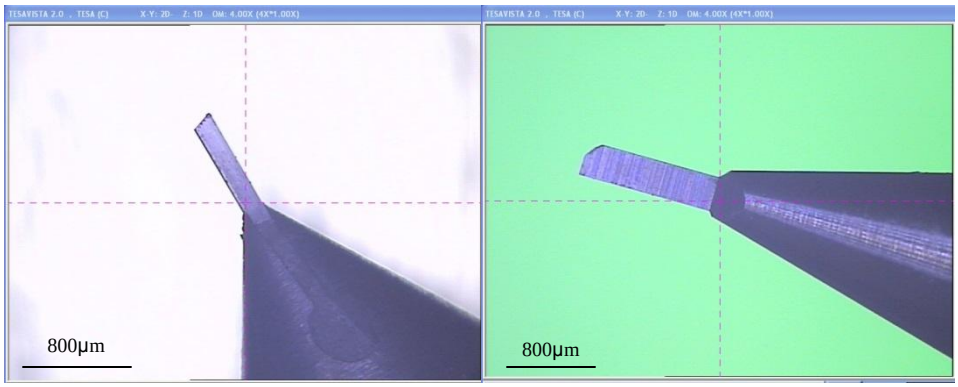

Figure 4.18 Single flute milling tool left: natural diamond; right: tungsten carbide

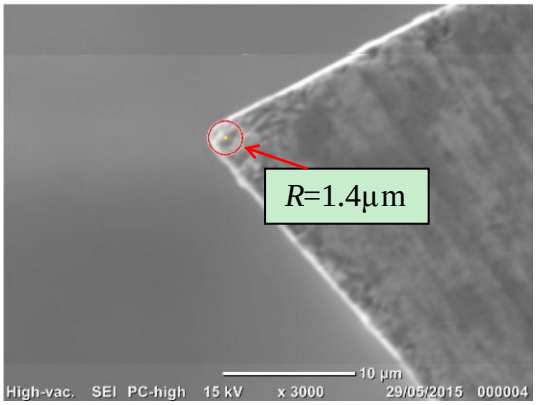

Figure 4.19 Cutting edge radius of the tungsten carbide tool

4.4.1.2 Experiment procedures

The experimental setup is shown in Figure 3.15, in order to inspect the chips formed under varied cutting parameters, series of cutting trials are carried out on both of the two tools. The chips are collected and observed under microscope and SEM; cutting forces are recorded using the data acquisition system shown in Figure 3.10. To synchronise the cutting process and force recording, the capacitive sensor is adopted. A mark is attached to the tool holder which is aligned with the single flute cutting edge. During machining, the mark is captured by the capacitive sensor which indicates the beginning of cutting process. Cutting forces are collected with a sampling rate of 51.2 KHz, which is high enough to accommodate most of the dynamic characteristic of the cutting process. The workpiece is attached to the dynamometer via bolts, as the non-rigid connection will change the dynamic response of the dynamometer, hammer test is performed to obtain the altered transfer function from workpiece to dynamometer, and collected cutting forces are compensated by applying an extended Kalman Filter. The principles and algorithm will be elaborated in the following chapter. Cutting parameters are listed in the following table, for each spindle speed, cutting trials are conducted at varied feedrate shown in table. The depth of cut is kept constant. Surface roughness and burrs are measured.

Table 4-7 Cutting parameters used in micro-milling

Tool / Process Variable	Single flute diamond tool	Single flute tungsten carbide tool
Cutting speed (m/min)	15/26.5/38	15/26.5/38
Depth of cut	20µm	20µm
Feed per tooth (µm)	0.2, 0.5, 1, 2, 3, 4, 5	0.5, 1, 2, 3, 4, 5

4.4.2 Experimental results and discussion

4.4.2.1 Chip morphology in micro milling

Chips in all experiments are collected and observed in SEM; the following figures show the produced chips at varied feedrate by diamond and tungsten carbide tools respectively. Owing to its very small cutting edge radius, the diamond tool can be treated as perfectly sharp, so the minimum chip thickness is ignored. The produced chips are shown in Figure 4.20, the front end and trailing edge can be both clearly identified in one chip segment, which means the chips are formed continuously in each revolution. The upper surface of chips exhibits ribbon-like topography which is the direct result of material shearing during chip formation; the diamond tool has very good surface finish on rake face and the frictional coefficient at the interface is also low. These properties make the chips less attachable to the tool, so the lower surface of the chip is very smooth. As the feedrate increases, the chip thickness and the stress at the interface increases as well, the lower surface becomes slightly rougher as shown in figure.

The overall length of chips at varied feedrate is measured around 250μm, and doesn't show much variation. While the theoretical chip length in full slot is around 630μm, we can know that the deformation make the chip shorter, consequently chip thickness increases. The maximum thickness along the chip is measured around 1, 5 and 9μm for the feedrate of 0.5, 2 and 4μm/tooth respectively. Thus the chip thickness ratio can be estimated to be around 2 for diamond tool.

Chips under varied cutting speed are also examined and results show no distinct variation in aspect of chip thickness, length and continuity. It can be concluded that cutting speed has very little influence on chip formation, this is in alignment with the material properties which is not sensitive to strain rate.

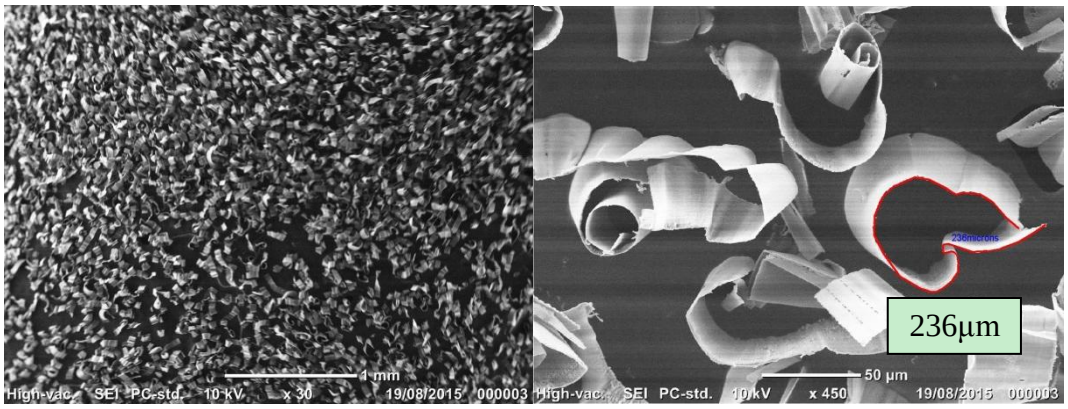

(a) Chips formed at feedrate 0.5µm/tooth. Left: 30×. Right: 450×

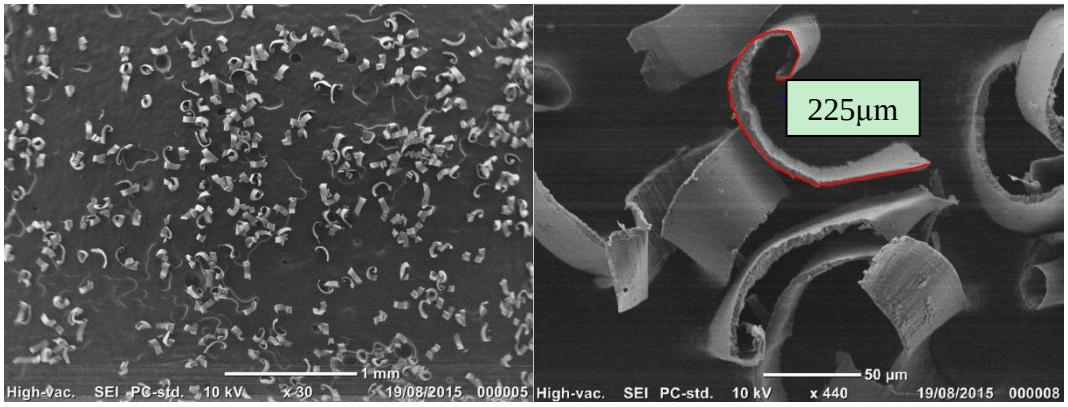

(b) Chips formed at feedrate 2µm/tooth. Left: 30×. Right: 440×

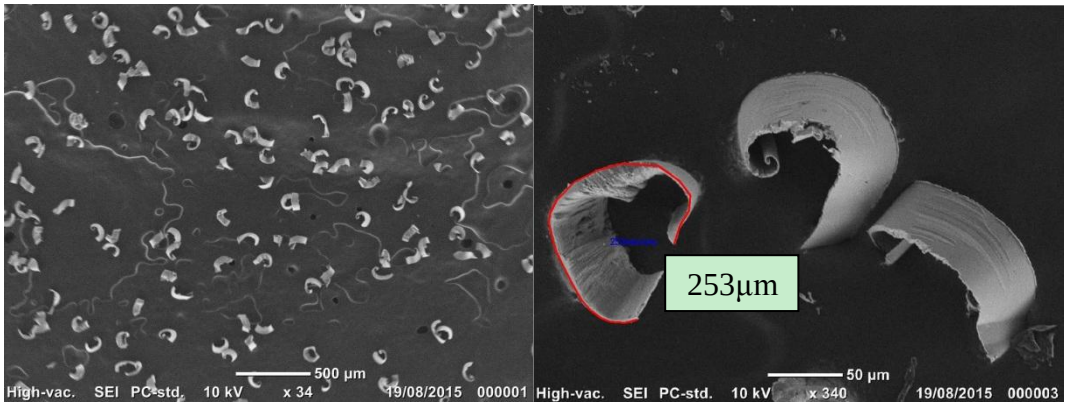

(c) Chips formed at feedrate 4µm/tooth. Left: 34×. Right: 340×

Figure 4.20 Chips formed by diamond tools (cutting speed: 26.5m/min)

For tungsten carbide tool, it has an edge radius around 1.4µm (Figure 4.19) which can't be ignored compared to the adopted cutting parameter. If the feedrate per tooth is less than the minimum chip thickness, chips will not be formed every revolution. Based on the ratio found in previous session, the minimum chip thickness is around 15% of the cutting edge radius, which is around 0.2µm in this case.

The feedrate is varied among 0.2, 0.5, 2 and 4 µm/tooth in the experiments. Chips formed in experiments are shown in Figure 4.21, it can be seen that as the feedrate increases, the chip becomes longer even though most of the chips are fragmented

which might be broken during collection. The chip length is indicated in the figure, it can be seen that chip length at 0.2μm/tooth feedrate is even longer than that at 0.5μm/tooth. However, considering the theoretical chip length is around 630μm, the real chip length is obviously much bigger. It should also be noted that chip thickness is very even along the chip in the figure; the measured thickness is around 3μm, 4μm, 11μm and 18μm respectively. The ratios between measure thickness and programmed feedrate/tooth are 15, 8, 5.5 and 4.5 respectively, which are quite larger than that for chips formed by diamond. This indicates the volume each chip represents far exceeds the volume that the tool can remove in single revolution. Based on the measured length and thickness, we can conclude that the long chips are consisted of many chips from consecutive revolutions. Due to the large cutting edge radius and strong interaction between the tool and material, the chip formed in preceding revolution may remain attached to the tool, and the chip from current revolution, the two chips will be joined together at the round tool tip under huge compressive and shearing stress. The larger the feedrate is, the more likely this phenomenon to happen. The material attachment in Figure 4.22 has proven this deduction.

The reason for longer chips at feedrate of 0.2μm/tooth than that at 0.5μm/tooth is related to the cutting edge radius, as chips may not form during one revolution until the accumulated chip thickness is big enough. The real chip thickness when chips are formed may be much bigger, thus results in longer chips.

Another point to notice is that the ribbon-like topography of upper surface is much more obvious, apart from the bigger friction at the interface, the large cutting edge radius, which subjects material to even severe shearing and deformation, can be another contributing factor. As in this case, the chips are assumed to be formed with a tool with large negative rake angle. The lower surface is comparatively smooth, as the chips move along tool rake face.

Experiments are also carried out at varied cutting speeds (Figure 4.23); results show no significant change in terms of average chip thickness, continuity, which is the same result as chips produced by diamond tool.

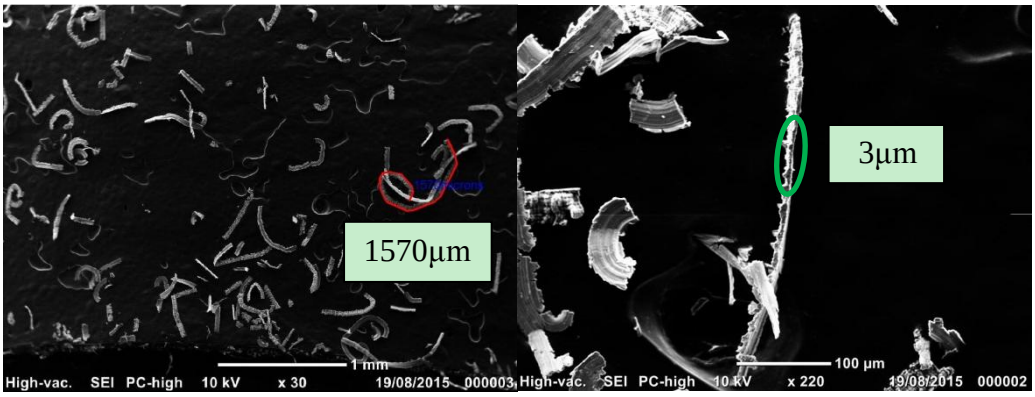

(a) Chips formed at feedrate 0.2µm/tooth. Left: 30×. Right: 220×

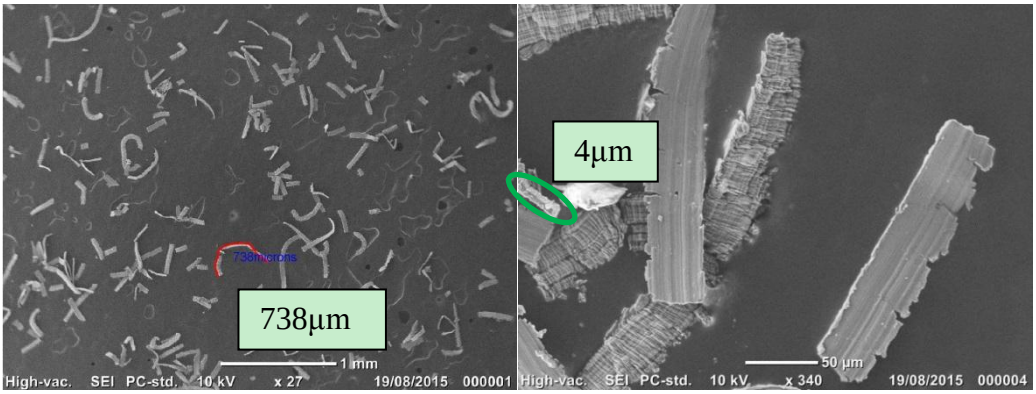

(b) Chips formed at feedrate 0.5µm/tooth. Left: 27×. Right: 340×

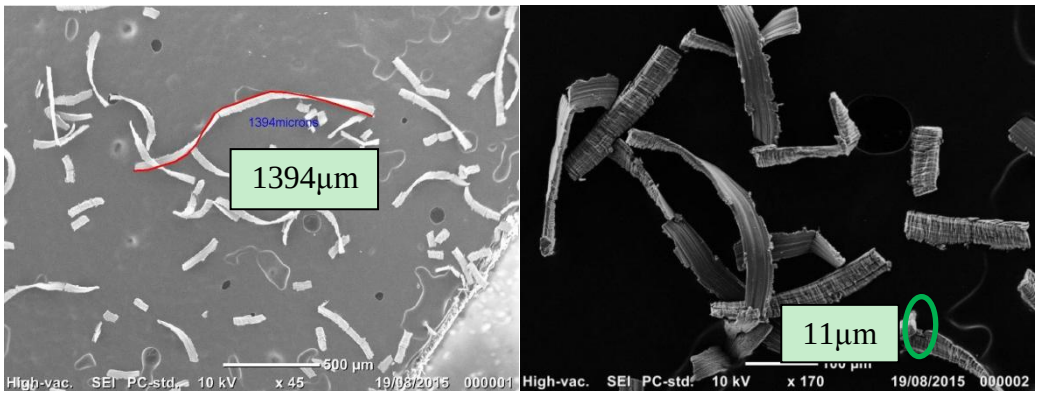

(c) Chips formed at feedrate 2µm/tooth. Left: 45×. Right: 170×

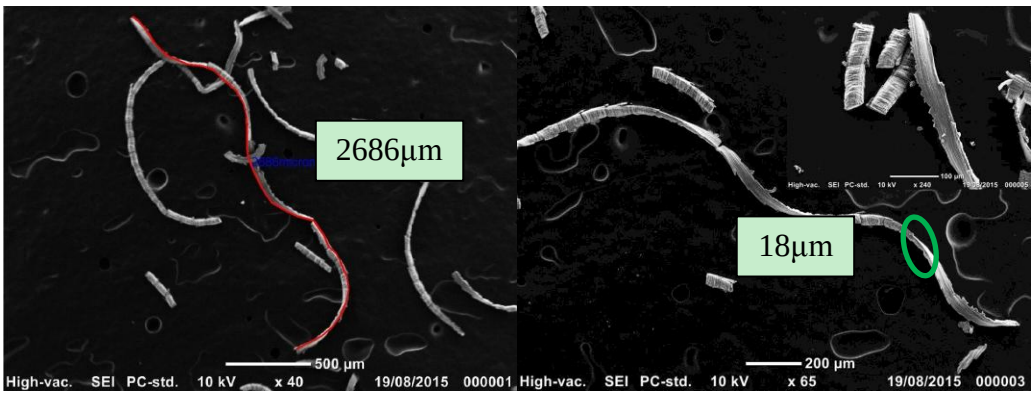

(d) Chips formed at feedrate 4µm/tooth. Left: 40×. Right: 65×

Figure 4.21 Chips formed by tungsten carbide tools (cutting speed: 26.5m/min)

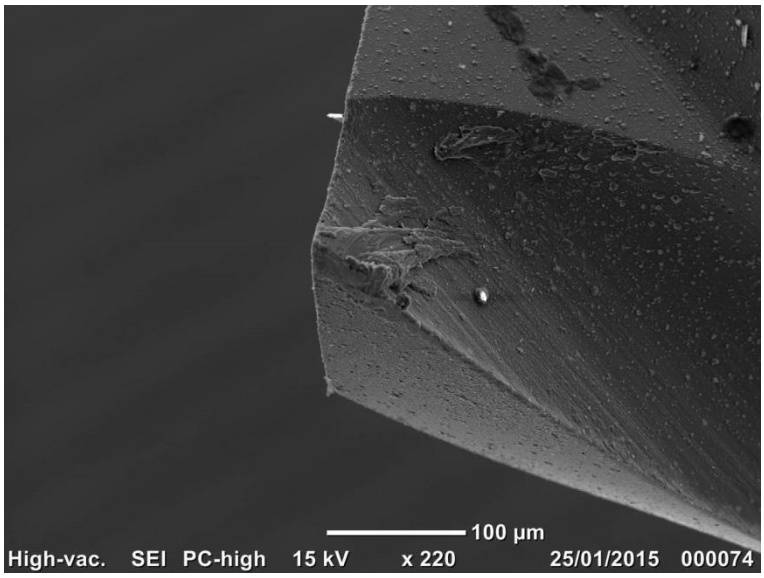

Figure 4.22 Material attachment on tungsten carbide tool

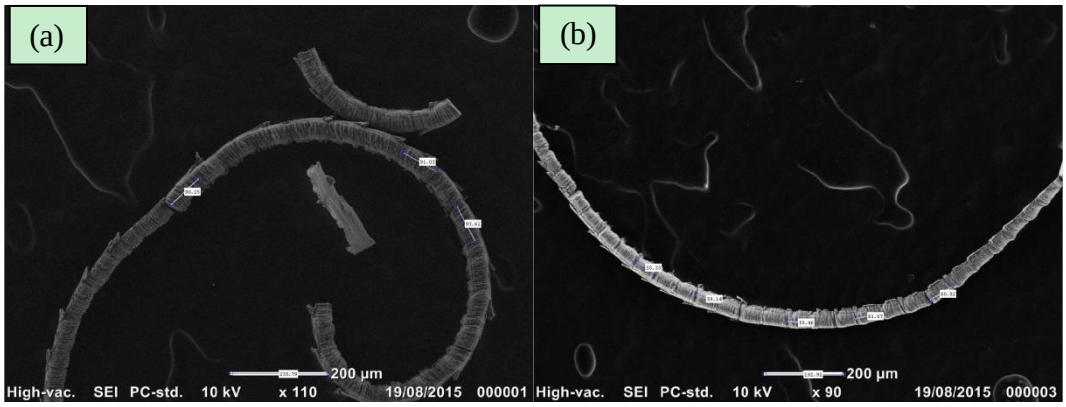

Figure 4.23 Chips formed at varied cutting speed (a) 12,000rpm (b) 30,000rpm

By comparing the results from diamond and tungsten carbide tools, we can see that the cutting edge radius may change the chip formation by concatenating chips among consecutive revolutions, which results in longer chips. In addition, the chip thickness will be more even compared to that formed by sharp edge diamond tool. Material is subject to more severe shearing and deformation under the condition of large cutting edge radius.

4.4.2.2 Cutting forces in micro milling

Cutting forces are collected to help interpret the cutting process and its dynamics, especially the influence of cutting edge radius on force variation. Figure 4.24 shows the cutting forces in three directions at feedrate of 4µm/tooth and cutting speed of 26.5m/min. It typically shows how the cutting forces evolve in micro-milling process. The chip formation is a cyclic and periodic process in which tool enters and exits

material periodically, so the cutting forces are also periodic. The black vertical line indicates the beginning position when tool starts cutting. We can see that cutting forces in three directions all increase as the machine continues, at about 30 ° the force in x direction reaches the positive maximum and then decreases, as the chip thickness becomes bigger gradually when the tool rotates; at about 136 °, it reaches the negative maximum and then increase again, as the chip thickness decreases and the tool tip approaches the exit point of cutting process. The force in y direction reaches positive maximum at the rotational angle around 70 ° and then decreases, at about 180 °, it reaches the negative maximum point; the cutting force in z direction also increases firstly following the increases of chip thickness, at about 130 °, it reaches the maximum, and then reduces to the minimum. In ideal situations, the tool exits and disengages the material at rotational angle 180 °, the cutting force in each direction should become zero, however, as shown in the latter half revolution in figure, the cutting forces are not zero.

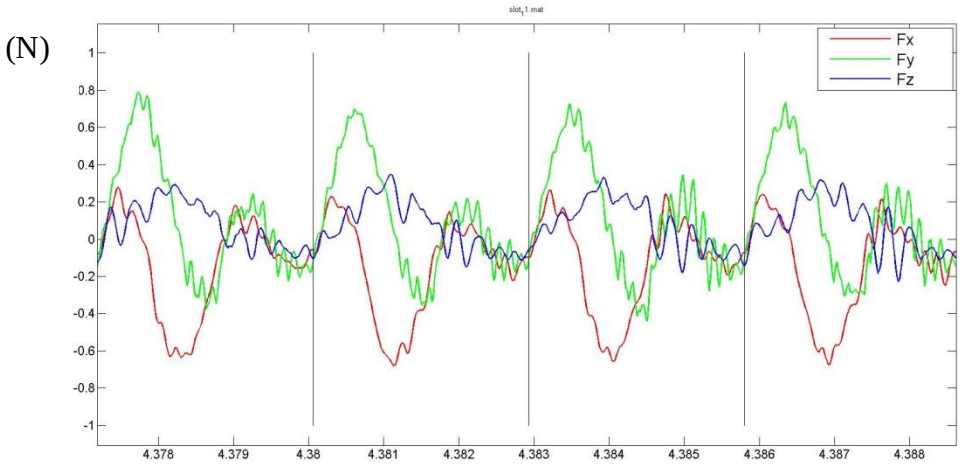

Figure 4.24 Cutting forces in machining by using tungsten carbide tools (feedrate 4μm/tooth)

Experiments are carried out with both tools at varied feedrate and cutting speed; Figure 4.25 shows the cutting forces in machining with tungsten carbide and diamond tools. Feedrates are varied among 0.5μm/tooth, 1μm/tooth, 2μm/tooth, 3μm/tooth, 4μm/tooth, which are above the minimum chip thickness 0.2μm to assure the chip formation. It can be seen that cutting forces in both columns increase as the feedrate increases; however, for diamond tool, the resultant cutting forces at the same cutting parameters are much smaller than that for tungsten carbide tool.

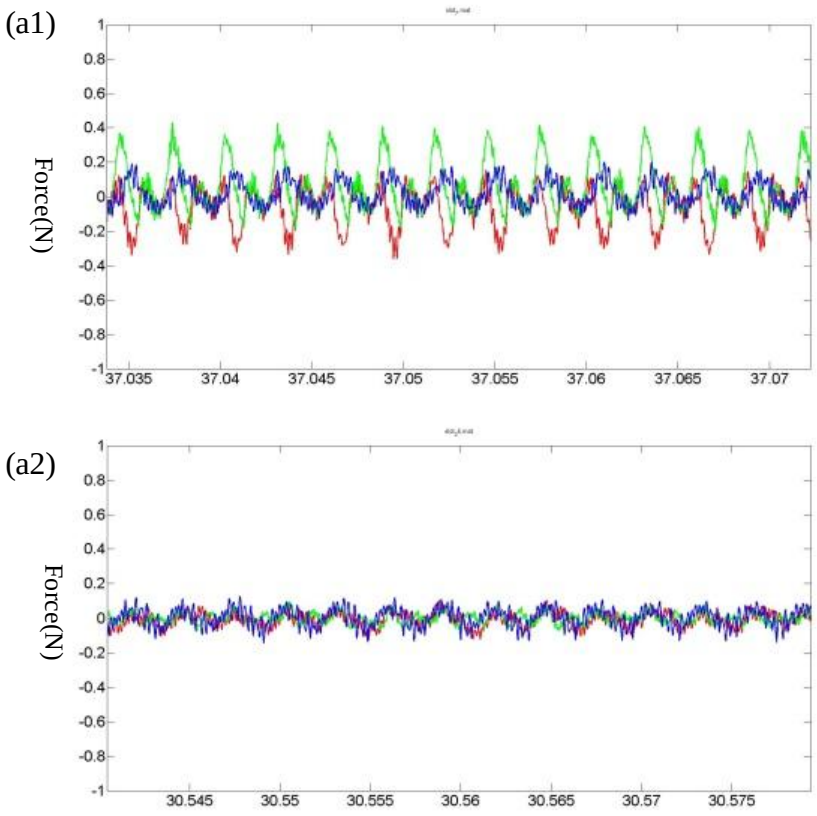

(a) Cutting forces at 0.5µm/tooth (a1): tungsten carbide (a2): diamond

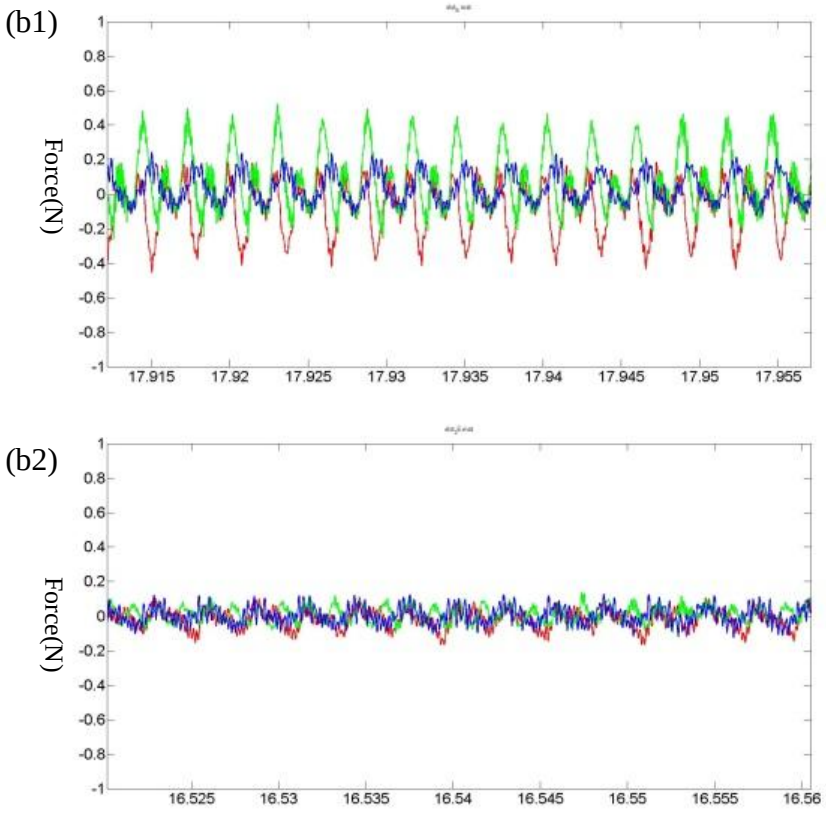

(b) Cutting forces at 1µm/tooth (b1): tungsten carbide (b2): diamond

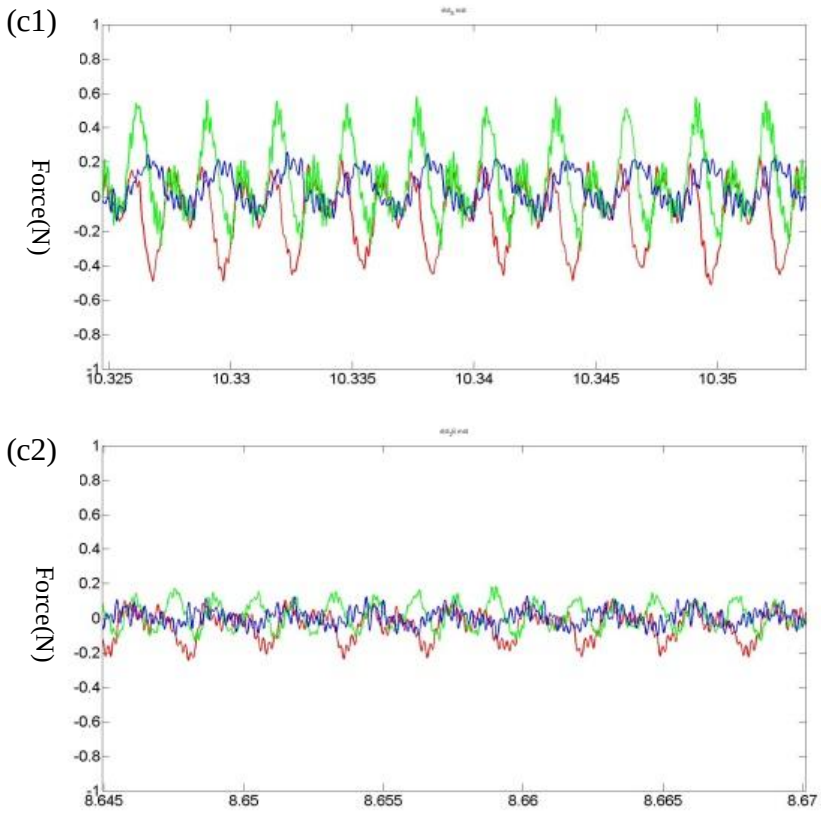

(c) Cutting forces at 2µm/tooth (c1): tungsten carbide (c2): diamond

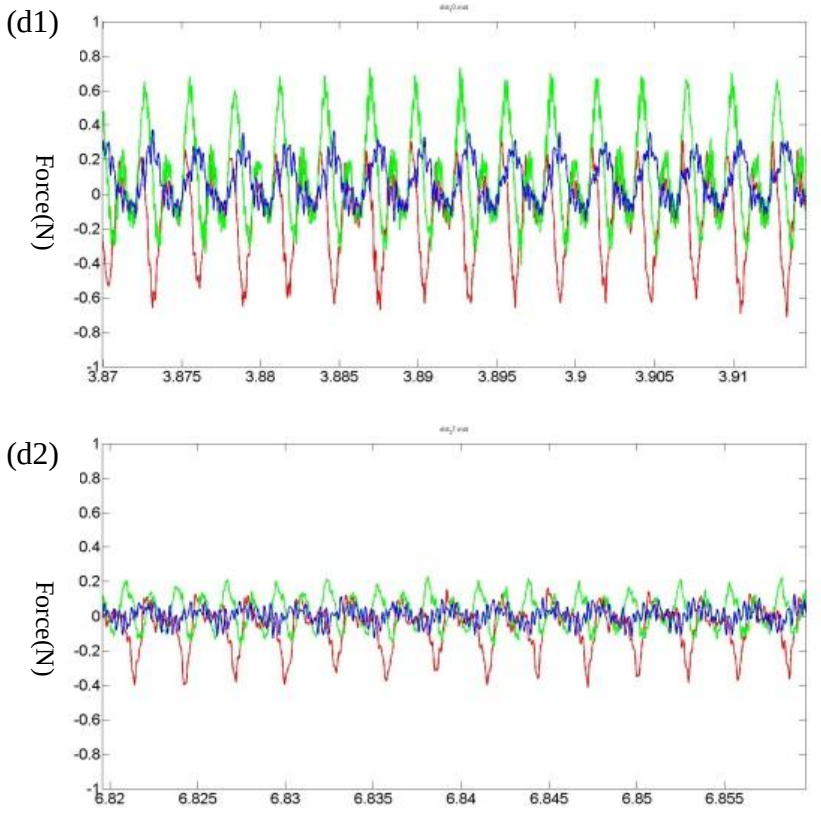

(d) Cutting forces at 3µm/tooth (d1): tungsten carbide (d2): diamond

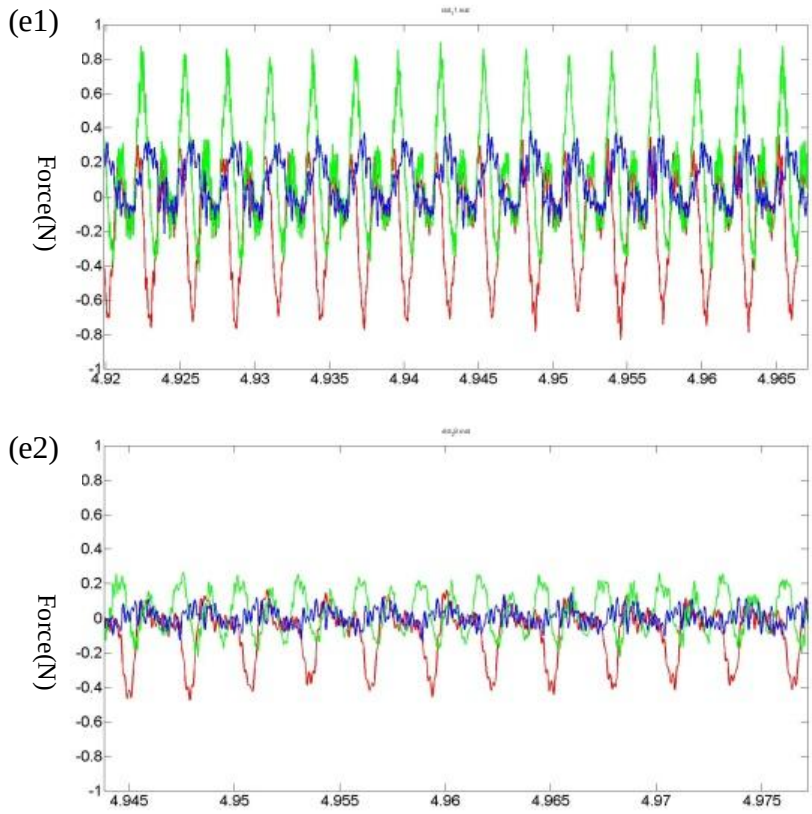

(e) Cutting forces at 4μm/tooth (e1): tungsten carbide (e2): diamond

Figure 4.25 Cutting forces at varied feedrate with two different tools (cutting speed 26.5m/min)

The peak-to-valley forces in x and y directions are plotted against the feedrate for the two tools as shown in Figure 4.26. The peak-to-valley force with tungsten carbide is usually 2~3 times higher than that with diamond tool. This might be the results of rough frictional properties and the large cutting edge radius of the tungsten carbide tools. To further analyse this, the cutting forces and thrust forces within each revolution are computed for both tool materials.

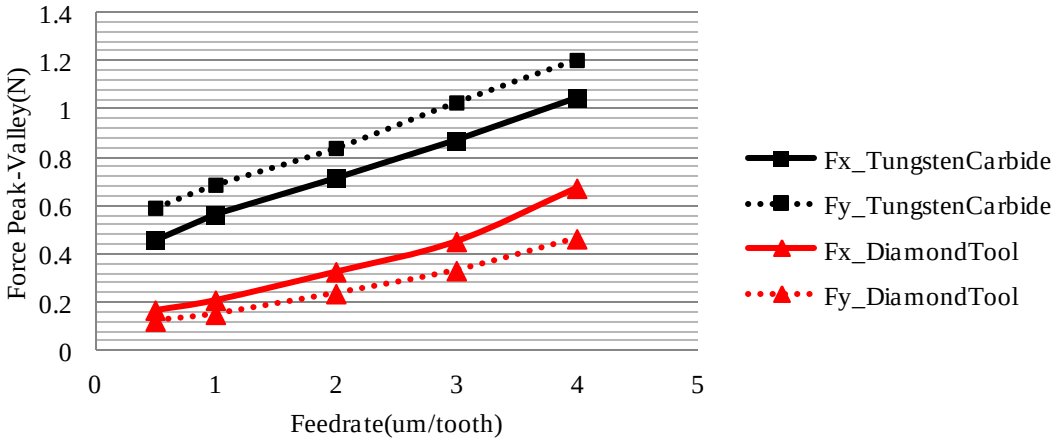

Figure 4.26 Peak-to-Valley force in x and y direction

The following images show the cutting and thrust forces in machining for tungsten carbide and diamond tools. It's clearly seen that both the cutting and thrust force are much bigger for tungsten carbide tools than that for diamond tools. However the force variations are quite different for two tools. For tungsten carbide tools, as commonly known, when chips are formed, the cutting forces must be bigger than thrust forces due to dominant shearing and cutting process. However, on the contrary, in (e1) tungsten carbide ;(e2) diamond

Figure 4.27, the left column shows that the magnitude of thrust force (red) is bigger than cutting force (green). Take (e1) tungsten carbide ;(e2) diamond

Figure 4.27(e1) as the example, It is found both the cutting and thrust forces increase as machining starts (vertical line), the thrust force quickly rises up and exceeds the cutting force, then continues to the maximum. Afterward it descends again below the cutting force and to the minimum as the tool exits material. The cutting force rises up simultaneously firstly with thrust force and then drops back to a local minimum; at about the same position where the thrust force descends, the cutting force increases again to the maximum, then it descends again to the minimum. Taking account of the chip formation process, the strong attachment between tool and material makes the produced chip adhere to the tool, which in result enlarges the actual cutting edge radius. The ploughing effect at the beginning of machining is more severe, so both cutting force and thrust force increase quickly. As the uncut chip thickness accumulates, the material starts to shear which results in the decline of cutting force, however as chips haven't been formed thrust force continues to rise. Once chips are formed and joined together with the chips formed in previous revolution, the thrust forces decline quickly and cutting forces rise to the maximum and then dec line due to the descending chip thickness.

(a1)

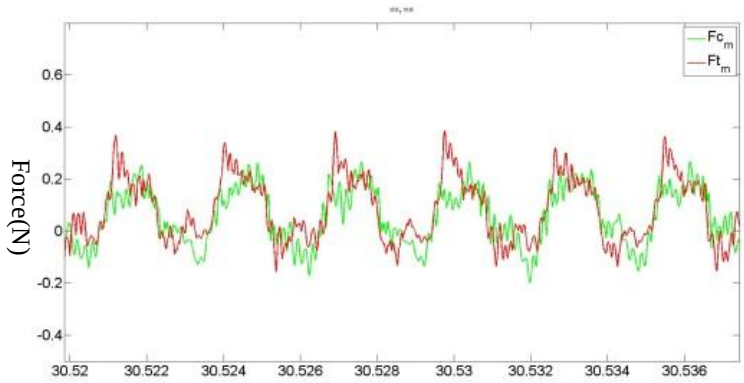

(a2)

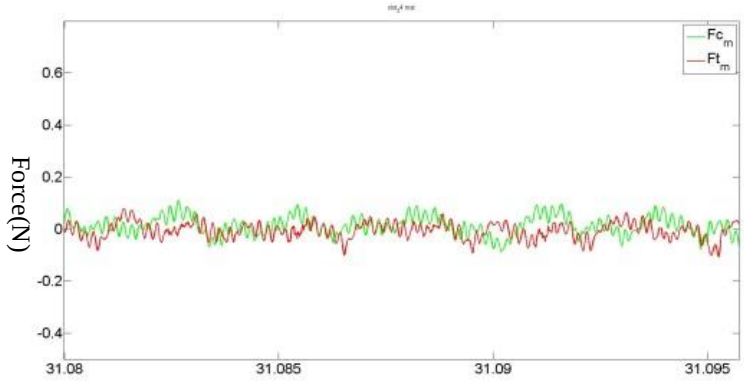

Cutting forces at 0.5µm/tooth (a1) tungsten carbide; (a2) diamond

(b1)

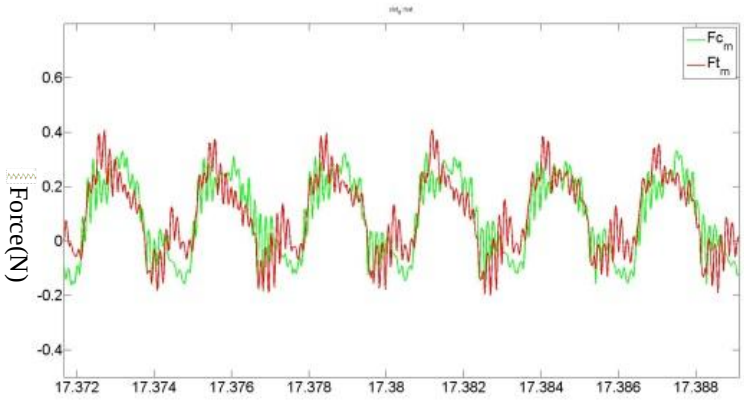

(b2)

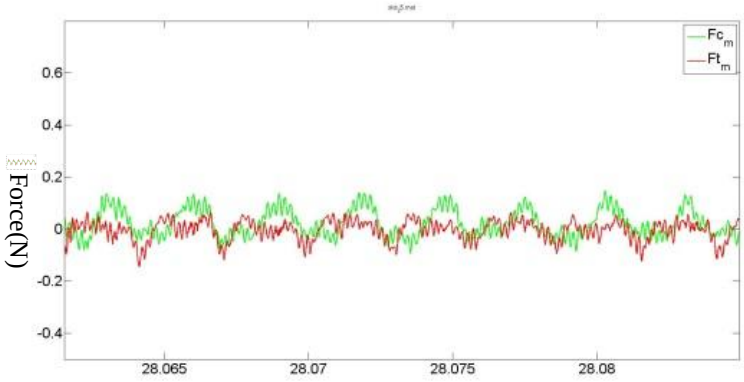

Cutting forces at 1µm/tooth (b1) tungsten carbide; (b2) diamond

(c1)

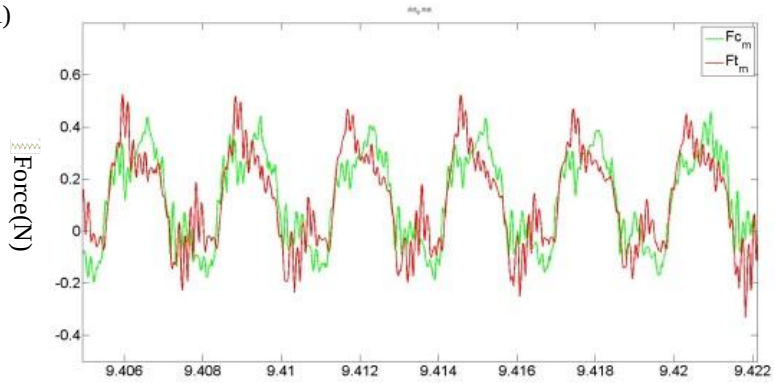

(c2)

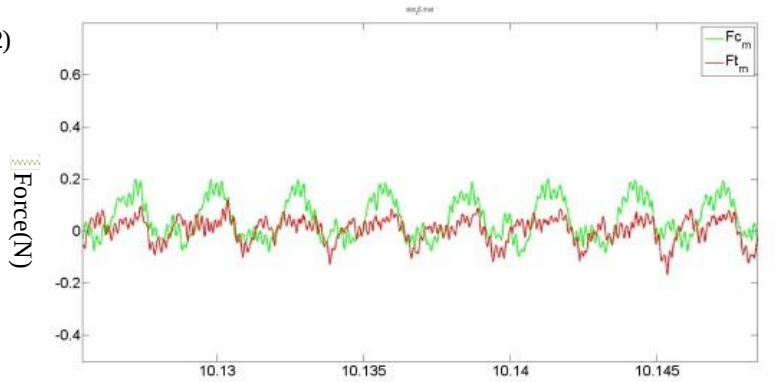

Cutting forces at 2µm/tooth (c1) tungsten carbide; (c2) diamond

(d1)

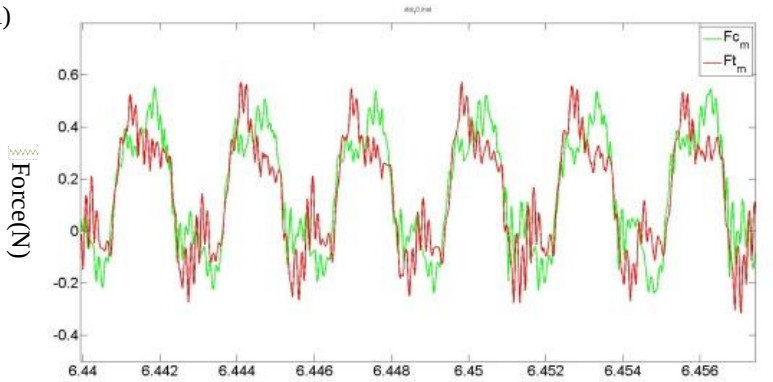

(d2)

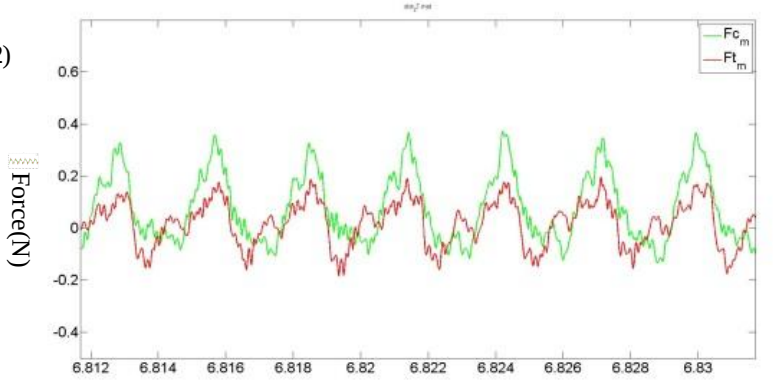

Cutting forces at 3µm/tooth (d1) tungsten carbide; (d2) diamond

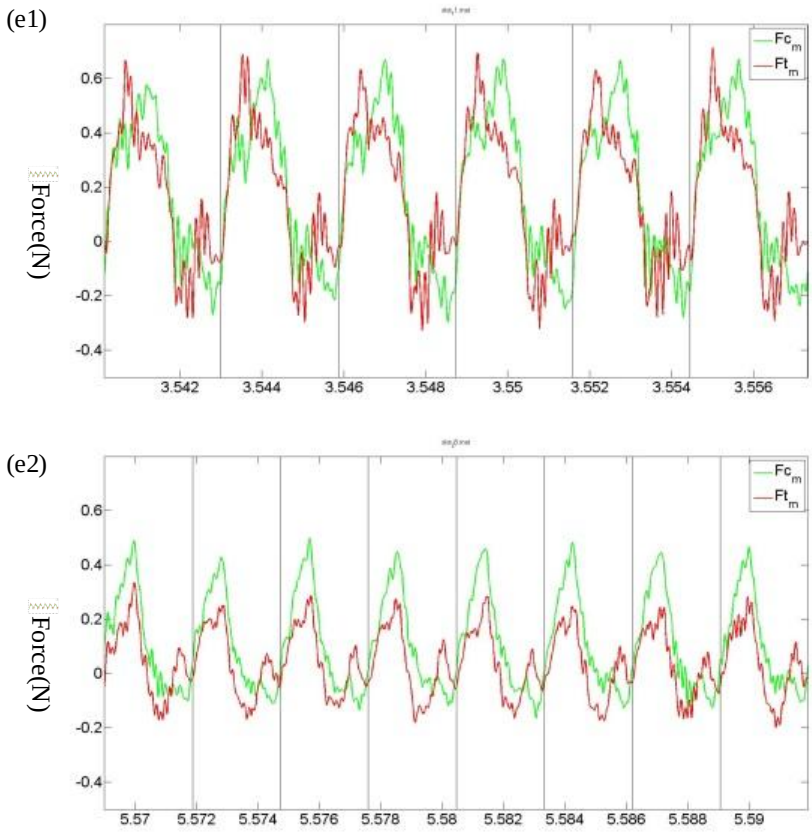

Cutting forces at 4μm/tooth (e1) tungsten carbide ;(e2) diamond

Figure 4.27 Cutting force and thrust force in machining with two different tools (R: thrust force; G: cutting force)

For diamond tool, the cutting and thrust forces are very small, as feedrate increases, the magnitude gradually increases. The difference between cutting force and thrust force becomes more obvious. As we know from Figure 4.20, intact chips are formed consecutively in every revolution, and the diamond tool is assumed to have sharp cutting edge compared to the cutting parameters. Related effect such as size effect and minimum chip thickness can't be observed in cutting forces. The forces in (e1)

tungsten carbide ;(e2) diamond

Figure 4.27(e2) reveal that cutting forces are always bigger than thrust forces during chip formation. Unlike tungsten carbide tool, the cutting and thrust forces reach the maximum at the same position in diamond machining, which is around 110 ° from the beginning point; besides we can also see that the noise in cutting force signals is much less which can be explained by the smooth interaction between diamond and material.

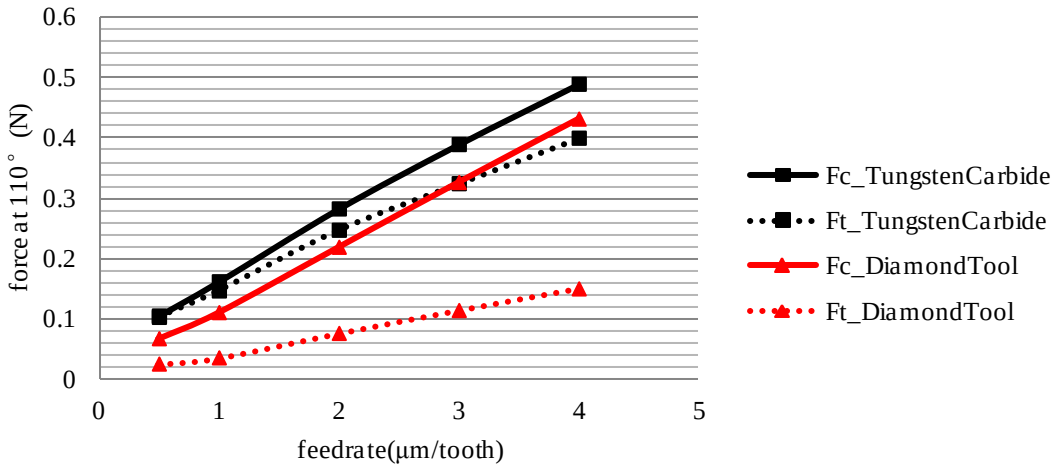

Figure 4.28 Cutting force and thrust force at 110° with two different tools versus feedrate

In order to analyse the influence of cutting edge radius on cutting forces, the thrust force and cutting force at about 110° are extracted and compared shown in Figure 4.28. The plot gives plenty of information into the influence of cutting edge radius on cutting forces. For tungsten carbide tool, the cutting force at feedrate of 0.5μm/tooth is almost the same with thrust force; whereas it is almost two times higher than thrust force for diamond tool. It can also be seen that both cutting and thrust forces increase almost linearly along with feedrate. The difference between cutting force and thrust enlarges accordingly, as the removed chip thickness increases; however, looking at the magnitude of cutting and thrust forces for two tools, It can be seen that the cutting force is about 3 times of thrust force for diamond tool; while the cutting force is only slightly higher than thrust force for tungsten carbide tool. Another fact to notice is that the difference between cutting force for two tools is almost the same and doesn't change too much along feedrate increase. Whether this is pure coincidence or result of tool/material interaction needs further study.

4.4.2.3 Minimum chip thickness in micro milling

From the previous simulation and experiment on turning machine, it is found that the minimum chip thickness is around 15% of cutting edge radius for tungsten carbide tools. Based on this finding and given the cutting edge radius of tungsten carbide tool (Figure 4.19) used in micro-milling, we can derive that the minimum chip thickness in micro-milling is around 15%×1.4μm≅0.21μm. To verify its validity, experiments are carried out at feedrate of 0.2μm/tooth. In fact, due to the tool's periodic rotation,

the chip thickness in each revolution changes from zero to the maximum and then reduces to zero again, the minimum chip thickness can be found in each revolution. Kim (2004) proposed a method based on the level of periodicity of cutting force at various feedrate to identify the minimum chip thickness; it found that there is a local maximum in radial thrust force in micro-milling process during the non-cutting regime. The resultant thrust force at feedrate of 0.2µm/tooth is shown in Figure 4.29. It can be seen that every two revolutions the thrust reaches a local maximum (black circle). By inspecting the force variation, we can conclude that this is due to the high ploughing effect during non-cutting regime; when chips are formed, the material shearing and fracture make the force more vibrant (green circle) and the peak value is smaller than maximum during ploughing.

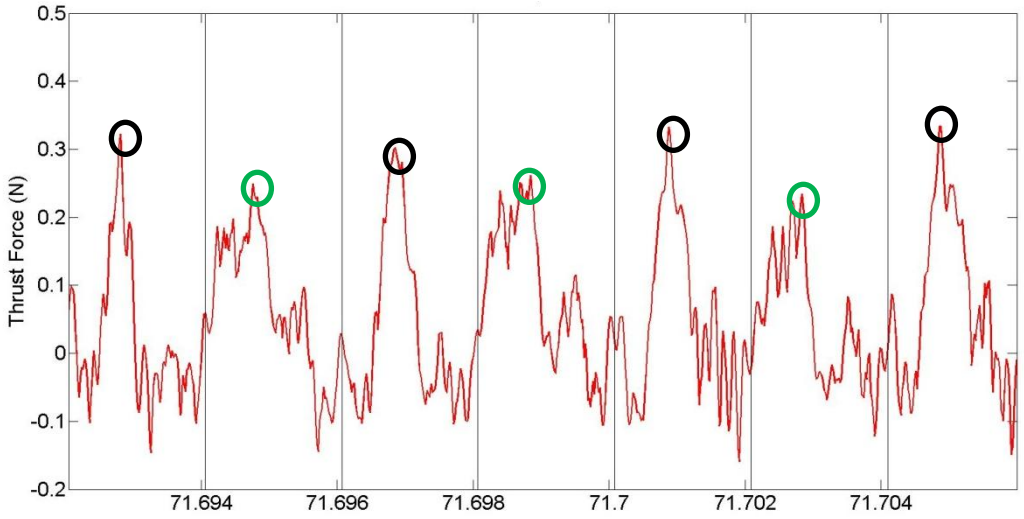

Figure 4.29 Thrust force at the feedrate of 0.2µm/tooth

The cutting and thrust forces at uncut chip thickness of 0.2µm among consecutive revolutions are extracted (Figure 4.30). It shows the cutting and thrust forces fluctuate at the approximate frequency of every two revolutions. Based on this, we can deduce that the minimum chip thickness is above 0.2µm.

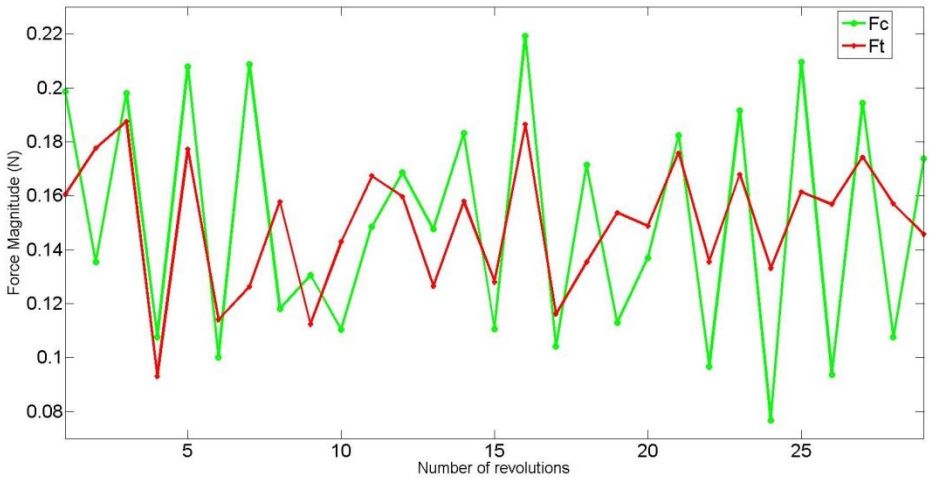

Figure 4.30 Cutting force and thrust forces among consecutive revolutions

The cutting and thrust force at position of 9 ° in revolution at feedrate of 2µm/tooth is computed, so the uncut chip thickness, by calculation with $2\sin(\theta)$, is approximately 0.3µm. The figure clearly reveals that the cutting force is much bigger than thrust force, which means the chips are formed in every revolution. The fluctuation of both cutting force and thrust force is acceptable taking account of other influencing factors such as tool vibration, material inhomogeneity and feed velocity variation.

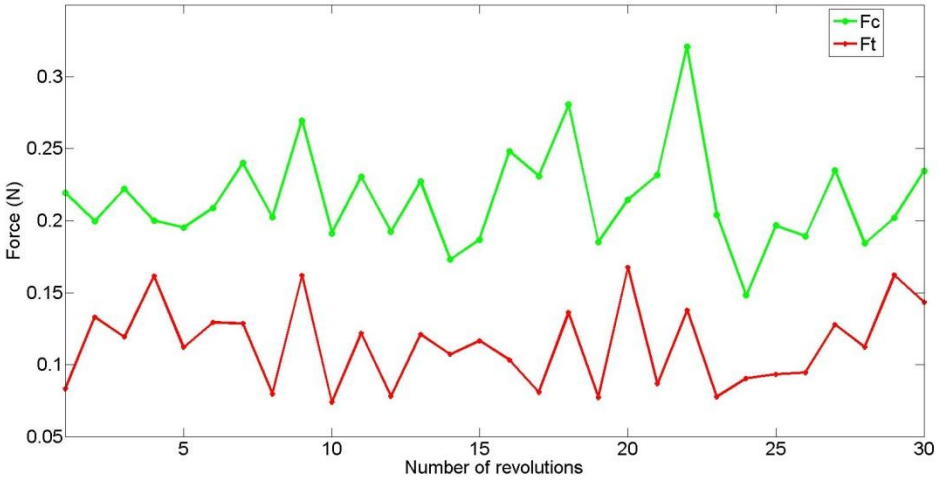

Figure 4.31 Extracted cutting and thrust forces at 0.3µm chip thickness.

Combining the previous findings, we can conclude that the minimum chip thickness for the tungsten carbide tool is approximately 0.2~0.3µm. Thus the ratio of minimum chip thickness to cutting edge radius (1.4µm) is around 14%~21%, which is in good alignment with the findings obtained from simulation and turning experiments.

4.5 Concluding remarks

This chapter presents the chip formation process in micro-cutting from various aspects: Both simulations and experiments are carried out to investigate the chip formation mechanism especially in the micro-milling process. Substantial research findings can be drawn up and further elaborated in the consequent sections below:

A FEM model is developed and finds that the main reason for the differences between macro-cutting and micro-cutting is the significant cutting edge radius compared to the cutting parameters. It also finds that the ratio of minimum chip thickness to cutting edge radius is 0.25 and 0.15 for diamond/aluminium and tungsten-carbide/aluminium, respectively. The position of stagnation point where material splits and forms the chip is determined.

Experiments on turning machine are conducted to validate the simulation results and find that experiment outcome is in good agreement with simulation. Experiment results also show that the value of minimum chip thickness doesn't change too much alongside the cutting speed, which is attributed to strain-rate-insensitive material properties.

The chip formation process is particularly investigated with tungsten carbide tool and diamond tool, where diamond tool is treated as sharp due to the extremely small cutting edge radius. For the first time, the difference between micro-cutting and conventional cutting is investigated experimentally. Outcomes show that for tungsten carbide tools, chips formed during consecutive revolutions will be joined together as a result of tool/material pair and cutting edge radius; whereas chips formed using diamond tool are intact and separate. Cutting forces are collected and the difference caused by cutting edge radius is firstly studied quantitatively. It shows that cutting force and thrust force are of the same order when cutting edge radius can't be ignored, while for diamond tool which has sharp edge, the cutting force is usually 2 times higher than thrust force. The minimum chip thickness found in micro-milling is also in good agreement with the simulation and experiment results.

5 Novel Approach to Model Micro-Milling Process and its Experimental Validation

5.1 Introduction

Cutting force can reflect most micro-milling phenomenon collectively such as size effect, chip formation and the influence of cutting temperature on material and cutting process. It's also an imperative process variable which indicates tool wear status. At the production level, the cutting force can help to optimize the machining conditions and tool geometry. Thus many researchers conducted extensive study on cutting force modeling and its application in interpreting cutting process (Arrazola et al. 2013).There are mainly four principal modeling technique based on different principles: analytical modeling, numerical modeling, empirical modeling and hybrid modeling which combines the strength of previous three approaches. However, the conventional model mainly focuses on prediction of the absolute value of cutting forces in machining; it is well known that the cutting forces in micro-milling process are usually less than 1N.

In this chapter, a new cutting force model in multiscale is proposed in response to the limitation that absolute value of cutting force is not appropriate in micro-cutting range. The cutting force modeling is developed in multiscale, e.g. cutting force on the unit length or area and cutting force on the unit volume in order to improve understanding of the micro-cutting mechanics in terms of size effect, tool wear mechanism and the cutting energy consumption. The mathematical modeling firstly starts with a novel instantaneous chip thickness algorithm, in which the real chip thickness is computed by taking account of the change of tool geometry brought about by the tool runout; then the collected cutting forces are utilized to calibrate the model coefficients. For accurate measurement on cutting forces, the Kalman Filter technique is employed to compensate the dynamic distortion of the measured cutting force. Model calibration is implemented using least-square method. The proposed cutting force model is then applied in micro-milling to represent the tool wear and

the cutting energy consumption. Further study on the surface generation simulation based on force model and its comparison with the machined surface are also performed.

5.2 Analytical chip thickness model

5.2.1 Conventional chip thickness model

In conventional milling process, the chip thickness is approximated by a sinusoidal function of feedrate per tooth as represented in Equation 5-1:

$$h_c(\theta) = f_t \sin\theta \tag{5-1}$$

where $h_c(\theta)$ is the uncut chip thickness in revolution, f_t is the feedrate per tooth and θ is the tool tip's position angle from the beginning of cutting. It has good approximation in conventional milling process when feedrate is comparatively large.

However, in micro-milling, the relationship presented in equation 5-1 doesn't apply any more, as it fails to take account of the translation movement of the tool centre. The tool diameter falls less than Φ1mm down to Φ100μm and feedrate usually ranges from 0.1μm to 10μm. The existence of cutting edge radius can't be ignored which makes the chip thickness in revolution even more complex. What's more, the tool run-out which is usually around 1μm to 5μm, this is very tiny in conventional milling, whereas the ratio of it to tool diameter becomes more significant in micro-milling, which must be accounted to calculate precise chip thickness in each revolution. Bao and Tansel (2000) proposed an analytical cutting force model which firstly includes the tool run-out effect. Zaman *et al* (2006) proposed a model which determines the theoretical chip area at any specific angular position of the tool cutting edge by considering the geometry of the path of the cutting edge. Li (2007) proposed a new algorithm to calculate the chip thickness considering the trochoidal trajectory of tool tip with run-out and the minimum chip thickness effect.

The above mentioned research all considered the tool run-out in the machine coordinate system and ignored the change on cutting tool geometry caused by tool run-out. This chapter proposes a new algorithm to accurately determine the chip thickness in the workpiece coordinate system based on the real trajectory of tool tip and the actual chip thickness is determined by comparing the theoretical chip thickness with minimum chip thickness at every position of rotational angle, thus

results in periodicity at certain positions of angle in chip formation.

Tool run-out may arise from many aspects including tool dynamics, manufacturing error, alignment error. Figure 5.1 illustrates a micro-milling tool with the run-out of r at angle α. Previous chip thickness model which includes the tool runout usually considers the tool centre rotates about the spindle centre O, which is expressed as:

$$\begin{cases} x = r\sin(wt+\alpha) + ft/60 \\ y = r\cos(wt+\alpha) \end{cases} \tag{5-2}$$

The trajectory of kth tool tip can be written as

$$\begin{cases} x(t,k) = r\sin(wt+\alpha) + ft/60 + r\sin(wt-2\pi k/N) \\ y(t,k) = r\cos(wt+\alpha) + r\cos(wt-2\pi k/N) \end{cases} \tag{5-3}$$

where w is the angular speed, N is the number of tool teeth and f is the feedrate.

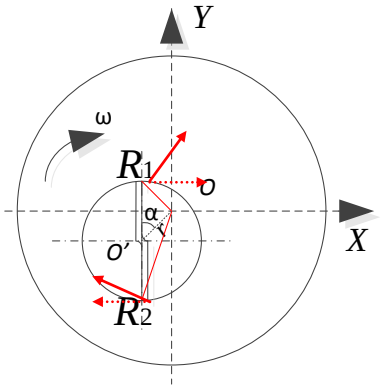

Figure 5.1 Tool run-out in micro-milling

5.2.2 Theoretical chip thickness model

Previous research considers the tool run-out in modeling the micro milling process, However, if we consider the tool rotation in workpiece coordinate system, each point on the cutting tool is rotating about the spindle centre O, the rotational radius of each tool tip has changed (represented by red line in figure). Given the nominal radius and tool run-out and its location angle, we have the following expression based on laws of cosines:

$$R_k = \sqrt{R^2 + r^2 - 2Rr\cos(2\pi/N\,(k-1) - \alpha)} \tag{5-4}$$

Where k is the tooth number and R is the nominal radius of each tool tip.

It also should be noted that the tool run-out also significantly changes the cutting edge's rake angle, as shown in figure, the actual velocity direction is indicated by solid red arrow in comparison with the nominal direction indicated by dashed arrow.

It can be seen that the nominal rake angle of the tool, if defined, is zero, whereas the actual rake angle becomes positive for tooth 1, but negative for tooth 2. The change of rake angle can be formulated by:

$$\gamma_c = (-1)^{k+1} \cos^{-1}\left(\frac{R^2 + R_k^2 - r^2}{2RR_k}\right) \tag{5-5}$$

The change of cutting geometry will significantly change the interaction between tool and material, and further influence the cutting process and tool performance, thus it's very important to take it into amount when modeling the micro-milling process.

Knowing the cutting tool's actual radius, the trajectory of each tool tip versus time can be expressed as:

$$\begin{cases} x(t,k) = \frac{ft}{60} + R_k \cos(wt - (k-1)\alpha) \\ y(t,k) = R_k \sin(wt - (k-1)\alpha) \end{cases} \tag{5-6}$$

The actual rotation centre O moves along the x axis at the speed of feedrate.

The following figure shows the real tool tip trajectory of a two-fluted tool in micro-milling process, it can be clearly seen that the trajectory is more trochoidal rather than circular. The biggest chip thickness locates slightly behind 90 °.

As shown in the figure, suppose the kth tool tip is located at point P_c (x, y) at time t, the tool rotation centre is located at position O_c, Thus the line P_cO_c has the following expression in the coordinate system:

$$y = R_k \tan^{-1}(wt - (k-1)\alpha)\,(x - ft/60) \tag{5-7}$$

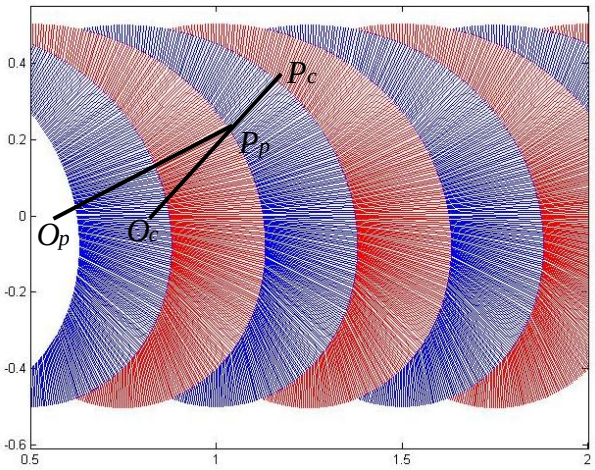

Figure 5.2 Real tool tip trajectory in micro-milling

The line P_cO_c which represents the cutting edge intersects with the trajectory of previous $(k-1)^{\text{th}}$ cutting edge at point $P_p\left(x_p, y_p\right)$. Suppose the $(k-1)$th tool tip

reaches point P_p (x_p, y_p) at time t_p, and the tool rotation centre is at point O_p. Similarly the line P_pO_p has the following expression:

$$y_p = R_{k-1}\tan^{-1}\left(wt_p - (k-1-1)\alpha\right)\left(x_p - ft_p/60\right) \tag{5-8}$$

Since it's known that point P_p (x_p, y_p) is also a point of line P_cO_c, by substituting equation 5-8 into equation 5-7, we can obtain the following equation to calculate time t_p.

$$R_{k-1}\tan^{-1}\left(wt_p - (k-1-1)\alpha\right)\left(x_p - \frac{ft_p}{60}\right) - R_k\tan^{-1}(wt - (k-1)\alpha)\left(x_p - \frac{ft_p}{60}\right) = 0 \tag{5-9}$$

Once t_p is known, the coordinates of point P_p can be obtained by applying equation 5-6. Thus the chip thickness is the distance between P_cP_p, which has following expression.

$$h(t,k) = \sqrt{\left(y - y_p\right)^2 + \left(x - x_p\right)^2} \tag{5-10}$$

or

$$h(t,k) = R_k - P_pO_c = R_k - R_{k-1}\cos\theta_p/\cos\theta \tag{5-11}$$

where θ is the position angle of kth tooth at time t, and θ_p is the position angle of $(k-1)$th tooth at time t_p.

Thus, it is essential to firstly determine the value of t_p, however, it is not easy to solve equation 5-9 analytically as it is very complex nonlinear polynomial equation. The iterative method named Newton-Raphson is utilized to approach t_p which satisfies equation 5-9. For this method, an initial value of t_p needs to be selected, and this value is updated each iteration and the algorithm searches in the direction which makes equation 5-9 reduce further to zero. Considering the time delay between each tooth passing the same position angle, the initial value is selected as:

$$t_p^0 = t - 2\pi/(wN) \tag{5-12}$$

Suppose the left of equation 5-9 names the function $F(t_p)$, the value will be updated according to the following formula:

$$t_p^{i+1} = t_p^i - \frac{F(t_p^i)}{F\prime(t_p^i)} \tag{5-13}$$

where i is the number of loops the algorithm proceeds. A threshold close to zero is defined, the algorithm stops when the absolute value of $F(t_p^i)$ become less than the

threshold, and it will finally converge to a solution which best fits equation 5-9. The procedures are shown in Figure 5.3.

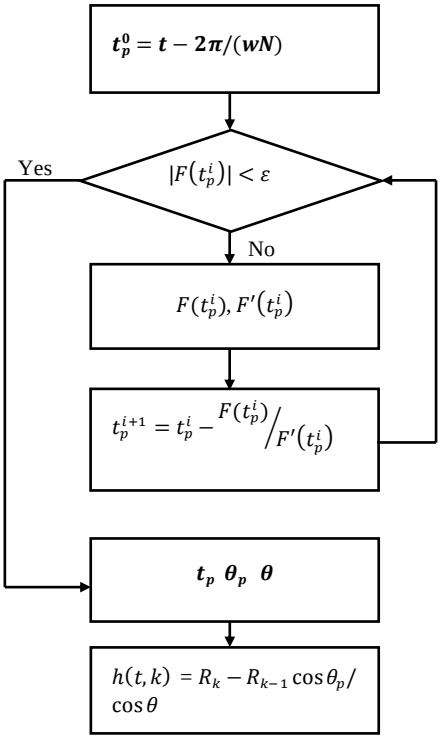

Figure 5.3 Procedures to calculate the chip thickness

5.2.3 Actual chip thickness model

In previous chapter, we discovered that for tungsten carbide tools, the minimum chip thickness is around 15% of the cutting edge radius; in micro-milling its existence can result in non-cutting movement if chip thickness is less than the minimum chip thickness, especially under conditions of small feedrate per tooth or at the entering and exiting point of machining.

When current chip thickness $h(t,k)$ is less than the minimum chip thickness, material undergoes elastic and plastic deformation, but is not removed. The residual chip thickness will be added to the next tooth path at the same position angle. This will repeat until the accumulated chip thickness becomes bigger than the minimum chip thickness, thus chip formation will take place every two or more tooth passes depending on the uncut chip thickness and minimum chip thickness. In this case, the chip thickness can be expressed as:

$$h_a(t+\Delta t,k+1)=h(t,k)+h(t+\Delta t,k+1) \tag{5-14}$$

If the uncut chip thickness in bigger than the minimum chip thickness, the actual chip thickness is equal to the theoretical chip thickness.

$$h_a(t,k)=h(t,k) \tag{5-15}$$

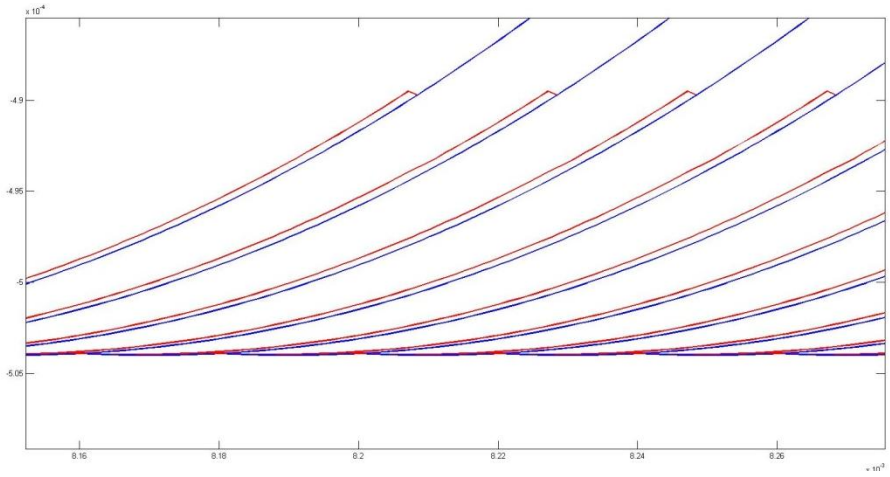

Figure 5.4 Nominal and actual chip thickness

The above figure shows the simulated chip thickness considering the minimum chip thickness in the vicinity of entering point. The blue curve represents the trajectory of tool tip and the red line represents the actual profile after material being removed. It can be seen that as a result of cutting edge radius, chips can't be formed at the beginning and material deforms plastically and recovers to certain level. Only if the

uncut chip thickness is bigger than minimum chip thickness, the machined profile overlaps with the tool tip trajectory.

5.3 Novel cutting force modeling in micro-milling

5.3.1 Cutting force modeling

5.3.1.1 Orthogonal cutting force in chip formation

Conventionally, the cutting forces in milling process are based on the assumption that the tool edge is perfectly sharp, which can't be applied in micro milling; as the existence of cutting edge radius, the cutting process in micro milling is clearly divided into two distinct cutting regimes, ploughing-dominant regime where material deforms plastically but no chips are formed, and shearing-dominant regime where material removed by chips. As discussed in chapter 4, under the round cutting edge, the material splits and separates, the upper part forms the chip and the lower part flows beneath the tool and forms the machined surface.

When cutting under minimum chip thickness, the ploughing forces are assumed to be proportional to the volume of interface between workpiece and tool (Malekian et al, 2009) computed by

$$\begin{cases} dF_{rp} = (K_{rp}A_p + K_{re})dz \\ dF_{tp} = (K_{tp}A_p + K_{te})dz \end{cases} \tag{5-16}$$

where K_{rp} and K_{tp} are the ploughing coefficients in radial and tangential directions, respectively, and A_p is the ploughed area between the tool and workpiece; K_{re} and K_{te} are the edge coefficients in radial and tangential directions, respectively; dz is the axial height of each differential flute elements;

There are two different cases for calculation of ploughed area, considering the elastic recovery and its relative location to the tangent point connecting cutting edge and flank face.

$$A_p = \begin{cases} 0.5r_e^2(\alpha_p + \Psi_e) + 0.5r_e l_{AD} - 0.5r_e l_{AB}\sin(\alpha_p + \Psi_e + \Psi_t) \\ \qquad if\ h_{er} \geq r_e(1 - \cos(\Psi_e)) \\ 0.5r_e^2(\alpha_p + \Psi_s - \sin(\alpha_p + \Psi_s)) \quad if\ h_{er} < r_e(1 - \cos(\Psi_e)) \end{cases} \tag{5-17}$$

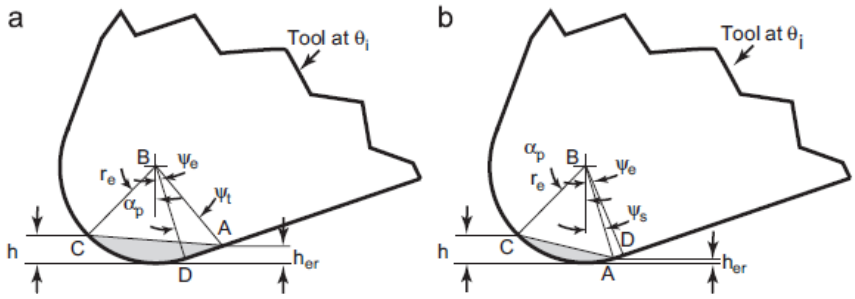

Figure 5.5 Ploughed area of two cases (Malekian et al, 2009)

When machining takes place at chip thickness bigger than minimum chip thickness, the tangential and radial cutting forces can be modelled as follows:

$$\begin{cases} dF_{rc} = (K_{rc}h(\theta_i(z)) + K_{re})dz \\ dF_{tc} = (K_{tc}h(\theta_i(z)) + K_{te})dz \end{cases} \quad (5\text{-}18)$$

where K_{rc} and K_{tc} are the radial and tangential cutting coefficients, respectively; $h(\theta_i(z))$ is the uncut chip thickness which is a function of tool position angle θ and axial height z.

The above cutting coefficients are related to the material shearing and edge coefficients are related to the friction and pressure between the tool and workpiece. These coefficients have to be calibrated against the model using collect cutting force from experiment. This can be achieved by fitting the cutting forces into the model and using least square methods to find the optimal coefficients.

5.3.1.2 Transformation to milling tool geometry

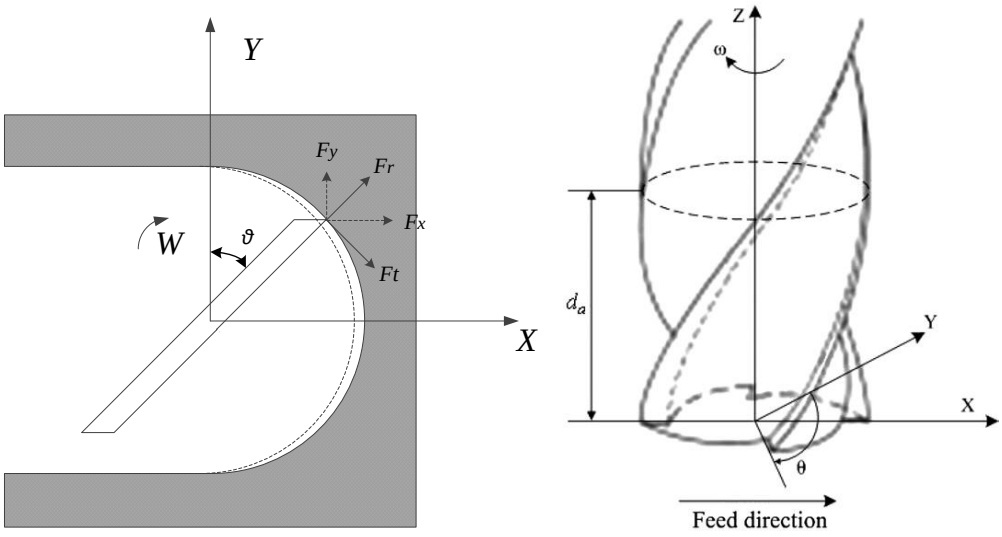

Figure 5.6 Coordinate system and end mill in micro-milling

The above figure shows a typical end mill and the coordinate system used in micro-machining. The radial and tangential cutting forces are decomposed into the coordinate system and described as follows:

$$\begin{cases} dF_x = F_r \sin\theta + F_t \cos\theta \\ dF_y = F_r \cos\theta - F_t \sin\theta \end{cases} \tag{5-19}$$

where θ is the tool tip position angle from the Y axis.

Substituting equation 5-16 and 5-18 into above equation, we have following expression:

$$\begin{cases} dF_x = \left[K_{rp}A_p \sin\theta + K_{re} \sin\theta + K_{tp}A_p \cos\theta + K_{te} \cos\theta\right]dz \\ dF_y = \left[K_{rp}A_p \cos\theta + K_{re} \cos\theta - K_{tp}A_p \sin\theta - K_{te} \sin\theta\right]dz \end{cases} \tag{5-20}$$

when the uncut chip thickness is less than the minimum chip thickness;

$$\begin{cases} dF_x = [K_{rc}h(\theta_i(z)) \sin\theta + K_{re} \sin\theta + K_{tc}h(\theta_i(z)) \cos\theta + K_{te} \cos\theta]dz \\ dF_y = [K_{rc}h(\theta_i(z)) \cos\theta + K_{re} \cos\theta - K_{tc}h(\theta_i(z)) \sin\theta - K_{te} \sin\theta]dz \end{cases} \tag{5-21}$$

when the uncut chip thickness is greater than the minimum chip thickness.

As the tool is simulated by a number of slices along cutting flute, each infinite small slice can be treated as straight cutting edge, so the total force is the sum of differential force acting on each slice.

Considering the helix angle, the position angle of each slice will change with its height, so will the chip thickness according to equation 5-11. The height has the following relation with helix angle:

$$\frac{Rd\theta}{dz} = \tan\beta \tag{5-22}$$

where β is tool's helix angle.

Thus the differential equation 5-21 can be converted to:

$$\begin{cases} dF_x = \left[K_{rp}A_p \sin\theta + K_{re} \sin\theta + K_{tp}A_p \cos\theta + K_{te} \cos\theta\right]R \cot\beta \, d\theta \\ dF_y = \left[K_{rp}A_p \cos\theta + K_{re} \cos\theta - K_{tp}A_p \sin\theta - K_{te} \sin\theta\right]R \cot\beta \, d\theta \end{cases} \tag{5-23}$$

when $h < h_{min}$;

$$\begin{cases} dF_x = [K_{rc}h(\theta_i(z)) \sin\theta + K_{re} \sin\theta + K_{tc}h(\theta_i(z)) \cos\theta + K_{te} \cos\theta]R \cot\beta \, d\theta \\ dF_y = [K_{rc}h(\theta_i(z)) \cos\theta + K_{re} \cos\theta - K_{tc}h(\theta_i(z)) \sin\theta - K_{te} \sin\theta]R \cot\beta \, d\theta \end{cases} \tag{5-24}$$

when $h \geq h_{min}$;

The cutting forces can be integrated over the range of engagement of each cutting flute with material, there is:

$$\begin{cases} F_x(t,k) = R \cot\beta \int_{\theta_{en}}^{\theta_{ex}} \left(K_{rp}A_p \sin\theta + K_{re} \sin\theta + K_{tp}A_p \cos\theta + K_{te} \cos\theta\right) d\theta \\ F_y(t,k) = R \cot\beta \int_{\theta_{en}}^{\theta_{ex}} \left(K_{rp}A_p \cos\theta + K_{re} \cos\theta - K_{tp}A_p \sin\theta - K_{te} \sin\theta\right) d\theta \end{cases} \tag{5-25}$$

when $h < h_{min}$;

$$\begin{cases} F_x(t,k) = R\cot\beta \int_{\theta_{en}}^{\theta_{ex}} \begin{pmatrix} K_{rc}h\big(\theta_i(z)\big)\sin\theta + K_{re}\sin\theta + \cdots \\ K_{tc}h\big(\theta_i(z)\big)\cos\theta + K_{te}\cos\theta \end{pmatrix} d\theta \\ F_y(t,k) = R\cot\beta \int_{\theta_{en}}^{\theta_{ex}} \begin{pmatrix} K_{rc}h\big(\theta_i(z)\big)\cos\theta + K_{re}\cos\theta - \cdots \\ K_{tc}h(\theta_i(z))\sin\theta - K_{te}\sin\theta \end{pmatrix} d\theta \end{cases} \quad (5\text{-}26)$$

when $h \geq h_{min}$; where θ_{en} and θ_{ex} are the entry angle and exit angle of cutting flute when it engages and disengages with material.

It should be noted that as the chip thickness changes periodically, both ploughing dominant cutting and shearing dominant cutting will take place in one revolution, so the cutting forces should be calculated using both equations 5-25 and 5-26.

5.3.2 An innovative approach to cutting force modeling

Using the above proposed model, we can predict the cutting forces in micro-milling, however, previous research and experiments show that cutting force in micro machining is very small down to 0.1~1N in magnitude. The direct usage of absolute cutting force in understanding micro-milling process would be less accurate and difficult in terms of cutting size effect, tool wear mechanism etc. Therefore, a new model is proposed based on the absolute cutting forces which can provide insightful quantitative analysis into the machining process. It can be formulated in three aspects.

5.3.2.1 Cutting force on unit length

The cutting force on unit length can provide force distribution at changing positions. Considering the existing helix angle, the total length of cutting flute engaged with material is expressed as follows:

$$l = R(\theta_{ex} - \theta_{en})/\sin\beta \quad (5\text{-}27)$$

Thus the cutting force on unit length is represented as:

$$F_{lx}(t,k) = \frac{F_x(t)\cos\beta}{(\theta_{ex}-\theta_{en})}; F_{ly}(t,k) = \frac{F_y(t)\cos\beta}{(\theta_{ex}-\theta_{en})} \quad (5\text{-}28)$$

5.3.2.2 Cutting force on unit area

The cross section of chip in micro milling is also a function of position angle; it can be formulated as follows:

$$s = \frac{R}{\sin\beta}\int_{\theta_{en}}^{\theta_{ex}} h(\theta_i(z))\, d\theta \tag{5-29}$$

The cutting force on unit area is calculated by:

$$F_{sx}(t,k) = \frac{F_x(t)\sin\beta}{R\int_{\theta_{en}}^{\theta_{ex}} h(\theta_i(z))d\theta}; F_{sy}(t,k) = \frac{F_y(t)\sin\beta}{R\int_{\theta_{en}}^{\theta_{ex}} h(\theta_i(z))d\theta} \tag{5-30}$$

5.3.2.3 Cutting energy on unit volume

The volume of material removed in micro-milling can be expressed approximately as

$$dV = vdtR\cot\beta\int_{\theta_{en}}^{\theta_{ex}} h(\theta_i(z))d\theta \tag{5-31}$$

As the cutting force on unit volume doesn't have any physical meaning, the energy consumption on unit volume is calculated instead, thus it has following formula:

$$e = \frac{Fvdt}{dV} = \frac{F\tan\beta}{R\int_{\theta_{en}}^{\theta_{ex}} h(\theta_i(z))d\theta} \tag{5-32}$$

5.4 Experimental validation

5.4.1 Experiment design and setup

Experiments are carried out on Kern micro-milling machine which has good motion accuracy to realise the necessary movement for different feedrates. The setup is shown in figure 3.17; the workpiece sits on top of the Kistler dynamometer 925C2 via connection of bolt. Since the connection is not rigid, transfer function from the workpiece to the dynamometer is inevitably changed, and this needs compensation in order to get the accurate measurement. Hammer test is performed to obtain the dynamic response of the force measuring system. Various milling tools are employed; including the two above-mentioned single-fluted tools and normal end mills with helix flutes. Experiments are conducted at varied feedrate and cutting speed to broadly study the machining process. The used cutting parameters are summarised in Table 5-1.

Table 5-1 Cutting parameters used in experiments

Tool type	0.4mm diamond tool	0.4 tungsten carbide tool	1mm tungsten carbide tool	1mm tungsten carbide tool
Number of Flutes	1 straight	1 straight	1 helix	2 helix
Feedrate(μm/tooth)	0.2 0.5 1 2 3 4 5	0.2 0.5 1 2 3 4 5	0.5 1 2 3 4 5 6 8 10 12 14	0.5 1 2 3 4 6 9 12
Cutting speed (m/min)	15 26.5 38	15 26.5 38	38 47.5 57 66.5 76 85.5 95	38 47.5 57 66.5 76 85.5 95
Cutting depth(μm)	20	20	20	20

5.4.2 Measurement of tool runout

The total net run out and its position angle are measured at the tool tip. There are many factors that contribute to the total value such manufacturing error, alignment error and tool dynamics. Previous research and experiments show that the most significant run-out error is introduced by the alignment error. It mainly consists of the parallel tool offset and the tilt error. For most cases in the experiment, the tilt error has very small effect on the tool run-out as the small depth of cut adopted in cutting trial. Thus the tool run-out error measurement is mainly focused on the tool parallel offset and its position angle.

The tool nominal diameter is firstly measured on the TESA-200 microscope, its rotational tool run-out is measured by using the capacitive sensor MicroSense 5810; To measure its location angle, two marks are attached to the tool which are aligned with the opposite two tool tips, so the increment angle is exactly 180°. The two marks are captured by the sensor, and by calculating the angle between them, the actual increment angle can be derived. The position angle of the tool runout can be determined by the difference.

5.4.3 Accurate measurement of cutting forces

In order to get the accurate measurement of cutting force, the transfer function from the workpiece to the dynamometer has to be identified first; due to its dynamic response, signal component at varied frequency has response of different amplitude

which has to be compensated to get the accurate measurement results. The procedures will be explained in this session.

5.4.3.1 Identification of the machining system transfer functions

Hammer test is performed on the workpiece at x y and z directions. The signal generated by the hammer is assumed to be pulse-like, thus it contains components of as wide range frequency as possible. It is input to the workpiece-dynamometer system as the excitation signal; the response signal is output by the dynamometer. An impact hammer 9722A500 with head of hard steel is utilized here. The dynamic characteristic of the force measuring system is modelled as a function of frequency f in Laplace form as shown in equation 5-33, where the $b_i(i = 0{\sim}m)$ and $a_i(i = 0{\sim}n)$ are the function coefficients. The objective of performing hammer test is to determine the transfer function which best represents the system dynamic characteristic in three directions.

$$H(s) = \frac{Y(s)}{X(s)} = \frac{b_1 s^m + b_2 s^{m-1} + \cdots + b_m s^1 + b_{m+1}}{s^n + a_1 s^{n-1} + \cdots + a_{n-1} s^1 + a_n} \tag{5-33}$$

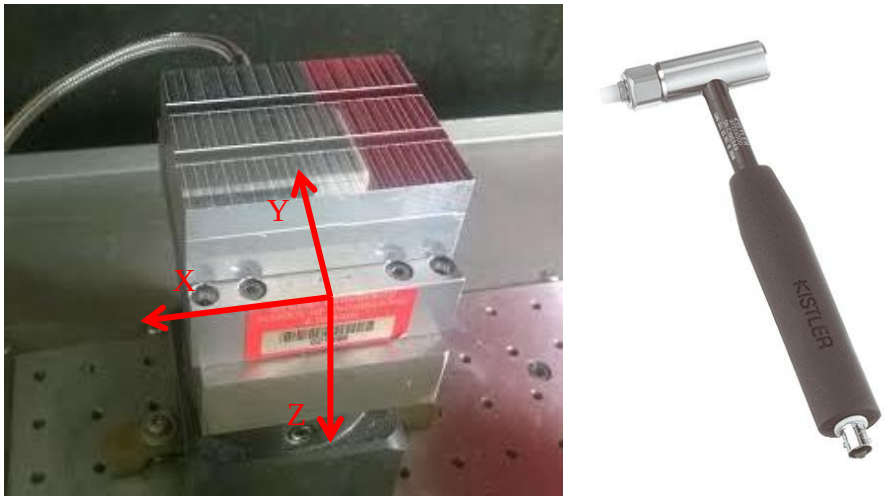

Figure 5.7 Experiment set-up and the utilized hammer

The actual input signals and output signals are shown in Figure 5.8~11, the input is impulse-like signal of very short time duration, while the output mostly follows the input but oscillates and gradually reduces to zero at the end. The frequency response shows spike at different locations, which are mostly around its natural frequency; and it can be also seen that the response gain is not all the unity at the full frequency range, which means the measured signal is actually amplified or diminished. It is very necessary to compensate the measured cutting force.

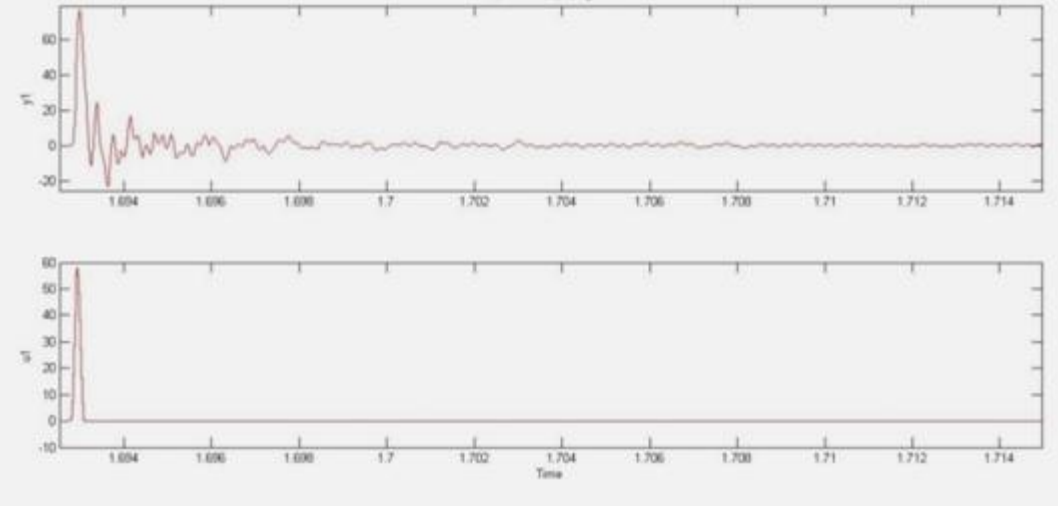

(a) System output and input signal

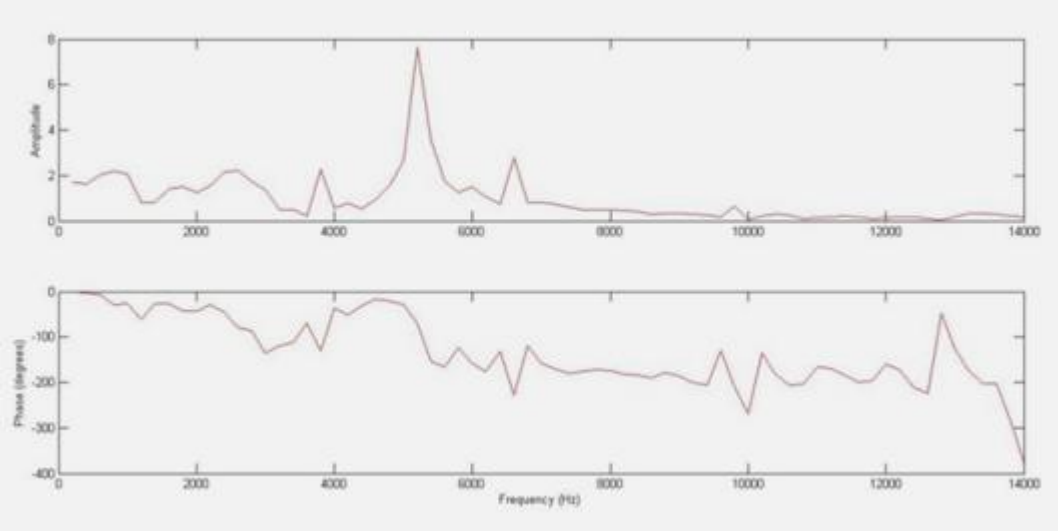

(b) System frequency response (amplitude and phase in degrees)

Figure 5.8 Signals and system frequency response in x direction

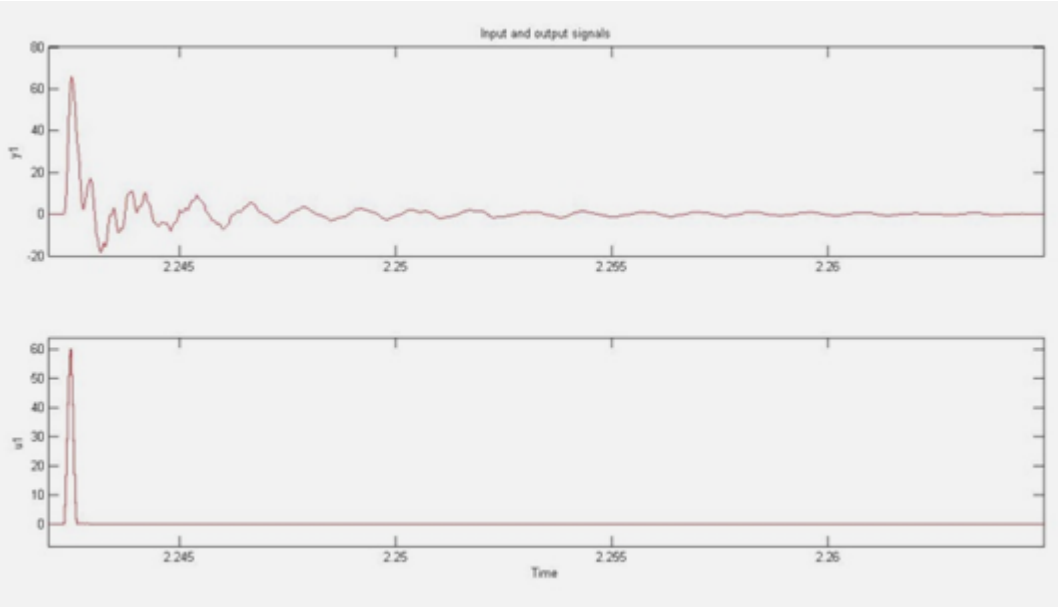

(a) System output and input signal

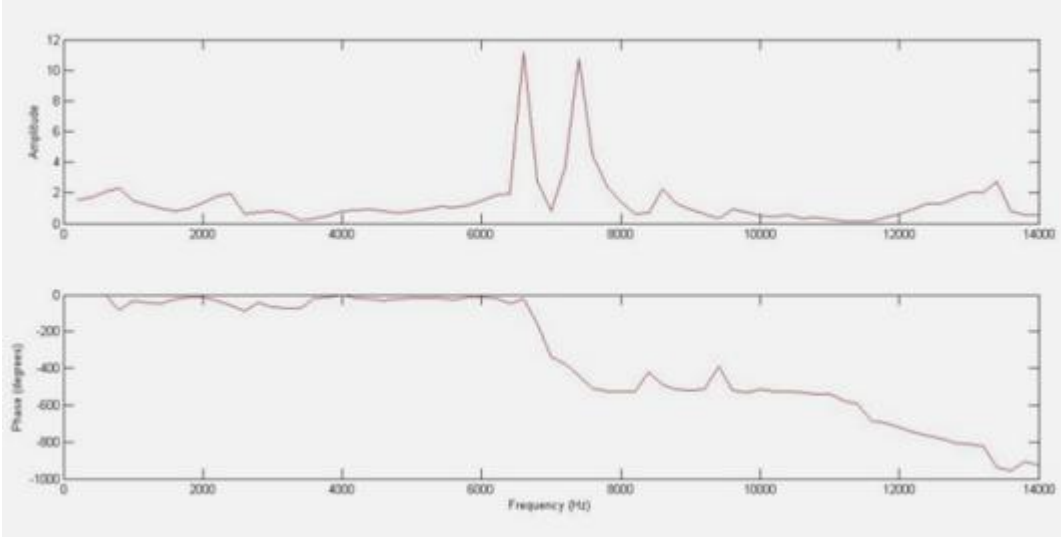

(b) System frequency response (amplitude and phase in degrees)

Figure 5.9 Signals and system frequency response in y direction

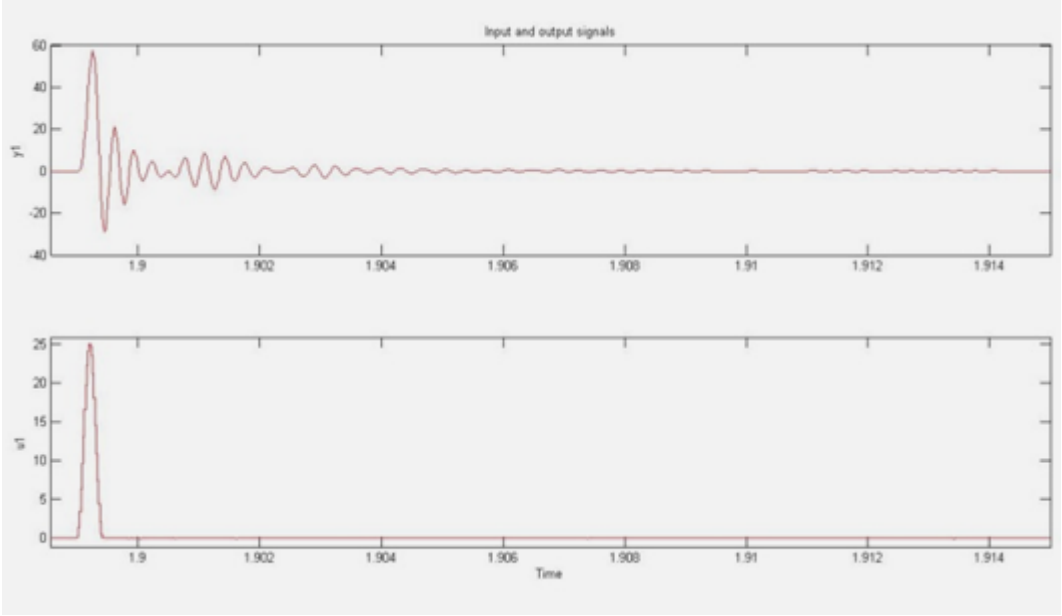

(a) System output and input signal

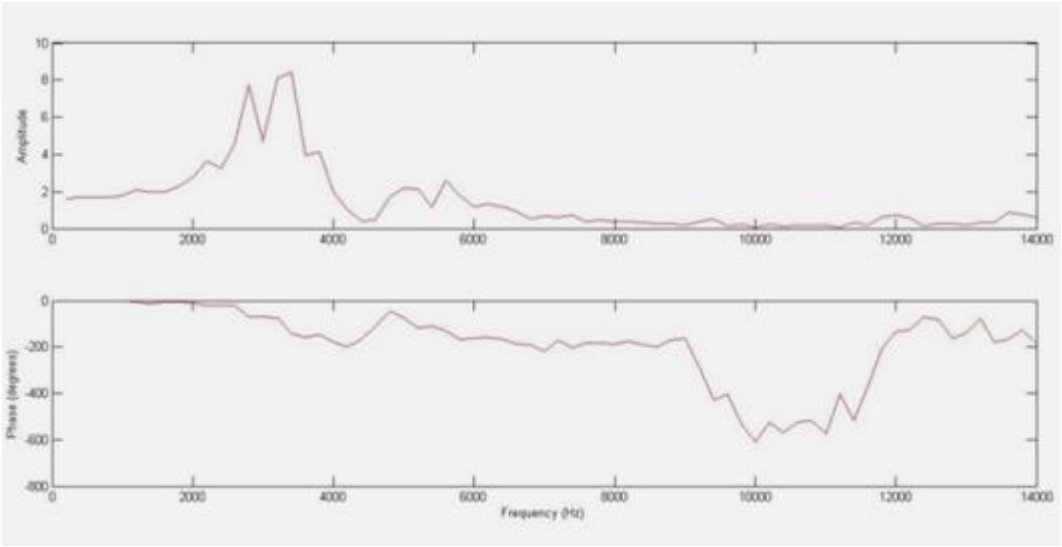

(b) System frequency response (amplitude and phase in degrees)

Figure 5.10 Signals and system frequency response in z direction

It is nearly impossible to directly derive an analytical function to represent the system frequency response. Instead, the transfer function is obtained by curve fitting the frequency response data as shown in Figure 5.11. The many spikes indicate that the dynamic characteristics of the workpiece-dynamometer is very complicated and curve fitting results validate this point.

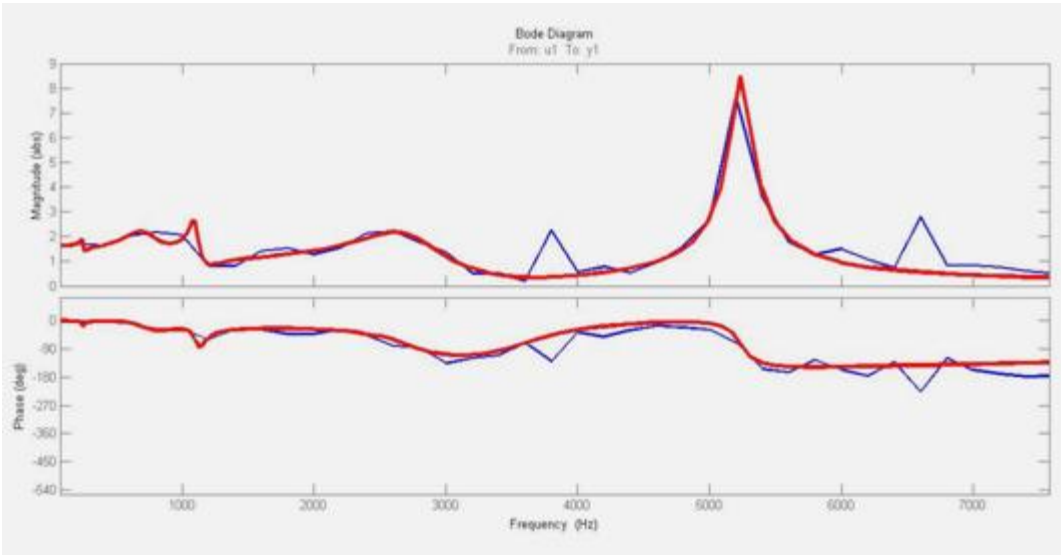

Figure 5.11 Curve fitting the frequency response in x direction (red: curved fitted; blue: actual response)

The transfer function in x direction:

Tfx=

1.03e04s^11 + 5.626e08s^10 + 2.474e13s^9 + 4.716e17s^8 + 1.072e22s^7 + 7.755e25s^6 + 7.707e29s^5 + 3.265e33s^4 + 1.431e37s^3 + 2.935e40s^2 + 3.291e43s + 4.95e46

---

s^12+ 2.936e04s^11 + 1.669e09s^10+ 4.083e13s^9 + 6.756e17s^8 + 1.102e22 s^7+7.022e25s^6 + 6.372e29s^5 + 2.298e33s^4 + 9.857e36s^3+ 1.882e40s^2 + 2.137e43s + 3.039e46

(5-34)

It has 12 poles and 11 zeros, which demonstrate the complexity of the dynamic characteristics. The order of coefficients varies in a very large-scale.

The transfer functions in other directions are obtained in similar way.

The transfer function in y direction:

Tfy=

1.532e09s^10 + 1.526e13s^9 + 6.617e17s^8 + 3.402e21s^7 + 5.495e25s^6 + 1.043e29s^5 + 1.037e33s^4 + 2.679e35s^3 + 1.056e39s^2 + 8.816e40s + 1.512e4

---

s^12 + 1.103e04 s^11 + 2.6e09s^10 + 1.825e13s^9 + 7.284e17s^8 + 3.125e21 s^7+ 4.405e25s^6 + 7.654e28s^5 + 6.819e32s^4 + 1.864e35s^3+ 6.786e38 s^2 + 5.93e40s + 9.53e43

(5-35)

It has 12 poles and 10 zeros.

The transfer function in z direction:

Tfz=

1.026e04 s^7 + 8.166e08 s^6 + 2.158e13 s^5 + 8.287e17 s^4 + 9.737e21 s^3 + 2.521e26 s^2 + 1.201e30 s + 2.314e34

---

s^8 + 2.646e04 s^7 + 1.577e09s^6 + 2.563e13 s^5+ 8.476e17 s^4 + 7.891e21 s^3 + 1.861e26 s^2 + 7.702e29 s + 1.412e34

(5-36)

It has 8 poles and 7 zeros.

5.4.3.2 Reconstruction of cutting forces

The above obtained transfer function shows that it will inevitably introduce signal distortion at particular frequencies, especially at frequencies around natural frequency. The reconstruction of cutting force requires reducing the distortion. The workpiece-dynamometer system can be schematically represented as Figure 5.12. The transfer function is represented as $H(s)$. The output signal is related to the input signal by the transfer function. To reconstruct the original input signal, the direct mean is to apply another filter whose transfer function is the inverse form of $H(s)$, i.e $H^{-1}(s)$. Thus the final output is equal to the input. However, for most physical systems, it is very difficult to find a unique analytical solution to this. A disturbance Kalman filter (Park, 2003) which acts similarly to the inverse filter is used to compensate the distortions in this study.

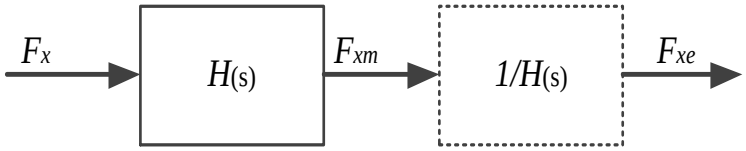

Figure 5.12 Schematic diagram of the cutting force measuring system

Take the cutting forces in x direction as an example, the transfer function is firstly converted to state space form, which has following expression:

$$\begin{aligned} \dot{x} &= Ax + Bu \qquad (state\ equation) \\ z &= Cx \qquad (measurement\ equation) \end{aligned} \tag{5-37}$$

where x is the state vector, $u = F_x$ is the actual cutting force in x direction and $z = F_x$ is the measured cutting force in x direction. A, B and C are the coefficient matrixes obtained from transfer function 5-34.

The transfer function in x direction is converted to

$$\begin{bmatrix} \dot{x}_1 \\ \dot{x}_2 \\ \vdots \\ \dot{x}_{11} \\ \dot{x}_{12} \end{bmatrix} = \begin{bmatrix} -a_1 & -a_2 & \cdots & -a_{11} & -a_{12} \\ 1 & 0 & \cdots & 0 & 0 \\ & \vdots & \ddots & \vdots & \\ 0 & 0 & \cdots & 0 & 0 \\ 0 & 0 & \cdots & 1 & 0 \end{bmatrix} \begin{bmatrix} x_1 \\ x_2 \\ \vdots \\ x_{11} \\ x_{12} \end{bmatrix} + \begin{bmatrix} 1 \\ 0 \\ \vdots \\ 0 \\ 0 \end{bmatrix} F_x$$

$$[F_{xm}] = [b_1 \quad b_2 \quad \cdots \quad b_{11} \quad b_{12}] \begin{bmatrix} x_1 \\ x_2 \\ \vdots \\ x_{11} \\ x_{12} \end{bmatrix} \tag{5-38}$$

where the a_i and b_i are the coefficients of the denominator and numerator in descending order of s in the transfer function, respectively. Its corresponding value can be found in Table 5-2.

Table 5-2 Coefficients obtained from the transfer function

a_1	a_2	a_3	a_4	a_5	a_6	a_7	a_8	a_9	a_{10}	a_{11}	a_{12}
2.93 e4	1.66 e9	4.08 e13	6.75 e17	1.10 e22	7.02 e25	6.37 e29	2.29 e33	9.85 7e36	1.88 2e40	2.13 7e43	3.03 9e46
b_1	b_2	b_3	b_4	b_5	b_6	b_7	b_8	b_9	b_{10}	b_{11}	b_{12}
1.03 e04	5.62 e08	2.47 e13	4.71 e17	1.07 e22	7.75 e25	7.70 e29	3.26 e33	1.43e 37	2.93e 40	3.29e 43	4.95e 46

It can be seen that both matrix A and C contain very large number and the order differs greatly. They are both poorly conditioned matrixes which could cause problem in inversion and eigenvalue analysis, so pre-conditioning is applied. A similarity transformation matrix,T, is used to transform the system into an equivalent system. The updated state space model is shown as:

$$\begin{cases} \dot{x} = A_t x + B_t u & (state\ equation) \\ z = C_t x & (measurement\ equation) \end{cases} \tag{5-39}$$

where

$$A_t = T \times A_t \times T^{-1}\ ,\ B_t = T \times B_t,\ C_t = C_t \times T^{-1}$$

For simplification, this can be achieved in Matlab by pre-scaling the state space model.

The transformed coefficient matrixes are:

$A_t =$

-29358	-25465	-19011	-19202	-19113	-7434	-4117	-1812	-1898	-885	-981	-1362
65536	0	0	0	0	0	0	0	0	0	0	0
0	32768	0	0	0	0	0	0	0	0	0	0
0	0	16384	0	0	0	0	0	0	0	0	0
0	0	0	16384	0	0	0	0	0	0	0	0
0	0	0	0	16384	0	0	0	0	0	0	0
0	0	0	0	0	16384	0	0	0	0	0	0
0	0	0	0	0	0	8192	0	0	0	0	0
0	0	0	0	0	0	0	4096	0	0	0	0
0	0	0	0	0	0	0	0	4096	0	0	0
0	0	0	0	0	0	0	0	0	1024	0	0
0	0	0	0	0	0	0	0	0	0	1024	0

B_t =[256 0 0 0 0 0 0 0 0 0 0 0]^T

C_t =[40.22 33.53 44.99 52.35 72.65 32.07 19.45 10.06 10.76 5.38 5.90 8.67]

The above state space model is expanded and converted to following form:

$$\begin{bmatrix} \dot{x}_1 \\ \dot{x}_2 \\ \vdots \\ \dot{x}_{11} \\ \dot{x}_{12} \\ \dot{F}_x \end{bmatrix} = \begin{bmatrix} [A_t]_{12\times12} & [B_t]_{12\times1} \\ [0]_{1\times12} & 0 \end{bmatrix} \begin{bmatrix} x_1 \\ x_2 \\ \vdots \\ x_{11} \\ x_{12} \\ F_x \end{bmatrix} + \begin{bmatrix} [0]_{12\times1} \\ 1 \end{bmatrix} \omega$$
$$[F_{xm}] = [b_1 \quad b_2 \quad \cdots \quad b_{11} \quad b_{12} \quad 0] \begin{bmatrix} x_1 \\ x_2 \\ \vdots \\ x_{11} \\ x_{12} \\ F_x \end{bmatrix} + v_{1\times1} \tag{5-40}$$

where ω is the process noise, and v is the measurement noise.

In the above model, the actual cutting force F_x is modelled as:

$$\dot{F}_x = 0 \times F_x + \omega \tag{5-41}$$

Since the sampling rate of data collection is quite high compared to the tooth passing frequency, thus the input cutting force can be treated as piecewise constant signal, thus its derivative is only the process noise ω.

Based on the expanded state space model, the Kalman filter is constructed to estimate the state vector $\hat{x}_e$ which can minimise its steady-state error covariance.

$$P = \lim_{t\to\infty} E(\{x - \hat{x}_e\}\ \{x - \hat{x}_e\}^T) \tag{5-42}$$

The Kalman filter can be expressed as:

$$\dot{\hat{x}}_e = \begin{bmatrix} [A_t]_{12\times12} & [B_t]_{12\times1} \\ [0]_{1\times12} & 0 \end{bmatrix} \hat{x}_e + L(F_{xm} - [b_1 \quad b_2 \quad \cdots \quad b_{11} \quad b_{12} \quad 0]\,\hat{x}_e)$$
$$\begin{bmatrix} \hat{F}_{xm} \\ \hat{x}_e \end{bmatrix} = \begin{bmatrix} [b_1 \quad b_2 \quad \cdots \quad b_{11} \quad b_{12} \quad 0] \\ I \end{bmatrix} \hat{x}_e \tag{5-43}$$

Rewriting equation 5-42, there is:

$$\dot{\hat{x}}_e = \left(\begin{bmatrix} [A_t]_{12\times12} & [B_t]_{12\times1} \\ [0]_{1\times12} & 0 \end{bmatrix} - L[b_1 \quad b_2 \quad \cdots \quad b_{11} \quad b_{12} \quad 0] \right) \hat{x}_e + LF_{xm}$$
$$\dot{\hat{x}}_e = (A_e - LC_e)\,\hat{x}_e + LF_{xm} \tag{5-44}$$

where L is the gain of the Kalman filter. It is determined by minimising the steady state error covariance P. To do this, the following equation which is called algebraic Riccati equation has to be solved.

$$A_e^T P + P A_e - P C_e R^{-1} C_e^T P + Q = 0 \tag{5-45}$$

where Q and R are the process noise covariance and measurement noise covariance, respectively. $Q = E(\omega\ \omega^T) = 1e9$ and $R = E(v\ v^T) = 0.08$ for the signal in x direction.

The Kalman filter gain is obtained:

$$L = R^{-1} {C_e}^T P \tag{5-46}$$

Computing results give $L = [331.70\ \ 837.35\ 335.00\ 94.90\ \ 30.56\ \ -7.16\ \ -9.26\ \ -14.90\ \ -7.92\ \ 7.08\ \ 1.15\ \ -0.19\ \ 111803.39]^T$

For the estimated $\widehat{F}_x$, the following relation holds:

$$\widehat{F}_x = C_x \times \hat{x}_e = [0\ 0\ 0\ 0\ 0\ 0\ 0\ 0\ 0\ 0\ 0\ 0\ 1] \begin{bmatrix} x_1 \\ x_2 \\ \vdots \\ x_{11} \\ x_{12} \\ F_x \end{bmatrix} \tag{5-47}$$

Thus the transfer function from $\widehat{F}_x$ to F_{xm} can be obtained, and by applying the transfer function to the measured cutting force, the estimated input cutting force is obtained.

$$T(s) = \frac{\widehat{F}_x(s)}{F_{xm}(s)} = C_x(sI - (A_e - LC_e))^{-1} L \tag{5-48}$$

The two-tier cutting force measuring system can be schematically illustrated as:

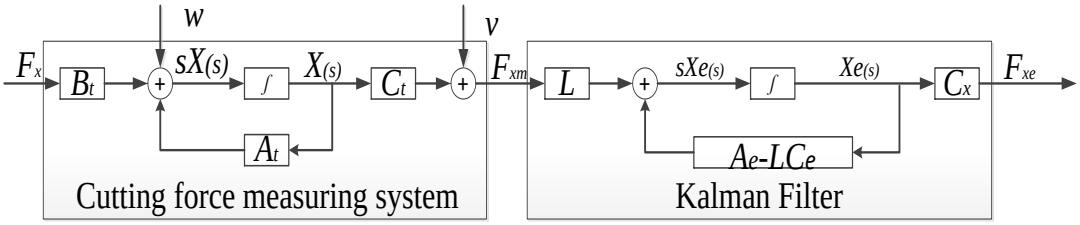

Figure 5.13 Block diagram of the two-tier force measuring system

The derived transfer function of the Kalman filter in x direction gives:

$T_x(s)$=

1.118e05 s^12 + 3.282e09 s^11 + 1.866e14 s^10 + 4.565e18 s^9 + 7.554e22 s^8+ 1.232e27 s^7 + 7.851e30 s^6 + 7.124e34 s^5 + 2.569e38 s^4 + 1.102e42 s^3+ 2.105e45 s^2 + 2.389e48 s + 3.397e51

---

s^13 + 9.148e04 s^12 + 5.422e09 s^11 + 2.044e14 s^10 + 5.533e18 s^9 + 1.032e23 s^8 + 1.578e27 s^7 + 1.211e31 s^6 + 1.007e35 s^5 + 4.264e38 s^4 + 1.724e42 s^3 + 3.421e45 s^2 + 3.885e48 s + 5.534e51

(5-49)

Similarly, the transfer function of Kalman filter in y direction is derived:

$T_y(s) =$

2.236e05 s^12 + 2.433e09 s^11 + 5.417e14 s^10 + 4e18 s^9 + 1.461e23 s^8 + 6.645e26 s^7 + 8.272e30 s^6 + 1.575e34 s^5 + 1.224e38 s^4 + 3.386e40 s^3 + 1.099e44 s^2 + 1.136e46 s + 1.26e49

---

s^13 + 1.272e05 s^12 + 1.046e10 s^11 + 4.143e14 s^10 + 7.57e18 s^9 + 1.459e23 s^8 + 1.074e27 s^7 + 1.064e31 s^6 + 2.778e34 s^5 + 1.86e38 s^4 + 5.686e40 s^3 + 1.703e44 s^2 + 1.886e46 s + 1.992e49

(5-50)

and the transfer function of Kalman filter in z direction is derived:

$T_z(s) =$

3.162e05 s^8 + 8.367e09 s^7 + 4.987e14 s^6 + 8.105e18 s^5 + 2.68e23 s^4 + 2.495e27 s^3 + 5.887e31 s^2 + 2.436e35 s + 4.464e39

---

s^9 + 1.392e05 s^8 + 1.091e10 s^7 + 4.77e14 s^6 + 1.35e19 s^5 + 3.507e23 s^4+ 4.958e27 s^3 + 9e31 s^2 + 5.429e35 s + 7.319e39

(5-51)

The performance of the Kalman filter is examined by comparing the frequency response before and after applying it as shown in Figure 5.14-16. It can be seen that the amplitude response of the combined system after compensation is very close to unity at all frequencies except the region of natural frequencies where the magnitude has small oscillation, however, the distortions at the these regions are greatly reduced.

From the combine frequency response function, we can conclude that the measurement accuracy of the workpiece-dynamometer system is significantly improved.

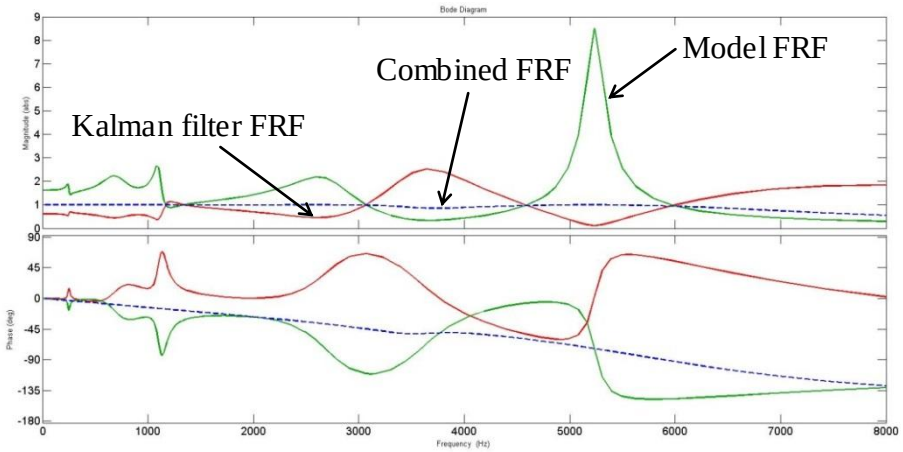

Figure 5.14 Frequency response function of the measuring system, Kalman filter and combined measuring system in x direction

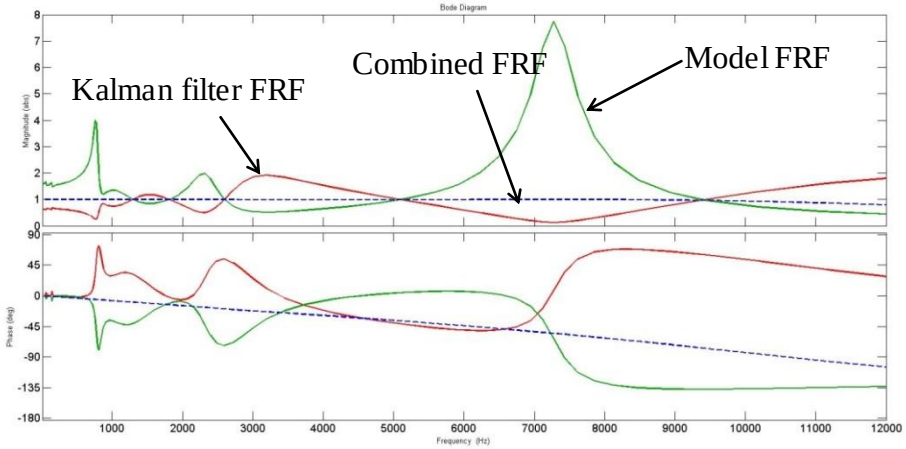

Figure 5.15 Frequency response function of the measuring system, Kalman filter and combined measuring system in y direction

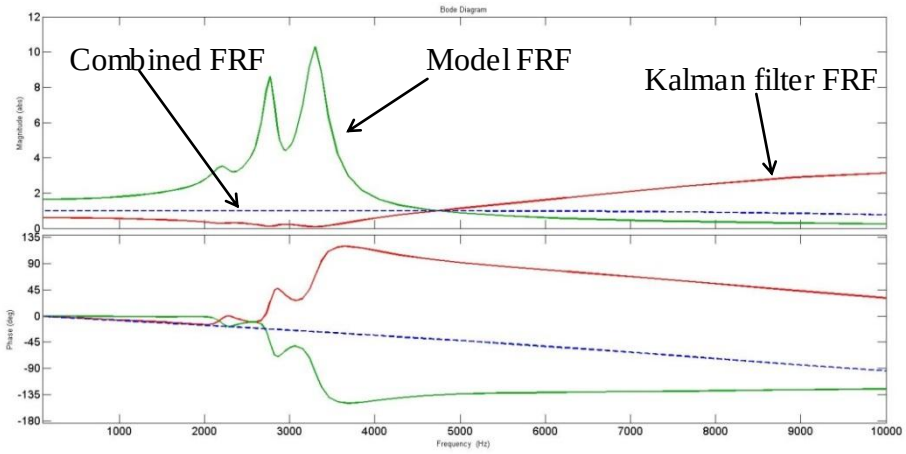

Figure 5.16 Frequency response function of the measuring system, Kalman filter and combined measuring system in z direction

The effectiveness of applying Kalman filter on measured cutting forces is shown in Figure 5.17, Figure 5.18 and Figure 5.19. Cutting tests were performed at spindle speed of 12,000rpm (cutting speed 38m/min); the feedrate per revolution is 4μm. The images show that there are distinct differences between the two signals before and after compensation, firstly the magnitude of the cutting forces is significantly reduced which means the distortion at most frequencies is diminished; secondly, the compensated signal is less fluctuating which indicates Kalman filter also removes the noise signals. Frequency domain analysis shows that most dominant component takes place at the tooth passing frequency and its harmonics. Amplification of cutting force at regions of natural frequency is significantly compressed, as shown in the figure, especially at 5,100Hz in x direction, 7,200Hz in y direction and 3,000Hz in z direction, which demonstrates the effectiveness of Kalman filter. The cutting forces used in other analysis are all compensation with this technique unless specified. It should be reminded that the accuracy of this technique depends heavily on the related instruments and accuracy of the identified transfer function. Thus the hammer which is used as the force reference sensing unit should have high accuracy. The closer the curved fitted transfer functions to the system frequency response, the more accurate compensation results we can get.

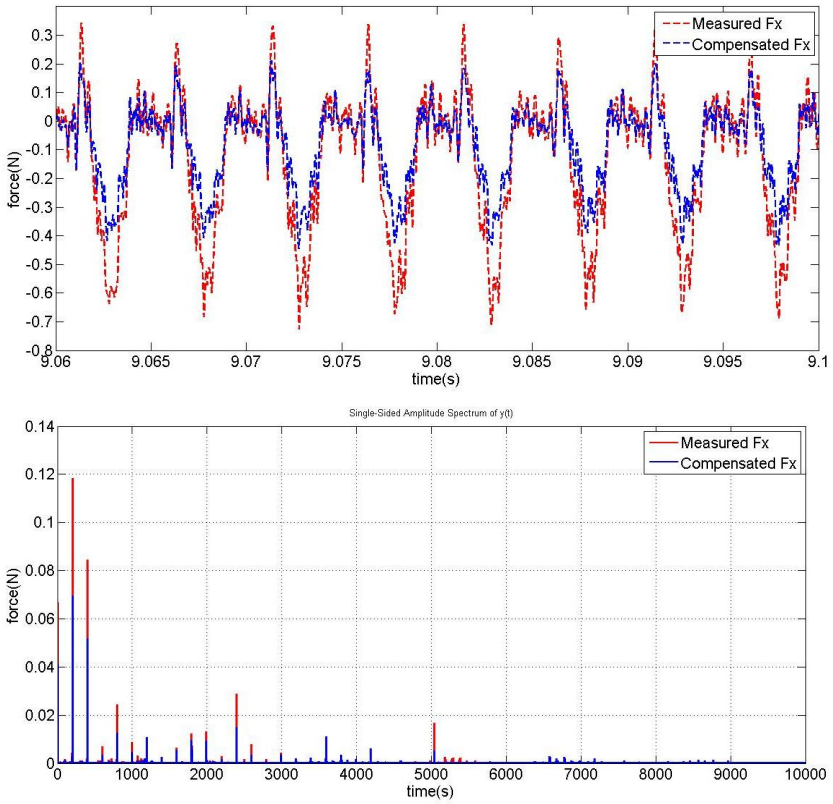

Figure 5.17 Cutting force measurement in x direction (time and frequency domain)

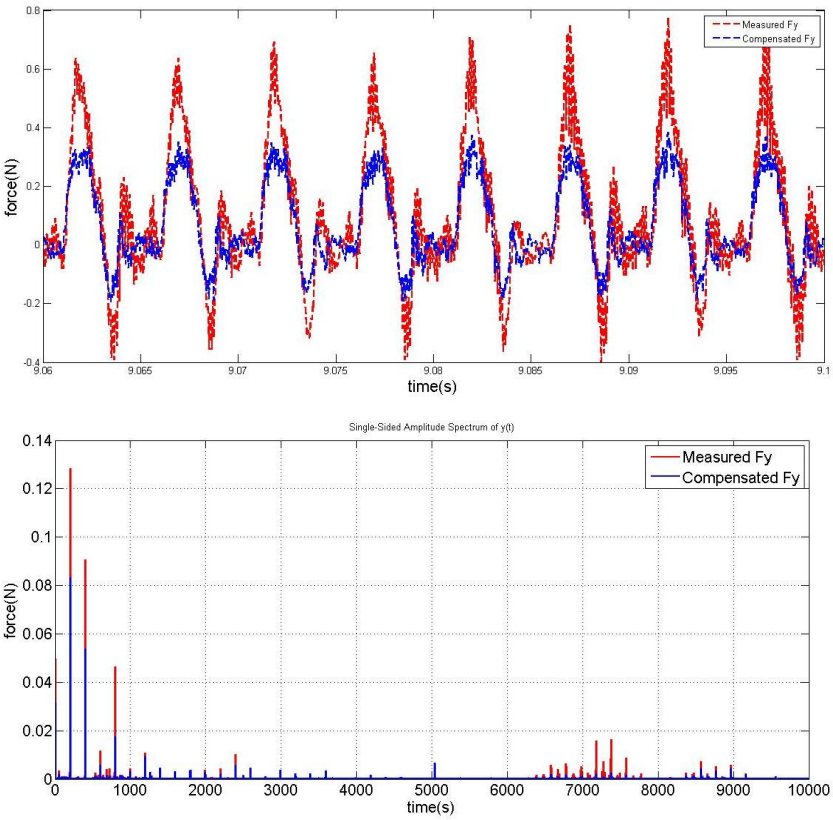

Figure 5.18 Cutting force measurement in y direction (time and frequency domain)

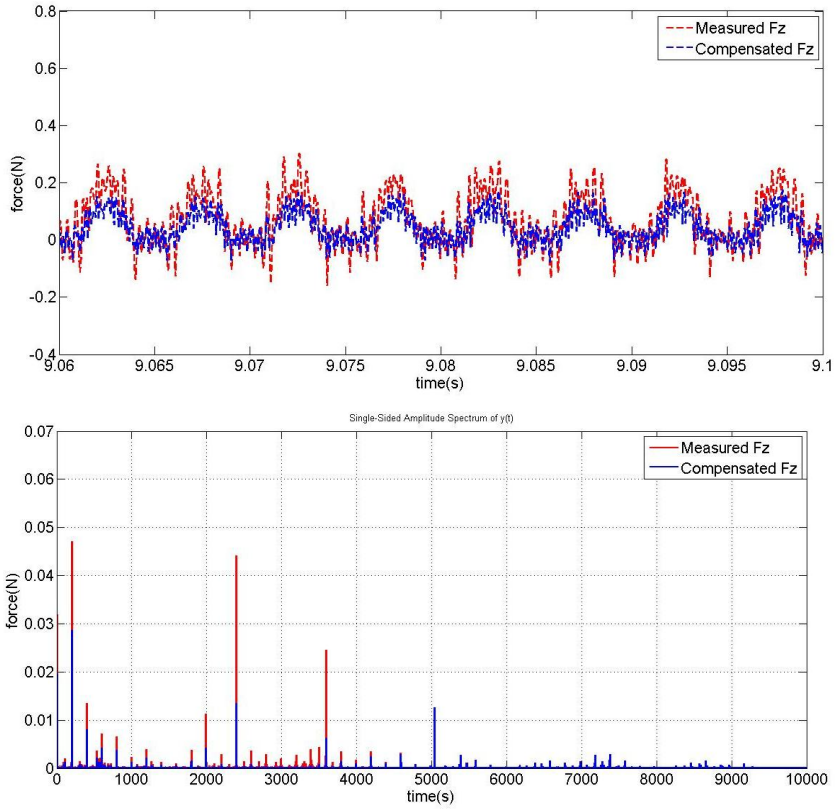

Figure 5.19 Cutting force measurement in z direction (time and frequency domain)

5.4.4 Model calibration and validation

5.4.4.1 Parameter calibration

Experiments are carried out at varied feedrates and spindle speeds as shown in Table 5-1. The collected forces are used to compute the coefficients in the model; due to the periodical change of chip thickness in each revolution, the process experiences both ploughing and shearing dominant cutting; the transition is determined by comparing the actual chip thickness with the minimum chip thickness. The actual chip thickness is obtained using the algorithm proposed in 5.1. The minimum chip thickness, as discovered in previous chapter, is around 20% of the cutting edge radius which is 1.4μm as shown in Figure 4.19. The cutting forces are divided into two groups based on different cutting regime. The ploughing and edge coefficients are obtained by fitting forces into equation 5-16, and cutting and edge coefficients are obtained by fitting forces into equation 5-18. For this purpose, the least square method is adopted in which the coefficients are determined once the sum of squares of the error between predicted force and experimental results reaches minimum:

$$E = \sum_{i=1}^{n} \sum_{j=1}^{m} \left(F_{pre} - F_{exp}\right)^2 \quad (5\text{-}52)$$

where n is the number of feedrates used in curve fitting, and m is the number of data points. F_{pre} is the predicted force by the model, and F_{exp} is the collected experimental force. In this study, 5 feedrates and 300 data points for each feedrate are used to derive the coefficients. The obtained coefficients which satisfy equation 5-49 are shown in Table 5-3.

Table 5-3 Model coefficients for different cutting regime

Material	Cutting regime	K_{rc} (N/mm^2)	K_{re} (N/mm)	K_{tc} (N/mm^2)	K_{te} (N/mm)
Aluminium 6082-T6		2476	5.44	1808	6.05
	Ploughing regime	K_{rp} (N/mm^3)	K_{tp} (N/mm^3)		
		1150	1480		

5.4.4.2 Model validation

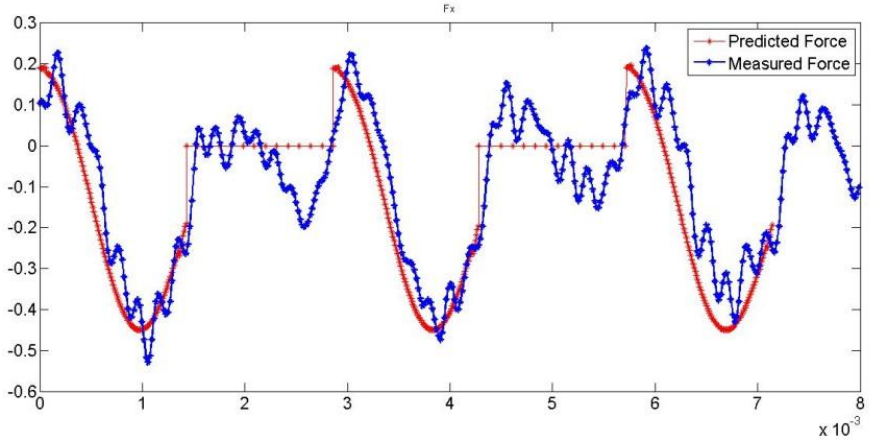

(a) Simulated and experimental cutting forces in x direction

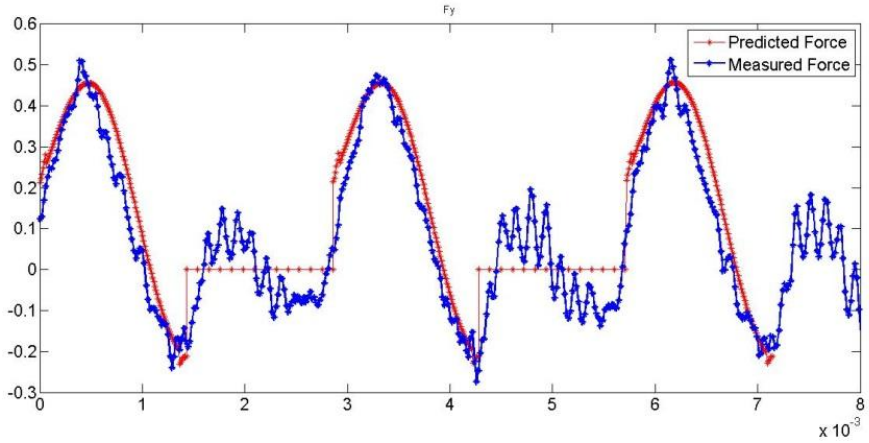

(b) Simulated and experimental cutting forces in y direction

Figure 5.20 Comparison between simulated and experimental cutting forces (slot-milling; single flute tool; spindle: 21000rpm; federate: 2μm/tooth)

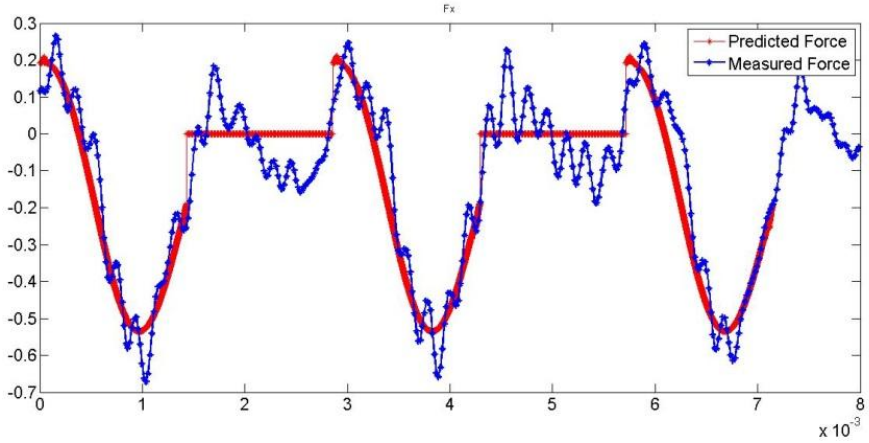

(a) Simulated and experimental cutting force in x direction

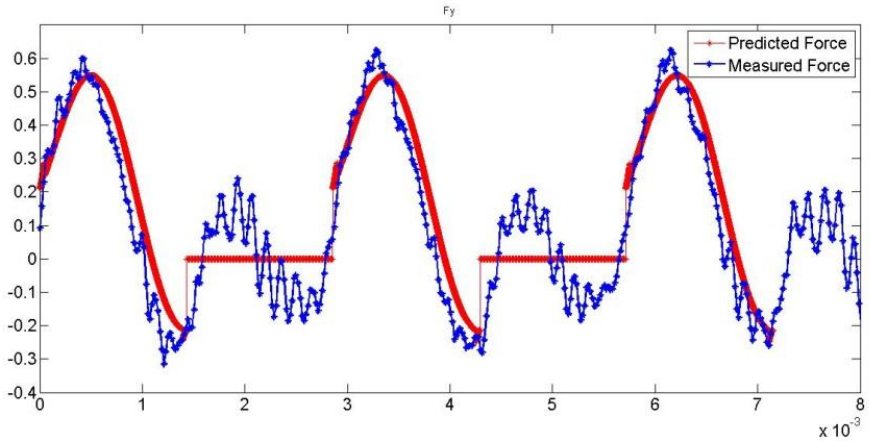

(b) Simulated and experimental cutting forces in y direction

Figure 5.21 Comparison between simulated and experimental cutting forces (slot-milling; single flute tool; spindle: 21000rpm; federate: 3μm/tooth)

Figure 5.20 and Figure 5.21 plot the simulated and experimental cutting force at varied feedrates which shows good agreement between each other. The peak difference between prediction and measurement is less than 10%, The model can predict the evolution and magnitude of the cutting force, but fail to explain the fluctuation in real cutting forces due to the limitation of the modeling technique. These fluctuations, considering the machining process, are introduced by machine and tool vibrations. The single flute tungsten carbide tool is used; only one chip is formed in each revolution. The predicted cutting forces are zero since the tool disengages material in the latter half revolution, while the measured forces show otherwise, the reason for this is probably the strong attachment of material to the tool which continues scratching the material and causes the fluctuation in the cutting force.

5.4.5 Understanding the machining process with the proposed model

The proposed model is used to understand the micro-cutting mechanics in three aspects including the resultant cutting force on unit length or area, and the energy consumption in unit volume as calculated at varied feedrates. For the single straight flute tools, the force on unit length is quite like the resultant force. Figure 5.22 shows the calculation result at different feedrate for both diamond and tungsten carbide tools.

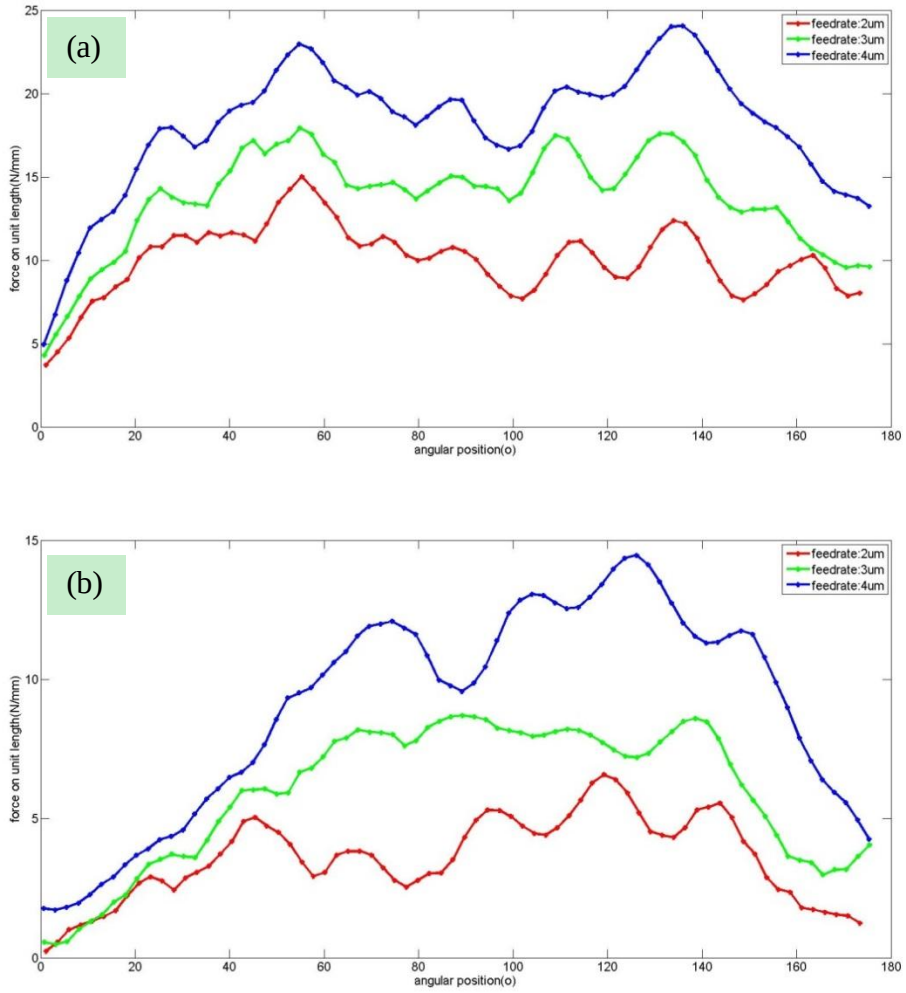

Figure 5.22 Cutting force on unit length versus the angular position, spindle speed 21,000rpm (a) tungsten carbide tool (b) diamond tool

It can be seen that the magnitude increases along with feedrate. The fluctuations are due to material impurity, tool vibration and different chip formation mechanism as found in previous chapter. It should be noted that the magnitude at proximity of 180^{o} is higher than that at 0^{o}, which is shown in both plots. This is probably due to the

reason of intact chips being removed by the tool at 180^o, while the tool just engages with material at 0^o and doesn't remove any of it until chips are formed.

The following figures plot the energy consumption in unit volume of material for both tungsten carbide tools and diamond tools. It clearly shows that at the entry and exit proximity, the energy consumed is much higher than that in the middle of revolution, especially at the exit proximity the energy consumption rises up exponentially. The order of magnitude can be 10 times higher for tungsten carbide tool as shown in Figure 5.23(a) and Figure 5.23 (b), which is a strong indication of the size effect due to the existence of relatively large cutting edge radius. However, the energy consumed in the middle of revolution doesn't change too much, and almost stays constant, as can be seen in both plots. This indicates that when chips are formed, the energy consumption in unit volume of material doesn't change a lot along with the cutting depth. Comparing the energy consumed with different tools; it is found that more energy is depleted using tungsten carbide tools, which is not only due to tool properties, but the large cutting edge radius.

As for straight flute cutting tools, the cutting force on unit area and energy consumption on unit volume of material are the same from the point of mathematical computation. Figure 5.23 also indicates the stress exerted on the tool, at around 180 °, the stress rises up quickly from 50GPa to 500GPa. Comparing it with the major properties of tungsten carbide tool, shear modulus of 274GPa, tensile strength of 344MPa and compression strength of 2.7GPa, we can see that although the force magnitude is small, the stresses the tool is exposed to are extremely big, this may explain the tool wear in micro-milling process. The constituent elements of tool are gradually removed in every revolution.

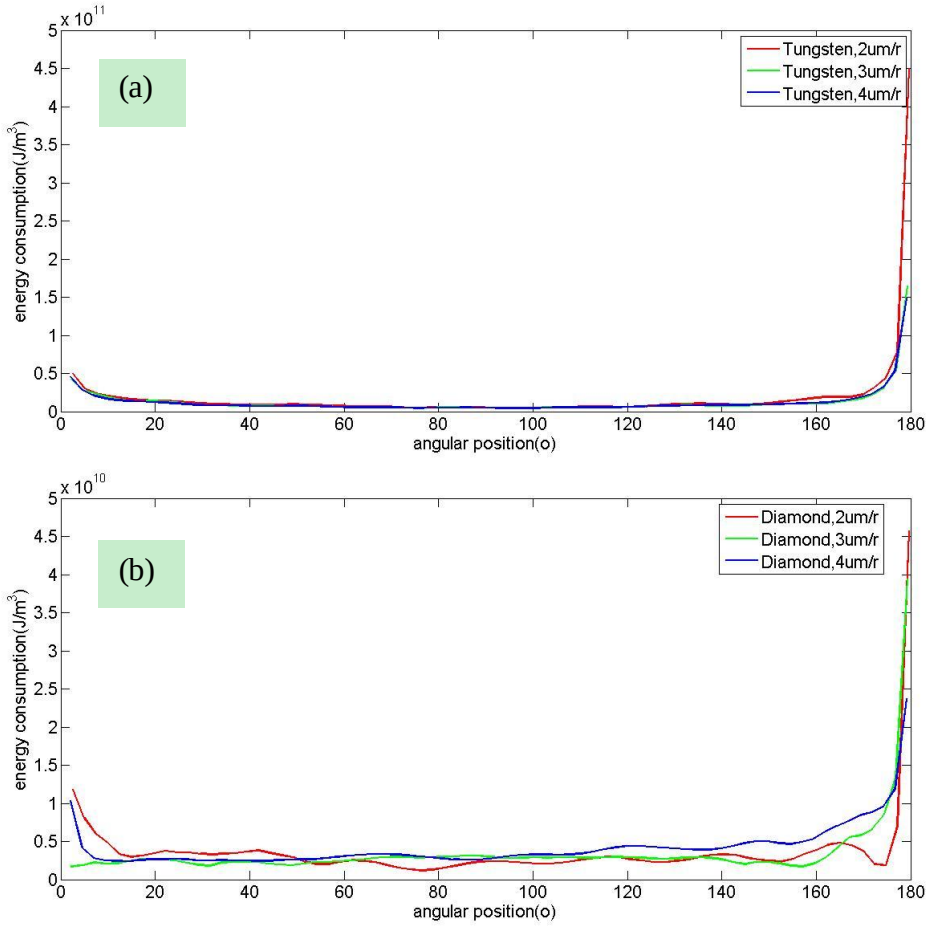

Figure 5.23 Energy consumption on unit volume at varied federate (a) tungsten carbide (b) diamond tool

The proposed model is applied to more general tools, i.e. tool with helix angle. For tungsten carbide tools with helix angle, the contact length at certain moment depends on the axial cutting depth and tool position angle. Since the tool is discretised in axial direction, the contact length can be approximated by considering the helix angle and axial depth of cut:

$$L = \sum_1^n d \times \tan^{-1}\beta \tag{5-53}$$

where d is the depth of incremental element.

The instantaneous volume of material can be approximated as follows:

$$V = S \times v \times dt \tag{5-54}$$

where v is the cutting speed and dt is the data sampling interval, S is the contact area, and it has following expression:

$$S = \sum_1^n (h(\theta,k) \times d \times \tan^{-1}\beta) \tag{5-55}$$

Experiments are carried out at wide range of feedrate from 1μm to 14μm per tooth, and results are shown in Figure 5.24 and Figure 5.25. It shows the force on unit cutting length has the similar form as the total resultant cutting force, which indicates

for such small depth of cut, the change of position angle caused by helix angle is not obvious. The energy consumption on unit volume of material shows that as the feedrate increases, the size effect becomes less and less obvious. At lower feedrates, the chip thickness at the proximity of entry and exit points is near to the cutting edge radius, however, the chip thickness at the same position angle at larger feedrates are much higher than the cutting edge radius, so the chips are formed quickly and the cutting energy consumed on unit volume of material decreases quickly and levels. It should be noted that as the feedrate becomes bigger, the energy consumed on unit volume of material, on the contrary, becomes less as shown in Figure 5.25. The zoom-in view shows that the difference among different feedrate also gets smaller. This finding indicates that once chips are formed, the bigger cutting depth, the less energy will be consumed on unit volume of material. The relation between them is not linear, which implies a sharper cutting edge will makes material removal easier from another aspect. Based on this finding, we can also predict that when tool wear occurs, the energy consumed on unit volume of material at same feedrate will increase due to more distinct size effect. The tool wear mechanism and its manifestation in cutting forces will be investigated in the latter chapter.

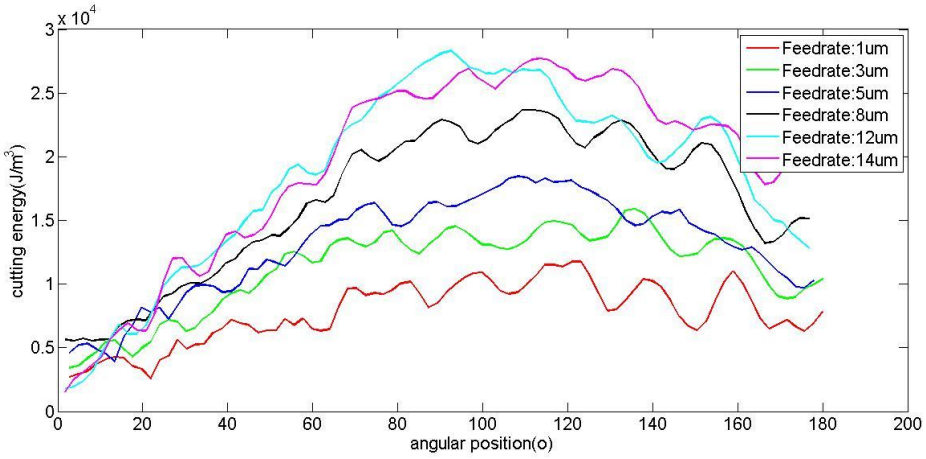

Figure 5.24 Cutting force on unit cutting length at varied feedrate

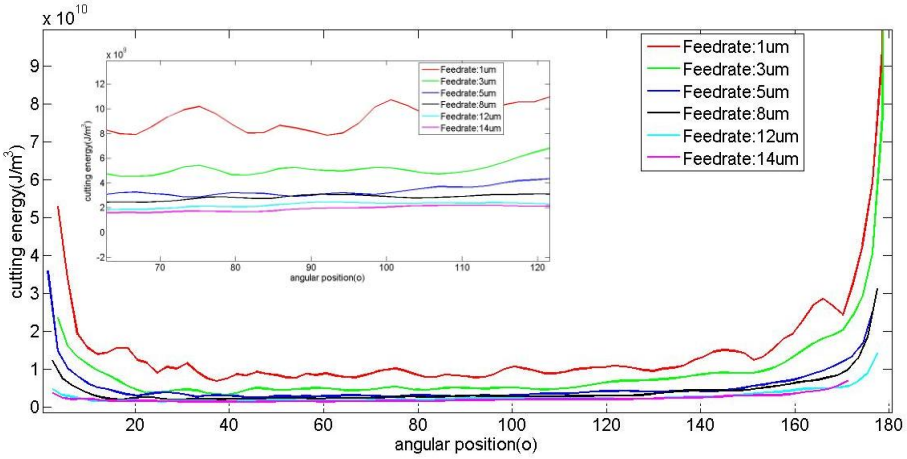

Figure 5.25 Energy consumption on unit volume of material at varied federate.

5.5 Surface generation in micro-milling

5.5.1 Tooling-workpiece system dynamics

In previous section, the cutting force prediction is based on the mechanistic model, it has good capability in estimating the static magnitude of cutting force; the model has the underlying assumption that both the tool and workpiece are rigid system, whereas in fact both of them act like spring-damper system under cutting conditions. Both the tool and workpiece will vibrate and deviate from the predicted tool trajectory which results in the fluctuation in the measured cutting forces. The tooling and workpiece system are schematically represented in Figure 5.26, the tool and workpiece vibration will change the real tool trajectory in machining, this section attempts to simulate the surface generation based on the real tool trajectory.

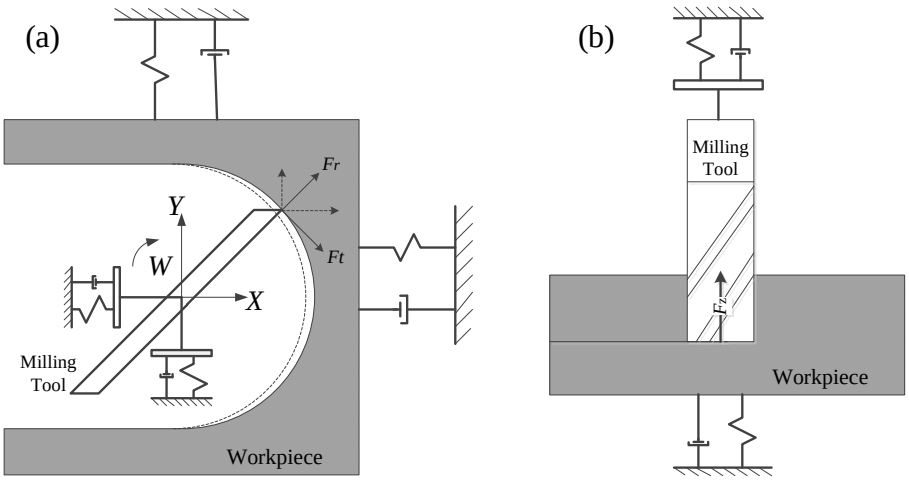

Figure 5.26 Schematic diagram of tooling and workpiece spring-damper system
(a) bottom view (b) side view

The relations between dynamic displacement and cutting force in x, y and z directions for tool and workpiece can be characterized approximately by the following transfer functions in Laplace form.

$$\begin{aligned}
\frac{x(s)}{F_x(s)} &= \frac{1}{m_x s^2 + c_x s + k_x} \\
\frac{y(s)}{F_y(s)} &= \frac{1}{m_y s^2 + c_{yt} s + k_y} \\
\frac{z(s)}{F_z(s)} &= \frac{1}{m_z s^2 + c_z s + k_z} \\
\frac{X(s)}{F_x(s)} &= -\frac{1}{M_x s^2 + C_x s + K_x} \\
\frac{Y(s)}{F_y(s)} &= -\frac{1}{M_y s^2 + C_y s + K_y} \\
\frac{Z(s)}{F_z(s)} &= -\frac{1}{M_z s^2 + C_z s + K_z}
\end{aligned} \tag{5-56}$$

where $M_{x,y,z}$, $C_{x,y,z}$ and $K_{x,y,z}$, $m_{x,y,z}$, $c_{x,y,z}$ and $k_{x,y,z}$ are the mass, damping coefficient and stiffness in each direction of the workpiece and tool respectively. As the tool has similar shape with axis-symmetrical bodies, thus the transfer functions of the tool in x and y directions are assumed identical. The minus sign in workpiece transfer function indicates the opposite displacement to the tool.

The transfer function of the workpiece in each direction can be obtained directly through hammer test by using the kistler hammer 9722A500 and capacitive sensor 5810, which can provide the excitation signal and capture the dynamic displacement, respectively.

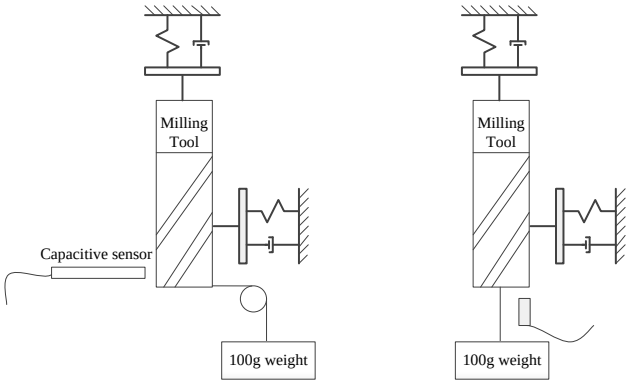

Figure 5.27 Determination of the transfer function of micro-milling tool

However, the hammer test can't be applied to the micro-milling tool, due to its tiny diameter and low resistance to impact. Instead of the sudden strike on the tool, a step signal is utilized. The signal is implemented by the sudden drop of a 100g weight as shown in Figure 5.27, which can approximately simulate 1N force signal. The transfer function in z direction is obtained with the same means.

Given the mechanistic model and transfer function of the tool-workpiece system, the static cutting force are calculated and then fed into the transfer functions, so we get the dynamic displacements at each time increments. The total displacement in each direction is the sum of the displacement of the tool and workpiece. It is superimposed to the calculated chip thickness, thus we can obtain the dynamic chip thickness and real tool trajectory in cutting. The simulation of the dynamic response of tool and workpiece is implemented in Matlab Simulink. The output tool trajectory then serves as the input to simulate the topography of the machined surface using the algorithm proposed by Ding (2011).

The surface generation has to take the edge radius into account, as it has direct effect on surface topography. The tool tip is approximated by two straight lines representing the main cutting edge and secondary cutting edge and an arc representing the edge radius. In simulation, the generated surfaces are the superstition of the tool profiles along the real tool trajectories and feed direction. Due to the edge radius, material elastic recovery is also accounted. The method is illustrated in Figure 5.28.

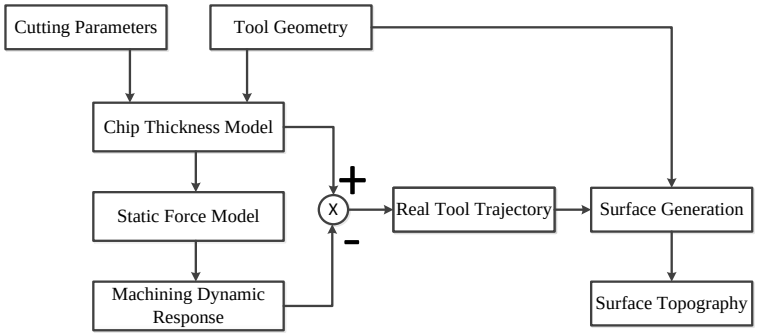

Figure 5.28 Machined surface topography simulation

5.5.2 Experiments and results

Experiment results are carried out with the diamond tool of 0.4mm in diameter and common tungsten carbide tool of 1mm in diameter with helix angle of 30°. The diamond tool, as mentioned previously, has very small cutting edge radius which can be ignored. The tungsten carbide tool has cutting edge of 3μm in radius. Spindle speed is set at 21,000rpm(66m/min) and 18,000rpm(56.5m/min), the feedrate is varied from 1μm incrementally to 4μm for diamond tool and 10μm for tungsten carbide tools. The machined surface topography is measured using Zygo white light interferometer.

The following set of figures show the machined topography at varied feedrates by different tools. It can be seen for diamond tool, on the left column, the tool marks are very clear compared to its counterpart machined by tungsten carbide tool on the right column. Only at bigger feedrates, the tool mark left by tungsten carbide tool can be shown, which indicates the strong influence of tool sharpness on surface generation.

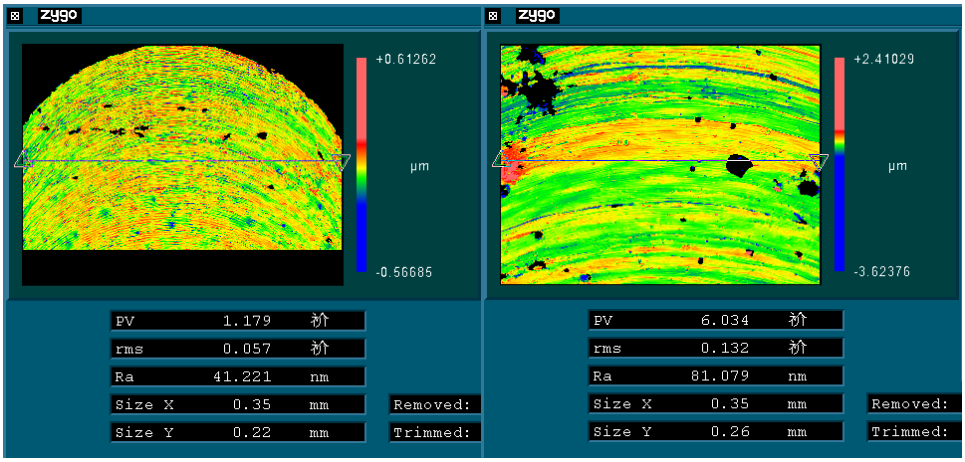

Feedrate (0.5µm/tooth)

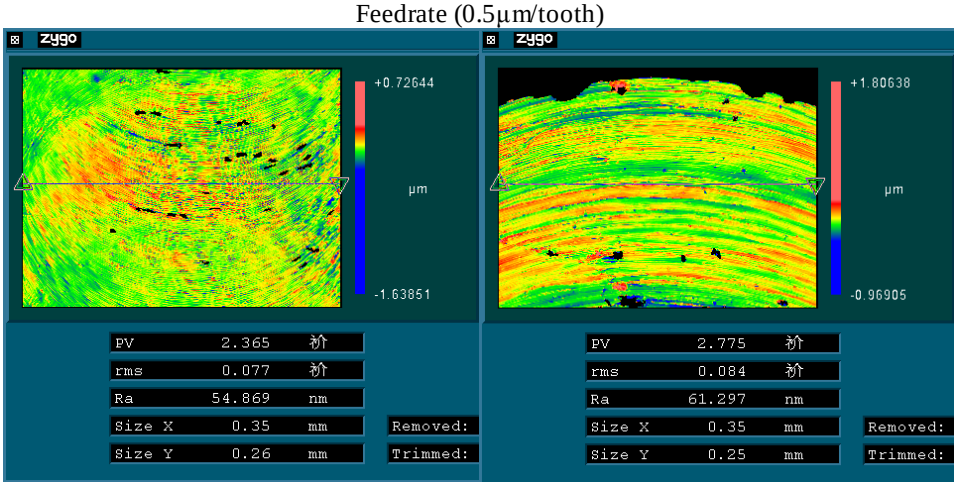

Feedrate (1µm/tooth)

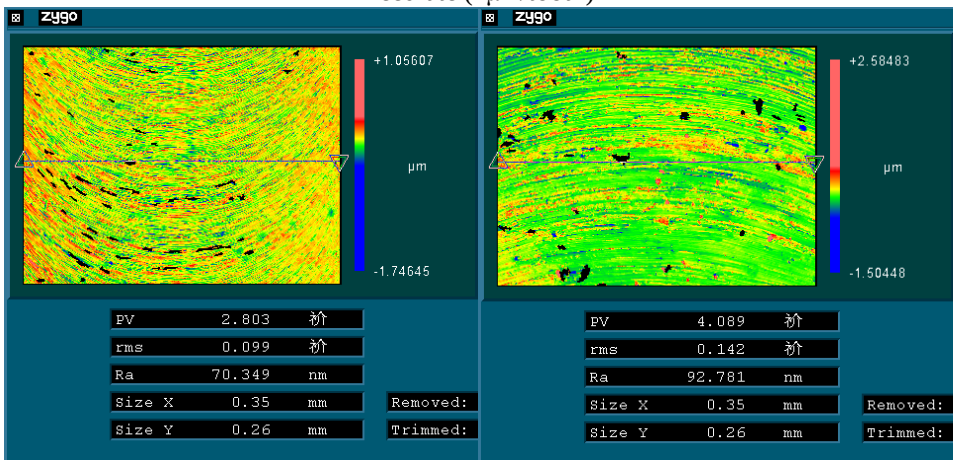

Feedrate (2µm/tooth)

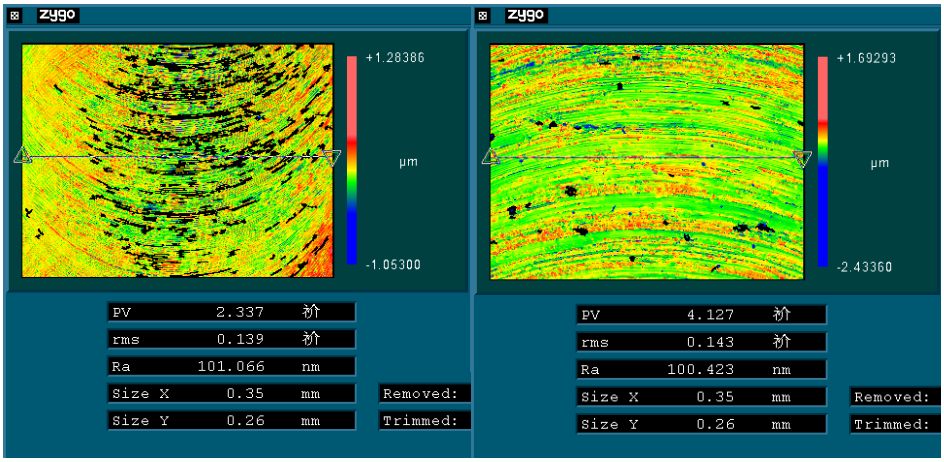

Feedrate (3µm/tooth)

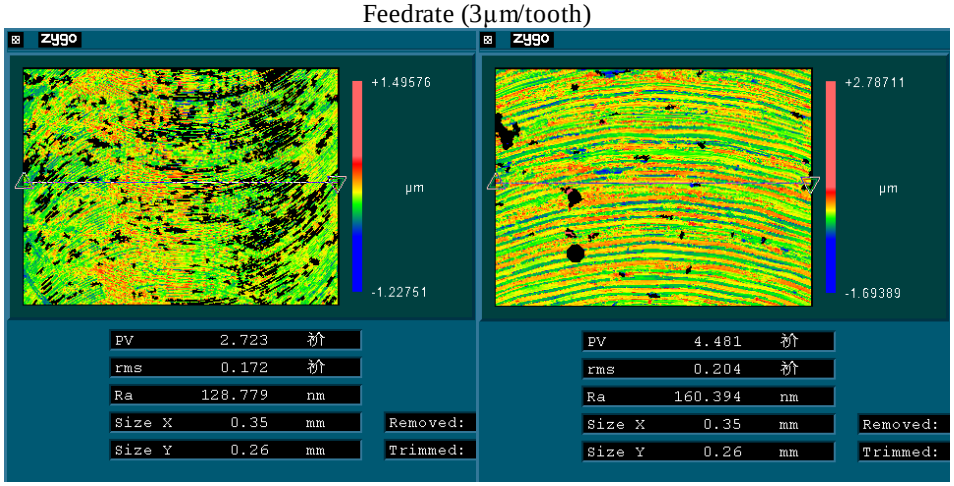

Feedrate (4µm/tooth)

Figure 5.29 Surface topography at varied feedrates (left: diamond; right: tungsten carbide)

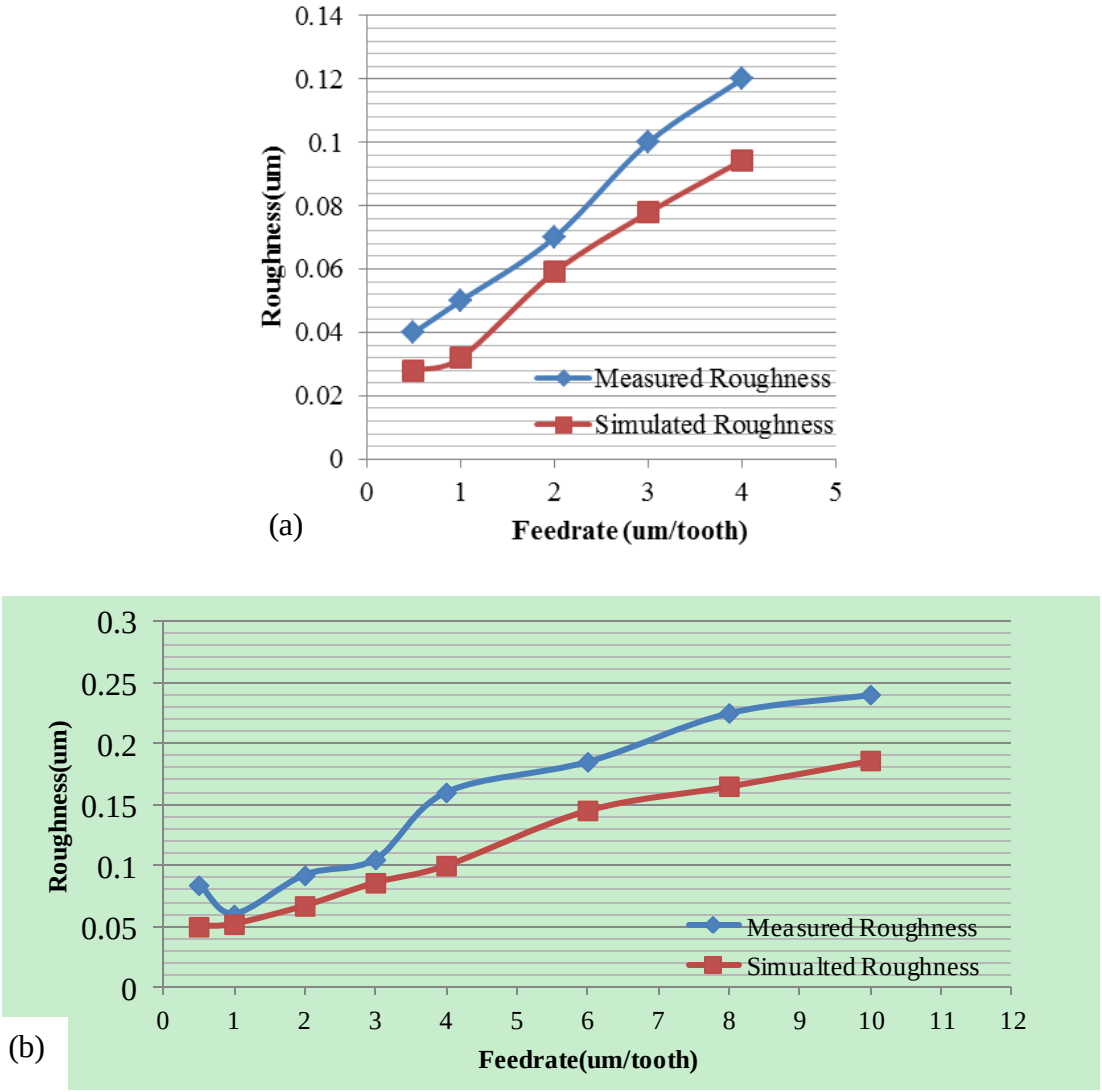

Figure 5.30 Comparison between the simulated and machined surface roughness
(a) diamond tool, (b) tungsten carbide tool

The differences between simulated and measured roughness for two tools are shown in Figure 5.30. The simulated surface roughness is slightly smaller than the measured roughness, this can be attributed to material properties and its interaction with tool, which is also the inability of the surface generation model, as it is built on the basis of tool geometry and its real trajectory. Material attachment and friction are not considered in the model. However, we can see that the differences are not big, and the tendency that surface roughness decreases as feedrate reduces is the same with experiment results. Another aspect is that the surface roughness machined by diamond tool is smaller than that produced by tungsten carbide tool.

For tungsten carbide tool, an exception is found at feedrate of 0.5μm/tooth, where measured roughness increases. Considering the comparatively large edge radius, this is probably due to the tool scratch and material squeezing under such small feedrate.

The measured and simulated surface topography is shown in Figure 5.31. It can be seen that in spite of the difference in roughness value, the simulated surface topography highly resembles the measured one; it successfully captures the tool mark left behind every revolution. The simulated figure presents much more regular topography compared to the measured, indicating the real surface generation is more complex process.

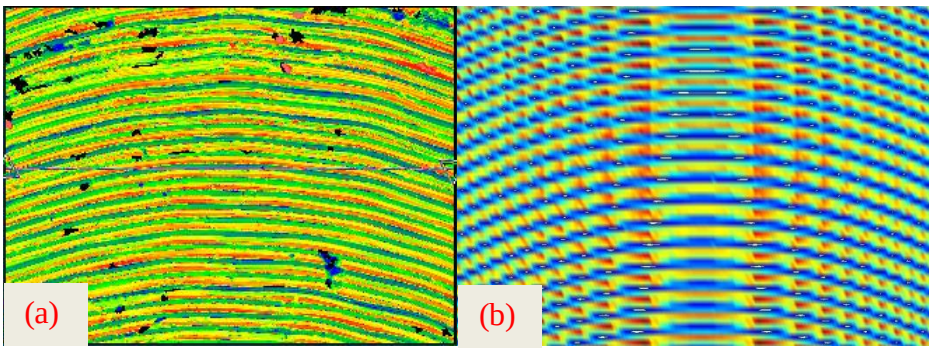

Figure 5.31 Surface topography at feedrate (10μm/tooth, tungsten carbide)
(a) machined surface (b) simulated surface

5.6 Concluding remarks

In this chapter, the micro-milling process has been analysed by cutting force modeling, experimental validation and surface generation. The conclusion can be drawn from several aspects.

A new model is proposed to calculate the instantaneous chip thickness in the workpiece coordinate system, taking tool runout into account; it shows the tool runout has changed distinctly the radius and cutting geometry of the tool. Besides, the minimum chip thickness found in previous chapter is also included in the new algorithm. The procedures and implementation of this new algorithm are presented.

Cutting forces in micro-milling are modelled from three angles including the cutting force on unit length, specific cutting force on unit area and energy consumption in unit volume of material. This model is proposed to help interpret the process under small cutting forces, as in micro-milling the absolute value of the cutting force won't help substantially understand the cutting mechanism.

Experiments are conducted to validate the cutting force model, from the proposed three different aspects. The method to determine tool runout is introduced. For cutting force measurement, a Kalman filter is applied to compensate the distortion in the cutting force signal due to the dynamic transmission characteristic of the tooling-

workpiece system. The application of Kalman filter proves useful in enabling accurate measurement of cutting force. Based on the compensated cutting force, the cutting force model is calibrated and proves good ability in predicting the cutting force. The cutting forces are analysed from the angle proposed by the new model.

Finally, the surface generation process is simulated based on the dynamic response of the tool and workpiece. The simulation successfully predicts the tendency of surface roughness and topography, although with slight difference due to limitation of the simulation process. Future work should include more factors to mimic the real surface generation process.

6. Cutting Temperature Partition in Micro-Milling

6.1 Introduction

Cutting temperature is of critical importance in investigating micro-milling process, as it has direct influence on material properties, cutting force magnitude, friction and tool wear mechanisms, surface generation and integrity and machining accuracy. Many researchers are concerned with the temperature field and its influence on cutting process. However, the cutting temperature and heat partition still remains a challenge for micro-milling process (Arrazola et al. 2013). Moriwaki (1990) studied the effect of cutting heat on the machined accuracy on copper component and found that even with small amount of heat generated, it can cause great expansion in the tool and result in poor machining accuracy. Kim (1999) conducted FEA simulation on material of OFHC copper at varied depth of cut and found that even at small depth of cut, the temperature rise in the local area can reach high temperature. It also suggested that the flow stress of material will be over-estimated if temperature is ignored, which can lead to twice higher in estimating cutting force. Lazoglu (2002) conducted both simulation and experiment research into this particular issue, and found that cutting temperature is a severe constraint on tool life.

Therefore, it is essential to gain a scientific understanding of the heat generation and temperature distribution in micro-milling process, especially on how it affects the material and tool properties and other process variables such the cutting force and friction etc. This chapter presents the simulation-based study on cutting temperature and heat partition in the micro-milling process, while focusing on the difference introduced by the significant cutting edge radius in micro-cutting.

6.2 FE-based simulation on micro-cutting temperature

Micro cutting is a very complex material removal process involving solid mechanics, fluid mechanics, thermodynamics, heat transfer, material science and tribology etc. most of the physics are strongly coupled and will affect each other, which further

complicate its understanding. For instance, temperature and material property are two fully coupled variables; material properties are strongly temperature-dependent, while in return, the change in material property alters the work done to remove chips away and subsequently the heat and temperature distribution. The thermal-mechanical interaction between tool and workpiece is constructed in simulation.

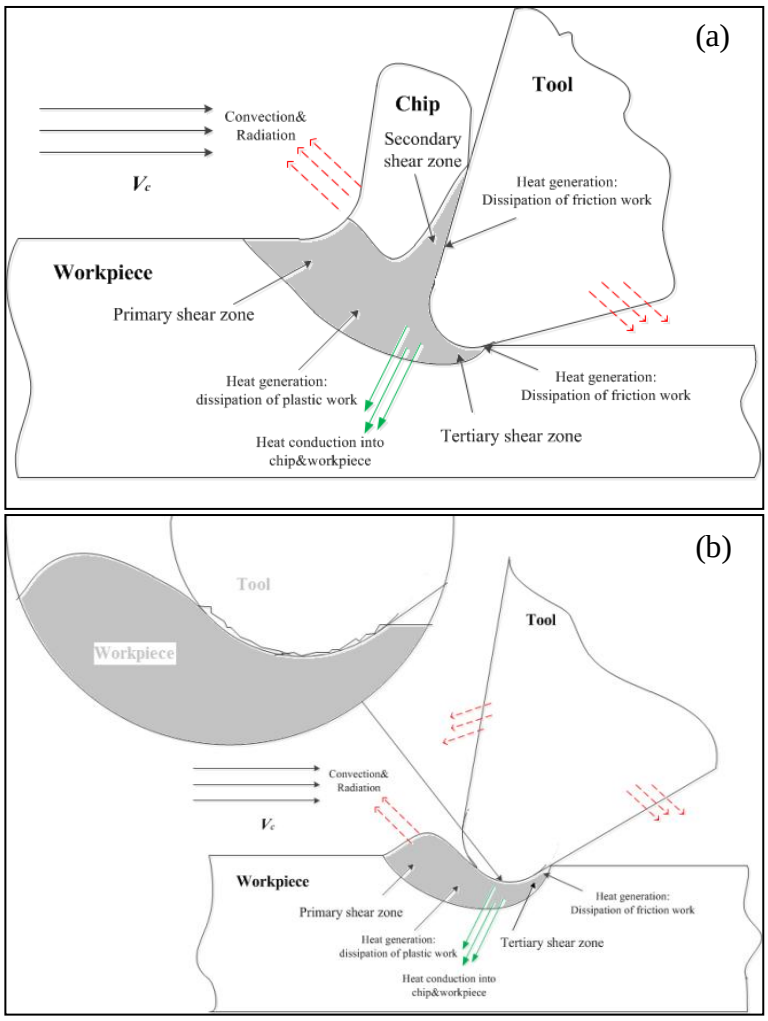

Figure 6.1 Orthogonal micro-cutting (a) heat transfer in micro-cutting with chip formation (b) heat transfer in micro-cutting without chip formation

Figure 6.1 shows micro-cutting taking place at different cutting regimes and the respective heat transfer process. It can be seen that due to the cutting edge radius, the three shear zones in conventional cutting are almost merged into one. There are mainly two heat sources, the dissipated work due to material deformation is assumed to convert into heat by 100%, and cause temperature rise in the chip and workpiece; the other heat source comes from the friction at the interface of chip and tool. The ambient temperature is assumed to stay constant during machining, thus part of the heat will lose to the environment owing to convection and radiation.

6.2.1 Heat transfer at the interface of tool and material

Figure 6.2 Tool-workpiece interface at the micro level

Figure 6.2 shows that the contact between tool and workpiece has very small gap instead of zero clearance, the relative movement between the two results in friction-caused heat, and conducted between the two surfaces.

Heat flux at the interface can be formulated as following:

$$\begin{cases} -\mathbf{n}_d * (-k_d \nabla T_d) = -h(T_u - T_d) + rQ_{fric} \\ -\mathbf{n}_u * (-k_u \nabla T_u) = -h(T_d - T_u) + (1-r)Q_{fric} \end{cases} \tag{6-1}$$

k_d and k_u are conductivities of the downside and upside surface respectively; r is the heat partition rate; h is the joint conductance, which is comprised as

$$h = h_c + h_g + h_r \tag{6-2}$$

h_c is the constriction conductance calculated by Cooper-Mikic-Yovanovich (CMY) Correlation

$$h_c = 1.25 \frac{2k_u k_d}{k_u + k_d} \times \frac{m_{asp}}{\sigma_{asp}} \left(\frac{p}{H_c}\right)^{0.95} \tag{6-3}$$

where k_u and k_d are upside and downside surface conductivities, respectively; m_{asp} and σ_{asp} are parameters to describe surface asperities. p is the contact pressure at the interface; H_c is the micro hardness of softer material of the two contacting surface.

h_g is the gap conductance, as interstitial fluid. In the simulation it is air and cannot be neglected due to high contact pressure;

$$h_g = \frac{k_g}{Y + \alpha\beta \frac{k_B (T_u + T_d)}{2\sqrt{2}\pi D^2 p_g}} \tag{6-4}$$

α is the contact thermal accommodation parameter, β is a gas property parameter, k_B is the Boltzmann constant, D is the average gas particle diameter, p_g is the gas pressure, T_u and T_d are temperature of the two contacting surfaces. h_r is the radiative conductance.

$$h_r = \sigma \frac{\varepsilon_u \varepsilon_d}{\varepsilon_u + \varepsilon_d - \varepsilon_u \varepsilon_d} (T_u^3 + T_u^2 T_d + T_u T_d^2 + T_d^3) \tag{6-5}$$

ε_u and ε_d are surface emissivity. Frictional heat is portioned at the interface according to Charron's relation (Issa et al. 2011)

$$r = \frac{1}{1+\sqrt{\frac{\rho_u C_{p,u} k_u}{\rho_d C_{p,d} k_d}}} \tag{6-6}$$

where $C_{p,u}$ and $C_{p,d}$ are heat capacity of upper and down surfaces. Besides, the heat is also released to environment by convection due to workpiece movement; radiation from the tool and workpiece also causes energy loss to the environment.

6.2.2 Simulation results and discussion

The simulation setup is explained in session 4.2.1, workpiece material is aluminium 6082; tools are made of diamond or tungsten carbide with varied edge radius. Simulation is carried out at varied cutting speed and depth of cut.

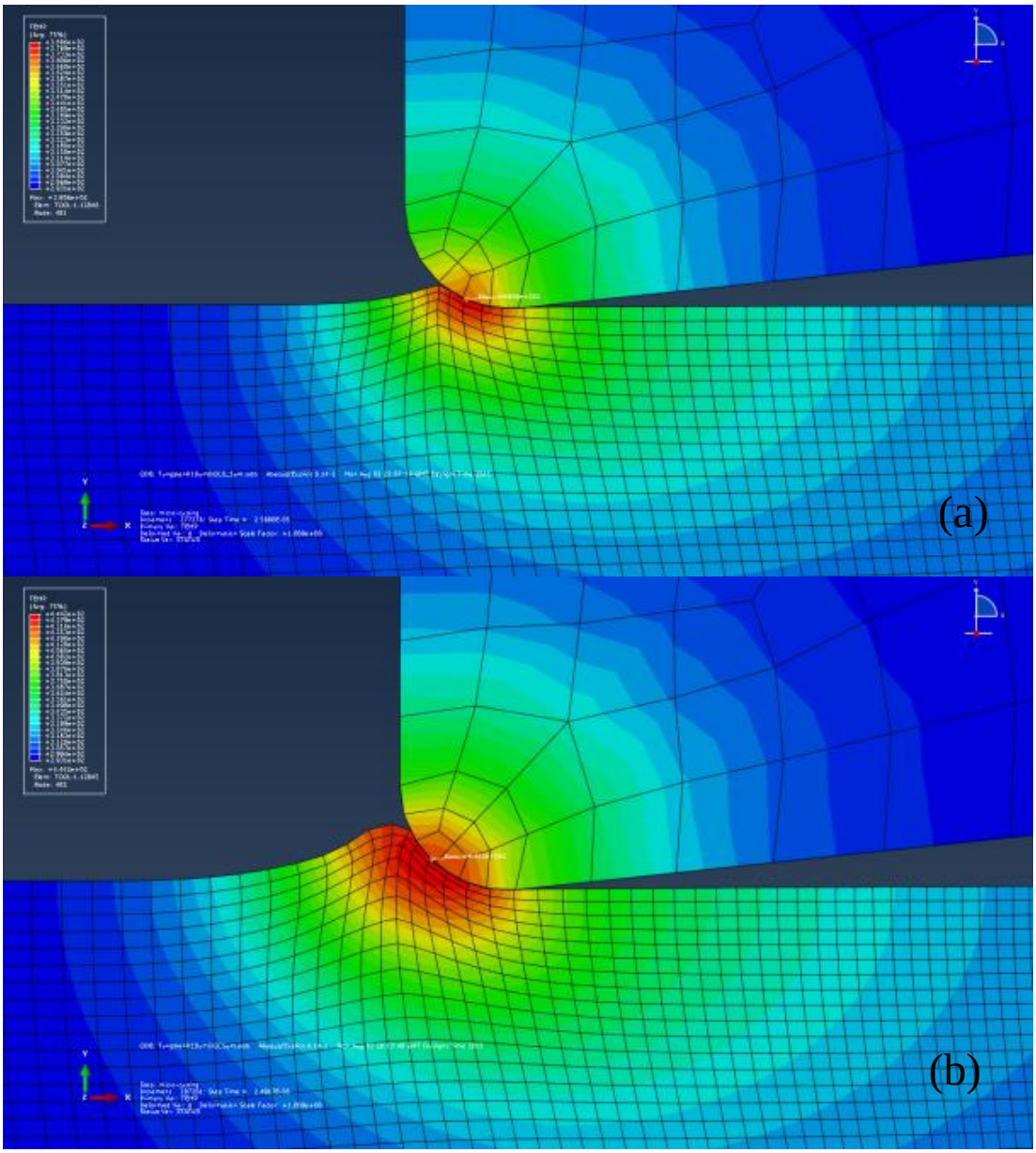
(a)
(b)

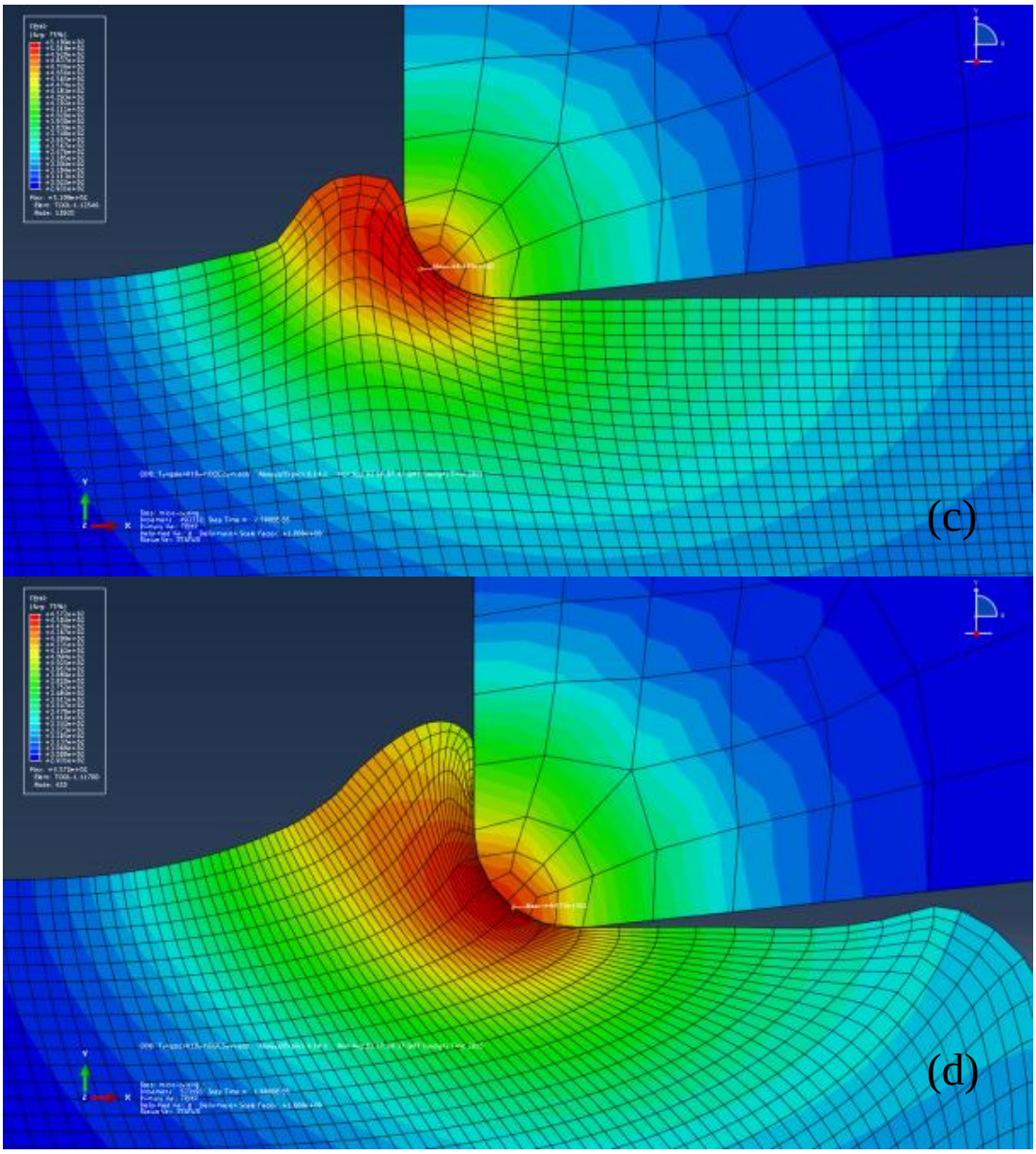

Figure 6.3 Cutting temperature distribution at varied ratio of cutting depth to edge radius
(a) 1/20 (b) 1/10 (c) 1/5 (d) 1/2

The above figure shows the temperature distribution at varied depth of cut using the tungsten carbide tool with 10μm of cutting edge radius, the cutting length is the same. It can be seen that the highest temperature in the material always occurs near the rounded edge. It should be pointed out that the positions are not where the bigger plastic deformation takes place, which is always along the edge radius in the simulation. The highest temperature in the tool always occurs on the rounded edge. Considering the two heat sources in machining, the highest temperature in the material is determined by the conduction of heat generated by plastic deformation

and part of the heat generated by friction at the interface. The temperature is purely determined by the heat flux from conducted from the interface of tool and workpiece.

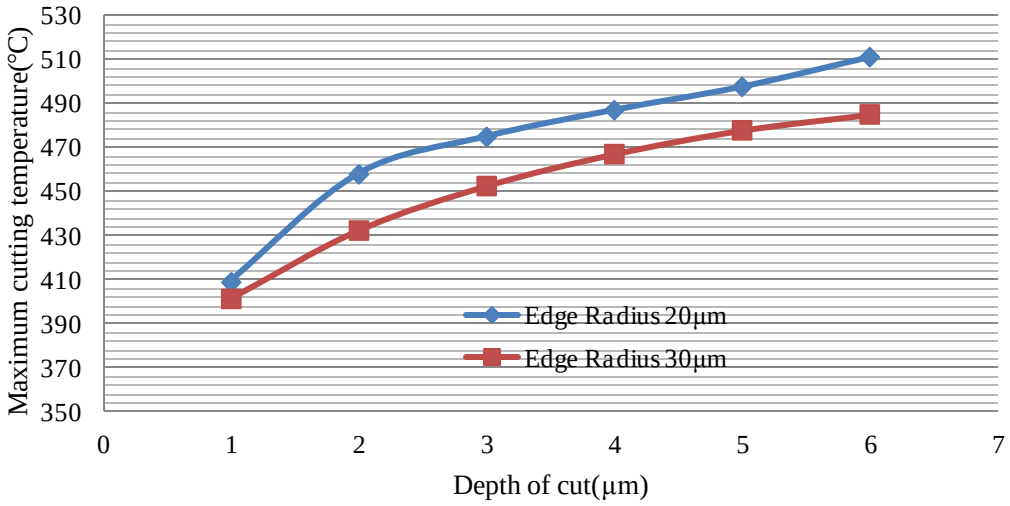

Figure 6.4 Maximum cutting temperature at varied depth of cut

The above figure shows the maximum temperature in the material with tools of different cutting edge radius, it's interesting to notice that the maximum temperature obtained with larger edge radius is lower. One possible explanation is that at same depth of cut, the tool with larger edge radius results in small plastic deformation, as the ploughing effect becomes more dominant. In this case, less heat is generated as the less material deformation takes place.

Figure 6.5 compares the equivalent plastic strain during machining at the same depth of cut. It can be seen that the maximum plastic strain with tool edge radius of 20µm is 4.26, while it is 3.125 for tool with cutting edge radius of 30µm, which means less deformation generated and ploughing is the dominant factor. The Figure 6.6 shows the total energy density in each element due to plastic deformation. It can be seen that the value of plastic dissipation energy with smaller cutting edge radius is 459, while that for the tool with larger cutting edge radius is much smaller, 281. Thus this finding proves the above speculation.

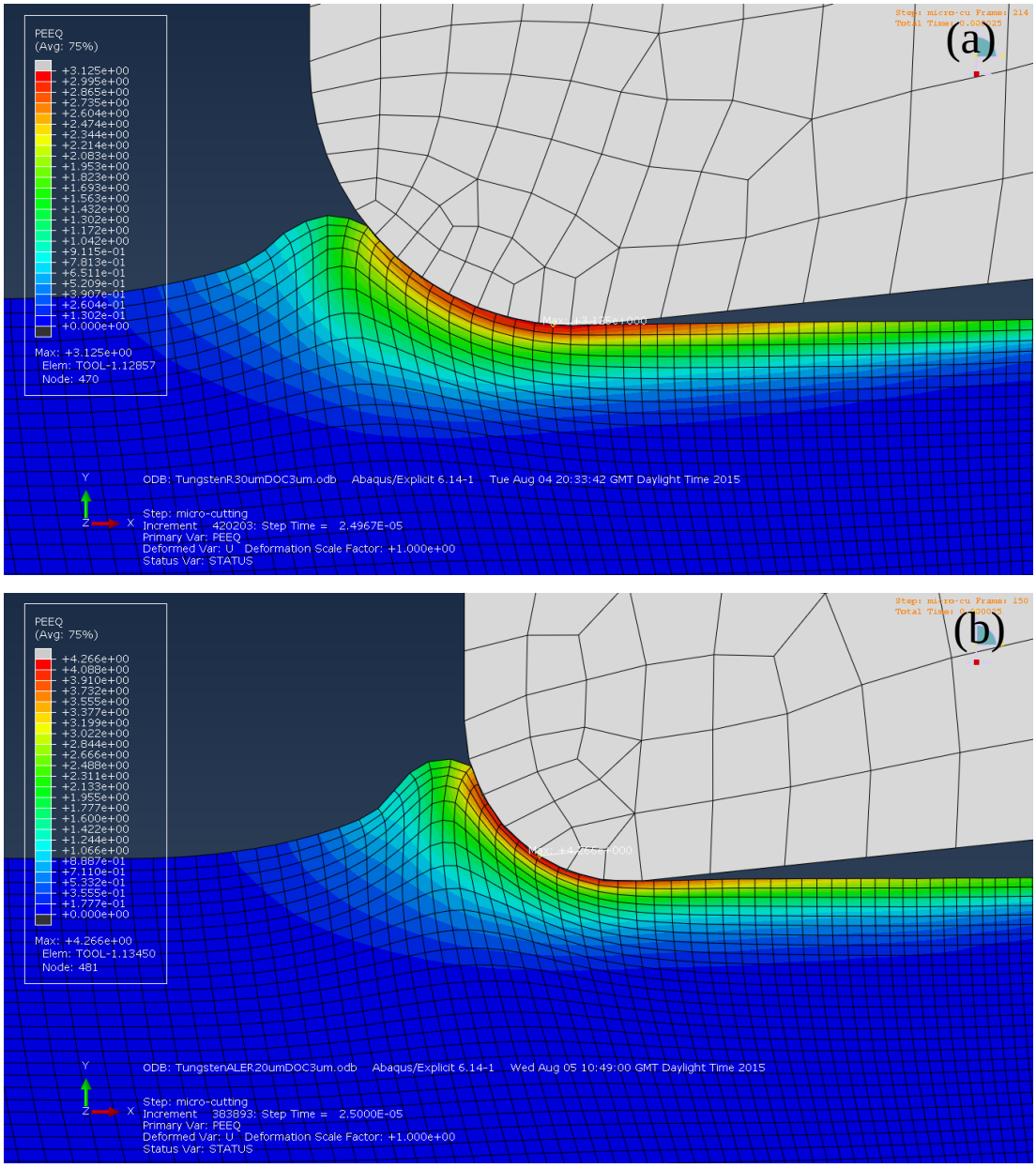

Figure 6.5 Equivalent plastic strain at the same depth of cut

(a)edge radius:30μm (b)edge radius20μm

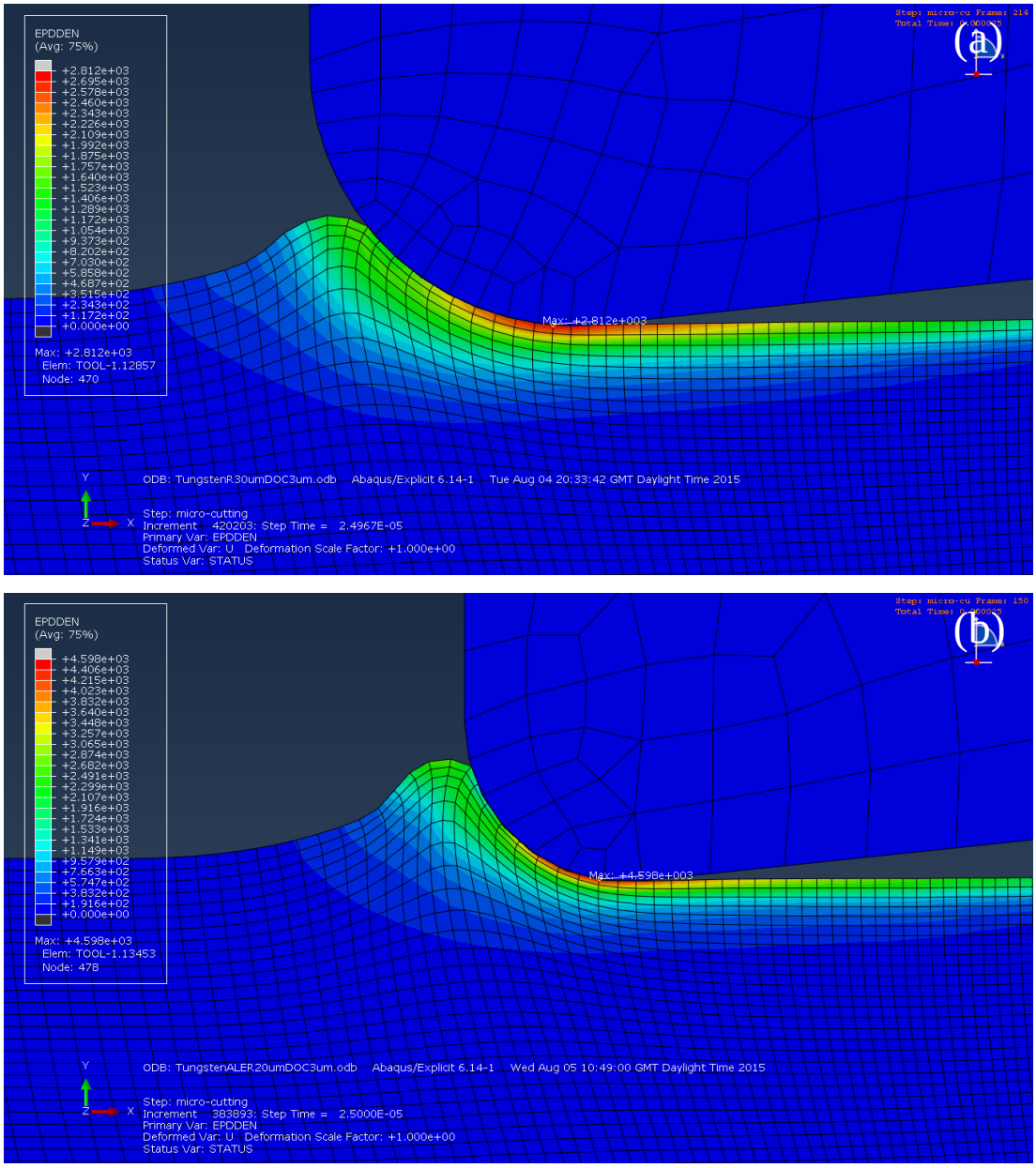

Figure 6.6 Total plastic dissipation energy density in each element

(a) edge radius:30μm (b) 20μm

6.3 Concluding remarks

This chapter presents the simulation-based study on cutting temperature and heat partition in the micro-milling process, while focusing on the difference introduced by the significant cutting edge radius in micro-cutting. Results show that the highest temperature in the material always occurs near the rounded edge. The highest temperature in the tool always occurs on the rounded edge. The highest temperature in the material is determined by the conduction of heat generated by plastic

deformation and part of the heat generated by friction at the interface. The temperature in the tool is purely determined by the heat flux from conducted from the interface of tool and workpiece.

7 Tool Wear and the Machining Process Optimization

7.1 Introduction

Tool wear is a critical research aspect in micro-milling process. Excessive tool wear can seriously deteriorate the quality of machined geometry directly, it can also lead to other defects such as poor surface roughness and surface integrity, the latter includes residual stress, micro-hardness, cracks and scratches, which will affect the serving life of machined components.

Tool wear in micro-milling, due to the tool's small geometrical features, exhibits different tool wear mechanism compared to that in the conventional milling process. So tool wear types in the micro-cutting process should be firstly investigated and properly characterized. Magnitude of the tool wear on axial direction should also be quantified via feasible techniques available in lab environment. This chapter aims to develop an engineering feasible approach to assess the tool wear and predict the tool wear in-process through continuous monitoring of some decisive parameters by modeling and related analysis.

7.2 Experimental setup

Two methods can be applied to measure tool wear, direct method and indirect method. Director methods refer to techniques able to give deterministic magnitude of tool wear in terms of micrometers or nanometers; while indirect methods imply that record of wear-influenced signals such as forces, acoustic emission, surface roughness and burrs height. Through particular analysis technique based on these signals, tool wear can be modelled and predicted.

The online tool length and its variation are measured using the laser system mounted on the machine as shown in Figure 7.1, and the offline tool length, the tool wear form and types are measured and categorized by the TESA-200 machine. Cutting force

and surface roughness can also give information on tool wear status. Frequency and wavelet-based analysis will be utilized to interpret the tool wear process.

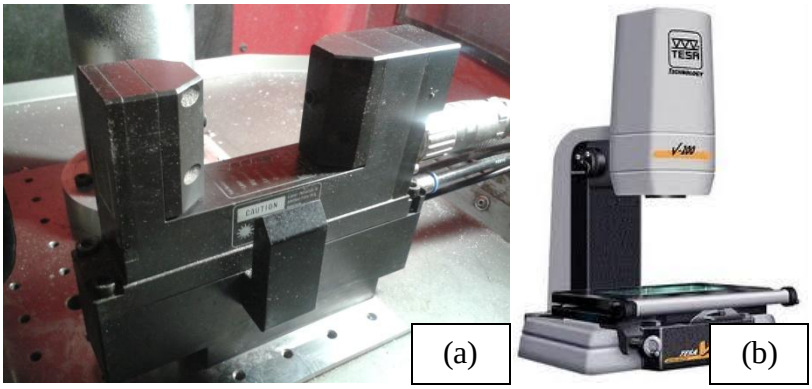

Figure 7.1 Equipment used for in-process and offline measuring of tool wear (a) Laser measuring system (b) Optical microscope TESA-200

Key equipment used for in-process and offline measuring of tool wear is shown in Figure 3.17. Two workpieces are utilized, the first one serves as the artefact to wear the tool, while the other one functions as the media, reference workpieces as what we called, to record signals and enable visual inspection via optical microscope and whitelight interferometer for information related to tool wear.

A two-fluted square end mill with diameter of 1mm was used (Tool Number: SGS 41505). Cutting parameters involved are listed:

Spindle speed: 22,000rpm(cutting speed: 70m/min)

Federate: 200mm/min

Depth of Cut (DOC): 50 μm

Cross-feedrate: 500 μm

One surface area of 70mm×100mm is machined with an average machining time of 10min with pre-listed parameters. Tool length was measured both before and after machining to detect if any wear happened using laser beam measuring system fixed on machine. After each surface finished, a slot was milled on the reference workpiece with force and acoustic emission signals recorded simultaneously. Most importantly, the slot was machined with identical parameters. Then the tool was put under optical microscope to inspect tool wear conditions and measure magnitude of wear in various directions. In total, 11 surfaces were machined and 12 sets of corresponding signals are collected through the acquisition system.

7.3 Tool wear characterization

7.3.1 Tool wear types

In conventional milling process, the tool mainly wears in two forms, i.e. abrasive wear, adhesive wear. Tool edge chipping is another aspect which causes tool failure.. However, in micro-milling process, according to our observation, tool wear usually appears in forms of abrasive wear on the bottom face and edge chipping on the tool edges. Figure 7.2 shows the geometry and morphology of a new tool.

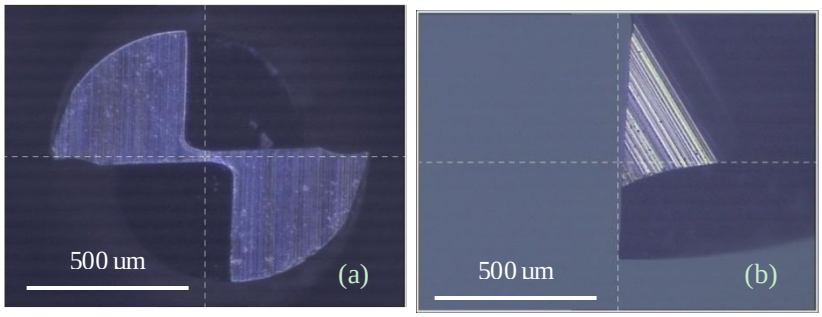

Figure 7.2 Geometry of a new micro-milling tool (SGS41505) (a) bottom face (b) rake face

It can be seen that the two-fluted milling tool is not flat on the bottom, the position at the tool center is slightly shorter than tool tip, the angle roughly is at 87^{o}. The depth of the center measuring from tool tip along axial direction is about 30 µm. Bearing this in mind, when tool wear exceeds this value, the tool should be regarded as seriously worn and not be used any more. But for research interest, tool performance and tool wear mechanism beyond this value are also investigated here.

Figure 7.3 shows the tool wear conditions after 10 minutes (3 meters) machining. At this stage, tool wears in the form of abrasive wear due to the friction on the bottom face between tool and workpiece. Cutting edge still possesses the sharpness to split materials. The tool length, according to optical measurement, has reduced by 20 µm.

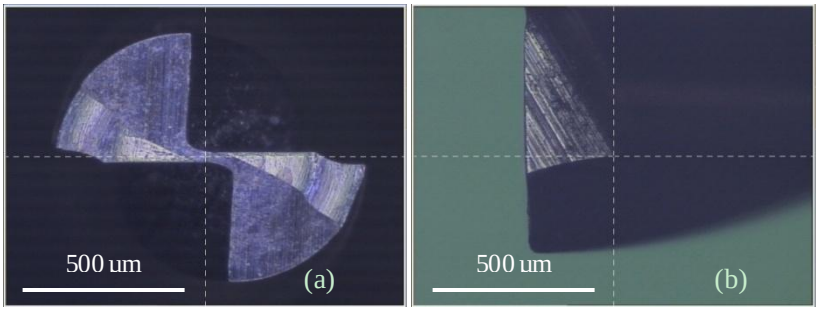

Figure 7.3 Step 1: tool wear after machining 3 meters in distance
(a) tool wear on bottom face (b) wear on rake face

Figure 7.4 exhibits the tool wear conditions after 20 minutes (6 meters) machining. It can be seen that at this stage of tool wear, the reduction in length direction has exceeded 30 μm which we defined as the threshold. From the figures, the exterior cutting edge wears more quickly than tool center, it is attributed to the existence of clearance angle in tool geometry, another reason is the cutting speed at the exterior is much larger compared to that in the centre. The tool wear is measured to be 34 μm in axial direction. Further inspection of the cutting edge shows that, from this moment on and afterward, edge chipping on tool edges starts to appear, as shown in Figure 7.5. Considering the machining process, when the tool wears on the bottom face, contact area between tool and workpiece are increasing, so is the cutting force exerted on the cutting edge. And also due to the nature of milling process, the forces are cyclically loaded on the cutting edge which could lead to its fatigue fracture. These are merely initial speculations which still need to be further investigated in future.

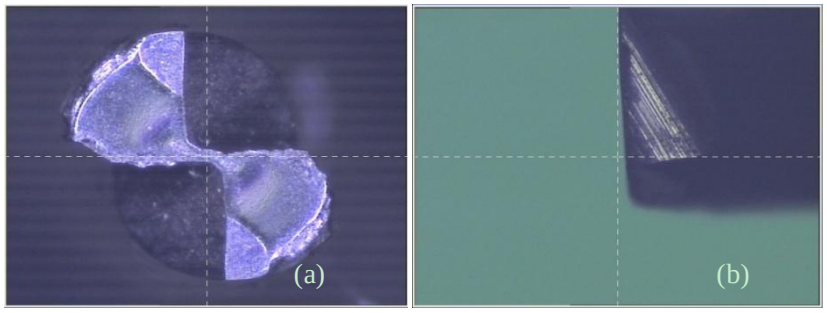

Figure 7.4 Step 2: tool wear after machining 6 meters in distance(a) bottom face (b) rake face

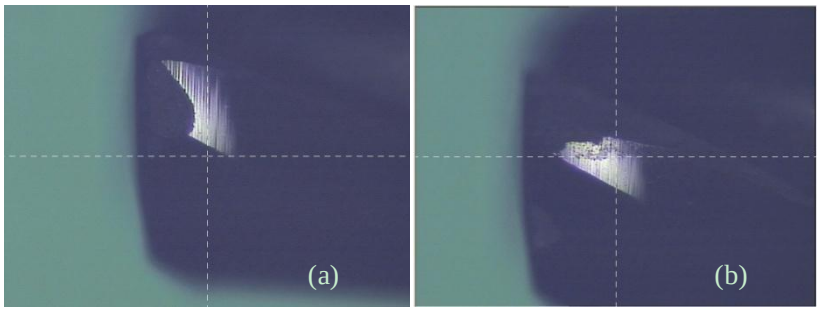

Figure 7.5 Edge chipping on two flutes

Later inspection of tool condition shows that no additional type of tool wear is discovered. Figure 7.6 depicts the tool wear progress throughout the 11 machining iterations.

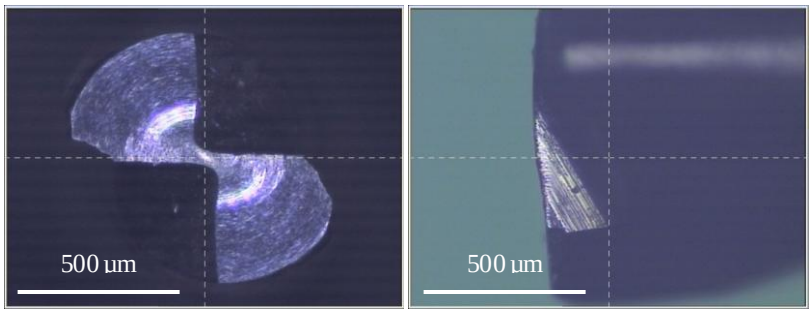

Step3/30mins/9meters

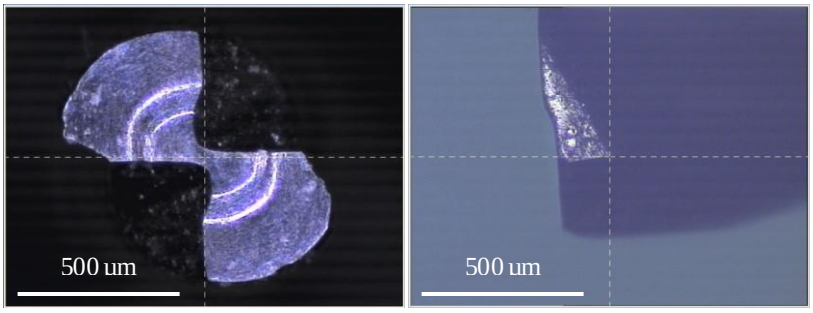

Step4/40mins/12meters

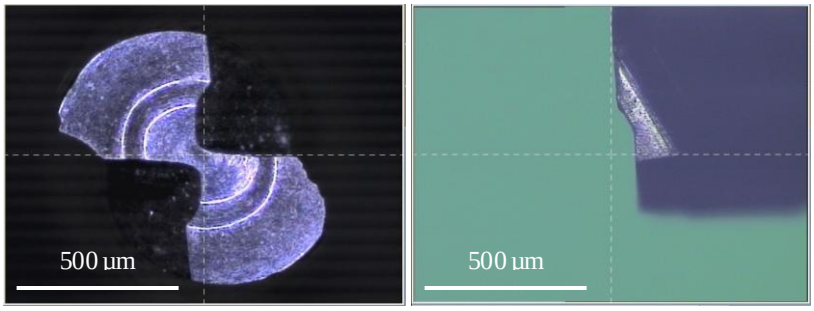

Step5/50mins/15meters

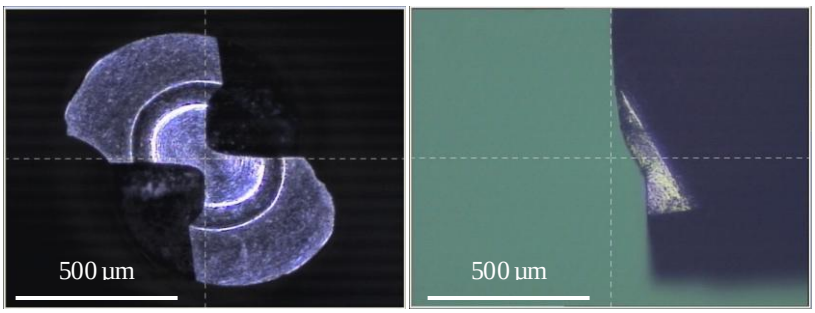

Step6/60mins/18meters

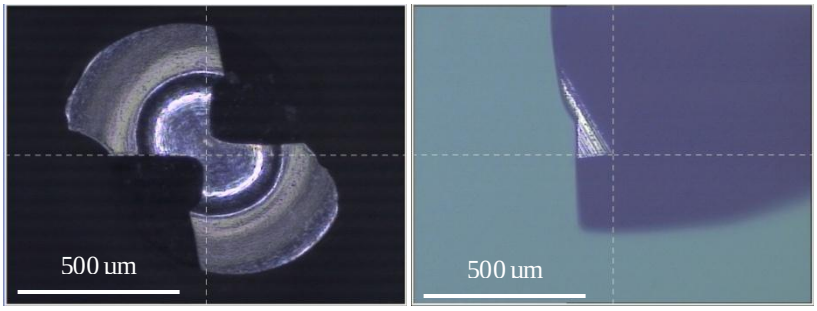

Step7/70mins/21meters

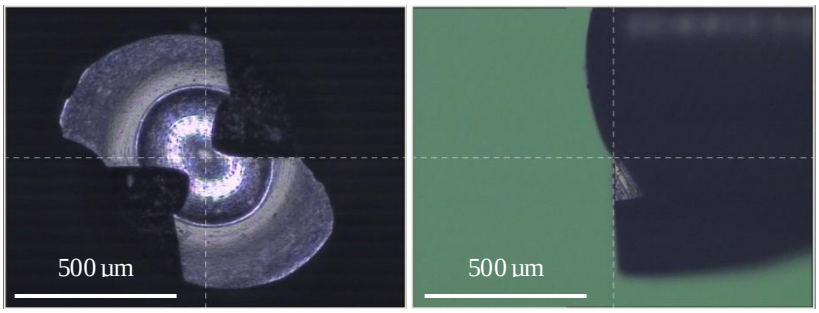

Step8/90mins/27meters

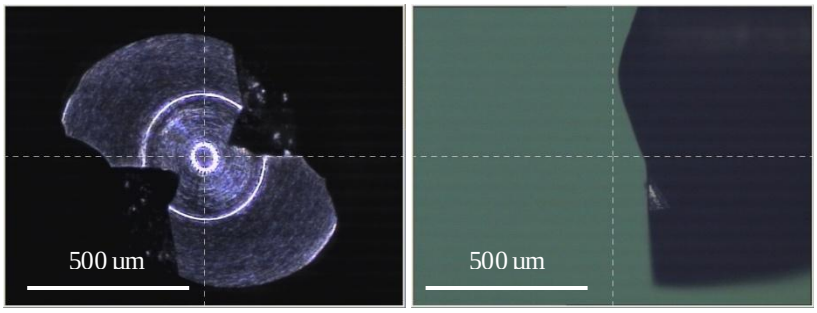

Step9/110mins/33meters

Figure 7.6 Tool Wear Progress

Based on above figure depicting tool wear, we can speculate its process. Firstly, due to direct contact with material, wear on bottom face appears first, as shown in Figure 7.3. After 20 mins machining, due to repetitive cyclic loads on cutting edges, cutting edges fracture and chip due to fatigue while bottom face withstands frictions and undergoes abrasive wear, as displayed in Figure 7.4Figure 7.5. When tool continues wearing, tool material at exterior diameter wears more quickly than that at tool center, as shown in Figure 7.6/step3 and 4. And this leads to generation of hump at the tool center, during later machining, the tool wear in two directions, its length reduces in axial direction and the hump gradually decreases in size towards the shape displayed in Figure 7.6/step 9.

7.3.2 Tool wear measurement

Tool wear magnitude is measured using the optical microscope. The laser beam system is used to measure the changes in tool length before and after machining, and the optical microscope is able to measure the magnitude of tool wear off-line. The measured tool wear magnitude in axial direction is shown in Table 7-1.

Table 7-1 Magnitude of tool wear by TESA200

Machining time(mins)	Tool wear(μm)	steps
10	17	1
20	15	2
30	14	3
40	5	4
50	8	5
60	8	6
70	6	7
90	8	8
110	20	9
Total	101	

It can be seen that from the table at the initial stage, the tool wears quickly, after around 30mins machining, the wear rate drops to small range and holds almost constant until the tool are seriously worn and wear rate increases to another high level. This finding is consistent with the wear model discovered in conventional cutting process.

7.4 Fourier and wavelet analysis on tool wear

7.4.1 Frequency analysis on cutting forces

As tool wears, it will directly change the contact behavior between the tool and workpiece. Tool wear on the bottom face changes the material removal mechanism from cutting to rubbing and ploughing which need more power and could generate more heat, and inversely accelerate the tool wear process. Rounded and chipped edge could change the chip load on each flute due to more material pushed beneath the cutting edge. These changes inevitably cause influence on cutting force. It is collected and analyzed at different stages of tool wear process.

The model proposed in chapter 5 is utilized to interpret the tool wear process; as the tool wears, energy consumption increases. The following table and figure show the average cutting energy consumption in each direction in each cycle. It can be clearly seen that the energy consumed increases rapidly for the first 3 steps and then drops significantly at the 4^{th} and 5^{th} step before it gradually increases again. Associating the plot with the tool wear in Figure 7.6, we can find that after 3 steps, the minor cutting edge has been completely worn, and the perimeter of the tool is even shorter than the

center. The rapid increase in the first 3 steps can be explained by the increasing contact area between the tool's clearance face and the material. The minor cutting edge has an clearance angle of 10 °, as the tool wears firstly at the perimeter, the contact area increases thus make the friction increase, in return, the energy required to overcome this are improved.

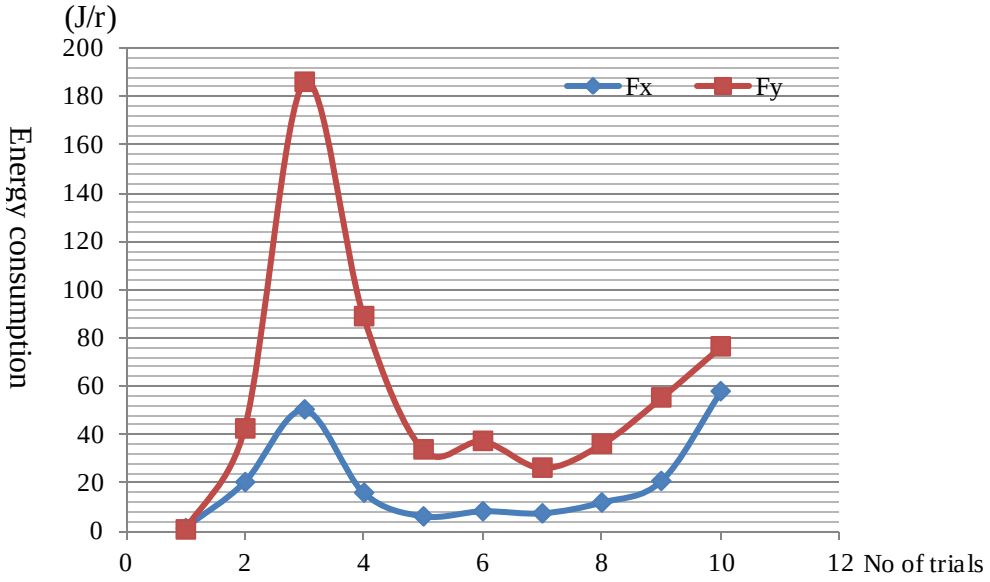

Figure 7.7 Average energy consumption in every revolution

Frequency analysis is adopted in interpreting these force signals which is able to provide in-depth understanding of this physical process of tool wear. Firstly, Fast Fourier Transform is implemented on each signal of the 10, and PSD spectrums are obtained. Power spectral density (PSD) describes how the power of a signal is distributed over the different frequencies. Then by careful inspection of PSD spectrums, a series of characteristic frequencies are identified. On these frequencies, the magnitude of PSD changes in a way that is closely related and proportional to the magnitude of tool wear. Once these frequencies are determined, a plot showing the evolution of PSD value on each frequency can be drawn. In-depth analysis based on these plots will give reasonable physical explanation to the changes of PSD value and tool wear process.

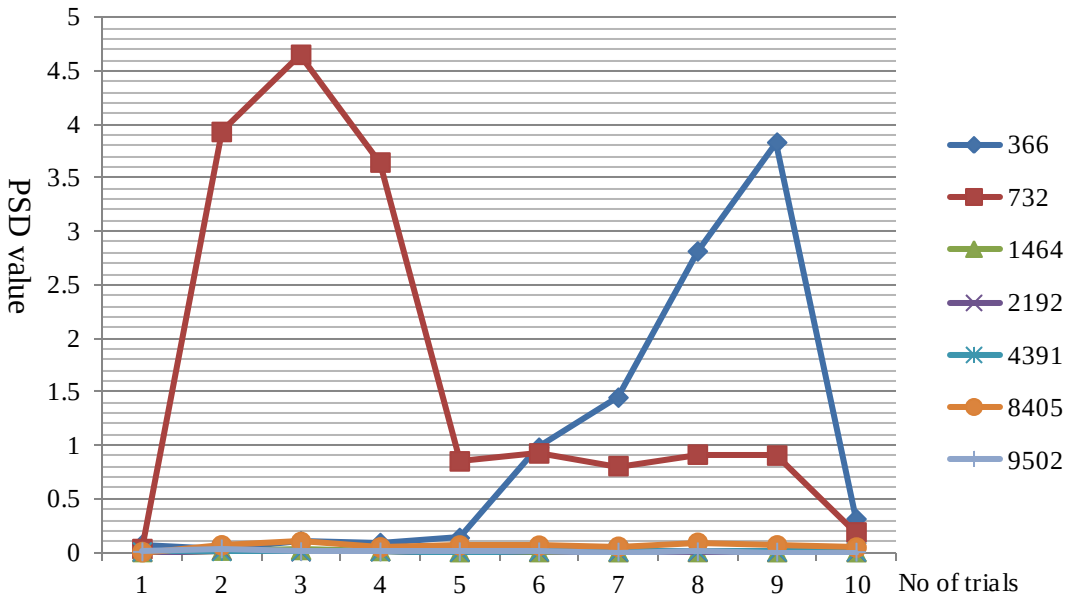

Figure 7.8 PSD evolution in x direction

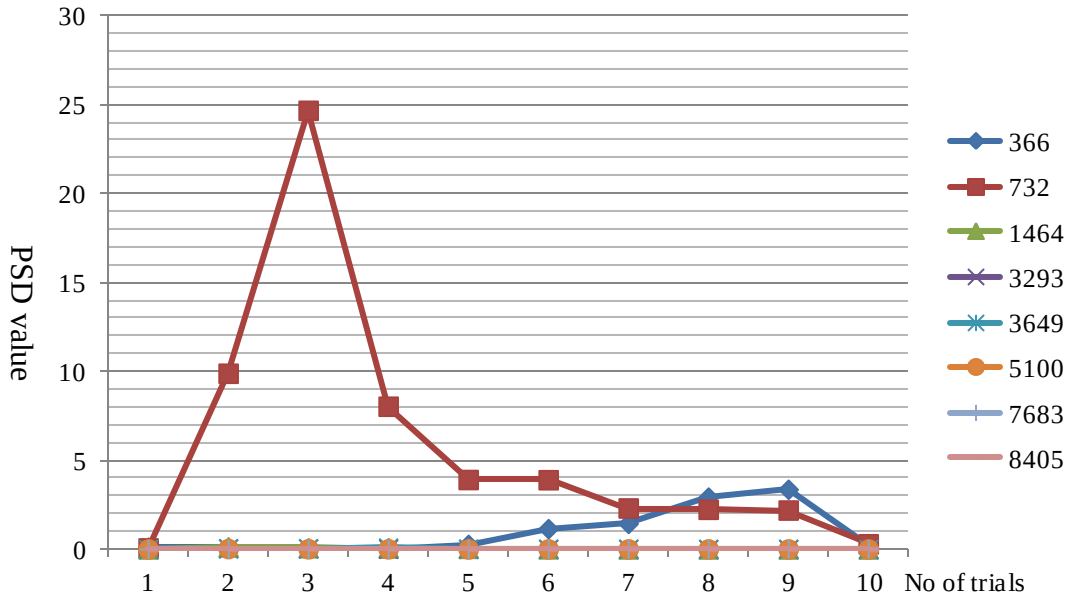

Figure 7.9 PSD evolution in y direction

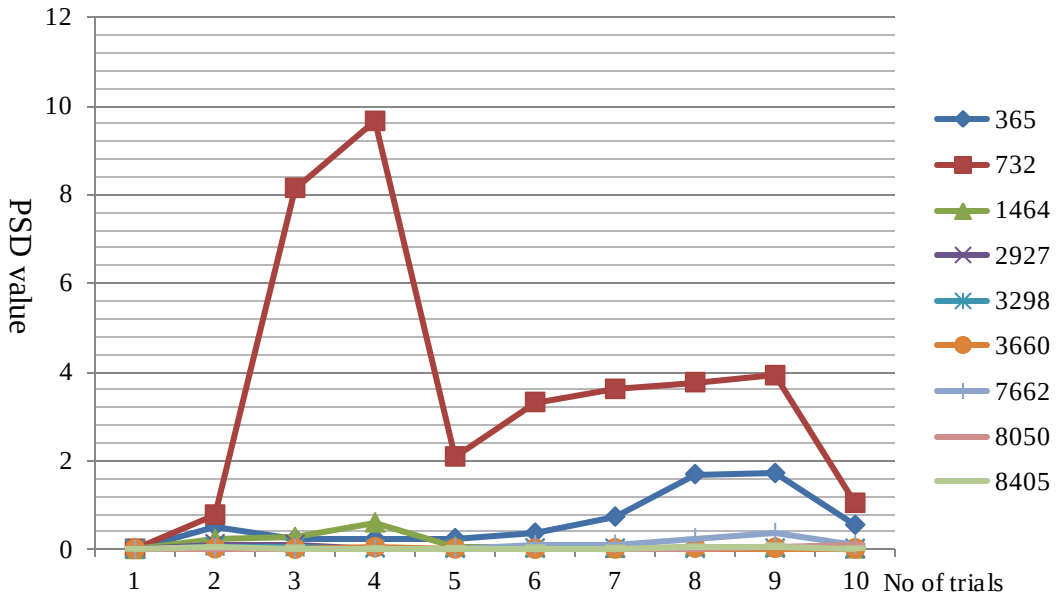

Figure 7.10 PSD evolution in z direction

The spindle spins at a fundamental frequency of 366.67Hz. Examining the prelisted characteristic frequencies, all are its harmonics, which means for signal in x direction tool wear usually happens in several specific frequencies. Figures above plot the PSD evolution on each individual frequency. It is noticed that 365 is the fundamental frequency and 732 is the tool's tooth passing frequency.

Comparing the PSD values, it can be seen that PSD values are small for new tool, but when tool wears, even slightly, PSD increases significantly at some particular frequencies, the value at fundamental frequency and tooth passing frequency are much bigger than components at other frequencies. The energy distributed at tooth passing frequency is most dominant in all three directions. However the signal in x direction shows otherwise, the energy consumed at tooth passing frequency drops below that at the fundamental frequency after the first 5 steps, this can be explained by the severely worn tool tip at the perimeter which is even short than the tool center in length. In this case, signal component at the tooth passing frequency has been significantly minimized. From the magnitude, we can also see that the energy consumed in y direction is much bigger than that in the other two directions.

7.4.2 Wavelet analysis on cutting forces

7.4.2.1 Discreet wavelet transforms

A wavelet is a waveform of effectively limited duration that has an average value of zero. Comparing wavelets with sine waves, which are the basis of Fourier analysis, Sinusoids do not have limited duration — they extend from minus to plus infinity. Sinusoids are smooth and predictable; wavelets tend to be irregular and asymmetric, which gives itself the advantage of interpret more complex and highly variable signal. It is capable of revealing aspects of data that other signal analysis techniques miss aspects like trends, breakdown points, discontinuities in higher derivatives, and self-similarity.

Discrete wavelet analysis can decompose the signal into approximations and details. The approximations are the high-scale, low-frequency components of the signal. The details are the low-scale, high-frequency components. One-stage of wavelet decomposition is shown in below diagram. After decomposition, the output is two sets of coefficients representing high frequency components and low frequency components respectively, cD and cA.

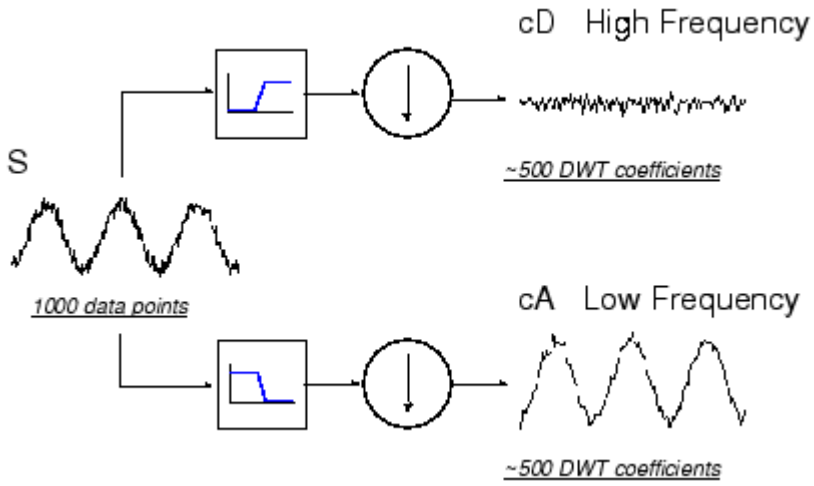

Figure 7.11 One-stage wavelet decomposition

The decomposition process can be iterated, with successive approximations being decomposed in turn, so that one signal is broken down into many lower resolution components. This is called the wavelet decomposition tree. Theoretically, decomposition can be implemented indefinitely until the level you obtain sufficient information, but in fact, he decomposition can proceed only until the individual

details consist of a single sample or pixel. In practice, the number of decomposition level should be selected based on the nature of signal and aimed information.

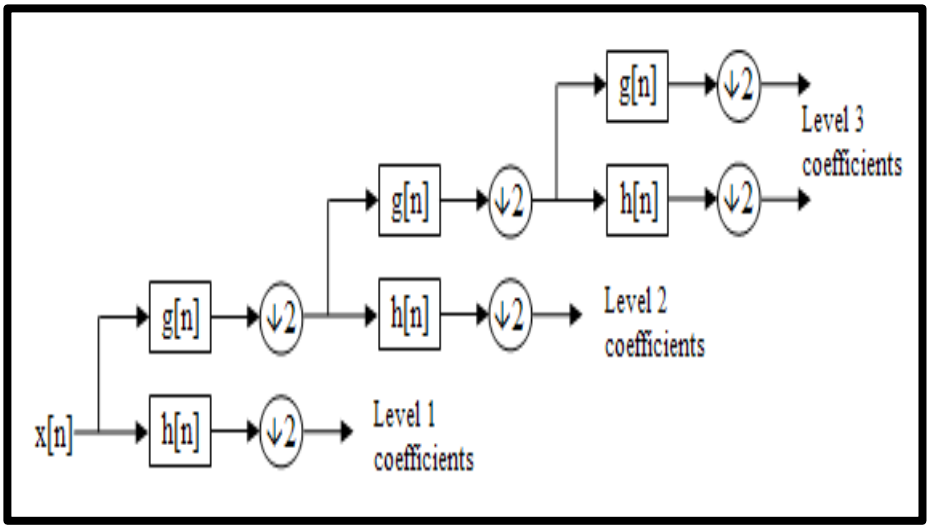

Figure 7.12 Block diagram of the multi-level wavelet decomposition

Each wavelet has a central frequency, and based on the selected scale, the corresponding pseudo-frequency could be computed following equation below.

$$F_a = \frac{F_c}{a \cdot \Delta} \tag{7-1}$$

Where a is a scale. Δ is the sampling period. Fc is the center frequency of a wavelet in Hz. Fa is the pseudo-frequency corresponding to the scale a, in Hz.

Based on this equation, wavelet coefficients can be examined within particular frequency ranges. As discussed in frequency analysis, the characteristic frequency at 732Hz and 1,464Hz are closely associated with tool wear progress.

7.4.2.2 Wavelet analysis on the tool wear

Following figure shows the plot of wavelet coefficients from the first 3 slots where tool wear is 0 µm, 20 µm and 32 µm. Amplitudes of coefficients at different locations vary significantly, the green area which represents tool wear at 0 µm, is immersed in the other two colours due to the great difference. And the difference between coefficients at 20 µm and 32 µm is also quite large, comparing light blue area and light red area. To better interpret these coefficients, and find a quantitative parameter to describe tool wear progress, variance of each set of coefficients is calculated which shows even bigger difference. Variance at different stage of tool wear could change by several times, especially at initial stage of tool wear.

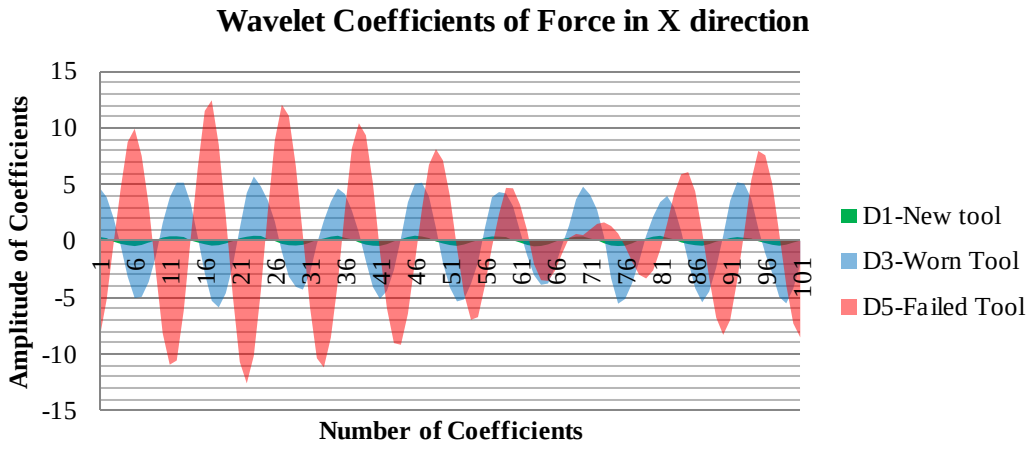

Figure 7.13 Wavelet coefficients at different stage of tool wear

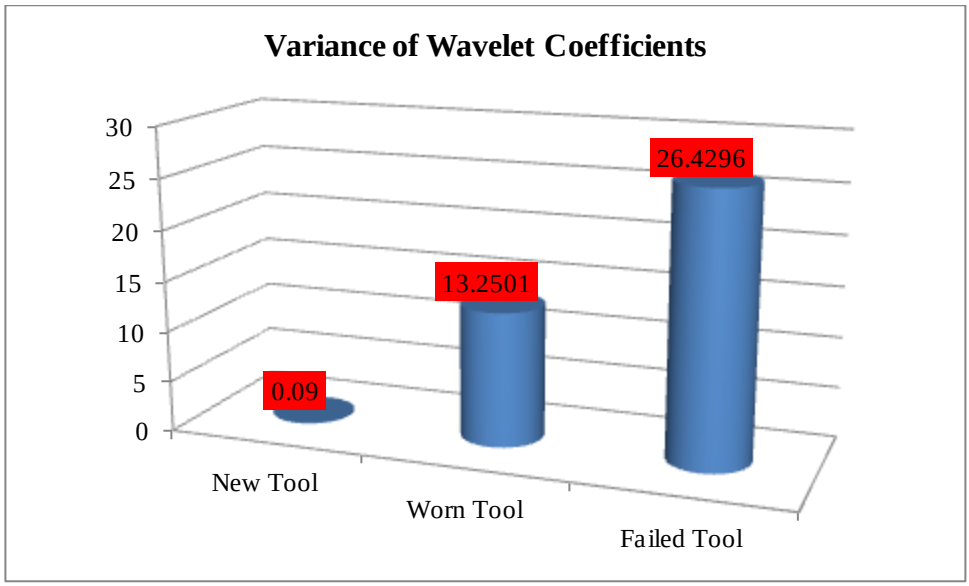

Figure 7.14 Variance of wavelet coefficients (force in x direction)

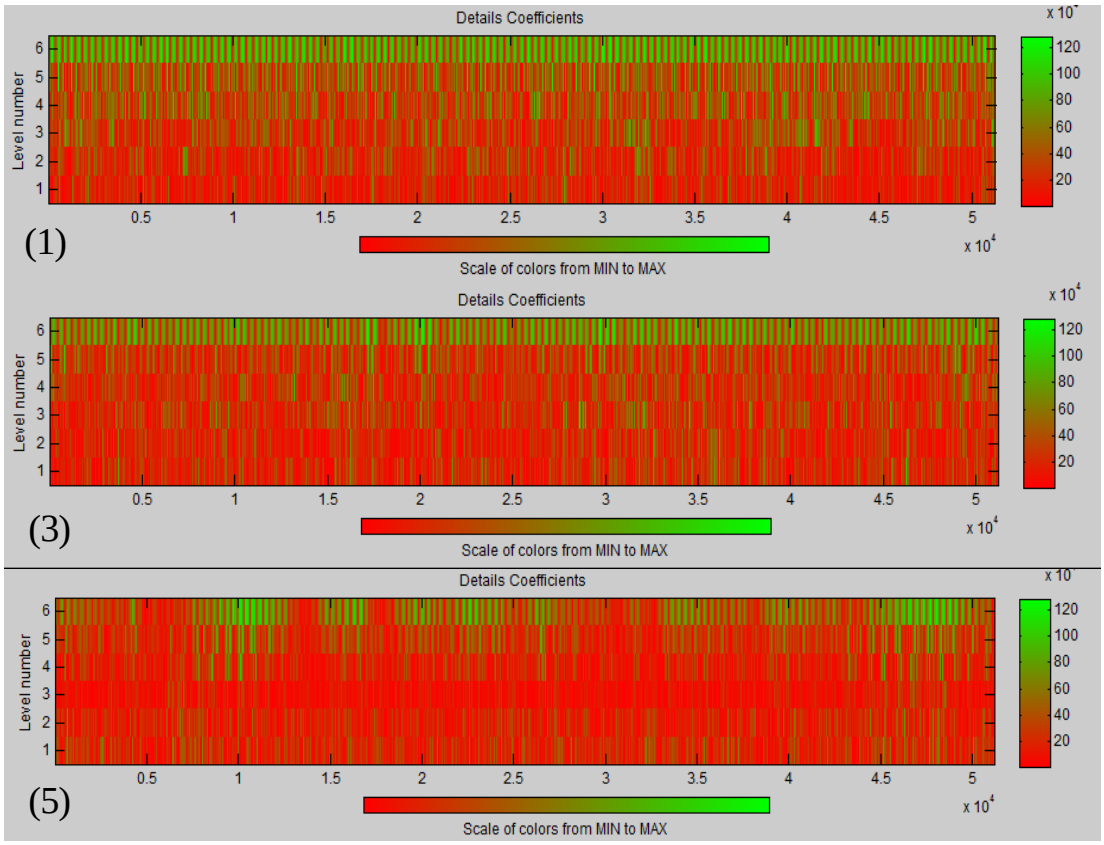

Figure 7.15 Wavelet coefficients of all level at different stage of tool wear (x)

Figure 7.15 shows us detailed coefficients of different levels, the scale increases as the colour turns green from red. The greener it is, the bigger the similarity between the analysing wavelet and signal at corresponding level is. Looking at Figure 7.15(1), a number of peaks can be detected at level 6, which corresponds to a frequency range of 400Hz-800Hz. This implies that when the tool is new, most of the signal energy is concentrated on the tool passing frequency and its proximity. Compare Figure 7.15(1) and Figure 7.15(3), at this moment, the energy is still mostly concentrated at level 6, however, more peaks start to appear more frequently at lower levels, such as 4 and 5. This becomes more obvious in Figure 7.15(5), where level 5 corresponds to frequency range of 800Hz-1,600Hz and level 4 corresponds to frequency range of 1,600Hz -3,200Hz. Another characteristic frequency sensitive to tool wear at 1,464Hz is included in this range.

7.5 Industrial case studies

7.5.1 Micro-cutting of micro-featured surface

7.5.1.1 Feature design and experiment setup

Micro-structured surfaces for friction and drag reduction purposes have gain wide research interest in recent year. An innovative shape of Serrate-Semi-Circular ribleted surfaces has been specially designed to fulfill this purpose, which shows good performance in simulation (Sayad Saravi, 2012). The designed shape is shown in Figure 7.16, supported with further details as shown in Table 7-2.

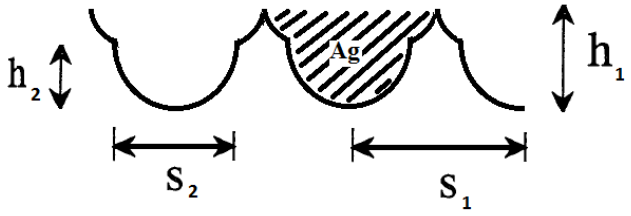

Figure 7.16 Serrate-Semi-Circular riblets

Table 7-2 Optimized sizes (mm) of the designed riblet

Model	$h_1^+(h_1)$	$h_2^+(h_2)$	$s_1^+(s_1)$	$s_2^+(s_2)$
M.6	(0.11)	(0.08)	(0.21)	(0.16)

Experiments are conducted on the Kern machine; Workpiece is an aluminium alloy 6082 plate with machining area of 200mm×80mm which is initially ground to achieve flatness error within 2μm. Given the designed geometry, it is known over 380 riblets are to be manufactured. Preliminary cutting trial shows that tungsten carbide tools breaks quickly and machining efficiency is too low to machine such large area of structured surfaces. Therefore two specially designed CVD tools are produced with nominal radius of 150μm and 75μm; the tools are attached to a boring bar of Φ10mm in diameter. The complete form of the tooling system is shown in Figure 7.17.

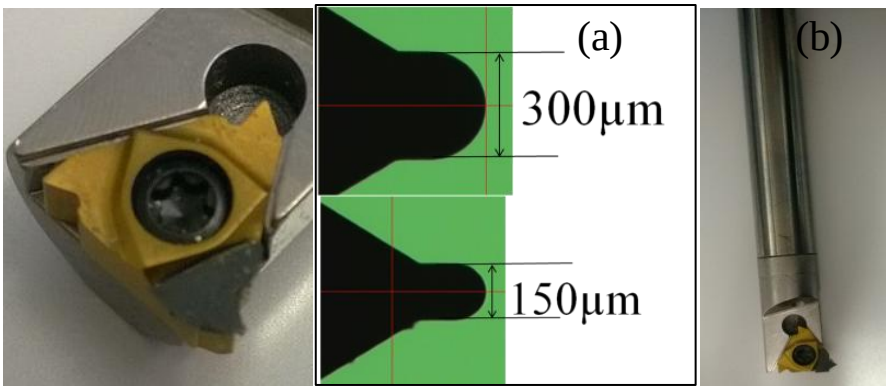

Figure 7.17 CVD diamond tools used in micro-milling

It is one advantage that micro-milling using CVD tool can significantly reduce machining time by adopting pre-decided cutting parameters. 300µm CVD tool is firstly employed to generate the upper semi-circle of the designed geometry, and then it is replaced by 150µm CVD tool to machine the lower small semi-circle. The following figure shows the experiment set-up.

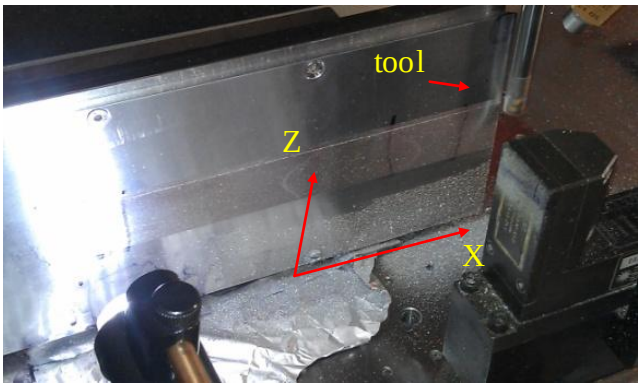

Figure 7.18 Experiment set-up for micro-milling structured surface

The suspended tooling system makes itself very sensitive to vibration, which could result in bad machined surface and broken structures. A series of cutting trials are conducted on aluminum workpiece with main purpose to improve surface quality and dimensional accuracy. Adopted tool diameter is 150µm. Machining parameters are listed in Table 7-3. Measurement is carried out on an Alicona InfiniteFocus 3D microscope to assess the machining quality, which has nanometer resolution in vertical direction. It is found that parameter set 3 can achieve good surface qualities, which is used as the machining parameter for the workpiece. The best surface roughness occurs at trial No 3 with Ra of 0.47µm, Rq of 0.61µm.

Table 7-3 Machining parameters for cutting trials

No	Spindle speed(rpm)	depth of cut(μm)	Feed/revolution(fpr:μm)	cutting direction	Ra(μm)	Rq(μm)
1	5000	30	30	down milling	0.85	0.98
2	5000	40	30	down milling	0.61	0.83
3	5000	50	30	down milling	0.47	0.61
4	5000	50	50	down milling	0.82	0.97
5	5000	50	70	down milling	0.94	1.1
6	6000	50	30	down milling	0.85	1.07
7	6000	50	50	down milling	0.95	1.17
8	6000	50	70	down milling	1.07	1.24
9	7000	50	70	down milling	0.92	1.15
10	7000	50	50	down milling	0.85	1.11
11	7000	50	30	down milling	1.09	1.31
12	8000	50	30	down milling	0.48	0.58
13	8000	50	50	down milling	0.66	1.01
14	8000	50	70	down milling	0.88	1.03
15	5000	50	70	up milling	1.06	1.21
16	5000	50	50	up milling	1.36	1.59
17	5000	50	30	up milling	1	1.27
18	6000	50	30	up milling	0.56	0.7
19	6000	50	50	up milling	1.08	1.24
20	6000	50	70	up milling	0.91	1.02
21	7000	50	70	up milling	0.87	1.07
22	7000	50	50	up milling	0.87	1.11
23	7000	50	30	up milling	0.89	1.07
24	8000	50	30	up milling	1.12	1.23
25	8000	50	50	up milling	0.8	0.96
26	8000	50	70	up milling	0.86	1.35

7.5.1.2 Machining accuracy

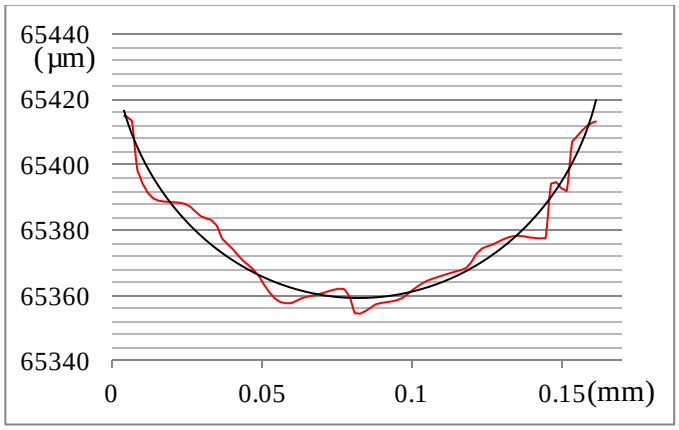

Figure 7.19 Measurement result from the trial No3

(Red: machined groove; black: fitted circle)

The machining accuracy of both single slot and machined structures will be discussed. Figure 7.19 shows the cross section of the groove from trial No 3, the profile fluctuates significantly. Three reasons may explain the fluctuation; it may be due to the manufacturing errors of CVD tool, as cross-section directly results from the shape of the tool. The other reason may lie in the tool runout, which changes the tool's actual rake angle and clearance angle, so the flank face contacts with and

scratches over material. Thirdly, the dynamical response of the tool makes itself deviate from and penetrate into the material, thus results in such fluctuation. The profile is fitted with a circle using nonlinear least squares algorithm. A very good agreement between fitted circle, whose radius is 81.71µm, and actual tool radius, 80µm is found, this shows the good accuracy that fly-cutting can achieve.

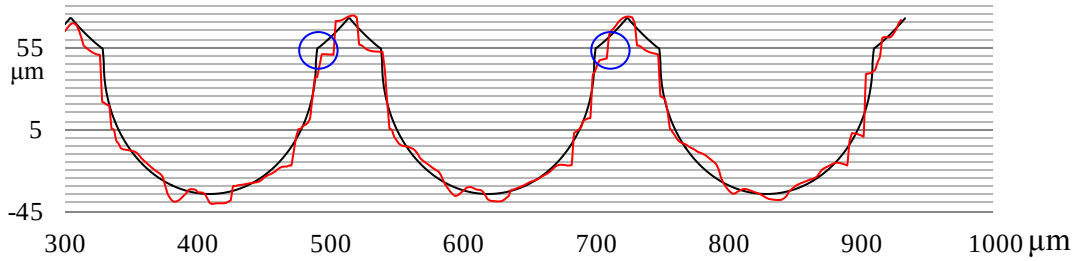

Figure 7.20 Cross-sections of machined structures
(Red: machined structure; Black:designed geometry)

Geometrical accuracy of the machined structures (red) is also examined versus designed geometry (black) as shown in Figure 7.20. The general form of the structure agrees with well with designed form, but with clear discrepancy at certain locations. As most of the structure is consisted of the lower circle, the bottom section exhibits similar form as Figure 7.19, due to the previous 3 possible reasons. The greatest discrepancy occurs at intersection between 300µm arc and 160µm arc. Critical dimensions listed in table 1 are all measured and show good machining accuracy as summarized in Table 7-4. Considering the machining process, machining results can be improved via using more rigid tooling system and reducing tool runout.

Table 7-4 Designed and measured critical dimensions

	h1(mm)	*h2(mm)*	*s1(mm)*	*s2(mm)*
Designed	0.107	0.08	0.210	0.160
Machined	0.108 ±0.003	0.082 ±0.004	0.210 ±0.002	0.160 ±0.004

7.5.1.3 Machining consistency

Structured surfaces, by quoted definition, are surfaces with a deterministic pattern of usually high aspect ratio geometric features designed to give a specific function; they typically are periodic in at least one dimension and have some symmetry. For our

study, over 380 periodic ribblets are fabricated; the consistency of manufacturing process is requisite to guarantee the successful delivery of expected function. While literatures focusing on assessment of machining consistency are hardly available, this study seeks to find factors that may disturb the machining consistency when machining structured surfaces and methods to evaluate the consistency in quantitative way. To do this, correlation coefficient, which calculates the resemblance between two profiles, is adopted. Machining consistency is studied in two forms. Consistency in one machined ribblet is named as short-term machining consistency, while machining consistency evaluated across the whole structured surfaces is named as long-term machining consistency, and factors that may affect these two are explored.

Machining consistency in short duration

Consistency is firstly considered in every machined groove. For short-term consistency, it is affected by cutting parameters including feedrate, spindle speed, which are directly related to the generation of the groove. Tool runout and tilting errors, which will change the cutting tool geometry, are other contributing factors. Besides, tool's dynamic response makes itself deviate from commanded cutting depth; this may also result in form variations.

The machined groove, shown in Figure 7.19, is extracted from position 1 in Figure 7.21. It has a fitted circle of 81.71μm in radius. Groove profiles at four evenly distributed locations are extracted and shown in Figure 7.21(b). All compared with line No1, correlation coefficients are 0.9945, 0.9937, 0.9929, respectively, which means that these four profile are very much the same.

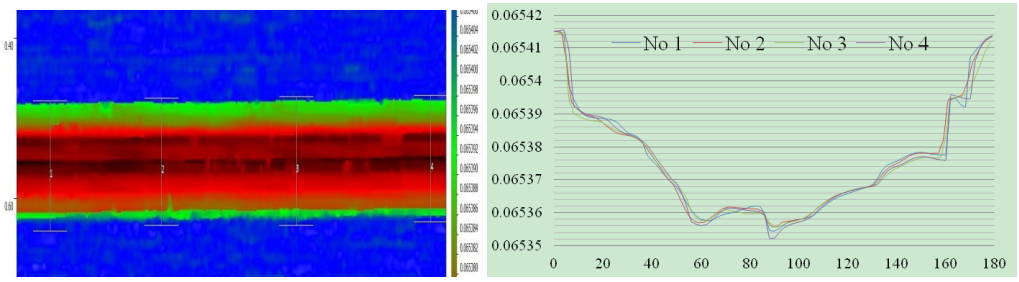

Figure 7.21 Cross-section profiles, location and form

Machining consistency in long duration

This refers to consistency through the whole machining, between the first structure and the final one. As machining time extends and tool travels long, machine tool may change in stability; volumetric error including positioning, straightness and

squareness error, are introduced; tool wear may also increases. These are the possible influencing factors; each could change the engagement conditions of the tool and material, and deteriorate machining consistency.

There are over 300 ribblet machined in total, it's better to compare each of these data in order not to miss any influencing factors. In order to save time, only the first and last ribblets are compared in this study (Figure 7.22). Note that the tool has travelled over 60meters and machined continuously for over 6 hours. The result shows that two profiles agree very well with each other. Quantitative analysis reveals that their correlation coefficient reaches highly up to 0.9955, which reveals good machining stability and consistency.

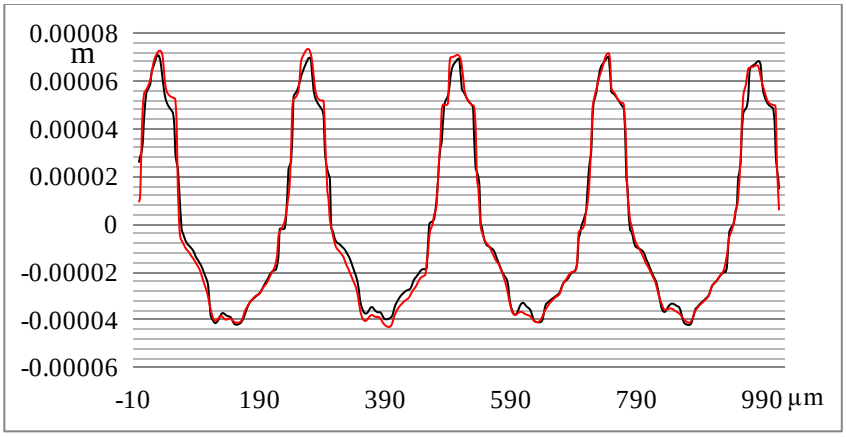

Figure 7.22 Comparison of cross-section at first and last location (black: first red: last)

The machined micro-structured surface has been tested in the wind tunnel to validate its performance, and experimental results show that the Serrate-Semi-Circular riblet surface can reduce drag reduction by 7% compared to flat surface, which is better than other riblet configurations (Samira Sayad Saravi,2014).

7.5.2 Nanometric level surface roughness on PMMA

7.5.2.1 Experiments facilities and setup

Experiments on micro-milling of material such as Poly methyl methacrylate (PMMA) are also carried out towards nanometre surface roughness. To achieve optical surface finish, a CVD diamond milling tool made by Contour Fine Tooling is utilized. CVD diamond tools, compared with natural diamond tools, can achieve similar machining quality, and it also has the advantage of being able to machine ferrous materials that cannot be machined by natural diamond tools. Experiments are conducted on the

ultra-precision micro-milling milling machine (UltraMill), It has three linear axes and two rotary axes which offer the maximum flexibility to machine different structures. Each linear axis has a resolution of 5nm while each rotary axis owns a resolution of 0.02arsec. The whole experimental setup is shown in Figure 7.23 including the tool used and the workpiece.

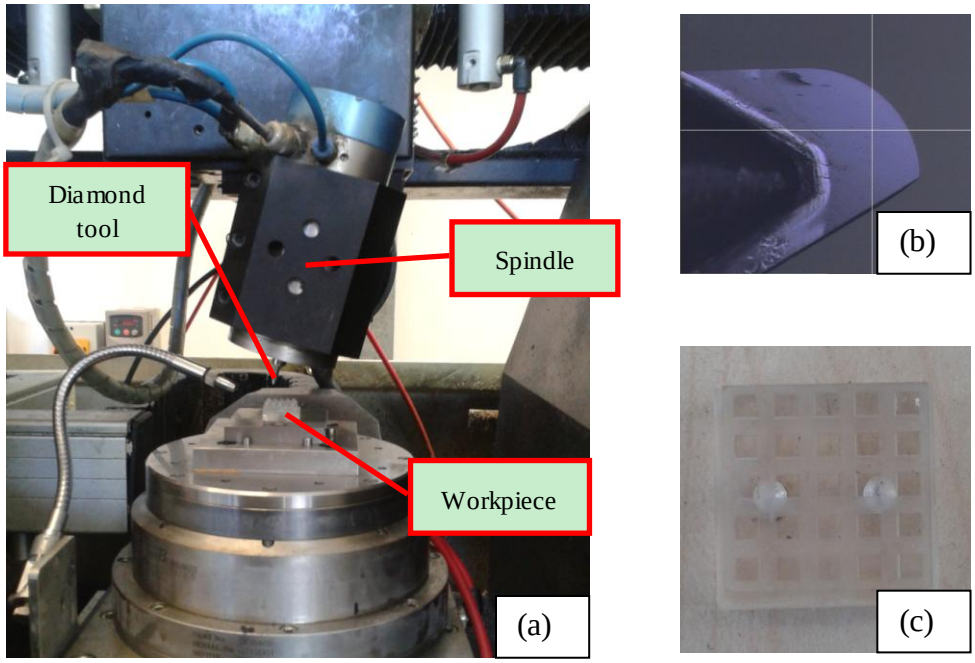

Figure 7.23 Experiment set-up (a) Machine set-up; (b) CVD tool; (c) Machined workpiece

7.5.2.2 Experimental cutting trials

Climb-milling is recommended to obtain better surface finish in conventional milling process. To investigate the scenario in micro-milling, four kinds of machining strategy are performed as shown in the Figure 7.24. To avoid zero cutting speed which could result in squeezing and rubbing, and consequently bad surface roughness, the tool is tilted at an angle of 15 degrees throughout all the following cutting trials, whether lean angle or lead angle. The lean angle is the angle between vertical axis and tool axis in the plane which is perpendicular to the feedrate direction, while the lead angle represents the angle in the plane in the feedrate direction and orthogonal to the workpiece surface. The rotational speed of the spindle is set to 36,000rpm, and thus the maximum cutting speed is 365mm/s. The depth of cut is kept constant at 50 μm. The feedrate, which is more concerned with machined surface roughness, is set to 2.7 μm, 2 μm and 1 μm respectively.

In Figure 7.24(a) and 7.24(b), the tool is tilted with a lean angle of 15 degree, Figure 7.24(a) resembles up milling, in which cutting direction is opposite to feed direction; while Figure 7.24(b) resembles down-milling, in which cutting and feed have same direction. In Figure 7.24(c) and (d), tool is tilted with a lead angle of 15 degree, Figure 7.24(c) represents feed direction pushing tool away from engagement while Figure 7.24(d) displays feed direction pushing tool towards deeper engagement. Each slot is measured using a white light interferometer (Zygo NewView 5000) at five different locations to reduce uncertainty and assess repeatability. The averaged value is used as surface roughness.

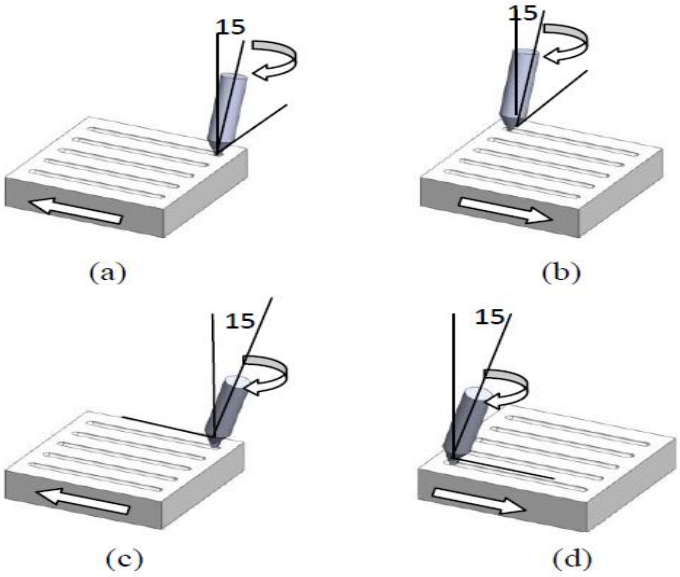

Figure 7.24 Four different machining strategies (a)15^{o} lean angle, up-milling (b) 15^{o} lean angle, down-milling (c) 15^{o} lead angle, feed from left to right (d) 15^{o} lead angle, feed from right to left

To investigate strategy for optical surface finish and reveal the difference between slot machining and area machining, experiments are conducted with varying cutting parameters based on previously obtained experience and result mainly through varying stepover. The experimental matrix and measurement results are listed in Table 7-5.

Table 7-5 Experimental matrix for micro-milling

Number	Spindle rpm	Lean °	Lead °	Federate mm/min	Stepover (μm)	DOC (μm)	Cutting direction	Roughness (nm)
1	36000	15	0	100	1	50	(a)	57.995
2	36000	15	0	100	1	50	(b)	73.658
3	36000	0	15	100	1	50	(c)	67.649
4	36000	0	15	100	1	50	(d)	79.47
5	36000	15	0	100	1	50	two way	10.312
6	36000	0	15	100	1	50	two way	25.247
7	36000	15	0	100	1	30	two way	10.35
8	36000	10	0	100	1	50	two way	12.282
9	36000	5	0	100	5	50	two way	69.137
10	36000	5	0	100	2	50	two way	17.009
11	36000	5	0	100	1.2	50	two way	19.134
12	36000	5	0	100	1	50	two way	8.717
13	36000	5	0	100	0.5	50	two way	65.306

7.5.2.3 Results and discussion

(1) Surface roughness in slot micro-milling

Surface roughness obtained in each slot is listed in Table 7-6. Better results are observed using C and D strategy. Considering the cutting geometry of different strategies, cutting direction at the tool tip in A and B is the same with feedrate, while cutting direction in C and D is perpendicular to feedrate. A zoom-in section of cutting process at the tool tip is displayed in Figure 7.25(a) and (b), so the machined surface in A and B is generated by the replication of the tool geometry, the uneven wear of flank face is also replicated onto the generated surface. In C and D, however, the machined surface is generated by the lowest point on the cutting edge, thus even in presence of tool wear on the flank face, a smooth surface could also be obtained. With decreased federate, distance between two consecutive tool cuttings becomes smaller, the roughness is significantly improved in C and D, while due to unevenness of flank face, roughness in A and B didn't change a lot. A comparison of the cross-section profile of the slots A and C at federate 100mm/min is shown below. Cylinder tendency are removed in both profiles. It shows that roughness of slot C, 30.146nm, is much better than that of slot A, 130.671nm, which proves speculations above.

However, the profile along the feed direction reveals other phenomenon. Profile of slot B and D at feedrate 36mm/min in the feed direction is shown below. Slot B,

although more irregular, has a roughness of 20.46nm. While profile of slot D, regular due to fixed feedrate, has a roughness of 32.895nm. This may indicate that when the slot is expanded orthogonally to the feed direction, a better surface finish is more likely if adopting strategy A or B.

Roughness observed in D is slightly better than that in C, one explanation is that the force exerted onto the tool tip is pushing the tool away from the workpiece which generates tool bounce at the cutting edge, while the force in D is trying to press the tool onto the workpiece which leads to more stable cutting conditions. Due to the unevenness of the flank face, roughness observed in A and B didn't change too much as shown by the result.

Table 7-6 Machining parameters in slots micro-milling

Machining path / feedrate	(a)	(b)	(c)	(d)
100 mm/min	108 nm	104 nm	56 nm	61 nm
72 mm/min	105 nm	110 nm	49 nm	44 nm
36 mm/min	105 nm	104 nm	40 nm	36 nm

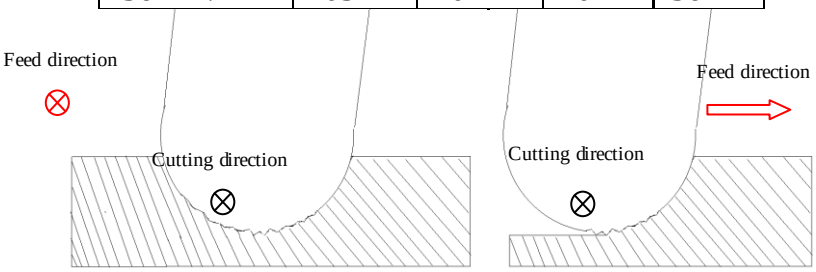

(a) Cutting with lean angle (b) Cutting with lead angle

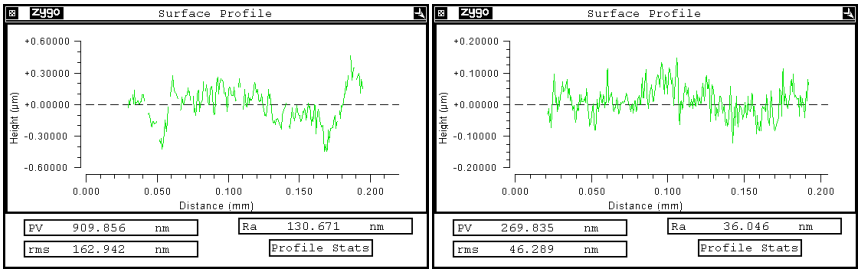

(c)Cross-section of slot with lean angle (d) cross-section of slot with lead angle

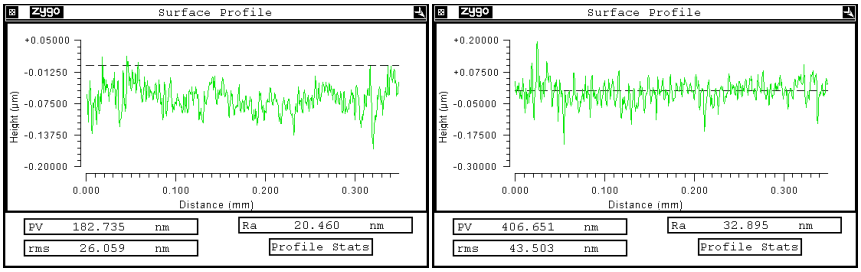

(e) Bottom line of slot with lean angle (f) Bottom line of slot with lead angle

Figure 7.25 Difference between strategies with lean angle and lead angle

(2) Surface roughness in areal micro-milling

With knowledge of results by different strategies, cutting trials are conducted on 2×2 mm^2 surface as shown in Table 7-5. First, cutting trials are implemented by adopting four strategies separately. However, results are much worse than anticipated. Examine the surface profile, a regular sinusoidal pattern can be seen, as shown in Figure 7.26(a). The explanation could only be found by correlating this with dynamic machining process. The repetitive and frequent up-down movements of Z axis could cause slight variation at commanded position. Besides, air pressure variation could also result in fluctuation in z axis which leads to this particular pattern.

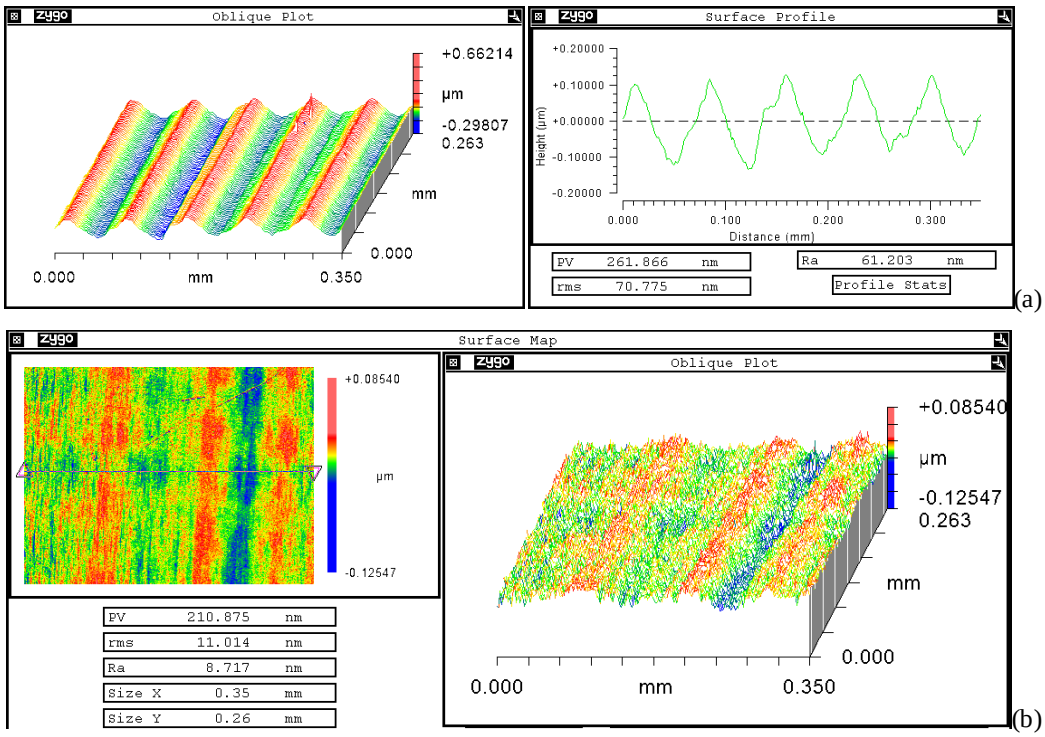

Figure 7.26 Machined surface with (a) regular pattern (climb-milling) (b) nanometric roughness

To eliminate the influence of up-down movement of Z axis, two-way (up and down milling) joint machining strategy is adopted with lean angle of 15°. The roughness is significantly reduced to 10.312nm. Experiment 5 and 6 reveal that machining with lean angle can produce better surface roughness, comparing 10.312nm to 25.247nm obtained. This discovery is consistent with preceding discussion in Section 3.3.1.

Through adjusting other parameters mainly varying stepover, different results are obtained. Results show that appropriate selection of stepover is the most predominant factor to get better surface finish. Through varying stepover by 5, 2, 1.2, 1, 0.5 µm, there exists an optimum stepover which is around 1 µm. As the stepover increase from 1 µm, the distance between two adjacent tool pass are bigger, the cusp height

left behind becomes large, which result in bad surface finish. While when stepover is less than 1 μm, due to the minimum chip thickness effect, chip will not be formed during each tool pass, it accumulates until the minimum chip thickness is exceeded. It turns into cutting from rubbing and ploughing, the change of cutting mechanism could produce unpredictable tool vibration which deteriorates surface finish. Other parameters' influence on surface finish is going to be investigated further and should be closely associated with machining process dynamics.

The best surface finish is obtained at parameters used in experiment number 11. An optical surface with 8.717nm surface roughness is obtained as illustrated in Figure 7.26(b).

7.5.2.4 Micro-milling strategies toward nanometric level surface roughness

A CVD diamond ball endmill has been used to micro-mill PMMA components with nanometric surface roughness. Through a series of micro-milling experiments, the following findings are worth discussing particularly on the adopted micro-milling strategies.

(1) Slot micro-milling experiments show that, by feeding the tool in the same direction of cutting direction, in C and D, a better surface finish could be obtained. However, comparing the profile in the direction of feedrate, strategies A and B may produce smoother profiles.

(2) When expanding the slot micro-milling to create big area (2×2 mm^2), none of the four strategies is able to produce good results. By joining up- and down-milling together, optical surfaces could be generated with roughness around 10nm.

(3) The stepover is most dominant factor affecting the machined surface roughness mostly. A stepover of 1 μm per tool pass is able to generate surface roughness of 8.717nm.

7.6 Concluding remarks

In this chapter, the tool wear process has been studied by experimental analysis; the findings out of this can be summarized in the following aspects:

The tool wear in micro milling process normally appears in the form of abrasive wear on the clearance face of the tool and edge chipping during machining. The perimeter wears more quickly than the centre of the tool, partly due to the clearance angle and higher cutting speed. However, when minor cutting edge is totally worn, the perimeter of the tool still wears more quickly than the tool centre. The proposed model in the previous chapter is applied to interpret the energy consumption at different stage of tool wear status. It finds the energy consumed increases as the tool wear accumulates. Frequency analysis is carried out and finds most of the cutting energy is concentrated on the fundamental and tooth passing frequency. The change of PSD value across the experiments can represent the tool wear process. Further analysis is conducted using wavelet analysis and finds that even slight change in tool wear can result in big variation in the wavelet coefficients. The future work should be concentrated on finding proper parameters that are independent of cutting parameter and closely related to the tool wear process.

Experiments on manufacturing industrial workpiece are also introduced in this chapter, the manufacturing of large area micro-featured surface requires stable machining technique, the applied micro-milling process manages to machine the design surface with good accuracy and consistency, experimental test reveals that the machined surface satisfies the designed requirement and has good performance in reducing friction and drag.

Experiments on machining PMMA components toward nano-metric surface finish are also conducted using CVD diamond tool. It shows by varying the machining strategies and properly selecting the machining parameters, micro-milling process is able to produce surface at best roughness around 8.7nm.

8. Conclusion and Recommendations for Future Work

8.1 Conclusions

In this research, the micro-cutting mechanics with application to micro-milling process is mainly investigated from the aspects of chip formation in micro-milling, novel cutting force modeling and tool wear mechanism. The distinctive conclusions can be drawn from following respects.

(1) FEM simulation is carried out with varied cutting edge radius, and simulation outcome shows the size effect is directly related to the large cutting edge radius compared to the cutting parameters. The larger the radius, the more obvious the increase in consumed energy.

(2) The minimum chip thickness for different tool/material pairs is identified by means of FE simulation and experiment. Experiments are carried out on ultra-precision turning machine. Outcomes by different approaches agree well. The identified MCT for tungsten/aluminium is around 17% of the cutting edge radius, while it is around 25% for the diamond/aluminium pair.

(3) The role of cutting edge radius in micro-cutting mechanics in micro-milling process is particularly investigated by adopting the perfectly sharpened diamond micro-milling tool and rounded tungsten carbide micro-milling tool of the same diameter. Thus quantitative analysis can be conducted to characterise the edge radius effect. It shows the force amplitude using tungsten carbide tool is usually 2~3 times higher than that using diamond tool; it also reveals cutting force is about 3 times of thrust force for diamond tool; while the cutting force is only slightly higher than thrust force for tungsten carbide tool. This substantially proves the influence of cutting edge radius on micro-milling process

(4) The chip morphology produced by both tools is observed in the SEM, results shows that for tungsten carbide tool, the chip is consisted of material removed in several revolutions, while the chips are formed separately in each revolution for diamond tool. The minimum chip thickness is predicted on basis of the simulation outcome, and compared with other researcher's work which has good

agreement.

(5) The instantaneous chip thickness in micro-milling are calculated based on a novel chip thickness model, which take into account of the tool geometry change caused by the tool alignment error, in the workpiece coordinate system which resembles more closely to the real machining geometry.

(6) The novel cutting force model in three aspects is proposed and applied to interpret the micro-milling process, it finds that cutting forces at the entry and exit point of cutting are not the same; it also attempts to explain the reason for tool wear, which shows the stress concentration on the tool at micro-cutting parameters far exceeds the material physical strength. The cutting energy in micro-milling reveals that once chips are formed, energy consumption in unit volume doesn't change too much.

(7) The Kalman filter is utilized to compensate the distortion in the measured cutting forces due to the dynamic transfer characteristics from the workpiece to the dynamometer. The application of the filter turns out to be very effective in compressing and compensating unwanted deviations.

(8) Cutting temperature partition in micro-cutting is investigated by means of simulation. Simulation outcome shows the cutting edge radius can change the position of the highest temperature in material and tool. It also finds the larger cutting edger radius results in smaller temperature rise due to less plastic deformation.

(9) Experimental investigation on tool wear is carried out, the main tool wear types in micro-milling are characterised. Both Fourier and Wavelet transform are utilized to seek the parameters that can represent tool wear status. Frequency analysis is carried out and finds most of the cutting energy is concentrated on fundamental and tooth passing frequency. The change of PSD value across the experiments can represent the tool wear process. Further analysis is conducted using wavelet analysis and finds that even slight change in tool wear can result in big variation in the wavelet coefficients.

(10) Machining trials are carried out to manufacture structured surface and nano-metric level surface finish. The cutting tool geometry and machining strategy are properly selected and optimised. Results show the prominence of micro-milling process in manufacturing large area structured surfaces and surface generation quality

8.2 Contribution to knowledge

Major contribution to the knowledge can be summarised below:

(1) The minimum chip thickness in micro-milling is determined by combination of simulation and experimental validation. It shows the minimum chip thickness depends on not only cutting edge radius, but also the tool/material pair.

(2) The real instantaneous chip thickness model in the workpiece coordinate system is established, taking account of the variation in tool geometry caused by tool run-out.

(3) The novel cutting force model in multiscale, i.e. force on unit length or area and cutting energy in unit volume of material is proposed in endeavour to better interpret the micro-cutting mechanics in terms of size effect, tool wear and cutting energy. Surface generation process is also simulated based on the force model.

(4) The tool wear process throughout its lifespan is characterised. Fourier and Wavelet transform are able to provide key parameter to represent tool wear status.

8.3 Recommendations for future work

(1) The current simulation setup hasn't take account of the material micro-structure effect including grain size of close to tool dimension, inhomogeneity and anisotropy in material properties, which is an important influencing factor for micro-machining process. This topic is worth investigating the following work.

(2) More powerful cutting force models are needed, as the current cutting force model in multiscale hasn't taken the tool wear into modeling, which can obviously change the cutting force behaviour at different tool wear magnitude.

(3) Surface generation on the side wall should also be studied carefully, as many structures have high aspect ratio in micro-milling, good machining performance on side wall accuracy and surface quality are required.

(4) Feasible and robust methods to conduct the online tool condition monitoring are still highly needed which has not yet satisfied.

References

AFAZOV, S.M., RATCHEV, S.M. and SEGAL, J., 2010. Modeling and simulation of micro-milling cutting forces. *Journal of Materials Processing Technology,* 210(15), pp. 2154-2162.

ALTING, L., KIMURA, F., HANSEN, H.N. and BISSACCO, G., 2003. Micro Engineering. *CIRP Annals - Manufacturing Technology,* 52(2), pp. 635-657.

ALTINTAS, Y., 1992. Prediction of cutting forces and tool breakage in milling from feed drive current measurements. *Journal of Engineering for Industry,* 114(4), pp. 386-392.

ALTINTAS, Y., 2000. *Manufacturing Automation: Metal Cutting Mechanics, Machine Tool Vibrations, and CNC Design.* Cambridge: Cambridge University Press.

ARRAZOLA, P.J., ÖZEL, T., UMBRELLO, D., DAVIES, M. And JAWAHIR, I.S., 2013. Recent advances in modeling of metal machining processes. *CIRP Annals - Manufacturing Technology,* 62(2), pp. 695-718.

ADAMS, D.P., VASILE, M.J. and KRISHNAN, A.S.M., 2000. Microgrooving and microthreading tools for fabricating curvilinear features. *Precision Engineering,* 24(4), pp. 347-356.

ADAMS, D.P., VASILE, M.J., BENAVIDES, G. And CAMPBELL, A.N., 2001. Micromilling of metal alloys with focused ion beam–fabricated tools. *Precision Engineering,* 25(2), pp. 107-113.

ALTINTAS, Y., 1992. Prediction of cutting forces and tool breakage in milling from feed drive current measurements. *Journal of engineering for industry,* 114(4), pp. 386-392.

ARAMCHAROEN, A. And MATIVENGA, P.T., 2009. Size effect and tool geometry in micromilling of tool steel. *Precision Engineering,* 33(4), pp. 402-407.

ARMAREGO, E.J.A., 1962. On the size effect in metal cutting. *International Journal of Production Research,* 1(3), pp. 75; 75-99; 99.

ARRAZOLA, P.J. and ÖZEL, T., 2010. Investigations on the effects of friction modeling in finite element simulation of machining. *International Journal of Mechanical Sciences,* 52(1), pp. 31-42.

BAO, W.Y. and TANSEL, I.N., 2000. Modeling micro-end-milling operations. Part I: analytical cutting force model. *International Journal of Machine Tools and Manufacture,* 40(15), pp. 2155-2173.

BRUZZONE, A.A.G., COSTA, H.L., LONARDO, P.M. and LUCCA, D.A., 2008. Advances in engineered surfaces for functional performance. *CIRP Annals - Manufacturing Technology,* 57(2), pp. 750-769.

BISSACCO, G., HANSEN, H.N. and DE CHIFFRE, L., 2006. Size effects on surface generation in micro milling of hardened tool steel. *CIRP Annals - Manufacturing Technology,* 55(1), pp. 593-596.

BISSACCO, G., HANSEN, H.N. and SLUNSKY, J., 2008. Modeling the cutting edge radius size effect for force prediction in micro milling. *CIRP Annals - Manufacturing Technology,* 57(1), pp. 113-116.

CHAE, J., PARK, S.S. and FREIHEIT, T., 2006. Investigation of micro-cutting operations. *International Journal of Machine Tools and Manufacture,* 46(3–4), pp. 313-332.

Cheng, K. and HUO, D., 2013. *Micro-Cutting: Fundamentals and Applications.* John Wiley & Sons.

CHAE, J., PARK, S.S. and FREIHEIT, T., 2006. Investigation of micro-cutting operations. *International Journal of Machine Tools and Manufacture,* 46(3–4), pp. 313-332.

CHENG, X., 2010. Design and development of PCD micro straight edge end mills for micro/nano machining of hard and brittle materials. *Journal of Mechanical Science and Technology*, 24(11), pp 2261-2268

CHERN, G. And CHANG, Y., 2006. Using two-dimensional vibration cutting for micro-milling. *International Journal of Machine Tools and Manufacture,* 46(6), pp. 659-666.

CHERN, G. And DORNFELD, D.A., 1996. Burr/breakout model development and experimental verification. *Journal of Engineering Materials and Technology, Transactions of the ASME,* 118(2), pp. 201-206.

CLAUDIU FLORINEL BISU, 2011. Envelope dynamic analysis: a new approach for milling process monitoring. *The International Journal of Advanced Manufacturing Technology,* 62(5), pp 471-486

DING, H. 2010. Dynamic surface generation modeling of two-dimensional vibration-assisted micro-end-milling. *The International Journal of Advanced Manufacturing Technology,* 53(9-12), 1075-1079.

D. DORNFELDA, S. MINA, Y. TAKEUCHIB, 2007. Recent Advances in Mechanical Micromachining. *CIRP Annals-Manufacturing Technology,* 55(2), 745-768.

DE OLIVEIRA, F.B., RODRIGUES, A.R., COELHO, R.T. and DE SOUZA, A.F., 2015. Size effect and minimum chip thickness in micromilling. *International Journal of Machine Tools and Manufacture,* 89, pp. 39-54.

EHMANN, K.F., BOURELL, D., CULPEPPER, M.L., HODGSON, T.J., KURFESS, T.R., MADOU, M., RAJURKAR, K. And DEVOR, R.E., 2005. *International assessment of research and development in micro-manufacturing.* WORLD TECHNOLOGY EVALUATION CENTER INC BALTIMORE MD.

EVANS, C.J. and BRYAN, J.B., 1999. "Structured", "Textured" or "Engineered" Surfaces. *CIRP Annals - Manufacturing Technology,* 48(2), pp. 541-556.

FANG, N., JAWAHIR, I.S. and OXLEY, P.L.B., 2001. Universal slip-line model with non-unique solutions for machining with curled chip formation and a restricted contact tool. *International Journal of Mechanical Sciences,* 43(2), pp. 557-580.

FRIEDRICH, C.R. and VASILE, M.J., 1996. Development of the micromilling process for high-aspect-ratio microstructures. *Journal of Microelectromechanical Systems,* , 5(1), pp. 33-38.

FRIEDRICH, C., COANE, P., GOETTERT, J. And GOPINATHIN, N., 1998. Direct fabrication of deep x-ray lithography masks by micromechanical milling. *Precision Engineering,* 22(3), pp. 164-173.

FURUKAWA, Y. And MORONUKI, N., 1988. Effect of material properties on ultra precise cutting processes. *CIRP Annals - Manufacturing Technology,* 37(1), pp. 113-116.

FLEISCHER, J. 2008. Design and manufacturing of micro milling tools. *Microsystem Technologies,* 14(9-11), 1771-1775.

GHANI, J.A., CHOUDHURY, I.A. and HASSAN, H.H., 2004. Application of Taguchi method in the optimization of end milling parameters. *Journal of Materials Processing Technology,* 145(1), pp. 84-92.

GHOSH, N., RAVI, Y.B., PATRA, A., MUKHOPADHYAY, S., PAUL, S., MOHANTY, A.R. and CHATTOPADHYAY, A.B., 2007. Estimation of tool wear during CNC milling using neural network-based sensor fusion. *Mechanical Systems and Signal Processing,* 21(1), pp. 466-479.

GILLESPIE, L.K. and BLOTTER, P.T., 1976. Formation and properties of machining burrs. *Journal of Manufacturing Science and Engineering,* 98(1), pp 66-74.

HASHIMURA, M., HASSAMONTR, J. And DORNFELD, D.A., 1999. Effect of in-plane exit angle and rake angles on burr height and thickness in face milling operation. *Journal of Manufacturing Science and Engineering, Transactions of the ASME,* 121(1), pp. 13-19.

HOLME, N.C.R., BERG, T.W. and DINESEN, P.G., 2008. Diamond micro-milling for array mastering. *Proc.SPIE 7062, Laser Beam Shaping IX, 70620J (September 17, 2008);*

ISSA, M., SAANOUNI, K., LABERGÈRE, C. And RASSINEUX, A., 2011. Prediction of serrated chip formation in orthogonal metal cutting by advanced adaptive 2D numerical methodology. *International Journal of Machining and Machinability of Materials,* 9(3-4), pp. 295-315.

JUN-HONG ZHOU, CHEE KHIANG PANG, ZHAO-WEI ZHONG and LEWIS, F.L., 2011. Tool wear monitoring using acoustic emissions by dominant-feature identification. *Instrumentation and Measurement, IEEE Transactions on,* 60(2), pp. 547-559.

JIN, M., GOTO, I., WATANABE, T., KUROSAWA, J. And MURAKAWA, M., 2007. Development of CBN ball-nosed end mill with newly designed cutting edge. *Journal of Materials Processing Technology,* 192–193, pp. 48-54.

JUN, M.B.G., DEVOR, R.E. and KAPOOR, S.G., 2006. Investigation of the dynamics of microend milling - Part II: Model validation and interpretation. *Journal of Manufacturing Science and Engineering, Transactions of the ASME,* 128(4), pp. 901-912.

JASPERS, S.P.F.C. and DAUTZENBERG, J.H., 2002a. Material behaviour in conditions similar to metal cutting: flow stress in the primary shear zone. *Journal of Materials Processing Technology,* 122(2–3), pp. 322-330.

JASPERS, S.P.F.C. and DAUTZENBERG, J.H., 2002b. Material behaviour in metal cutting: strains, strain rates and temperatures in chip formation. *Journal of Materials Processing Technology*, 121(1), pp. 123-135.

JOHNSON, G.R. and COOK, W.H., 1983. A constitutive model and data for metals subjected to large strains, high strain rates and high temperatures, *Proceedings of the 7th International Symposium on Ballistics* 1983, The Netherlands, pp. 541-547.

KANG, I., KIM, J., KIM, J., KANG, M. And SEO, Y., 2007. A mechanistic model of cutting force in the micro end milling process. *Journal of Materials Processing Technology,* 187, pp. 250-255.

KANG, I.S., KIM, J.S. and SEO, Y.W., 2011. Investigation of cutting force behaviour considering the effect of cutting edge radius in the micro-scale milling of AISI 1045 steelg. *Proceedings of the Institution of Mechanical Engineers, Part B: Journal of Engineering Manufacture,* 225(2), pp. 163-171.

KIM, C., MAYOR, J.R. and NI, J., 2004. A static model of chip formation in microscale milling. *Journal of Manufacturing science and engineering,* 126(4), pp. 710-718.

KIM, K.W., LEE, W.Y. and SIN, H., 1999. A finite element analysis for the characteristics of temperature and stress in micro-machining considering the size effect. *International Journal of Machine Tools and Manufacture,* 39(9), pp. 1507-1524.

KO, S. And DORNFELD, D.A., 1991. A study on burr formation mechanism. *Journal of Engineering Materials and Technology,* 113(1), pp. 75-87.

KIM, GI D. 1999. Indirect Cutting Force Measurement Considering Frictional Behaviour in a Machining Centre Using Feed Motor Current. *The International Journal of Advanced Manufacturing Technology,* 15(7), pp 478-484

LIU, X., DEVOR, R.E., KAPOOR, S.G. and EHMANN, K.F., 2005. The mechanics of machining at the microscale: assessment of the current state of the Science. *Journal of Manufacturing Science and Engineering,* 126(4), pp. 666-678.

LI, HONGTAO. 2007. Modeling and experimental analysis of the effects of tool wear, minimum chip thickness and micro tool geometry on the surface roughness in micro-end-milling. *Journal of Micromechanics and Microengineering,* 18(2), pp 025006-025018

LAI, X., LI, H., LI, C., LIN, Z. And NI, J., 2008. Modeling and analysis of micro scale milling considering size effect, micro cutter edge radius and minimum chip thickness. *International Journal of Machine Tools and Manufacture,* 48(1), pp. 1-14.

LAZOGLU, I. and ALTINTAS, Y., 2002. Prediction of tool and chip temperature in continuous and interrupted machining. *International Journal of Machine Tools and Manufacture,* 42(9), pp. 1011-1022.

LEE, K. and DORNFELD, D.A., 2005. Micro-burr formation and minimization through process control. *Precision Engineering,* 29(2), pp. 246-252.

LEKKALA, R., BAJPAI, V., SINGH, R.K. and JOSHI, S.S., 2011. Characterization and modeling of burr formation in micro-end milling. *Precision Engineering,* 35(4), pp. 625-637.

LI, P., 2010. Micromilling of thin ribs with high aspect ratios. *Journal of Micromechanics and Microengineering,* 20(11), 115013.

LIU, X., DEVOR, R.E. and KAPOOR, S.G., 2005a. An analytical model for the prediction of minimum chip thickness in micromachining. *Journal of Manufacturing Science and Engineering,* 128(2), pp. 474-481.

LUCCA, D.A., RHORER, R.L. and KOMANDURI, R., 1991. Energy Dissipation in the Ultraprecision Machining of Copper. *CIRP Annals - Manufacturing Technology,* 40(1), pp. 69-72.

LUCCA, D.A., SEO, Y.W. and KOMANDURI, R., 1993. Effect of Tool Edge Geometry on Energy Dissipation in Ultraprecision Machining. *CIRP Annals - Manufacturing Technology,* 42(1), pp. 83-86.

MAMALIS, A.G., HORVÁTH, M., BRANIS, A.S. and MANOLAKOS, D.E., 2001. Finite element simulation of chip formation in orthogonal metal cutting. *Journal of Materials Processing Technology,* 110(1), pp. 19-27.

MASUZAWA, T. And TÖNSHOFF, H.K., 1997. Three-dimensional micromachining by machine tools. *CIRP Annals - Manufacturing Technology,* 46(2), pp. 621-628.

MASUZAWA, T. 2000. State of the Art of Micromachining. *CIRP Annals - Manufacturing Technology,* 49(2), pp. 473-488.

MCCALL, B. and TKACZYK, T.S., 2010. Fabrication of plastic microlens array for array microscopy by three-dimensional diamond micromilling. *Optical Engineering (Redondo Beach, Calif.),* 49(10), 103401–4.

MIAO, J. C. CHEN, G. L. LAI, X. M. LI, H. T. LI, C. F. 2007. Review of dynamic issues in micro-end-milling. *The International Journal of Advanced Manufacturing Technology,* 31(9-10), 897-904.

M'SAOUBI, R. And CHANDRASEKARAN, H., 2004. Investigation of the effects of tool micro-geometry and coating on tool temperature during orthogonal turning of quenched and tempered steel. *International Journal of Machine Tools and Manufacture,* 44(2–3), pp. 213-224.

MALEKIAN, M., MOSTOFA, M.G., PARK, S.S. and JUN, M.B.G., 2012. Modeling of minimum uncut chip thickness in micro machining of aluminum. *Journal of Materials Processing Technology,* 212(3), pp. 553-559.

MALEKIAN, M., PARK, S.S. and JUN, M.B.G., 2009. Modeling of dynamic micro-milling cutting forces. *International Journal of Machine Tools and Manufacture,* 49(7–8), pp. 586-598.

MALEKIAN, M., PARK, S.S. and JUN, M.B.G., 2009. Tool wear monitoring of micro-milling operations. *Journal of Materials Processing Technology,* 209(10), pp. 4903-4914.

MIAN, A.J., DRIVER, N. And MATIVENGA, P.T., 2011. Identification of factors that dominate size effect in micro-machining. *International Journal of Machine Tools and Manufacture,* 51(5), pp. 383-394.

MORIWAKI, T., 1989. Machinability of copper in ultra-precision micro diamond cutting. *CIRP Annals - Manufacturing Technology,* 38(1), pp. 115-118.

MORIWAKI, T., HORIUCHI, A. And OKUDA, K., 1990. Effect of cutting heat on machining accuracy in ultra-precision diamond turning. *CIRP Annals - Manufacturing Technology,* 39(1), pp. 81-84.

MOVAHHEDY, M.R., GADALA, M.S. and ALTINTAS, Y., 2000. Simulation of chip formation in orthogonal metal cutting process: an ALE finite element approach. *Machining Science and Technology,* 4(1), pp. 15-42.

NAKAYAMA, K. And TAMURA, K., 1968. Size effect in metal-cutting force. *Journal of Engineering for Industry,* 90(1), pp. 119-126.

NATARAJAN, 2011. Multiple-response optimization for micro-endmilling process using response surface methodology. *The International Journal of Advanced Manufacturing Technology,* 56(1-4), 177-185.

OUTEIRO, J. C., UMBRELLO, D., M'SAOUBI, R., AND JAWAHIR, I. 2015. Evaluation of present numerical models for predicting metal cutting performance and residual stresses. *Machining Science and Technology*, 19(2), 183-216.

ÖZEL, T. And ZEREN, E., 2005. A Methodology to Determine Work Material Flow Stress and Tool-Chip Interfacial Friction Properties by Using Analysis of Machining. *Journal of Manufacturing Science and Engineering,* 128(1), pp. 119-129.

RAMOS, A.C., AUTENRIETH, H., STRAUSS, T., DEUCHERT, M., HOFFMEISTER, J. And SCHULZE, V., 2012. Characterization of the transition from ploughing to cutting in micro machining and evaluation of the minimum thickness of cut. *Journal of Materials Processing Technology,* 212(3), pp. 594-600.

SCHALLER, T., BOHN, L., MAYER, J. And SCHUBERT, K., 1999. Microstructure grooves with a width of less than 50 µm cut with ground hard metal micro end mills. *Precision Engineering,* 23(4), pp. 229-235.

SON, S.M., LIM, H.S. and AHN, J.H., 2005. Effects of the friction coefficient on the minimum cutting thickness in micro cutting. *International Journal of Machine Tools and Manufacture,* 45(4-5), pp. 529-535.

SIMONEAU, A., NG, E. And ELBESTAWI, M.A., 2006a. Chip formation during microscale cutting of a medium carbon steel. *International Journal of Machine Tools and Manufacture,* 46(5), pp. 467-481.

SIMONEAU, A., NG, E. And ELBESTAWI, M.A., 2006b. The Effect of Microstructure on Chip Formation and Surface Defects in Microscale, Mesoscale, and Macroscale Cutting of Steel. *CIRP Annals - Manufacturing Technology,* 55(1), pp. 97-102.

SHAW, M.C, 2003. The size effect in metal cutting. *Sadhana*, 28(5), 875-896.

SOORAJ, V. S. 2011. An experimental investigation on the machining characteristics of microscale end milling. *The International Journal of Advanced Manufacturing Technology,* 56(9-12), 951-958.

T. GIETZELT, 2008. Manufacturing of microstructures with high aspect ratio by micromachining. *Microsystem Technologies,* 14(9-11), 1525-1529.

TANSEL, I., TRUJILLO, M., NEDBOUYAN, A., VELEZ, C., BAO, W., ARKAN, T.T. and TANSEL, B., 1998. Micro-end-milling—III. Wear estimation and tool breakage detection using acoustic emission signals. *International Journal of Machine Tools and Manufacture,* 38(12), pp. 1449-1466.

TANSEL, I.N., ARKAN, T.T., BAO, W.Y., MAHENDRAKAR, N., SHISLER, B., SMITH, D. And MCCOOL, M., 2000. Tool wear estimation in micro-machining.:

Part I: tool usage–cutting force relationship. *International Journal of Machine Tools and Manufacture,* 40(4), pp. 599-608.

THEPSONTHI, T., 2012. Multi-objective process optimization for micro-end milling of Ti-6Al-4V titanium alloy. *The International Journal of Advanced Manufacturing Technology,* 63(9-12), 903-914.

TO, S., LEE, W.B. and CHAN, C.Y., 1997. Ultraprecision diamond turning of aluminium single crystals. *Journal of Materials Processing Technology,* 63(1–3), pp. 157-162.

UEDA, T., HOSOKAWA, A., ODA, K. And YAMADA, K., 2001. Temperature on Flank Face of Cutting Tool in High Speed Milling. *CIRP Annals - Manufacturing Technology,* 50(1), pp. 37-40.

UHLMANN, E. And SCHAUER, K., 2005. Dynamic Load and Strain Analysis for the Optimization of Micro End Mills. *CIRP Annals - Manufacturing Technology,* 54(1), pp. 75-78.

VOGLER, M.P., DEVOR, R.E. and KAPOOR, S.G., 2004. On the modeling and analysis of machining performance in micro-endmilling, part i: Surface generation. *Journal of Manufacturing Science and Engineering, Transactions of the ASME,* 126(4), pp. 685-694.

VOGLER, M.P., DEVOR, R.E. and KAPOOR, S.G., 2003. Microstructure-level force prediction model for micro-milling of multi-phase materials. *Journal of Manufacturing Science and Engineering, Transactions of the ASME,* 125(2), pp. 202-209.

VOGLER, M.P., LIU, X., KAPOOR, S.G., DEVOR, R.E. and EHMANN, K.F., 2002. Development of meso-scale machine tool (mmt) systems. *Technical Paper - Society of Manufacturing Engineers.MS,* (MS02-181), pp. 1-9.

VOGLER, M.P., KAPOOR, S.G. and DEVOR, R.E., 2005. On the modeling and analysis of machining performance in micro-endmilling, part ii: cutting force prediction. *Journal of Manufacturing Science and Engineering,* 126(4), pp. 695-705.

VOLLERTSEN, F., BIERMANN, D., HANSEN, H.N., JAWAHIR, I.S. and KUZMAN, K., 2009. Size effects in manufacturing of metallic components. *CIRP Annals - Manufacturing Technology,* 58(2), pp. 566-587.

VOGLER, M.P., DEVOR, R.E. and KAPOOR, S.G., 2003. Microstructure-Level Force Prediction Model for Micro-milling of Multi-Phase Materials. *Journal of Manufacturing Science and Engineering,* 125(2), pp. 202-209.

WANG, J. S. 2007. Surface generation analysis in micro end-milling considering the influences of grain. *Microsystem Technologies,* 14(7), 937-942.

WECK, M. 1996. Fabrication of microcomponents using ultraprecision machine tools, *Nanotechnology,* 8(3), pp 145.

WAN-HAO HSIEH, 2012. Application of backpropagation neural network for spindle vibration-based tool wear monitoring in micro-milling. *The International Journal of Advanced Manufacturing Technology,* 61(1-4), 53-61.

WEULE, H., HÜNTRUP, V. And TRITSCHLE, H., 2001a. Micro-cutting of steel to meet new requirements in miniaturization. *CIRP Annals - Manufacturing Technology*, 50(1), pp. 61-64.

WISSMILLER, D.L. and PFEFFERKORN, F.E., 2009. Micro end mill tool temperature measurement and prediction. *Journal of Manufacturing Processes,* 11(1), pp. 45-53.

WOON, K.S., RAHMAN, M., FANG, F.Z., NEO, K.S. and LIU, K., 2008a. Investigations of tool edge radius effect in micromachining: A FEM simulation approach. *Journal of Materials Processing Technology*, 195(1-3), pp. 204-211.

WOONG YOUN, J., YANG YANG, M. And YOUNG PARK, H., 1994. Detection of cutting tool fracture by dual signal measurements. *International Journal of Machine Tools and Manufacture,* 34(4), pp. 507-525.

YUAN, Z.J., ZHOU, M. And DONG, S., 1996. Effect of diamond tool sharpness on minimum cutting thickness and cutting surface integrity in ultraprecision machining. *Journal of Materials Processing Technology,* 62(4), pp. 327-330.

YUAN, Z.J., LEE, W.B., YAO, Y.X. and ZHOU, M., 1994. Effect of crystallographic orientation on cutting forces and surface quality in diamond cutting of single crystal. *CIRP Annals - Manufacturing Technology,* 43(1), pp. 39-42.

YANG K, 2010. Tool edge radius effect on cutting temperature in micro-end-milling proc*ess. The International Journal of Advanced Manufacturing Technology,* 52(9-12), 905-912.

ZAMAN, M.T., KUMAR, A.S., RAHMAN, M. And SREERAM, S., 2006. A three-dimensional analytical cutting force model for micro end milling operation. *International Journal of Machine Tools and Manufacture,* 46(3–4), pp. 353-366.

ZHOU, J. H., PANG, C. K., ZHONG, Z. W., AND LEWIS, F. L, 2011. Tool wear monitoring using acoustic emissions by dominant-feature identification. *Instrumentation and Measurement, IEEE Transactions on,* 60(2), pp. 547-559.

ZHU, K., MEI, T., and YE, D, 2015. Online Condition Monitoring in Micromilling: A Force Waveform Shape Analysis Approach. *Industrial Electronics, IEEE Transactions on,* 62(6), pp. 3806-3813.

Appendices

Appendix 1:

List of Publications Arising from the Research

1. F. Jiao, K. Cheng. "Micro-milling of micro-featured surfaces: micro-cutting mechanics, implementation and application perspectives", euspen topical meeting: Structured and Freeform Surfaces, 5th~6th 2012; Teddington, United Kingdom

2. F. Jiao, K. Cheng. "An innovative investigation on chip thickness model with application to cutting forces modeling in micro milling", the 29th ASPE Annual Meeting, November 9-14, 2014; Boston, Massachusetts USA

3. F. Jiao and K. Cheng. "An experimental investigation on micro-milling of polymethyl methacrylate components with nanometric surface roughness." Proceedings of the Institution of Mechanical Engineers, Part B: Journal of Engineering Manufacture (2013): 0954405413507251.

4. F. Jiao, S. Saravi and K. Cheng. "Investigation on an integrated approach to design and micro fly-cutting of micro-structured riblet surfaces. " Proceedings of the Institution of Mechanical Engineers, Part C: Journal of Mechanical Engineering Science, 2015 (submitted)

5. F. Jiao, K. Cheng. "Investigation on an Innovative Tool Wear Monitoring Approach to Micro Milling Based on Joint Spectrum and Wavelet Analysis of Cutting Forces. " Proceedings of the Institution of Mechanical Engineers, Part B: Journal of Engineering Manufacture, 2015(submitted)

6. F. Jiao, K. Cheng. "Experiment-based investigation on chip formation mechanisms in micro-milling with natural diamond and tungsten carbide tools. " Proceedings of the Institution of Mechanical Engineers, Part B: Journal of Engineering Manufacture, 2015(submitted)

Appendix 2:

Technical Specifications of Zygo NewView 5000

System Overview

Zygo NewView 5000

Tool Overview:

The Zygo NewView 5000 is a non-contact 3D surface profiler that uses scanning white light interferometry to image and measure the microstructure and topography of surfaces. It provides graphic images and high-resolution numerical analysis to accurately characterize the surface structure of test parts.

Tool Capabilities/Limitations:

- Objectives: 5x, 10x, 50x
- Vertical Resolution: 0.1-20nm (FDA resolution setting dependent)
- Lateral Resolution Range: 0.64 – 2.6µm (objective dependent)
- Max Vertical Step Height: 5mm
- Vertical scan rate: ≤ 10µm/sec
- Sample specifications:
  - Type: opaque and transparent surfaces
  - Max Roughness: ≤ 100µm Rp
  - Reflectivity: 4-100%
  - Max Sample Thickness: 104mm
  - Note: If your sample has surfaces with dissimilar optical properties, the accuracy of step height measurements from one material to the other may be degraded. The dissimilar optical properties cause relative phase shift error in the measured vertical heights of the dissimilar materials.

Appendix 3:

Technical Specifications of Kistler 9256C2 and its Calibration Certificate

Force

KISTLER
measure. analyze. innovate.

MiniDyn

Type 9256C...

Multicomponent Dynamometer up to 250 N

Multicomponent dynamometer for measuring the three orthogonal components of a force. Its very low threshold allows measuring extremely small forces.

- For cutting force measurements in ultra precise machining
- Small design
- High sensitivity and natural frequency
- Small temperature error
- Top plate made of titanium

Type 9256C2

Description

The dynamometer consists of four 3-component force sensors mounted under high preload between the cover plate and the two lateral base plates.
A low temperature error is obtained by this special mounting of the sensors. Each force sensor contains three crystal rings, of which one is sensitive to pressure in the y-direction and the two others to shear in the x- and z-directions. The forces are measured practically without displacement.
The outputs of the four mounted force sensors are fed to the 7-pole flanged socket. There are also multicomponent force-moment measurements possible.
The four sensors are fitted so that they are ground-isolated. This largely eliminates ground loop problems.
The dynamometer is corrosion-resistant and protected against penetration by splashing water or cutting fluid. The dynamometer including connecting cable Type 1696A5 or Type 1697A5 meets the degree of protection IP67.

Examples of Application

- Cutting force measurement in precision machining such as:
  - cutting wafers
  - grinding hard-disk read heads
  - diamond turning
  - high speed machining
  - micromachining
- Ultra-high precision machining of brittle hard materials
- Multicomponent force measurement of small forces
- Force measurement in confined spaces

Technical Data

Measuring range	F_x, F_y, F_z	N	–250 ... 250
Type 9256C1	M_x, M_z	N·m	–8 ... 8
Type 9256C2	M_x, M_z	N·m	–11 ... 11
Calibrated measuring range			
100 %	F_x, F_y, F_z	N	0 ... 250
10 %	F_x, F_y, F_z	N	0 ... 25
Overload	F_x, F_y, F_z	N	–300/300
Threshold		N	<0,002
Sensitivity	F_x, F_z	pC/N	≈–26
	F_y	pC/N	≈–13
Linearity, all ranges		%FSO	≤±0,4
Hysteresis, all ranges		%FSO	≤0,5
Crosstalk		%	≤±2
Rigidity	c_x, c_z	N/µm	>250
	c_y	N/µm	>300
Natural frequency (mounted on rigid base)			
Type 9256C1	f_n (x)	kHz	≈5,1
	f_n (y)	kHz	≈5,5
	f_n (z)	kHz	≈5,6
Type 9256C2	f_n (x)	kHz	≈4,0
	f_n (y)	kHz	≈4,8
	f_n (z)	kHz	≈4,6
Operating temperature range		°C	0 ... 70
Insulation resistance		Ω	$>10^{13}$
Ground isolation		Ω	$>10^{8}$
Degree of protection EN60529 (with connecting cable Type 1696A5/1697A5)			IP67
Weight			
Dynamometer	Type 9256C1/C2	kg	0,75/0,87
Top plate	Type 9256C1/C2	kg	0,24/0,36
Clamping area			
Type 9256C1		mm	39x80
Type 9256C2		mm	55x80

9256C_000-484e-08.10

KISTLER
measure. analyze. innovate.

Kalibrierschein
Calibration Certificate

Type Kistler 9256C2 **Serial No.** 4277565

Kalibriert durch Calibration Technician	Datum Date
K. Ta	15. Jun. 2012

Referenzgeräte Reference Equipment	Typ Type	Serien-Nr. Serial No.
Gebrauchsnormal Working Standard	Kistler 9251A	446442
	Kistler 9252A	517947
	Kistler 9252A	550683
Ladungskalibrator Charge Calibrator	Kistler 5395A	441991

Umgebungstemperatur Ambient Temperature °C	Relative Feuchte Relative Humidity %
24	53

Messergebnisse Results of Measurement

Kalibrierter Bereich Calibrated Range N		Empfindlichkeit Sensitivity pC / N	Linearität Linearity ≤ ± %FSO	Übersprechen Cross talk %	%
Fx	0 ... 250	-25,37	0,06	*Fx* → *Fy* 0,5	*Fx* → *Fz* -0,5
Fx	0 ... 25	-25,31	0,03	*Fx* → *Fy* 0,5	*Fx* → *Fz* -0,4
Fy	0 ... 250	-12,72	0,11	*Fy* → *Fx* 0,5	*Fy* → *Fz* 0,3
Fy	0 ... 25	-12,67	0,06	*Fy* → *Fx* 0,7	*Fy* → *Fz* 0,1
Fz	0 ... 250	-25,67	0,07	*Fz* → *Fx* -0,6	*Fz* → *Fy* 0,8
Fz	0 ... 25	-25,60	0,07	*Fz* → *Fx* -0,8	*Fz* → *Fy* 0,7

Messverfahren **Kontinuierliche Kalibrierung, Vergleichsverfahren**
Measurement Procedure Continuous Calibration, Comparison Method

Kistler betreibt die SCS Kalibrierstelle Nr. 049, akkreditiert nach ISO 17025. SCS Kalibrierzertifikate sind auf Bestellung erhältlich.
Kistler operates the SCS Calibration Laboratory No. 049, which is accredited per ISO 17025. SCS Calibration Certificates are available on request.

Bestätigung Confirmation

Das oben durch die Serienummer identifizierte Gerät entspricht der Vereinbarung der Bestellung und hält die Herstelltoleranzen gemäss den Spezifikationen der Datenblätter ein. Dieses Dokument erfüllt die Anforderungen von EN 10204 Abnahmeprüfzeugnis "3.1". Alle Messmittel sind auf nationale Normale rückverfolgbar. Das Kistler Qualitätsmanagement System ist nach ISO 9001 zertifiziert. Dieses Dokument ist ohne Unterschrift gültig.
The equipment mentioned above and identified by Serial Number complies with the agreement of the order and meets the manufacturing tolerances specified in the data sheets. This document fulfils the requirements of EN 10204 Inspection Certificate "3.1". All measuring devices are traceable to national standards. The Kistler Quality Management System is certified per ISO 9001. This document is valid without a signature.

Kistler Instrumente AG
Eulachstrasse 22
PO Box
CH-8408 Wintherthur
Tel. +41 52 224 11 11
Fax +41 52 224 14 14
info@kistler.com
ZKB Winterthur BC 732
Swift: ZKBKCHZZ80A
Account: 1132-0374.628
IBAN: CH67 0070 0113 2003 7462 8
VAT: 229 713
ISO 9001 certified
www.kistler.com

Appendix 4:

Technical Specifications of Nanotech 250UPL

Nanotech 250UPL^{v2} Specification Overview

General	Description
System Configuration	Ultra-Precision two, three, or four axis CNC contouring machine with "T" axis orientation
Workpiece Capacity	300mm diameter x 200mm long (150mm diameter swing capability over the optional rotary B-Axis)
Base Structure	Natural Black Granite with integral slide channels and protective stainless steel apron
Vibration Isolation	Optimally located air isolation system. Optional Shear Damped Air Isolation System with Self Leveling
Computer System Specifications	Intel i5 2.4 GHz processor running Windows 7 Professional 64-bit with 16GB DDR3 1600MHz memory, 10/100/1000 Base-T external customer Ethernet connection, DVD RW Drive, 500GB 7200 RPM removeable Hard Drive. Pendant features a 22" wide projected capacitive multi-touch display. Customer USB ports provided on front of PC and also on operator pendant.
Control System	Delta Tau 1GHz PowerPMAC Embedded Real-time 64-bit Linux Motion Controller with Nanotech's NEW Windows 7 based HMI with a Touch / Swipe Gesture Interactive display.
Programming Resolution	0.01 nanometer linear / 0.0000001° rotary
Functional Performance (As measured with laser interferometer & white light interferometer on same part)	Material – High Purity Aluminum Alloy Form Accuracy (P-V): ≤ 0.1µm / 75mm diameter, 250mm radius convex sphere. Surface Finish (Ra): ≤ 2.0 nanometers *(Important Notice: Both Form & Surface Finish measured on the same part, same surface!)*

Workholding Spindle	Heavy Duty (Standard)
Type	Exclusive impact resistant porous graphite air bearing with center mounted thrust face
Liquid Cooling (optional)	To maintain thermal stability and tool center repeatability, a closed loop chiller provides recirculating temperature controlled water to cooling channels located around the motor and bearing journals of the air bearing spindle. The chiller has an integral PID controller which maintains temperature control to ± 0.5°F.
Speed Range	50 to 10,000 rpm, bi-directional
Swing Capacity	Up to 300mm diameter (without risers)
Working Load Capacity (Radial)	85 Kg @ 7bar (185 lbs @ 100psi.) / 102 Kg @ 10bar (225 lbs @ 145psi.) @ spindle nose
Working Load Capacity (Axial)	197 Kg @ 7bar (435 lbs @ 100psi.) @ spindle nose
Axial Stiffness	228 N/µm @ 7bar (1,300,000 lbs/in @ 100psi) / 260 N/µm @ 10bar (1,500,000 lbs/in @ 145psi)
Radial Stiffness (at nose)	98 N/µm @ 7bar (560,000 lbs/in @ 100psi) / 140 N/µm @ 10bar (800,000 lbs/in @ 145psi)
Drive System	Frameless, Brushless DC motor
Motion Accuracy	Axial: ≤ 12.5 nanometers (0.5µ") Radial: ≤ 12.5 nanometers (0.5µ")

Linear Axes	X	Z	Y (Vertical) – Option
Type	Fully constrained oil hydrostatic, box way slide	Fully constrained oil hydrostatic, box way slide	Fully constrained oil hydrostatic box way slide with adaptively controlled air bearing counterbalance to negate gravitational forces & varying loads.
Travel	200mm (8")	200mm (8")	100mm (4")
Drive System	Brushless DC Linear Motor	Brushless DC Linear Motor	Brushless DC Linear Motor
Feedback Type	Laser holographic linear scale	Laser holographic linear scale	Laser holographic linear scale
Feedback Resolution	0.0084 nanometer	0.0084 nanometer	0.0084 nanometer
Feed Rate (maximum)	4500mm/min	4500mm/min	1500mm/min
Straightness in critical direction	0.2µm (8µ") over full travel	0.2µm (8µ") over full travel	0.2µm (8µ") over full travel
Hydrostatic Oil Supply	Compact, low flow, low pressure system with closed loop servo control and pressure accumulator to minimize pump pulsation.		

Optional Rotational Axes	B	C (Work Spindle Option)
Type	Groove Compensated Air Bearing	Porous Graphite Air Bearing (liquid cooled)
Travel	360° (Bi-directional)	360° (Bi-directional)
Drive System	Brushless DC motor	Brushless DC motor
Axial Stiffness	280 N/µm (1,600,000 lbs./in.)	See **Workholding Spindle** Specifications Listed Above
Radial Stiffness (at nose)	100 N/µm (540,000 lbs./in.)	See **Workholding Spindle** Specifications Listed Above
Positioning Accuracy	± 1.0 arc seconds (compensated)	± 1.0 arc seconds (compensated)
Feedback Resolution	0.005 arc seconds	0.01 arc seconds
Maximum Speed (Positioning Mode)	50 rpm	3,000 rpm
Motion accuracy	Axial: ≤ 0.05µm (2µ") Radial: ≤ 0.05µm (2µ")	Axial: ≤ 12.5nm (0.5µ") Radial: ≤ 12.5nm (0.5µ")

Utility Requirements	Air	Electrical	Machine Footprint (includes utilities cabinet)
For optimal cutting results, facility thermal stability should be held within ±0.5°C (±1.0°F)	7 to 10 bar (100 – 145 psi) 280 liters/min (10 scfm) Dry to 10°C pressure dew point and pre-filtered to 10µm	230 VAC; 1 Phase; 50/60hz; (35 amp) (3 phase available by request)	1.50m L x 1.30m D x 1.60m H; Approx. 1,500 Kg (Enclosure & Utilities Cabinet included, but not control pendant. Contact Nanotech for complete overall detailed layouts.)

Warranty	1 year full parts and labor warranty

Note: In an effort to continually improve our product performance, specifications are subject to change without notice.
(Please consult your Sales Representative for our latest specifications)

Rev.1014

Appendix 5:

Technical Specifications of JCM-6000 Benchtop SEM

NeoScope™

Specifications

Magnification	Secondary electron image: ×10 to ×60,000 Backscattered electron image: ×10 to ×30,000 (when image size is 128 mm × 96 mm)
Imaging mode	Secondary electron image, backscattered electron image
Accelerating voltage	Secondary electron image; 5 kV, 10 kV, 15 kV (3 stages) Backscattered electron image; 10 kV, 15 kV (2 stages)
Electron gun	Small gun with cartridge filament integrating wehnelt
Bias current	Auto bias (linked to accelerating voltage and filament current)
Condenser lens	Two stage electromagnetic zoom condenser lens
Objective lens	Electromagnetic lens
Auto magnification correction	Magnification corrected with reference to sample height (7 mm, WD56 to 53 mm, WD10)
Preset magnification	6 levels, user programmable
Specimen stage	Manual control for X and Y: X: 35 mm, Y: 35 mm
Maximum sample size	70 mm diameter × 50 mm height
Specimen exchange	Draw-out mechanism
Image memory	One, 1,280 × 960 × 16 bits
Pixels	640 × 480, 1,280 × 960
Image processing	Pixel accumulation Image accumulation (recursible)
Automated functions	Filament, alignment, focus, stigmator, exposure
Metrology	Distance between 2 points, angles
File format	BMP, TIFF, JPEG
Computer	PC (desktop PC), OS Windows®7
Monitor	23 inch wide LCD monitor (touch panel)
Evacuation system	Fully automatic, TMP: 1, RP: 1

Optional accessories

◆ Tilt rotation motorized holder
Tilt: -15° to +45°; rotation: 360°
◆ EDS

Installation requirements

Power supply	Voltage: Single phase AC 100 V (120 V, 220 V, 240 V) 50/60 Hz, 700 VA (AC 100 V), 840 VA (AC 120 V), 880 VA (AC 220 V), 960 VA (AC 240 V), Fluctuation ±10% or less, with grounding
Installation Room	
Room temperature	15 to 30°C
Humidity	60% or less
Operation table	Sturdy table with a loading capacity of 100 kg or more
Weight	Main console: approximately 50 kg RP: approximately 9 kg Power supply box: approximately 10 kg
Base unit dimensions	(Width) (Depth) (Height) 325 mm × 490 mm × 430 mm

* Specifications subject to change without notice.
* The official name of Windows7 is Microsoft(R), Windows(R), Operating System.
* Windows is a registered trademark of Microsoft Corp. in the U.S.
* Other trademarks referenced in this catalog and marked with* are the property of our allied companies.

System composition

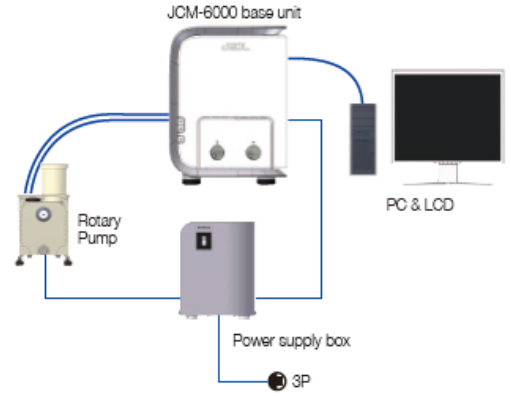

15

Appendix 6:

Cutting Forces in Tool Wear Monitoring and PSD Spectrums

New Tool: (0mins, 0meter)

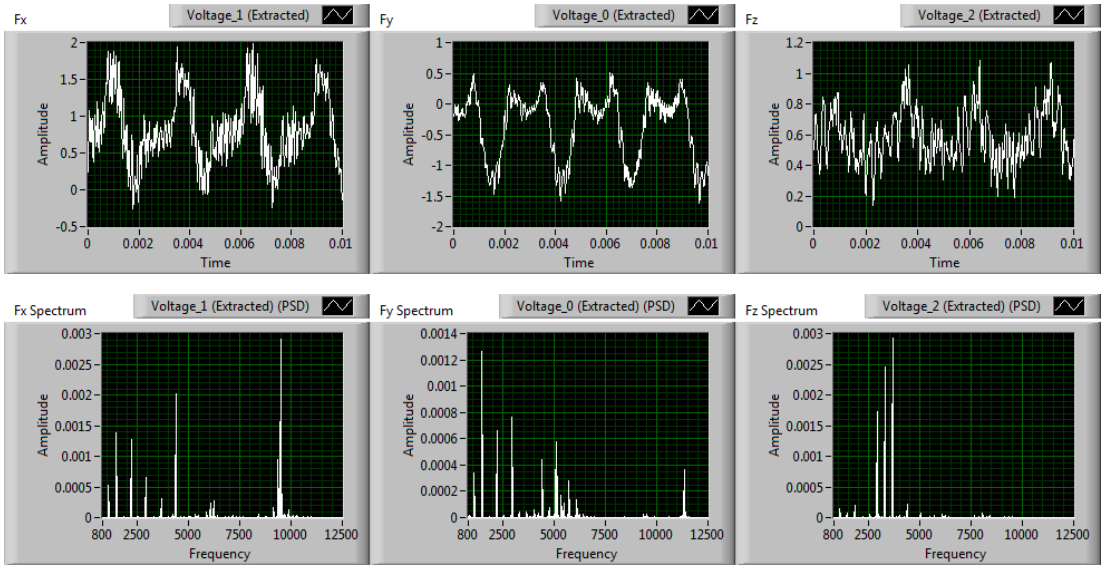

Step 1: (10mins, 3meters)

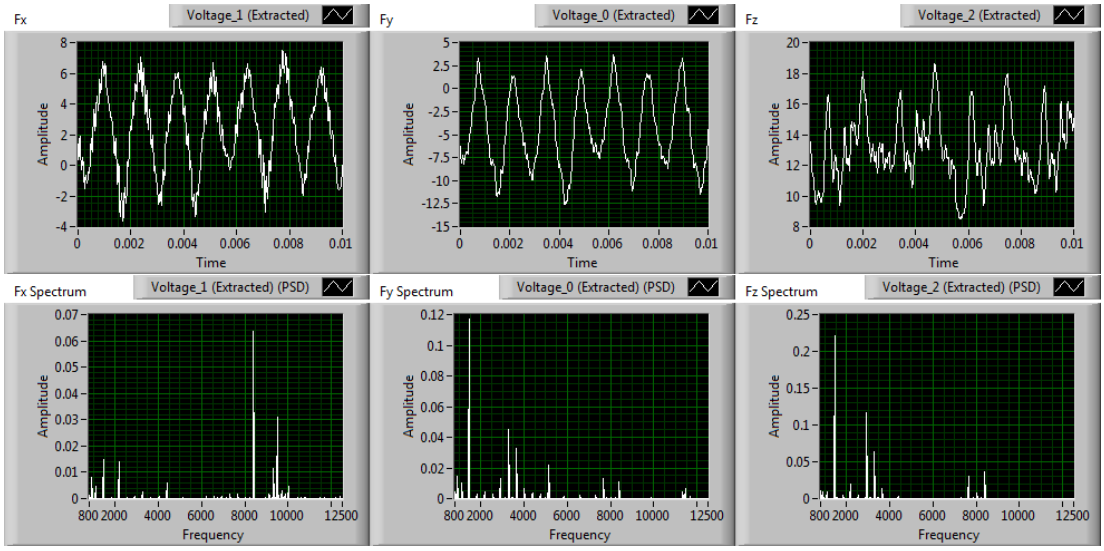

Step 2: (20mins, 6meters)

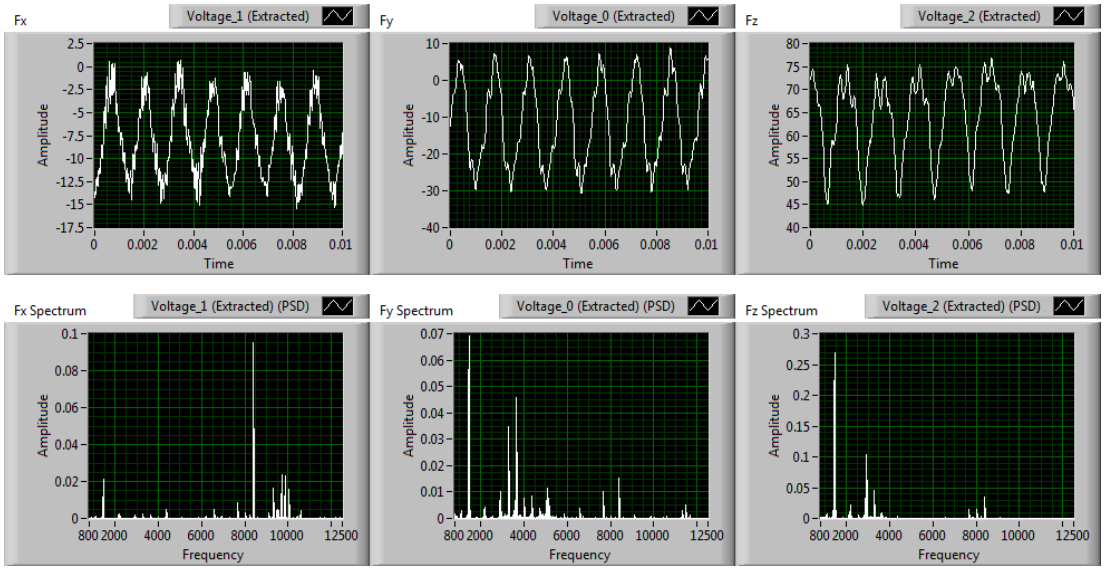

Step 3: (30mins, 9meters)

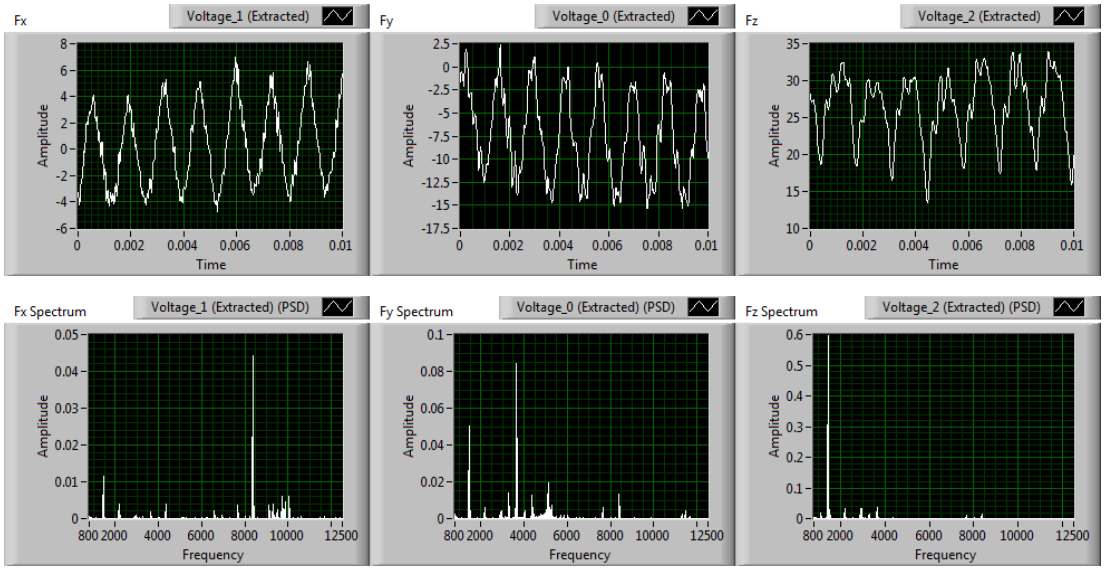

Step 4: (40mins, 12meters)

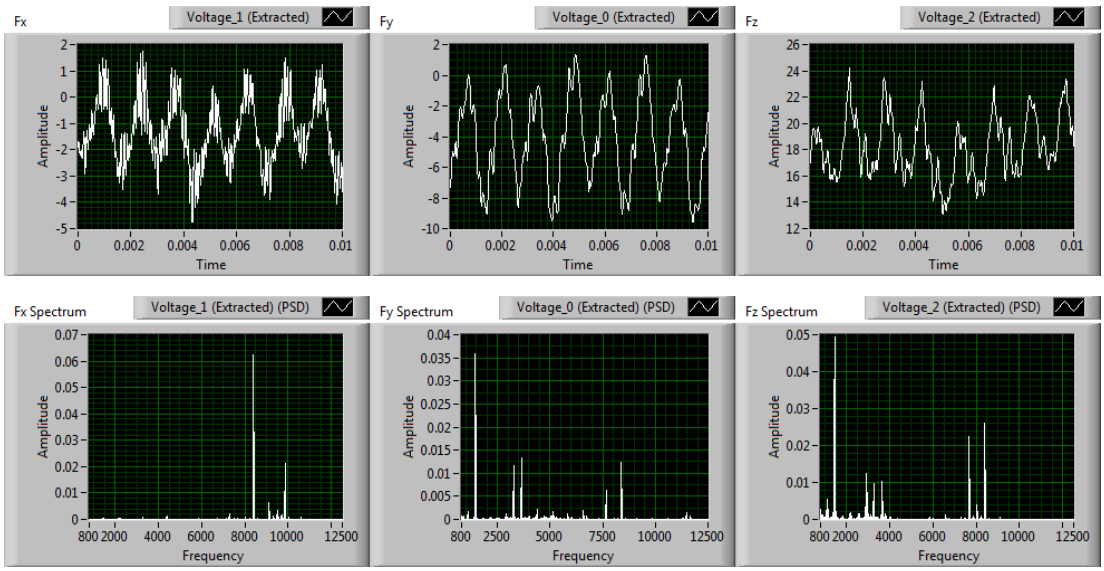

Step 5: (50mins, 15meters)

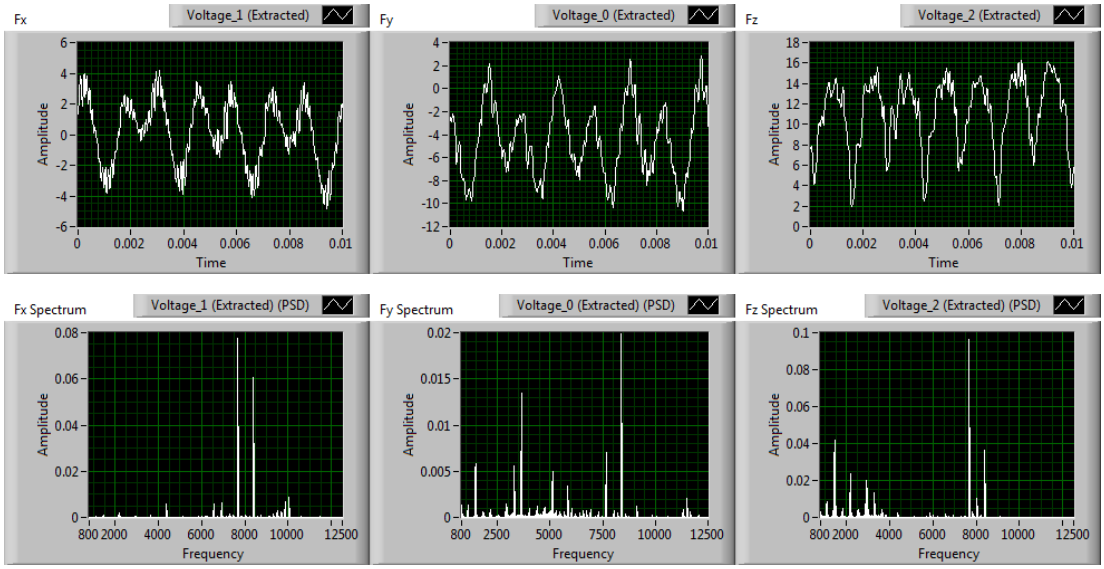

Step 6: (60mins, 18meters)

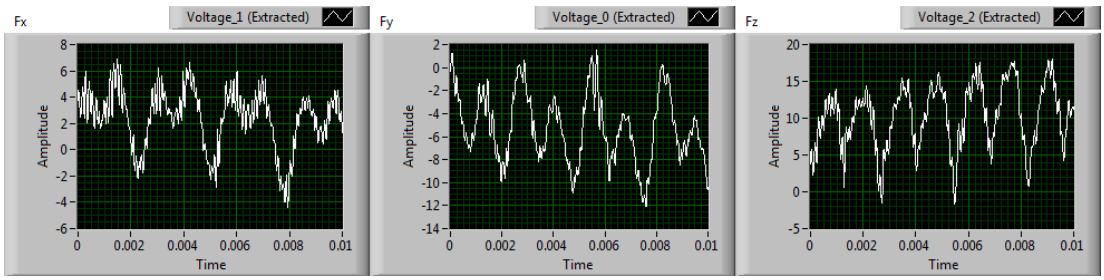

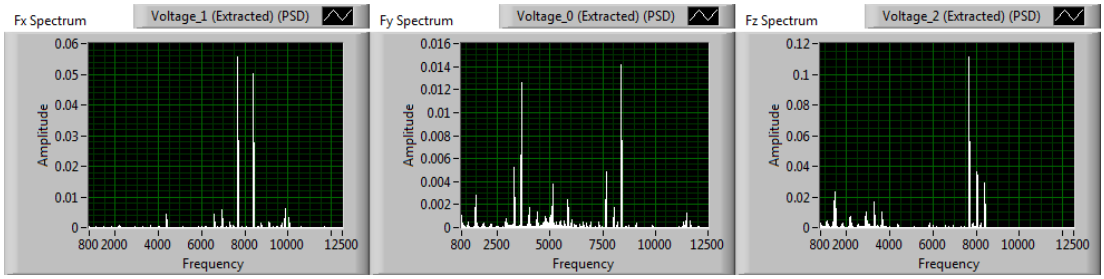

Step 7: (70mins, 21meters)

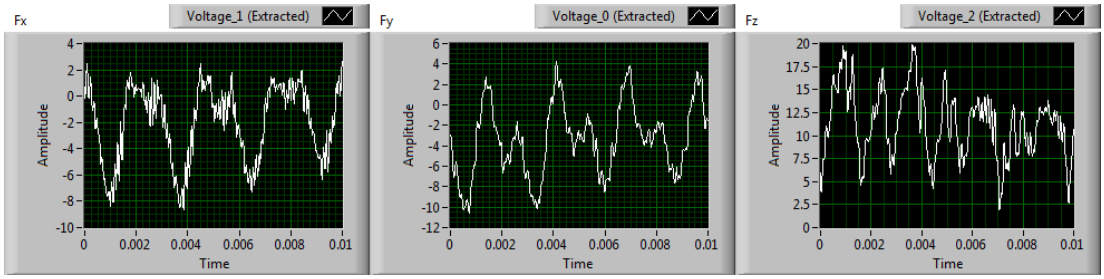

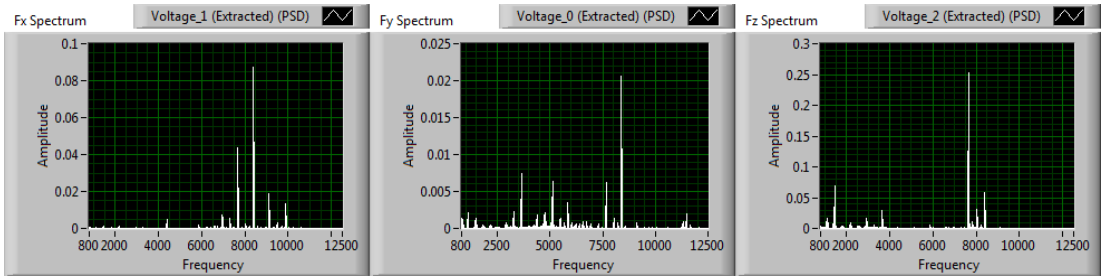

Step 8: (90mins, 27meters)

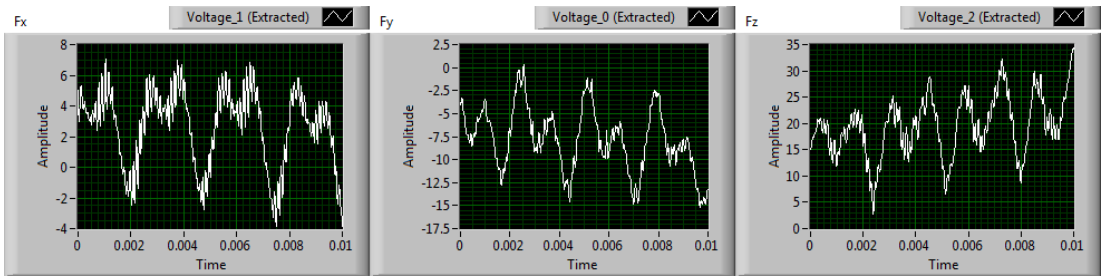

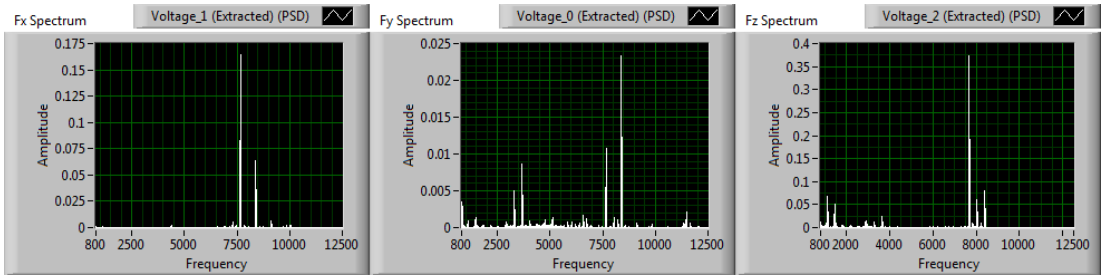

Step 9: (110mins, 33meters)

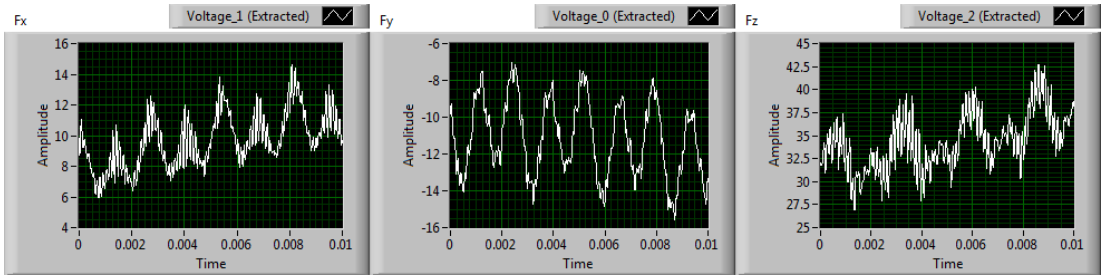

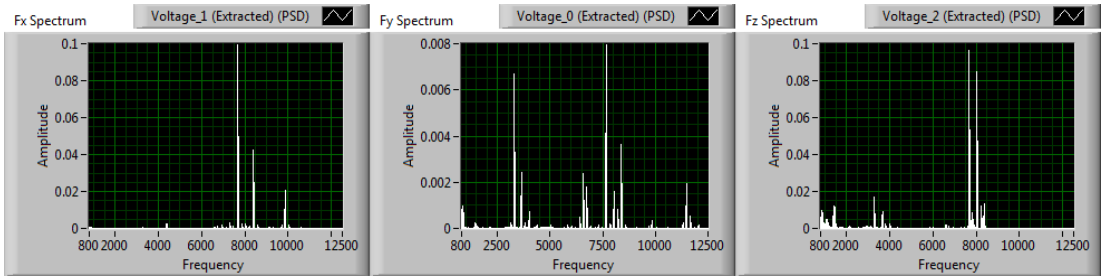

Appendix 7:

Part of the Program to Measure Cutting Edge Radius (MATLAB)

```
% this program calculates the approximate cutting edge radius by selecting
% points that consists of the edge circle based on  least-square algorithm
% and draws the fitted circle and its center.
clc
clear all
[FileName,PathName] = uigetfile('*.jpg','Select the Image');
IM=imread(FileName);
I=rgb2gray(IM);
imshow(I);
% Get size of image.
m = size(I,1);
n = size(I,2);
% Get center point of image for initial positioning.
midy = ceil(m/2);
midx = ceil(n/2);
% get resolution every pixel represents
r=find(I(:,midx)==255,1);
s=find(I(r+3,:)==255,1,'first');
e=find(I(r+3,s:end)<=250,1,'first');
% l=e-s+1; % pixels of the scale bar
l=e;
prompt = {'Enter bar length:','Enter zoom factor:'};
IN=inputdlg(prompt);
bl=str2num(IN{1}); %bar length in um
d=bl/l;
% zoom in on tool tip
zoom(str2num(IN{2}))
```

```
% select points that consists of cutting edge circle
[x, y]=getpts(gcf);

% solve for parameters a, b, and c in the least-squares sense by
% using the backslash operator
abc = [x y ones(length(x),1)] \ -(x.^2+y.^2);
a = abc(1); b = abc(2); c = abc(3);

% calculate the location of the center and the radius
xc = -a/2;
yc = -b/2;
radius = sqrt((xc^2+yc^2)-c);
% display circle
viscircles([xc yc],radius);
% display calculated center
hold on;
plot(xc,yc,'yx','LineWidth',2);
Ra=radius*d;
title(['The estimated radius is ',num2str(Ra),' microns'],'FontSize',16,'Color','b');
```

Appendix 8:

Part of Programs in Force Modeling (MATLAB)

(1) Theoretical instantaneous chip thickness

```
function InsChp=InsChpTck_Gem(DOC)
% programme to compute the instaneous chip thickness taking tool runout into account, without considering minimum chip thickness and elastic restoration
% output matrix is InsChp,
%[time h1 x1(tt1) y1(tt1) xs2(ts2) ys2(ts2) xo1 theta1 ts2 h2 x2(tt2) y2(tt2) xs1(ts1) ys1(ts1) xo2 theta2 ts1]
% used in zhuhanshu


% written by Feifei Jiao
% created on 25/11/2013, last revised on 15:00pm 09/12/2013
% revision made on introduction of DOC and lag angle da
% data saving format
%%
% r: tool runout in micron
% gama: tool runout angle
% Rn: nominal radius in micron
% K: number of tool flutes, tooth order is counted counter-clockwisely
% w: spindle circle speed
% f: feedrate
% t: time
% alpha: actual tooth distribution angle between current edge and edge No.1
% xs x coordinate of point on previous tool pass
% ys y coordinate of point on previous tool pass
% ts time for xs ys coordinate



%%
%initialisation
syms t t1 t2;
Rn=0.000504; %unit in m
f=0.480;     %unit in m/min
w=400*2*pi;  %unit in radian
BgnTim=1;    %unit in seconds
Step=0.000001;
EndTim=1.05;
HexAgl=pi/6;
da=tan(HexAgl)/Rn*(DOC-1)*1e-6; % position angle of the slices at height DOC from the tool end
```

```
K=1;

if K==1
   Ra1=Rn;
   Ra2=0;
   fedth=f/60/w*2*pi;
   angleofrunout=0;
elseif K==2
   fedth=f/60/w*2*pi/2;
   r=10e-6;            % tool runout in m
   gama=165/180*pi;    % from tooth No.1, clockwise it is plus.

% claculate the actual tool radius of each cutting edge
   Ra=zeros(1,2);
   for i=1:2
      Ra(i)=sqrt(Rn^2+r^2-2*Rn*r*cos(2*pi/K*(i-1)+gama));
   end
   Ra1=Ra(1);
   Ra2=Ra(2);

   Diameter=2*Rn;
% calculate actual distribution angle among each tool tip
   if gama>0
      angleofrunout=acos((Ra1^2+Ra2^2-Diameter^2)/2/Ra1/Ra2);
   elseif gama<0
      angleofrunout=2*pi-angleofrunout;
   end
end



Dr=abs(Ra1-Ra2);
Mode=(fedth>=Dr);

MchPmtr=[Ra1 Ra2 f w angleofrunout da Step];
save('MchPmtr.mat','MchPmtr');

%%
% Newton iterative method
% DOC=2;

if Mode==1
for k=0:1       %% number of teeth, for different tooth, equation to compute chip thickness
varies.
   if k==0
      n=1;
      for t=BgnTim:Step:EndTim      %%incremental step is 0.000001
         tst2=t-(2*pi-angleofrunout)/w;
         tst1=t-(2*pi)/w;
         theta=rem(w*t-da,2*pi);    %position angle
         x1=f*t/60+Ra1*sin(w*t-da);
         y1=Ra1*cos(w*t-da);
```

```
xo=f*t/60;
yo=0;
bijiao=(pi+1.5<theta)&&(theta<2*pi-1);
if ~bijiao   %effective angle where material cutting happens
   for i=1:50              %%Newton iterative method
      Fts=cos(w*t-da)*f*(tst2-t)/60+cos(w*t-da)*Ra2*sin(w*tst2-angleofrunout-da)-
sin(w*t-da)*cos(w*tst2-angleofrunout-da)*Ra2;  %equation to judge if two points are
colinear.
      fts=f*cos(w*t-da)/60+w*Ra2*cos(w*t-da)*cos(w*tst2-angleofrunout-
da)+w*Ra2*sin(w*t-da)*sin(w*tst2-angleofrunout-da);
      if abs(Fts)>0.0000001
         tst2=tst2-Fts/fts;  %% ts value for next iteration
      else

         xs2=f*tst2/60+Ra2*sin(w*tst2-angleofrunout-da);
         ys2=Ra2*cos(w*tst2-angleofrunout-da);

         if ((x1-xo)^2+(y1-yo)^2)>((xs2-xo)^2+(ys2-yo)^2)   % save valid data points.
distance between tool center and points on current toolpath should be bigger than that
between tool center and points on previous toolpath.

            for j=1:50              %%Newton iterative method
               FFts=cos(w*t-da)*f*(tst1-t)/60+Ra1*cos(w*t-da)*sin(w*tst1-da)-
Ra1*sin(w*t-da)*cos(w*tst1-da); %equation to judge if two points are colinear.
               ffts=f*cos(w*t-da)/60+w*Ra1*cos(w*t-da)*cos(w*tst1-
da)+w*Ra1*sin(w*t-da)*sin(w*tst1-da);
               if abs(FFts)>0.0000001
                  tst1=tst1-FFts/ffts;  %% ts value for next iteration
               else

                  xs1=f*tst1/60+Ra1*sin(w*tst1-da);
                  ys1=Ra1*cos(w*tst1-da);

                  if ((x1-xo)^2+(y1-yo)^2)>((xs1-xo)^2+(ys1-yo)^2)   % save valid data
points. distance between tool center and points on current toolpath should be bigger than that
between tool center and points on previous toolpath.

                     if ((xs2-xo)^2+(ys2-yo)^2)>((xs1-xo)^2+(ys1-yo)^2)
                        t1pp(n)=tst2;  %time of tooltip on previous toolpath
                        x1pp(n)=f*tst2/60+Ra2*sin(w*tst2-angleofrunout-da);
                        y1pp(n)=Ra2*cos(w*tst2-angleofrunout-da);
                        tt1(n)=t;   %time of tooltip on current toolpath
                        theta1(n)=theta;
                        h1(n)=sqrt((x1-xs2)^2+(y1-ys2)^2);  %chip thickness in real time
%                           ht(n)=Ra1-f*(t-tst2)/60*cos(pi/2+theta)-sqrt(Ra2^2-f^2*(t-
tst2)^2/60^2*(sin(pi/2+theta))^2);
                        n=n+1;
                     else
                        t1pp(n)=tst1;  %time of tooltip on previous toolpath
                        x1pp(n)=f*tst1/60+Ra1*sin(w*tst1-da);
                        y1pp(n)=Ra1*cos(w*tst1-da);
                        tt1(n)=t;   %time of tooltip on current toolpath
```

```
                        theta1(n)=theta;
                        h1(n)=sqrt((x1-xs1)^2+(y1-ys1)^2);  %chip thickness in real time
%                           ht(n)=Ra1-f*(t-tst1)/60*cos(pi/2+theta)-sqrt(Ra2^2-f^2*(t-
tst1)^2/60^2*(sin(pi/2+theta))^2);
                        n=n+1;
                    end
                    break;

                end
            end
        end
        break;
    end
  end
 end
 else
    continue;
 end
end
if exist('tt1','var')
    x1=f.*tt1/60+Ra1*sin(w.*tt1-da);
    y1=Ra1*cos(w.*tt1-da);
    xo=f.*tt1/60;
    yo=0;
    Chp1(:,1)=tt1'; %save useful data in one matrix
    Chp1(:,2)=h1';
    Chp1(:,3)=x1';
    Chp1(:,4)=y1';
    Chp1(:,5)=x1pp';
    Chp1(:,6)=y1pp';
    Chp1(:,7)=xo';
    Chp1(:,8)=theta1';
    Chp1(:,9)=t1pp';
    Chp1(:,17)=0;
%     plot(h1);
else
    tt1=BgnTim:Step:EndTim;
    x1=f.*tt1/60+Ra1*sin(w.*tt1-da);
    y1=Ra1*cos(w.*tt1-da);
    xo=f.*tt1/60;
    theta1=rem(w.*tt1-da,2*pi);
    Chp1(:,1)=tt1';
    Chp1(:,2)=0;
    Chp1(:,3)=x1';
    Chp1(:,4)=y1';
    Chp1(:,7)=xo';
    Chp1(:,8)=theta1';
    Chp1(:,17)=0;
end
%     plot(Chp1(:,3),Chp1(:,4),'g',Chp1(:,5),Chp1(:,6),':g');
hold on
elseif k==1
```

```
n=1;
for t=BgnTim:Step:EndTim
  tst1=t-angleofrunout/w;
  tst2=t-(2*pi)/w;
  x2=f*t/60+Ra2*sin(w*t-angleofrunout-da);
  y2=Ra2*cos(w*t-angleofrunout-da);
  xo=f*t/60;
  yo=0;
  theta=rem(w*t-angleofrunout-da,2*pi);
  bijiao=(pi+1.5<theta)&&(theta<2*pi-1);

  if ~bijiao
    for i=1:50   %Newton iterative method
      Fts=cos(w*t-angleofrunout-da)*f*(tst1-t)/60+cos(w*t-angleofrunout-
da)*Ra1*sin(w*tst1-da)-sin(w*t-angleofrunout-da)*cos(w*tst1-da)*Ra1;
      fts=f*cos(w*t-angleofrunout-da)/60+w*Ra1*cos(w*t-angleofrunout-
da)*cos(w*tst1-da)+w*Ra1*sin(w*t-angleofrunout-da)*sin(w*tst1-da);
      if abs(Fts)>0.0000001
        tst1=tst1-Fts/fts;
      else

        xs1=f*tst1/60+Ra1*sin(w*tst1-da);
        ys1=Ra1*cos(w*tst1-da);

        if ((x2-xo)^2+(y2-yo)^2)>((xs1-xo)^2+(ys1-yo)^2)

          for j=1:50          %%Newton iterative method
            FFts=cos(w*t-angleofrunout-da)*f*(tst2-t)/60+Ra2*cos(w*t-
angleofrunout-da)*sin(w*tst2-angleofrunout-da)-Ra2*sin(w*t-angleofrunout-
da)*cos(w*tst2-angleofrunout-da); %equation to judge if two points are colinear.
            ffts=f*cos(w*t-angleofrunout-da)/60+w*Ra2*cos(w*t-angleofrunout-
da)*cos(w*tst2-angleofrunout-da)+w*Ra2*sin(w*t-angleofrunout-da)*sin(w*tst2-
angleofrunout-da);
            if abs(FFts)>0.0000001
              tst2=tst2-FFts/ffts;  %% ts value for next iteration
            else

              xs2=f*tst2/60+Ra2*sin(w*tst2-angleofrunout-da);
              ys2=Ra2*cos(w*tst2-angleofrunout-da);

              if ((x2-xo)^2+(y2-yo)^2)>((xs2-xo)^2+(ys2-yo)^2)   % save valid data
points. distance between tool center and points on current toolpath should be bigger than that
between tool center and points on previous toolpath.
                if ((xs1-xo)^2+(ys1-yo)^2)>((xs2-xo)^2+(ys2-yo)^2)
                  t2pp(n)=tst1;  %time of tooltip on previous toolpath
                  x2pp(n)=f*tst1/60+Ra1*sin(w*tst1-da);
                  y2pp(n)=Ra1*cos(w*tst1-da);
                  tt2(n)=t;   %time of tooltip on current toolpath
                  theta2(n)=theta;
                  h2(n)=sqrt((x2-xs1)^2+(y2-ys1)^2);  %chip thickness in real time
                  n=n+1;
                else
```

```
                        t2pp(n)=tst2;  %time of tooltip on previous toolpath
                        x2pp(n)=f*tst2/60+Ra2*sin(w*tst2-angleofrunout-da);
                        y2pp(n)=Ra2*cos(w*tst2-angleofrunout-da);
                        tt2(n)=t;   %time of tooltip on current toolpath
                        theta2(n)=theta;
                        h2(n)=sqrt((x2-xs2)^2+(y2-ys2)^2);  %chip thickness in real time
                        n=n+1;
                    end
                    break;
                end
            end
        end

        break;
    end
  end
 end
 else
    continue;
 end
end
if exist('tt2','var')
    x2=f.*tt2/60+Ra2*sin(w.*tt2-angleofrunout-da);
    y2=Ra2*cos(w.*tt2-angleofrunout-da);
    xo=f.*tt2/60;
    yo=0;
    Chp2(:,1)=tt2';
    Chp2(:,10)=h2';
    Chp2(:,11)=x2';
    Chp2(:,12)=y2';
    Chp2(:,13)=x2pp';
    Chp2(:,14)=y2pp';
    Chp2(:,15)=xo';
    Chp2(:,16)=theta2';
    Chp2(:,17)=t2pp';
%     plot(h2);
else
    tt2=BgnTim:Step:EndTim;
    x2=f.*tt2/60+Ra2*sin(w.*tt2-angleofrunout-da);
    y2=Ra2*cos(w.*tt2-angleofrunout-da);
    xo=f.*tt2/60;
    theta2=rem(w.*tt2-angleofrunout-da,2*pi);
    Chp2(:,1)=tt2';
    Chp2(:,10)=0;
    Chp2(:,11)=x2';
    Chp2(:,12)=y2';
    Chp2(:,15)=xo';
    Chp2(:,16)=theta2';
    Chp2(:,17)=0;
end
%     plot(Chp2(:,11),Chp2(:,12),'r',Chp2(:,13),Chp2(:,14),'-.r');
end
```

```
end
ChpSum=[Chp1;Chp2];
elseif Mode==0
    [Rmx Idx]=max([Ra1 Ra2]);
    n=1;
    for t=BgnTim:Step:EndTim      %%incremental step is 0.0001
      ts=t-(2*pi)/w;
      theta=rem(w*t-(Idx-1)*angleofrunout-da,2*pi);    %position angle
      bijiao=(pi+1.5<theta)&&(theta<2*pi-1);
      if ~bijiao   %effective angle where material cutting happens
        for i=1:100              %%Newton iterative method
          Fts=cos(w*t-(Idx-1)*angleofrunout-da)*f*(ts-t)/60+Rmx*cos(w*t-(Idx-
1)*angleofrunout-da)*sin(w*ts-(Idx-1)*angleofrunout-da)-Rmx*sin(w*t-(Idx-
1)*angleofrunout-da)*cos(w*ts-(Idx-1)*angleofrunout-da); %equation to judge if two points
are colinear.
          fts=f*cos(w*t-(Idx-1)*angleofrunout-da)/60+w*Rmx*cos(w*t-(Idx-
1)*angleofrunout-da)*cos(w*ts-(Idx-1)*angleofrunout-da)+w*Rmx*sin(w*t-(Idx-
1)*angleofrunout-da)*sin(w*ts-(Idx-1)*angleofrunout-da);
          if abs(Fts)>0.0000001
            ts=ts-Fts/fts;  %% ts value for next iteration
          else
            x1=f*t/60+Rmx*sin(w*t-(Idx-1)*angleofrunout-da);
            y1=Rmx*cos(w*t-(Idx-1)*angleofrunout-da);
            xs2=f*ts/60+Rmx*sin(w*ts-(Idx-1)*angleofrunout-da);
            ys2=Rmx*cos(w*ts-(Idx-1)*angleofrunout-da);
            xo=f*t/60;
            yo=0;
            if  ((x1-xo)^2+(y1-yo)^2)>=((xs2-xo)^2+(ys2-yo)^2)      % save valid data
points. distance between tool center and points on current toolpath should be bigger than that
between tool center and points on previous toolpath.
              ts2(n)=ts;  %time of tooltip on previous toolpath
              tt1(n)=t;   %time of tooltip on current toolpath
              theta1(n)=theta;
              h1(n)=sqrt((x1-xs2)^2+(y1-ys2)^2);  %chip thickness in real time
              n=n+1;
              a=[x1,xs2];
              b=[y1,ys2];
              break;
            end
          end
        end
      else
        continue;
      end
    end
    x1=f.*tt1/60+Rmx*sin(w.*tt1-(Idx-1)*angleofrunout-da);
    y1=Rmx*cos(w.*tt1-(Idx-1)*angleofrunout-da);
    xs2=f.*ts2/60+Rmx*sin(w.*ts2-(Idx-1)*angleofrunout-da);
    ys2=Rmx*cos(w.*ts2-(Idx-1)*angleofrunout-da);
    xo=f.*tt1/60;
    yo=0;
    Chp1=zeros(length(tt1),17);
```

```
        Chp1(:,1)=tt1'; %save useful data in one matrix
        Chp1(:,2+(Idx-1)*8)=h1';
        Chp1(:,3+(Idx-1)*8)=x1';
        Chp1(:,4+(Idx-1)*8)=y1';
        Chp1(:,5+(Idx-1)*8)=xs2';
        Chp1(:,6+(Idx-1)*8)=ys2';
        Chp1(:,7+(Idx-1)*8)=xo';
        Chp1(:,8+(Idx-1)*8)=theta1';
        Chp1(:,9+(Idx-1)*8)=ts2';

        [Rmn Ide]=min([Ra1 Ra2]);
        tt3=find((tt1(2:end)-tt1(1:end-1))>10*Step);
        tt2=0;
        for i=1:length(tt3)
            tem=tt1(tt3(i)):Step:tt1(tt3(i)+1);
            tt2=[tt2,tem];
        end
        tt2(1)=[];
        x2=f.*tt2/60+Rmn*sin(w.*tt2-(Ide-1)*angleofrunout-da);
        y2=Rmn*cos(w.*tt2-(Ide-1)*angleofrunout-da);
        xo=f.*tt2/60;
        theta2=rem(w.*tt2-(Ide-1)*angleofrunout-da,2*pi);
        Chp2=zeros(length(tt2),17);
        Chp2(:,1)=tt2';
        Chp2(:,2+(Ide-1)*8)=0;
        Chp2(:,3+(Ide-1)*8)=x2';
        Chp2(:,4+(Ide-1)*8)=y2';
        Chp2(:,7+(Ide-1)*8)=xo';
        Chp2(:,8+(Ide-1)*8)=theta2';
        Chp2(:,9+(Ide-1)*8)=0;
        ChpSum=[Chp1;Chp2];
    end
    %%
    % reshape the chip thickness matrix and delete redundant data points
    % save data into struct InsChp

    GeoChp=sortrows(ChpSum,1);
    [row column]=size(GeoChp);
    % kk=1;
    for(kk=1:row-1)
    %     if kk==58677
    %         keyboard
    %     end
       vfst=GeoChp(kk,1);
       vsnd=GeoChp(kk+1,1);
       if vfst==vsnd
          GeoChp(kk,2:column)=GeoChp(kk,2:column)+GeoChp(kk+1,2:column);
          GeoChp(kk+1,1:column)=[0];
       else
          continue;
       end
    end
```

```
GeoChp(any(GeoChp,2)==0,:)=[];
InsChp=GeoChp;

% save('InsChp.mat','InsChp');
```

(2) Actual instantaneous chip thickness taking minimum chip thickness into account

```
function [PrvPath RealCT AcuCT]=InsChpTck_Real(InsChp,k,MCT)
% program to compute real time chip thickness considering material elastic restoriation and
minimum chip thickness effect
% used in zhuhanshu

% PrvPath contains all the points representing actual toothpath left after machining.
% RealCT contains real chip thickness
% AcuCT is mostly the same with RealCT depletion of  repetitive dimension,it will be used
in future programming.

% writen by Feifei Jiao
% created 27/11/2013, last revised 12:20pm 02/12/2013
% revision made to expand the toothpath matrix to form full-length chip

% clear all
% load('InsChp.mat');
%
% syms k      %% elastic coefficient, only applicable when chip thickness is below MCT
% syms MCT    %% minimum chip thickness
%
% k=0.4;
% MCT=20;

%%
% pick out each toothpath and put it into a cell array, then expand
% toothpath 2.....16

[toothpath tag]=readsplitdata(InsChp);
[d n]=size(toothpath);
% keyboard
for i=1:n
   if ~isempty(toothpath{1,i})
      Etoothpath(i)={Epndtothpth(toothpath{1,i},i,100,tag)};
   else
      break
   end
end
%%
%PrvPath saves array of chip thickness on current toothpath and points left
%behind cutting tooth first toolpath. [time chipthickness x y]
% PrvPath=[t h x y theta ts]
Le1=length(toothpath{1,5}(:,1));
Le2=length(toothpath{1,4}(:,1));
if Le1>=Le2
```

```
  for j=1:Le1
    if toothpath{1,5}(j,2)<MCT
      PrvPath{1,1}(j,1)=toothpath{1,5}(j,1);
      PrvPath{1,1}(j,2)=toothpath{1,5}(j,2);                    %chip thickness of the
first toothpath, under MCT no chip will be formed, this value will be used to calculate
rubbing and ploughing force
      PrvPath{1,1}(j,3)=toothpath{1,5}(j,3)-k*(toothpath{1,5}(j,3)-toothpath{1,5}(j,5));
      PrvPath{1,1}(j,4)=toothpath{1,5}(j,4)-k*(toothpath{1,5}(j,4)-toothpath{1,5}(j,6));
      PrvPath{1,1}(j,5)=toothpath{1,5}(j,8);
      PrvPath{1,1}(j,6)=toothpath{1,5}(j,9);
    else
      PrvPath{1,1}(j,1)=toothpath{1,5}(j,1);
      PrvPath{1,1}(j,2)=toothpath{1,5}(j,2);                    %chip thickness of the
first toothpath, when bigger than MCT, material will be removed completely.
      PrvPath{1,1}(j,3)=toothpath{1,5}(j,3);
      PrvPath{1,1}(j,4)=toothpath{1,5}(j,4);
      PrvPath{1,1}(j,5)=toothpath{1,5}(j,8);
      PrvPath{1,1}(j,6)=toothpath{1,5}(j,9);
    end
  end
else
  yf=toothpath{1,5}(1,4);
  pfs=find(toothpath{1,4}(:,4)<=yf);pf=pfs(1);
  PrvPath{1,1}(1:pf-1,3)=toothpath{1,4}(1:pf-1,3);
  PrvPath{1,1}(1:pf-1,4)=toothpath{1,4}(1:pf-1,4);
  ye=toothpath{1,5}(end,4);
  pes=find(toothpath{1,4}(:,4)<=ye);pe=pes(1);
  el=length(toothpath{1,4}(pe:end,4));
  PrvPath{1,1}(Le1+pf:Le1+pf+el-1,3)=toothpath{1,4}(pe:end,3);
  PrvPath{1,1}(Le1+pf:Le1+pf+el-1,4)=toothpath{1,4}(pe:end,4);
  for j=pf:Le1+pf-1
    if toothpath{1,5}(j-pf+1,2)<MCT
      PrvPath{1,1}(j,1)=toothpath{1,5}(j-pf+1,1);
      PrvPath{1,1}(j,2)=toothpath{1,5}(j-pf+1,2);                %chip thickness
of the first toothpath, under MCT no chip will be formed, this value will be used to calculate
rubbing and ploughing force
      PrvPath{1,1}(j,3)=toothpath{1,5}(j-pf+1,3)-k*(toothpath{1,5}(j-pf+1,3)-
toothpath{1,5}(j-pf+1,5));
      PrvPath{1,1}(j,4)=toothpath{1,5}(j-pf+1,4)-k*(toothpath{1,5}(j-pf+1,4)-
toothpath{1,5}(j-pf+1,6));
      PrvPath{1,1}(j,5)=toothpath{1,5}(j-pf+1,8);
      PrvPath{1,1}(j,6)=toothpath{1,5}(j-pf+1,9);
    else
      PrvPath{1,1}(j,1)=toothpath{1,5}(j-pf+1,1);
      PrvPath{1,1}(j,2)=toothpath{1,5}(j-pf+1,2);                %chip thickness
of the first toothpath, when bigger than MCT, material will be removed completely.
      PrvPath{1,1}(j,3)=toothpath{1,5}(j-pf+1,3);
      PrvPath{1,1}(j,4)=toothpath{1,5}(j-pf+1,4);
      PrvPath{1,1}(j,5)=toothpath{1,5}(j-pf+1,8);
      PrvPath{1,1}(j,6)=toothpath{1,5}(j-pf+1,9);
    end
  end
```

```
end
%%
% calculate real chip thickness
r=length(Etoothpath);

for i=6:r
  tag1=0;
  Li=length(toothpath{1,i}(:,1));
  Lp=length(toothpath{1,i-1}(:,1));
  if Li>=Lp
    [hang lie]=size(Etoothpath{i});
    for j=1:hang
      x=Etoothpath{1,i}(j,3);
      y=Etoothpath{1,i}(j,4);
      Cent_x=Etoothpath{1,i}(j,7);
      [Cod Sgn]=segmentsIntr(Cent_x,0,x,y,PrvPath{1,i-5});   %sgn indicates the state of the intersecting lines, 0 means no intersection for tool tip and previous toothpath, 1 means it exists, -1 means the two lines overlap
      if Sgn==0
        continue
      elseif Sgn==1
        Chp=sqrt((Cod(1)-Etoothpath{1,i}(j,3))^2+(Cod(2)-Etoothpath{1,i}(j,4))^2);
        if Chp<MCT
          PrvPath{1,i-4}(j,1)=Etoothpath{1,i}(j,1);
          PrvPath{1,i-4}(j,2)=Chp;                    %real chip thickness of ith toothpath based on previous toothpath.
          PrvPath{1,i-4}(j,3)=Etoothpath{1,i}(j,3)-k*(Etoothpath{1,i}(j,3)-Cod(1));  %toothpath after removing material
          PrvPath{1,i-4}(j,4)=Etoothpath{1,i}(j,4)-k*(Etoothpath{1,i}(j,4)-Cod(2));
          PrvPath{1,i-4}(j,5)=Etoothpath{1,i}(j,8);
          PrvPath{1,i-4}(j,6)=Etoothpath{1,i}(j,9);
        else
          PrvPath{1,i-4}(j,1)=Etoothpath{1,i}(j,1);
          PrvPath{1,i-4}(j,2)=Chp;                    %real chip thickness of ith toothpath based on previous toothpath.
          PrvPath{1,i-4}(j,3)=Etoothpath{1,i}(j,3);          %toothpath after removing material
          PrvPath{1,i-4}(j,4)=Etoothpath{1,i}(j,4);
          PrvPath{1,i-4}(j,5)=Etoothpath{1,i}(j,8);
          PrvPath{1,i-4}(j,6)=Etoothpath{1,i}(j,9);
        end
        tag1=1;
      elseif Sgn==-1
        Chp=sqrt((Cod(1)-Etoothpath{1,i}(j,3))^2+(Cod(2)-Etoothpath{1,i}(j,4))^2);

        if Chp<MCT
          PrvPath{1,i-4}(j,1)=Etoothpath{1,i}(j,1);
          PrvPath{1,i-4}(j,2)=Chp;                    %real chip thickness of ith toothpath based on previous toothpath.
          PrvPath{1,i-4}(j,3)=Etoothpath{1,i}(j,3)-k*(Etoothpath{1,i}(j,3)-Cod(1));  %toothpath after removing material
          PrvPath{1,i-4}(j,4)=Etoothpath{1,i}(j,4)-k*(Etoothpath{1,i}(j,4)-Cod(2));
```

```
                PrvPath{1,i-4}(j,5)=Etoothpath{1,i}(j,8);
                PrvPath{1,i-4}(j,6)=Etoothpath{1,i}(j,9);
            else
                PrvPath{1,i-4}(j,1)=Etoothpath{1,i}(j,1);
                PrvPath{1,i-4}(j,2)=Chp;                    %real chip thickness of
ith toothpath based on previous toothpath.
                PrvPath{1,i-4}(j,3)=Etoothpath{1,i}(j,3);          %toothpath after
removing material
                PrvPath{1,i-4}(j,4)=Etoothpath{1,i}(j,4);
                PrvPath{1,i-4}(j,5)=Etoothpath{1,i}(j,8);
                PrvPath{1,i-4}(j,6)=Etoothpath{1,i}(j,9);
            end
            tag1=1;
        end
    end

    if tag1==1
        ZeroM=find(PrvPath{1,i-4}(:,1)>0); %delete reduant points
        L_one=length(ZeroM);
        PrvPath{1,i-4}(1:ZeroM(1)-1,:)=[];
        VldL=length(PrvPath{1,i-4}(:,1));
        PrvPath{1,i-4}(find(PrvPath{1,i-4}(:,1)==0),:)=[];
        Etoothpath{1,i}(1:ZeroM(1)-1,:)=[];
        Etoothpath{1,i}(VldL+1:end,:)=[];
    elseif tag1==0                  %tag1 indicates if the current position of tool tip crosses
the previous toothpath, if not, tag1 remains 0 and it follows tha same procedure as first
toothpath
        rows=length(toothpath{1,i-1}(:,1));
        for j=1:rows
                PrvPath{1,i-4}(j,1)=toothpath{1,i}(j,1);
                PrvPath{1,i-4}(j,2)=0;                      %chip thickness of the first
toothpath, under MCT no chip will be formed, this value will be used to calculate rubbing
and ploughing force
                PrvPath{1,i-4}(j,3)=toothpath{1,i-1}(j,3);
                PrvPath{1,i-4}(j,4)=toothpath{1,i-1}(j,4);
                PrvPath{1,i-4}(j,5)=0;
                PrvPath{1,i-4}(j,6)=0;
        end
    end
  else
    yf=toothpath{1,i}(1,4);
    pfs=find(toothpath{1,i-1}(:,4)<=yf);pf=pfs(1);
    PrvPath{1,i-4}(1:pf-1,3)=toothpath{1,i-1}(1:pf-1,3);
    PrvPath{1,i-4}(1:pf-1,4)=toothpath{1,i-1}(1:pf-1,4);
    ye=toothpath{1,i}(end,4);
    pes=find(toothpath{1,i-1}(:,4)<=ye);pe=pes(1);
    el=length(toothpath{1,i-1}(pe:end,4));
    PrvPath{1,i-4}(Li+pf:Li+pf+el-1,3)=toothpath{1,i-1}(pe:end,3);
    PrvPath{1,i-4}(Li+pf:Li+pf+el-1,4)=toothpath{1,i-1}(pe:end,4);
    for j=pf:Li+pf-1
        if toothpath{1,i}(j-pf+1,2)<MCT
            PrvPath{1,i-4}(j,1)=toothpath{1,i}(j-pf+1,1);
```

```
            PrvPath{1,i-4}(j,2)=toothpath{1,i}(j-pf+1,2);                    %chip
thickness of the first toothpath, under MCT no chip will be formed, this value will be used to
calculate rubbing and ploughing force
            PrvPath{1,i-4}(j,3)=toothpath{1,i}(j-pf+1,3)-k*(toothpath{1,i}(j-pf+1,3)-
toothpath{1,i}(j-pf+1,5));
            PrvPath{1,i-4}(j,4)=toothpath{1,i}(j-pf+1,4)-k*(toothpath{1,i}(j-pf+1,4)-
toothpath{1,i}(j-pf+1,6));
            PrvPath{1,i-4}(j,5)=toothpath{1,i}(j-pf+1,8);
            PrvPath{1,i-4}(j,6)=toothpath{1,i}(j-pf+1,9);
         else
            PrvPath{1,i-4}(j,1)=toothpath{1,i}(j-pf+1,1);
            PrvPath{1,i-4}(j,2)=toothpath{1,i}(j-pf+1,2);                    %chip
thickness of the first toothpath, when bigger than MCT, material will be removed completely.
            PrvPath{1,i-4}(j,3)=toothpath{1,i}(j-pf+1,3);
            PrvPath{1,i-4}(j,4)=toothpath{1,i}(j-pf+1,4);
            PrvPath{1,i-4}(j,5)=toothpath{1,i}(j-pf+1,8);
            PrvPath{1,i-4}(j,6)=toothpath{1,i}(j-pf+1,9);
         end
      end
   end
end

%%
% keyboard

[dim cntr]=size(PrvPath);
[row1 cln1]=size(PrvPath{1,1});
if tag==1                        % tag represents engagement of tool and material, 1 means tip
1 engages material first, 2 means the second tip, 3 means only tip 1 removes material, 4
means only tip 2 cuts.
   RealCT(1:row1,1:6)=PrvPath{1,1};
   RealCT(1:row1,7:12)=0;
   for i=2:cntr
      if rem(i,2)==0
         [Ite cln]=size(RealCT);
         [hang1 lie1]=size(PrvPath{1,i});
         a=find(abs(PrvPath{1,i}(:,1)-RealCT(end,1))<1e-10);
         Mrk=isempty(a);
         if Mrk==1
            RealCT(Ite+1:Ite+hang1,7:12)=PrvPath{1,i};
         else
            [rowp clmp]=size(PrvPath{1,i-1});
            if rowp>=a
               b=Ite-a;
               RealCT(b+1:b+hang1,7:12)=PrvPath{1,i};
            else
               InM(1:hang1,1:6)=PrvPath{1,i};
               InM(a-rowp+1:a,7:12)=PrvPath{1,i-1};
               RealCT=[RealCT(1:end-rowp,:);InM];
            end
         end
      elseif rem(i,2)==1
```

```
            [Ite cln]=size(RealCT);
            [hang1 lie1]=size(PrvPath{1,i});
            Fnum=PrvPath{1,i}(:,1);
            a=find(abs((Fnum-RealCT(end,7)))<1e-10);
            Mrk=isempty(a);
            if Mrk==1
               RealCT(Ite+1:Ite+hang1,1:6)=PrvPath{1,i};
            else
               [rowp clmp]=size(PrvPath{1,i-1});
               if rowp>=a
                  b=Ite-a;
                  RealCT(b+1:b+hang1,1:6)=PrvPath{1,i};
               else
                  InM(1:hang1,7:12)=PrvPath{1,i};
                  InM(a-rowp+1:a,1:6)=PrvPath{1,i-1};
                  RealCT=[RealCT(1:end-rowp,:);InM];
               end
            end
         end
      end
   elseif tag==2
      RealCT(1:row1,7:12)=PrvPath{1,1};
      RealCT(1:row1,1:6)=0;
      for i=2:cntr
         if rem(i,2)==0
            [Ite cln]=size(RealCT);
            [hang1 lie1]=size(PrvPath{1,i});
            a=find(abs(PrvPath{1,i}(:,1)-RealCT(end,7))<1e-10);
            Mrk=isempty(a);
            if Mrk==1
               RealCT(Ite+1:Ite+hang1,1:6)=PrvPath{1,i};
            else
               [rowp clmp]=size(PrvPath{1,i-1});
               if rowp>=a
                  b=Ite-a;
                  RealCT(b+1:b+hang1,1:6)=PrvPath{1,i};
               else
                  InM(1:hang1,1:6)=PrvPath{1,i};
                  InM(a-rowp+1:a,7:12)=PrvPath{1,i-1};
                  RealCT=[RealCT(1:end-rowp,:);InM];
               end
            end
         elseif rem(i,2)==1
            [Ite cln]=size(RealCT);
            [hang1 lie1]=size(PrvPath{1,i});
            Fnum=PrvPath{1,i}(:,1);
            a=find(abs((Fnum-RealCT(end,1)))<1e-10);
            Mrk=isempty(a);
            if Mrk==1
               RealCT(Ite+1:Ite+hang1,7:12)=PrvPath{1,i};
            else
               [rowp clmp]=size(PrvPath{1,i-1});
```

```
            if rowp>=a
               b=Ite-a;
               RealCT(b+1:b+hang1,7:12)=PrvPath{1,i};
            else
               InM(1:hang1,7:12)=PrvPath{1,i};
               InM(a-rowp+1:a,1:6)=PrvPath{1,i-1};
               RealCT=[RealCT(1:end-rowp,:);InM];
            end
         end
      end
   end
elseif tag==3
   RealCT(1:row1,1:6)=PrvPath{1,1};
   RealCT(1:row1,7:12)=0;
   for i=2:cntr
      [Ite cln]=size(RealCT);
      [hang1 lie1]=size(PrvPath{1,i});
      RealCT(Ite+1:Ite+hang1,1:6)=PrvPath{1,i};
      RealCT(Ite+1:Ite+hang1,7:12)=0;
   end
elseif tag==4
   RealCT(1:row1,8:12)=PrvPath{1,1}(:,2:6);
   RealCT(1:row1,1)=PrvPath{1,1}(:,1);
   RealCT(1:row1,2:7)=0;
   for i=2:cntr
      [Ite cln]=size(RealCT);
      [hang1 lie1]=size(PrvPath{1,i});
      RealCT(Ite+1:Ite+hang1,8:12)=PrvPath{1,i}(:,2:6);
      RealCT(Ite+1:Ite+hang1,1)=PrvPath{1,i}(:,1);
      RealCT(Ite+1:Ite+hang1,2:7)=0;
   end
end

%% merge two matrix and put it in the order of time

AcuCT=RealCT;
if tag==1||tag==2
   c=AcuCT(:,1)&AcuCT(:,7);
   d=find(c);
   [hang2 lie2]=size(d);
   for i=1:hang2
      com=(abs(AcuCT(d(i),1)-AcuCT(d(i),7))<1e-10);
      if com==1
         AcuCT(d(i),7)=0;
      else
         [hang3 lie3]=size(AcuCT);
         AcuCT(hang3+1,1)=AcuCT(d(i),7);
         AcuCT(d(i),7)=0;
      end
   end

   AcuCT(:,1)=AcuCT(:,1)+AcuCT(:,7);
```

```
    AcuCT(:,7)=[];
    AcuCT=sortrows(AcuCT,1);
    AcuCT(find(AcuCT(:,1)==0),:)=[];
end
```

```
%%
% plot residual toothpath.

kk=length(PrvPath);
for i=5:kk
    plot(PrvPath{1,i-4}(:,3),PrvPath{1,i-4}(:,4),'r',toothpath{1,i}(:,3),toothpath{1,i}(:,4),'b');
    set(gcf,'units','normalized','position',[0,0,1,1]);
    hold on
%   plot(PrvPath{1,i+1}(:,3),PrvPath{1,i+1}(:,4),'b');
%   plot(Etoothpath{1,i}(:,3),Etoothpath{1,i}(:,4),'b');
%
%   set(gcf,'units','normalized','position',[0,0,1,1]);
end
% figure
```

(3) Computation of the transfer function of the filter

```
clear all
clc
num=[917408474.463208,7742917621693.31,9.72666477715286e+17,4.73157188131948e+
21,2.63656011749803e+26,3.75238552054343e+29,1.15282452286532e+34];          %
num denotes the numerator vector of the transfer function
den=[1,27449.7678684531,1959558785.57355,40046525763238.8,1.09338717152753e+18,
1.20047369589355e+22,1.99232497658009e+26,5.83482899336466e+29,6.6980013661924
0e+33];      % den denotes the denominator vector of the transfer function
%%%%%%%%%%%%%%%%%%%%%%%%%%%%%%%%%%%%%%%%%%%%%%%%%%%%%%%%%%%%%%%%%%%%%%%%%%%%
% create state space model with/without balancing %
% PTF=tf(num,den);              % create transfer function model
% [AA BB CC DD]=tf2ss(num,den);   % create transfer function
% PSSM=ss(AA,BB,CC,DD);          % create state space model
% [T B] = balance(PSSM.a);
% sysb = ss2ss(PSSM,inv(T));
% % sysb=PSSM;
%%%%%%%%%%%%%%%%%%%%%%%%%%%%%%%%%%%%%%%%%%%%%%%%%%%%%%%%%%%%%%%%%%%%%%%%%%%%
% create state space model and prescale it by using function 'prescale' %
PTF=tf(num,den);              % create transfer function model
```

```
[AA BB CC DD]=tf2ss(num,den);   % create transfer function
PSSM=ss(AA,BB,CC,DD);
sysb=prescale(PSSM);
%%%%%%%%%%%%%%%%%%%%%%%%%%%%%%%%%%%%%%%%%%%%%%
%%%%%%%%%%%%%%%%%%%%%%%%%%%%%%%%%%%%%%%%%%%
% % convert transfer function model to state space model %
% PTF=tf(num,den);              % create transfer function model
% PSSM=ss(PTF,'min');             % create state space model, ss  returns a modified version of
the controllable canonical form.
%                               % It uses an algorithm similar to tf2ss, but further rescales the state
vector to compress the numerical range in state matrix A and
%                            % to improve numerics in subsequent computations.
% [T B] = balance(PSSM.a);        % balancing turns out to be unnecessary.
% sysb = ss2ss(PSSM,inv(T));
%%%%%%%%%%%%%%%%%%%%%%%%%%%%%%%%%%%%%%%%%%%%%%
%%%%%%%%%%%%%%%%%%%%%%%%%%%%%%%%%%%%%%%%%%%
Ae=[sysb.a sysb.b];Ae(length(sysb.a)+1,length(sysb.a)+1)=0; % create new state matrix of
the kalman filter
Ce=[sysb.c 0];   % create new state matrix of the kalman filter
Q=1e9;           % system noise covariance
R=0.08;         % measurement noise covariance

% [X,L,G] = care(Ae',Ce',Q*eye(length(Ae)),R);   % function 'care' computes the unique
solution X of the continuous-time algebraic Riccati equation
syms s
Co=[zeros(1,length(Ce)-1) 1];
H=[Ae' -Ce'*R^(-1)*Ce;-Co'*Q*Co -Ae];
[VV DD]=reig(H);
PPPP=VV(length(Ae)+1:end,1:length(Ae))*VV(1:length(Ae),1:length(Ae))^(-1);
G=PPPP*Ce'*R^(-1);
% INADJ=adjoint(s*eye(length(Ae))-Ae+G'*Ce)/det(s*eye(length(Ae))-Ae+G'*Ce);
INAD=s*eye(length(Ae))-Ae+G*Ce;
TTKALF=Co*INAD^(-1)*G; % this equation computes the transfer funciton of the
constructed kalman filter.
[N D]=numden(TTKALF);
cnum=sym2poly(coeffs(N)); % find the coefficients of the numerator
cden=sym2poly(coeffs(D)); % find the coefficients of the denominator
scnum=fliplr(cnum/cden(end));
scden=fliplr(cden/cden(end));
Ftf=tf(scnum,scden);
figure;
h=bodeplot(Ftf,'r',PTF,'g',Ftf*PTF,'y--');
setoptions(h,'FreqUnits','Hz');
setoptions(h,'FreqScale','linear');
setoptions(h,'MagUnits','abs');
setoptions(h,'MagScale','linear');
% setoptions(h,'Xlim',{[0 2500]});

KK=Ae-G*Ce;
AAEE=exp(KK*1.953124999998224e-05);
[rree ccee]=size(KK);
for i=1:rree
```

```
    for j=1:ccee
        fun=@(t) exp(KK(i,j)*t);
        KKK(i,j)=integral(fun,0,1.953124999998224e-05);
    end
end
```